Matthias Steffan, Dipl.-Ing.

Machine-Tool for Research in Synchronous Grinding

Doctoral Thesis

submitted in fulfilment of the requirements

for the degree of doctor of engineering (Dr.techn.)

to the Faculty of Mechanical Engineering and Economic Sciences at

Graz University of Technology

Supervisor

Univ.-Prof. Dipl.-Ing. Dr.techn. Franz Haas
Institute of Production Engineering
Graz University of Technology

Assessors

Univ.-Prof. Dipl.-Ing. Dr.techn. Franz Haas

Univ.-Prof. Dipl.-Ing. Dr.techn. Friedrich Bleicher
Institute of Production Engineering and Laser Technology
Vienna University of Technology

Graz, Dec. 2017

Statutory Declaration

I declare that I have authored this thesis independently, that I have not used other than the declared sources / resources, and that I have explicitly marked all material which has been quoted either literally or by content from the used sources.

Graz, 12. Dec. 2017 _____

date signature

Eidesstattliche Erklärung

Ich erkläre an Eides statt, dass ich die vorliegende Arbeit selbstständig verfasst, andere als die angegebenen Quellen / Hilfsmittel nicht benutzt, und die den benutzten Quellen wörtlich und inhaltlich entnommenen Stellen als solche kenntlich gemacht habe.

Graz, 12. Dec. 2017 _____

date signature

Preface

The presented thesis evolved in the context with my activities as research associate at the Institute of Production Engineering (IFT) at Graz University of Technology. Therefore, I want to thank my supervisor Prof. Franz Haas, head of the Institute, for his support and confidence.

Moreover, I want to thank Prof. Friedrich Bleicher, head of the Institute of Production Engineering and Laser Technology at Vienna University of Technology, for the assessment of my written work and for his participation at my oral examination.

I also want to thank my colleges at IFT who supported mentally and provided amusement in times needed.

The most, I want to thank my family.
Special thanks to my parents for their benefit during my entire studies.
Huge thanks to Anna & Paul for their patients and endorsement.

Graz, Dec. 2017
Matthias Steffan

Abstract

The presented thesis examines the novel finishing technology of RPM-Synchronous Grinding. In addition, the development and application of a tailor-made machine tool system for research on high-end finishing processes constitute the core of this work.

The layout of the grinding machine considers both, the conventional high-end grinding process and the RPM-Synchronous Grinding process. The design, the power units, the drive systems and the machine control functionalities are all customized for research on present and future topics concerning circular and non-circular grinding. A light-weight structure of the compound X1-Z1-axis slide in combination with hydrostatic bearings facilitates an increase in efficiency of conventional non-circular grinding and speeds up the dressing procedure of non-circular grinding wheels for the RPM-Synchronous Non-Circular Grinding process.

By means of detailed parameter studies and by benchmarking of different tools with respect to grain size, bonding and porosity, process windows are found for the RPM-Synchronous Grinding process. The special kinematics of the process, in which the same cutting edges on the tool exclusively machine the same points on the workpiece, opens up immense potential. Micro-structures such as riblets for minimization of frictional as well as macro-structures like arbitrary three-dimensional non-circular and non-cylindrical geometries can be produced. Moreover, utilizing the RPM-Synchronous Grinding process, these two properties of the macro and micro-structures can be produced on the same workpiece in the same clamping situation in only one plunge grinding cycle for roughing and one for finishing.

The results of the work show that the high requirements in surface qualities can be reached by means of the RPM-Synchronous Grinding process, which meet the standards for finishing for the first time. An external control loop, which has been developed during the FFG project Adaptive Grinding Process (AGriPro), facilitates to achieve this goal. It enables a process adaption which is mainly deployed at the finishing procedure. In case of roughing, it is proven that the same material removal rates compared to conventional grinding can be achieved. Thereby, a reduction of machining forces and thus a reduced grinding wheel wear are simultaneously documented.

Kurzfassung

Die vorliegende Dissertation untersucht die neuartige Finishing-Technologie des Drehzahlsynchron-Schleifens. Außerdem stellt die Entwicklung und Anwendung einer maßgeschneiderten Werkzeugmaschine für die Erforschung von Hochleistungs-Schleifprozessen den Kern dieser Arbeit dar.

Die Betrachtung der Maschinenkonstruktion befasst sich sowohl mit der Umsetzung von konventionellem Hochleistungsschleifen als auch mit dem Drehzahlsynchron-Schleifen. Die Konstruktion und Auslegung sowie die Antriebs- und Führungskomponenten samt dessen Steuerung sind speziell für die Untersuchung aktueller und zukünftiger Forschungsthemen das Rund- und Unrundschleifen betreffend ausgelegt. Eine gewichtsoptimierte Struktur des Kreuzschlittens der X1-Z1-Achse in Kombination mit hydrostatischen Lagerungen ermöglicht die Effizienzsteigerung des konventionellen Unrundschleifprozesses und beschleunigt das Abrichten von unrunden oder strukturierten Schleifscheiben für den Drehzahlsynchron-Schleifprozess.

Durch detaillierte Parameterstudien und durch den Benchmark verschiedener Werkzeuge hinsichtlich Körnung, Bindung und Porosität werden Prozessfenster für den Drehzahlsynchron-Schleifprozess gefunden. Die spezielle Kinematik des Prozesses, bei welcher dieselben Schneidkanten an der Schleifscheibe immer dieselben Punkte am Werkstück bearbeiten, eröffnet großes Potential. So können Mikro-Strukturen wie Riblets zur Reibungsminimierung und Makro-Stukturen in Form von beliebigen dreidimensional unrunden Geometrien hergestellt werden. Darüber hinaus können mithilfe des Drehzahlsynchron-Schleifprozesses diese beiden Eigenschaften der Makro und Mirko-Strukturierung auf demselben Bauteil unter derselben Aufspannung in nur einem Einstech-Schleifzyklus für Schruppen und einem für Schlichten abgebildet werden.

Die Ergebnisse der Arbeit zeigen erstmals, dass mithilfe des Drehzahlsynchron-Schleifens Oberflächengüten erzeugt werden können, die den hohen Anforderungen an Finishing-Verfahren entsprechen. Ein externer Regelkreis, welcher im Zuge des FFG Projektes Adaptive Grinding Process (AGriPro) entwickelt wurde, hilft das Ziel zu erreichen. Dieser ermöglicht eine Prozesssadaptierung, welche vorrangig beim Schlichten eingesetzt wird. Beim Schruppen können nachweislich gleiche Zeitspanvolumina wie beim konventionellen Schleifen erreicht werden und das bei gleichzeitig reduzierten Bearbeitungskräften und somit reduziertem Schleifscheiben-Verschleiß.

Symbols

Symbol	Unit	Designation
a	$m \cdot s^{-2}$	acceleration
A	°	rotation around X-axis
a_d	mm	depth of cut at dressing
a_e	mm	amount of infeed / depth of cut
a_E	mm	major axis of ellipse
A_k	mm^2	contact area
B	°	rotation around Y-axis
$b_{c_{eff}}$	mm	effective cutting width
b_d	mm	active dressing tool width
b_E	mm	minor axis of ellipse
b_g	mm	width of grinding wheel
C	°	rotation around Z-axis
c_x	$N \cdot \mu m^{-1}$	rigidity in X-direction
c_y	$N \cdot \mu m^{-1}$	rigidity in Y-direction
c_z	$N \cdot \mu m^{-1}$	rigidity in Z-direction
C_1	$J \cdot s \cdot mm^{-6}$	constant - power function
C_2	-	constant - power function
C_3	$mm^{-2} \cdot s \cdot m^{-1}$	constant - technology and geometry parameters
d	°	center distance: grinding wheel - workpiece
d_g	mm	diameter of grinding wheel
d_w	mm	diameter of workpiece
$\vec{D}$	mm	vector of center distance
e_{pb}	mm	eccentricity pin bearing
f	s^{-1}	frequency
f_d	mm	dressing feed per revolution
F	N	force
F_a	N	axial force
F'_a	$N \cdot mm^{-1}$	specific axial force
F_{eff}	N	effective force
F_{infeed}	N	force due to infeed

Symbol	Unit	Designation
F_{ld}	N	force of linear drive
F_{MAX}	N	maximum force of linear drive
F_n	N	normal force
F'_n	N·mm^{-1}	specific normal force
F_N	N	rated force of linear drive
F_r	N	radial force
F'_r	N	specific radial force
$F_r(t)$	N	friction force
F_{rc}	N	constant component of friction force
F_{res}	N	resulting cutting force
F'_{res}	N·mm^{-1}	specific resulting cutting force
F_{rv}	N	velocity dependant component of friction force
F_{S_x}	N	force at support in X-direction
F_{S_y}	N	force at support in Y-direction
$F_{t,filter}$	N	filtered tangential force
$F_{t,max}$	N	maximum tangential force
F_t	N	tangential force
F'_t	N·mm^{-1}	specific tangential force
$F_{x_{sensor}}$	N	force in X-direction at the sensor
F_x	N	force in X-direction
$F_{y_{sensor}}$	N	force in Y-direction at the sensor
F_y	N	force in Y-direction
$F_{z_{sensor}}$	N	force in Z-direction at the sensor
F_z	N	force in Z-direction
G	-	grinding wheel wear ratio (G-ratio)
$h_{cu,eff}$	mm	effective chip thickness
h_{cu}	mm	chip thickness
h_m	mm	theoretical mean chip thickness
i_d	-	rotational ratio at dressing
i_g	-	rotational ratio at grinding
l_c	mm	contact length
m	kg	mass

Symbol	Unit	Designation
M_{nenn}	N·m	torque of linear drive
M_{nenn}	N·m	nominal torque of a drive
M_x	N·m	momentum X-axis
M_y	N·m	momentum Y-axis
M_z	N·m	momentum Z-axis
n	min^{-1}	revolutions per minute
n_{max}	min^{-1}	maximum revolutions per minute of rotatory axis
n_g	min^{-1}	grinding wheel rpm
n_w	min^{-1}	workpiece rpm
P'_c	$W \cdot mm^{-1}$	specific cutting power
P_{drive}	W	power of drive
$P(f)$	N	single-sided amplitude
Q	°	rotation around workpiece spindle axis
Q'_w	$mm^3 \cdot (mm \cdot s)^{-1}$	specific material removal rate
q_d	-	dressing-roll speed ratio
q_g	-	grinding velocity ratio
Q_w	$mm^3 \cdot s^{-1}$	material removal rate
$r_{g,max}$	mm	max. grinding wheel radius
$r_{g,min}$	mm	min. grinding wheel radius
r_g	mm	actual grinding wheel radius
$r_g(\varphi, z)$	mm	radius of non-circular tool at location φ and z
r_{gwpb}	mm	center point distance grinding wheel - pin bearing
r_{mb}	mm	radius main bearing
r_{pb}	mm	radius pin bearing
$r_{w,max}$	mm	max. workpiece radius
$r_{w,min}$	mm	min. workpiece radius
r_w	mm	actual workpiece radius
$r_w(\psi, z)$	mm	radius of non-circular workpiece at location ψ and z
r_g	mm	radius grinding wheel
$\vec{R}_g$	-	rotation matrix of the grinding wheel
R_t	mm	grinding wheel surface roughness
$\vec{R}_w$	-	rotation matrix of the workpiece

Symbol	Unit	Designation
$Sens_{F_x}$	$pC \cdot N^{-1}$	sensitivity in x-direction
$Sens_{F_y}$	$pC \cdot N^{-1}$	sensitivity in y-direction
$Sens_{F_z}$	$pC \cdot N^{-1}$	sensitivity in z-direction
t	s	time
T_μ	mm	critical chip thickness
t_{ges}	s	total time
u	%	override
u_d	-	overlap ratio
U_s	$J \cdot mm^{-3}$	specific grinding energy
v	$m \cdot s^{-1}$	velocity
$v_{c,max}$	$m \cdot s^{-1}$	maximum velocity
v_{eff}	$m \cdot s^{-1}$	effective velocity
v_{fa}	$mm \cdot min^{-1}$	velocity of axial infeed
v_{fd}	$mm \cdot min^{-1}$	dressing feed rate
$v_{fr,f}$	$mm \cdot min^{-1}$	feed rate for finishing
v_{fr}	$mm \cdot min^{-1}$	velocity of radial infeed
v_c	$m \cdot s^{-1}$	circumference velocity
V_g	mm^3	volume of grinding wheel wear
v_w	$m \cdot s^{-1}$	workpiece speed
V_w	mm^3	volume of cut workpiece material
$\vec{W}$	mm	vector of ellipsis
x	mm	X-coordinate
x_{POC}	m	X-position of contact point
y	mm	Y-coordinate
z	mm	Z-coordinate
z_{total}	mm	distance between supports
z_g	mm	distance grinding wheel - force sensor

Greek Symbols

Symbol	Unit	Designation
α	°	grinding wheel rotation angle
β	°	workpiece rotation angle
δ, ξ, κ	°	angles for beam length calculation
γ	°	workpiece angle
ΔF	N	force difference
$\hat{\psi}$	°	workpiece point angle
μ_g	-	cutting force ratio
μ_{rc}	-	coefficient of friction
μ_{rv}	$s \cdot m^{-1}$	velocity dependant coefficient of friction
ω_w	s^{-1}	angular frequency
ψ	°	contact point angle workpiece
φ	°	contact point angle grinding wheel

Abbreviations

Abbreviation	Designation
3D	three dimensional
AGriPro	Adaptive Grinding Process
BLCT	beam length calculation technique
CAD	computer-aided design
CAM	computer-aided manufacturing
CBN	Cubic-Boron-Nitride
CFRP	carbon-fibre-reinforced polymer
CG	conventional grinding
CGS	center grinding spindle
CNC	computerized numerical control
CP	center point
CPB	center bearing pin
CWP	center workpiece spindle
DIN	Deutsches Institut für Normung
DoE	design of experiments
FFG	Österreichische Forschungsförderungsgesellschaft
FFt	Fast Fourier transform
GST	Gesellschaft für Schleiftechnik GmbH
GUI	graphical user interface
HEDG	high efficiency deep grinding
HMI	human machine interface
HSG	high speed grinding
ID	impregnated diamond (dressing tool)
IFT	Institute of Production Engineering
ISO	International Organization for Standardization
MATLAB	matrix laboratory
MK	morse taper
NC	power control
NCU	numerical control unit
NI	National Instruments

Abbreviation	**Designation**
OLE	object linking and embedding
OPC	OLE for process control
OPC	Open Platform Communications (since 2011)
OPC UA	OPC unified architecture
OVR	override
PC	personal computer
PCU	power control unit
PID	proportional integral derivative
POC	point of contact
RGM	research grinding machine
RPM	revolutions per minute
RSG	RPM-synchronous grinding
RSNG	RPM-synchronous non-circular grinding
SD	single-point diamond (dressing tool)
SL	solution line
SP	service pack
TU Graz	Graz University of Technology

Contents

1 Introduction

The production process grinding deals with the finishing procedure of workpieces and represents one of the last stages of the value-added production chain. Within this step, workpiece geometry, accuracy and surface quality are determined. Therefore, grinding is a key technology for the production of high-precision parts.

Considerable costs and energy input have already been spent on components up to this processing stage. According to the current state of the art, therefore, large safety reserves are calculated in order to guarantee process capability and to avoid production rejects. This particular safety margin leads to considerable losses of overall process efficiency but preserves opportunities for optimization and the development of novel process designs. [1]

1.1 Consideration of Grinding Processes

Grinding is classified as a cutting process with geometrically undefined cutting edges according to DIN 8580. In general, the manufacturing process is characterized by a high number of simultaneously operating cutting grains with random geometry and orientation.[2] The process characteristics are chipping mechanisms resulting from intrusion of a large number of statistically distributed alignments and angles of grains called grits. These abrasive particles are embedded in a certain bonding matrix and partly surrounded by pores. In comparison to other production processes grinding works with a minor rise per tooth and negative angle of rake. The velocity of this cutting edges is high during the material removal at the workpiece. [3]

The demand for a high quality of surface condition of a workpiece rises while the degree of accuracy in dimensions and shapes increases. Therefore, grinding machines and processes have been optimized and material removal rates have been upped. Materials with difficult machining characteristics and high hardness require sophisticated chipping processes such as grinding. Due to keenly developed tools and processes, grinding is a highly productive manufacturing procedure.

[1] cf. Rowe B., 2014, p.5.
[2] cf. DIN 8580, 2003-09.
[3] cf. Heisel et al., 2014, p.531.

Grinding is the appropriate technology for production of advanced products in a diverse range of industries. It is usually employed when high accuracy is required. Surface texture requirements are reasons for selecting abrasive processes as well as high material removal rates or the necessity of machining hard materials. [4]

For automotive industries grinding has played an important role ever since. Components of internal combustion engines require high precision machining to ensure long lifetimes as well as low fuel consumption and low noise levels. In Germany, in 2015, 3.21 million new passenger cars were registered. The prognosis for the years 2016 and 2017 promises a slight increase. [5] A large percentage of these automotives are equipped with an internal combustion engine. Today's cars are either just driven by combustion motors or by a hybrid drive system or in minor cases fully electrically. In the year 2015, 12,363 fully electric cars were registered in Germany. In 2016 the number of new approvals of e-cars decreased slightly to 11,410. [6] Therefore, machining of classic combustion engine parts with extended manufacturing levels is still a big issue for automotive manufacturers and will be during the next decade. Since the focus was lead on downsizing and weight reduction due to newest legislation on emissions for passenger cars, materials of higher strength were introduced for highly stressed workpieces. The machining of these materials places special challenges for manufacturers and engineers.

Despite the imminent obstacles today, the electro-mobility will prevail. The general manufacturing expense may decline, but finishing processes such as grinding will gain in significance. Highest standards will be requested from gear shafts, bearings, shaft-hub connections etc. which are employed with ultra high rotational rates in the context of electro-mobility powertrains. The functional surfaces of those highly sophisticated workpieces are mainly finished through grinding processes.

[4] cf. Marinescu et al., 2016b, p.4.
[5] cf http://de.statista.com/, 2017/07/04b.
[6] cf http://de.statista.com/, 2017/07/04a.

1.2 Process Developments

Research related to the general grinding process has a long tradition at the Institute of Production Engineering (IFT) at Graz University of Technology (TU Graz). Several doctoral thesis have been carried out studying different topics concerning finishing machining of workpieces. The main focus has been laid on the production of non-circular geometries utilizing various grinding approaches.

Schmid has already investigated the general process of non-circular grinding on computer-controlled grinding machines already in 1986. [7] Later, in 1993, Wagner developed a process monitoring system for non-circular grinding machines. [8] Mayr developed an interlocking shaft-hub connection with internal grindable contour in the same year. [9]

First non-circular shaft-hub connections were produced on the grinding machine at the IFT. In 2002, Patzig came up with a machine integrated post-process measurement system for non-circular grinding machines. [10] Mautz investigated non-circular grinding processes regarding geometrical errors in 2003. [11] Later, in 2006, Zuderstorfer developed a special software for non-circular grinding machines. [12] This KelPoly software was used in combination with numerous grinding machines of different producers and is partly still used at IFT. Riemenschneider investigated and adapted different production processes for machining of non-circular workpiece contours such as polygon profiles according to DIN 32711 and DIN 32712 in 2009. [13]

Latest, in 2014, Ablinger took up the topic of RPM-Synchronous Non-Circular Grinding (RSNG) from a theoretical point of view. He developed a software for contour calculation and performed first general tests on an adapted FORTUNA grinding machine. [14] These experiments proved the concept for further research on RPM-Synchronous Grinding. Since the machine was not fully capable to meet the requirements of this special process, the resulting surface qualities were not satisfying industrial demands.

[7] cf. Schmid, 1986.
[8] cf. Wagner, 1993.
[9] cf. Mayr, 1993.
[10] cf. Patzig, 2002.
[11] cf. Mautz, 2003.
[12] cf. Zuderstorfer, 2006.
[13] cf. Riemenschneider, 2009.
[14] cf. Ablinger, 2014.

1.3 Grinding Machine Tool

Since mid-2016, the Institute of Production Engineering has a new research grinding machine at disposal. The Austrian company GST Ltd. developed and produced the machine in close collaboration with the IFT. The machine design is focused on conventional high-end processes for circular and non-circular grinding as well as on the research topic of RPM- Synchronous Grinding.

With the implementation of sensors, feedback- and control-loops and process adaption strategies into the grinding machine concept, the efficiency of the process can be increased. Nevertheless, the grinding machine tool must offer the possibility for smart devices and for in-process adaption to interfere with the standard process sequence. The design and the layout of this machine tool are of major importance to enable reduction of the mentioned reserves in productivity.

The main focus of this work lies on the layout of the grinding machine tool and its capacity for novel process concepts such as the RPM-Synchronous Grinding (RSG) process. This novel grinding approach offers new possibilities to generate defined macro- and microgeometries on workpieces. Moreover, the machine design enables the development of other high-end grinding processes.

With present technology, various macroscopic, non-circular geometries must be grinded subsequently in an oscillating process where the X-axis is coupled with the rotary workpiece-spindle axis (Q-axis). Such workpieces can be machined in an ordinary plunge grinding process by implementing the approach of RPM-Synchronous Non-Circular Grinding (RSNG). Therefore, the workpiece and the grinding wheel rpm rates are in a fixed ratio. A non-circular grinding wheel is used to transfer its geometry onto the workpiece. The unique grinding machine tool is custom made for research in the field of RPM-Synchronous Grinding. Highest revolution rates on the workpiece spindle are mandatory for a successful implementation of RSG.

1.4 Thesis' Structure

The presented doctoral thesis is structured in nine major chapters. After the Introduction (Chapter 1) and the Definition of Task (Chapter 2), major Principles of the Grinding Technology (Chapter 3) are discussed. The latter chapter, together with the chapters Synchronous Grinding (Chapter 4) and Adaptive Control for Grinding (Chapter 5) add up to the state of scientific research.

The chapter Machine Tool Development (Chapter 6) deals with major parts and functionalities and developments of the research grinding machine in order to be prepared (Experimental Setup - Chapter 7) for the Experimental Execution and Evaluation of Results (Chapter 8).

At last, a Summary and Outlook (Chapter 9) outline all major results. Moreover, the arising fields of application are mentioned on which should be focused in further scientific investigations.

2 Definition of Task

The presented doctoral thesis is dealing with the following research questions and objectives. Hypotheses and Antitheses are formulated which subsequently are proofed or refuted within this work.

2.1 Research Questions

2.1.1 Research Question 1

What makes a grinding machine ready to fulfil the needs of upcoming research-topics in precision manufacturing of hardened workpieces?

Hypothesis 1. *The future of grinding as a chip removing manufacturing process gains in significance when every single part of the process is optimized. The overall process consists of the machine, the tool, the coolant and the grinding technology itself.*

Antithesis 1. *If just one of those sub-processes is not improved continuously, the overall process will not enhance.*

2.1.2 Research Question 2

How to prepare and equip a new research grinding machine for the technology of RPM-Synchronous Grinding (RSG) and for conventional high-end non-circular grinding processes?

Hypothesis 2. *A highly dynamic X-axis slide is necessary for efficient dressing of non-circular grinding wheels for the RPM-Synchronous Non-Circular Grinding process. For conventional non-circular grinding the maximum acceleration and velocity determine the maximum rotational rates on the workpiece spindle. Therefore, the overall process efficiency is determined by the dynamics of the X-axis slide.*

2.1.3 Research Question 3

Is an adaptive grinding process guidance necessary to enhance quality aspects of machined workpieces? Is it possible to improve surface quality of workpieces grinded with the RPM-Synchronous technology by an adaptive process control strategy?

Hypothesis 3. *By using process control concepts, the efficiency of any circular or non-circular grinding process can be enhanced. Efficiency can be measured in output per time unit and in rejects per total number of workpieces. Moreover, surface qualities satisfying industrial demands can be achieved when an adaptive process control strategy is implemented.*

Antithesis 2. *Without process guidance strategies high surface qualities can not be achieved with the new technology of RPM-Synchronous Grinding. The reasons for this lies in the unknown state of grinding wheel condition caused by unequally distributed wear on the circumference of the grinding wheel.*

2.2 Research Objectives

The thesis' research objective is to prepare the new research grinding machine at the Institute of Production Engineering at Graz University of Technology for present and upcoming demands in grinding. More precisely, the main focus lies on the development of the technology of RPM-Synchronous Grinding with all its necessities:

- Adaptive grinding process guidance and control strategies to be able to react on any changes during single grinding processes.
- Highly dynamic X-axis slide for efficient dressing of non-circular grinding wheels for the RPM-Synchronous Non-Circular Grinding Process and for conventional high-end non-circular grinding of workpieces.
- Grinding wheel specification together with technological dressing and grinding parameters.

Altogether, the research objective is to reach industry-relevant surface roughness qualities on workpieces manufactured with the technology of RPM-Synchronous Grinding for the first time.

2.3 Technical Task

The purpose of the presented doctoral thesis can be divided into three main tasks. Here, these tasks are itemized in a chronological order of accomplishment but with equal importance.

2.3.1 Development of the Grinding Machine Tool System

The research grinding machine at the Institute of Production Engineering at Graz University of Technology has to be prepared for upcoming demands in scientific grinding studies. A highly dynamic X-axis slide is needed for efficient dressing of non-circular grinding wheels for the RPM-Synchronous Non-Circular Grinding Process and for conventional high-end non-circular grinding of workpieces. Sensors have to be incorporated in the design of the machine as well as control system for instant analysis of any condition during processing.

2.3.2 Development of Adaptive Grinding Process Guidance Strategies

Adaptive grinding process guidance and control strategies allow reaction on changes of any condition during single grinding processes based on sensors signals. Thereby, process optimization can be achieved with regard to the prevention of grinding burn or improvement of the workpiece surface qualities after finishing.

2.3.3 Development of RPM-Synchronous Grinding Process

The main focus lies on the development of the technology of RPM-Synchronous Grinding with all its necessities. Grinding wheel specification together with technological dressing and grinding parameters must be investigated. The research objective is to reach industry-relevant surface roughness qualities on workpieces manufactured with the technology of RPM-Synchronous Grinding.

In order to achieve these goals, every single part of the overall machine tool system has to be prepared to be in control of any upcoming challenge.

2.4 Thesis' Common Thread

The central framework of this thesis is illustrated in Figure 2.4.1. The overall system of the Grinding Machine Tool constitutes the center of this work. The forthcoming requirements for functional and integral micro-structures of grinded surfaces and the needs of three dimensional non-circular macroscopic workpiece geometries are the drivers for this thesis.

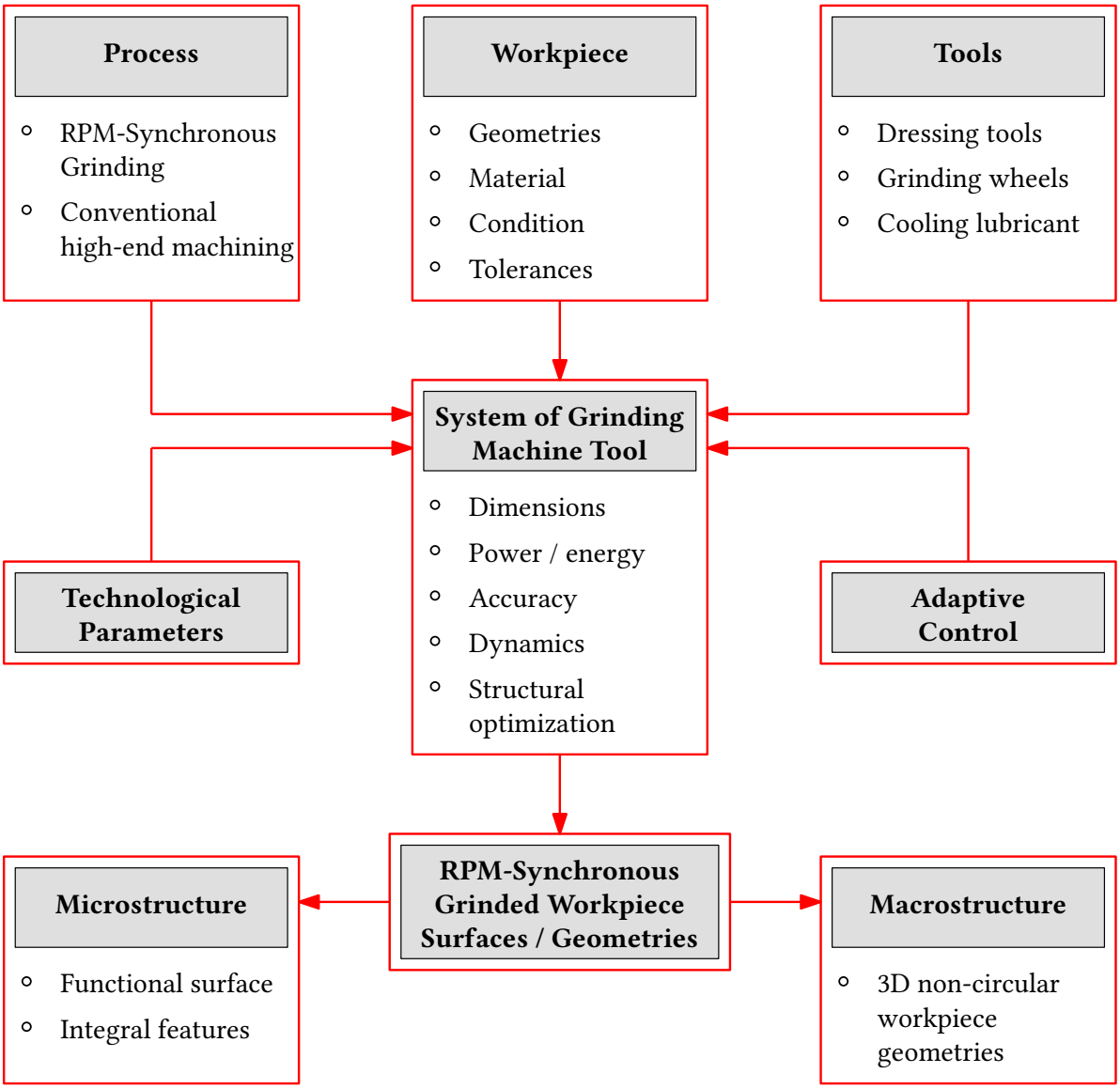

Figure 2.4.1: Illustration of the common (red) thread throughout this work, Source: own illustration.

Only close interaction of all inputs together with a tailored machine concept can satisfy those demands and can lead to successful research work. The major inputs are: the process, the technological parameters, all necessary tools, adaptive control strategies and the information about the workpiece during the process.

3 Principles of Grinding Technology

Grinding is the oldest processing method of mankind. First tools made of wood, animal bone, rock or later metal were treated with rough stones, reshaped or sharpened. [15] In the second half of the twentieth century manufacturers of aero-engines recognized that grinding is a strategic process for high-technology applications. Today, grinding is the key technology for achieving the necessary quality of workpieces in various fields of application. [16]

3.1 Chip Removal Mechanism

Grinding is defined as a machining process with geometrically undefined cutting edges according to DIN 8580, DIN 8589-0, DIN 8589-11. [17] Conventional grinding tools consist of grains, pores and bonding. Compared to machining processes with geometrically defined cutting edges such as milling, drilling or turning, the number of cutting edges is much higher while simultaneously the chip thickness is much smaller. Due to the varying distance between consecutive cutting edges, this chip thickness is not constant. All grains are stochastically orientated and possess randomly aligned cutting edge geometries. A high percentage of them has negative chipping angles. Tools can be dressed inside grinding machines, what renews the quality of the cutting edges and prevent geometrical deviations on the machined workpiece. Classic theories about chip removal in grinding are developed by einkorn-grain experiments. Therefore, a single grain in a rigid substrate is moved on a prescribed path through the material. [18]

In theoretical considerations the grain-material interaction can be separated in three sections as Figure 3.1.1 shows. In the first section (I) the grain scrubs on the surface of the material, causes elastic deformation and generates a heat input to the workpiece due to friction. In a next phase (II) reaming and furrowing additionally cause plastic deformations on the material. A scratch in the direction of movement and a bulge laterally emerge. The third phase (III) starts after obtaining the critical chip thickness T_μ. This last part is signified by chip forming and

[15] cf. Meister M., 2011, p.XV.
[16] cf. Rowe B., 2014, pp.2-3.
[17] cf. Heisel et al., 2014, p.531.
[18] cf. Masslow, 1952, n.p.

removal. In phase II & III heat input occurs due to internal material friction. Additionally, chip formation friction between the grain and the chip results in heat influx. [19] [20]

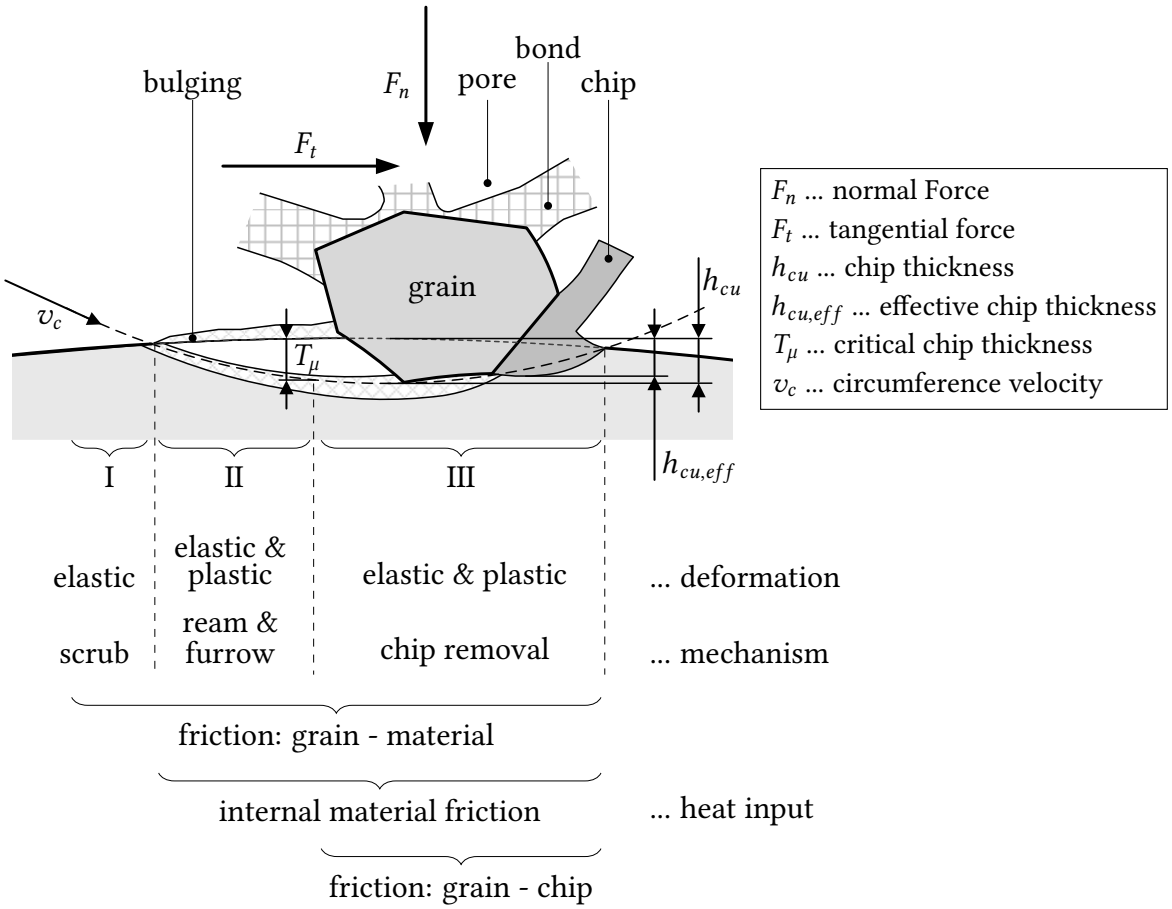

Figure 3.1.1: Deformations at the chip forming process - ductile material, Source: own illustration, based on Klocke, König, 2005 (p.9).

The cutting force during the grinding process on a single grain can be divided in two major components. In direction of the cutting velocity a tangential force F_t occurs while grinding. Perpendicular to this force component, a normal force F_n appears. The ratio of the two forces is called the cutting force ratio μ_g. [21]

$$\mu_g = \frac{F_t}{F_n} \tag{3.1.1}$$

[19] cf. Lortz, 1975, n.p.
[20] cf. Steffens, Lauer-Schmaltz, 1978, pp.49-50.
[21] cf. Klocke, König, 2005, p.13.

3.2 Grinding System

According to Kassen, the general grinding system can be divided into three main columns: input, process and result. [22] Figure 3.2.1 shows the modified system of this classification which was reconsidered by Messer [23] in 1983 and illustrated by Klocke and König. [24] The input parameters mainly concern the system: the machine, the workpiece, the tool grinding wheel, the dressing tool and the cooling system. Moreover, set-values are given as input on the general grinding process.

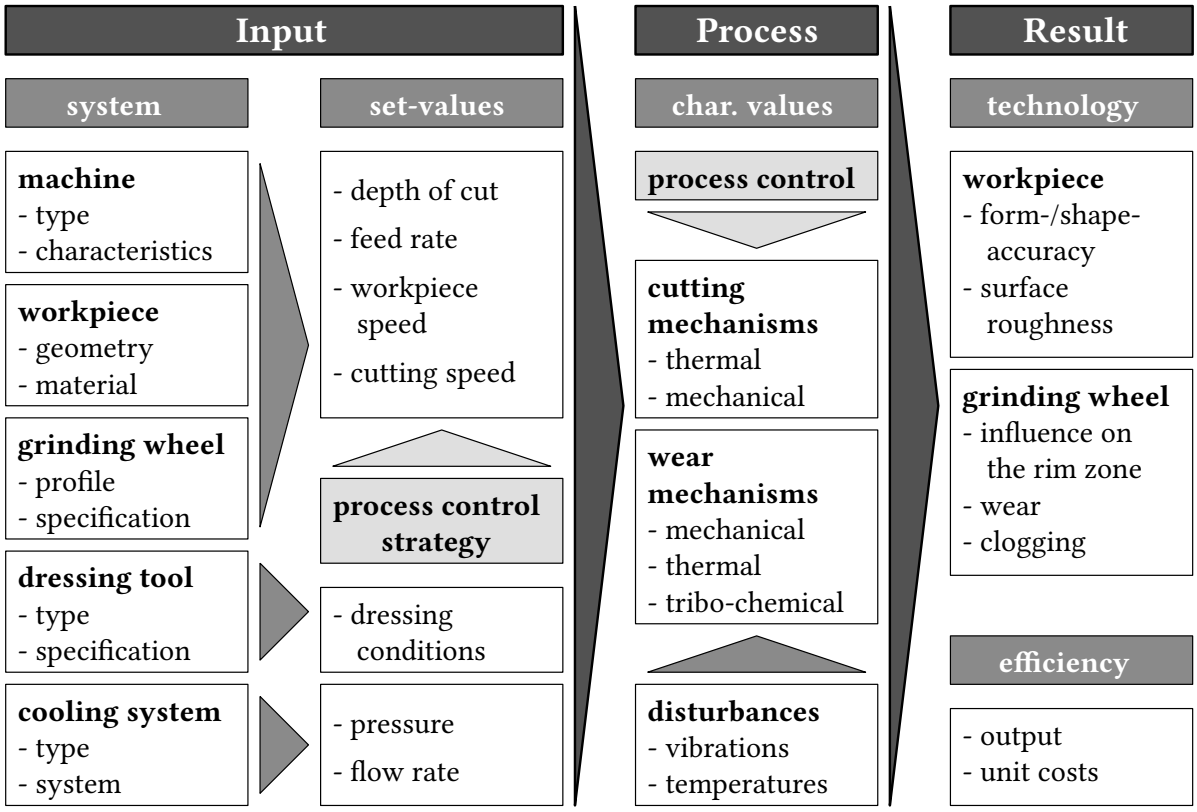

Figure 3.2.1: The Grinding System,
Source: own illustration, based on Kassen 1969 and Messer 1983.

Within the presented work, process control strategies are introduced, which are set as input values as well. These control concepts adapt classical set-values such as the feed rate during the grinding process according to a mathematical model. The process is dominated by characteristic values such as cutting and wear mechanisms and occurring disturbances. At last, the result of the grinding process is a workpiece with new form and shape properties and different surface roughness due to the interaction with the grinding wheel. Furthermore, the grinding wheel changes during the process. It is mainly influenced by wear and clogging. Figure 3.2.1

[22] cf. Kassen, 1969, n.p.
[23] cf. Messer, 1983, n.p.
[24] cf. Klocke, König, 2005, p.186.

shows the new interpretation of the classification. In the presented figure the process control strategy and the process control is added.

3.3 Grinding Parameters

Grinding on standard machine tools deals with several parameters which have differing influence on the result of the machining process. Concerning the workpiece, these parameters influence geometry and surface roughness qualities. Moreover, the parameters determine the productivity and additionally the grinding wheel wear. In Figure 3.3.1 main parameters for **plunge-grinding** are illustrated. These parameters refer to the general grinding process. The direction of movement of the grinding wheel is perpendicular to the rotational axis.

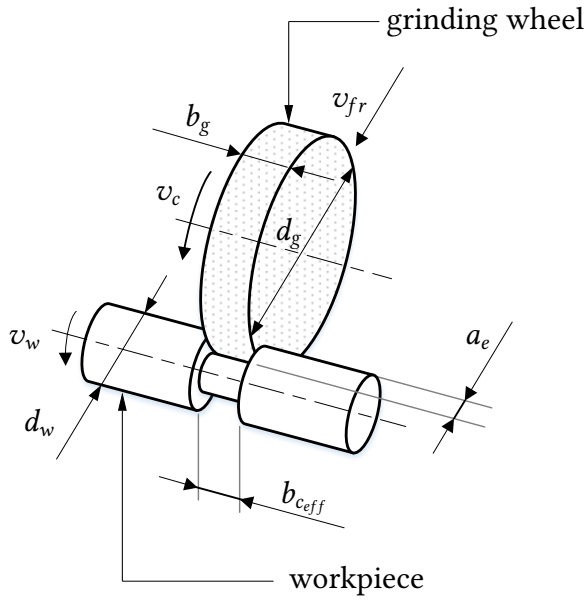

a_e ... amount of infeed / depth of cut
$b_{c_{eff}}$ ... effective cutting width
b_g ... width of grinding wheel
d_g ... diameter of grinding wheel
d_w ... diameter of workpiece
v_c ... cutting speed
v_{fr} ... velocity of radial infeed
v_w ... workpiece speed

Figure 3.3.1: Parameters for cylindrical plunge-grinding,
Source: own illustration.

3.3.1 Cutting Velocity and Workpiece Circumference Velocity

The cutting velocity v_c is the circumference speed of the grinding wheel and is calculated by the rotation n_g and the diameter of the grinding wheel d_g. It is a key parameter since all grinding wheels are permitted certain cutting velocities. Moreover, the link with amount of infeed for each workpiece rotation a_e classifies different process types as will be described later on. Analogously, the workpiece velocity v_w corresponds to the circumference speed of the workpiece and is expressed by the multiplication of the rotational rate n_w and the diameter of

the workpiece d_w. Since the infeed is minor in comparison to the tool dimensions at circular grinding, mainly, the circumference velocity is considered in formulas instead of the mean velocity. [25]

$$v_c = \pi \cdot d_g \cdot n_g \tag{3.3.1}$$

$$v_w = \pi \cdot d_w \cdot n_w \tag{3.3.2}$$

3.3.2 Counter- and Equal Direction Grinding

At counter direction grinding, the grinding tool and the workpiece rotate in the same direction - both clockwise or both counter-clockwise. Therefore, the velocity vectors in the contact area point in opposite directions. When grinding in counter direction is applied, the vectorial sum of the velocities v_c and v_w result in a higher effective velocity v_{eff} in the contact zone between grinding wheel and workpiece. For conventional grinding, where rotational rates of the workpiece are fairly small, this fact has just a minor impact. However, for RPM-Synchronous Grinding with high rotational rates at both sides (grinding wheel and workpiece) the grinding direction has considerable influence on the effective velocity and therefore on the process. Figure 3.3.2 illustrates the velocities at both, counter direction grinding a) and equal direction grinding b).

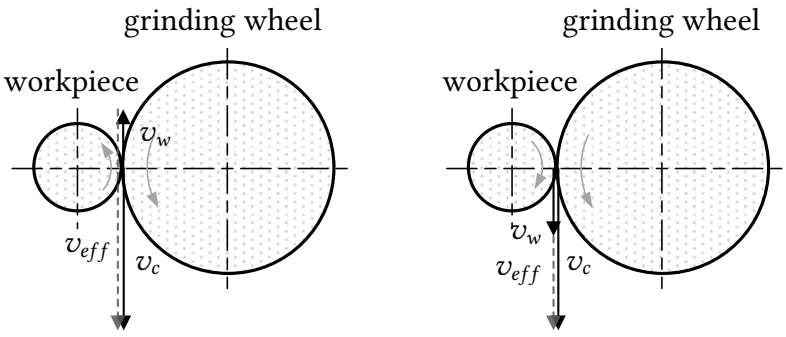

Figure 3.3.2: Effective velocities at counter- and equal direction grinding, Source: own illustration.

When grinding in equal direction, one of the working partners rotates clockwise and the other on counter-clockwise. As a result, the vectorial sum of the velocities v_c and v_w result in a smaller effective velocity v_{eff} in the contact zone between grinding wheel and workpiece.

[25] cf. Heisel et al., 2014, p.532.

Both, counter- and equal direction grinding have their advantages and disadvantages. For equal direction grinding the heat influenced zone on the workpiece surface is removed during the process. In contrast, for counter direction grinding it is not the case. [26]

The grinding velocity ratio q_g is the quotient of the grinding wheel circumference velocity v_c and the workpiece circumference velocity v_w. [27]

$$q_g = \frac{v_c}{v_w} \tag{3.3.3}$$

3.3.3 Theoretical Mean Chip Thickness

The theoretical mean chip thickness h_m defines a representable chip size witch would emerge if only a single grain would evoke the material removal. It is a theoretical quantity since grinding is characterized by the operation of an unknown number of grains at any time during the process.

$$h_m = \frac{a_e \cdot v_w}{v_c} \tag{3.3.4}$$

$$h_m = \frac{v_{fr} \cdot v_w}{n_w \cdot v_c} \tag{3.3.5}$$

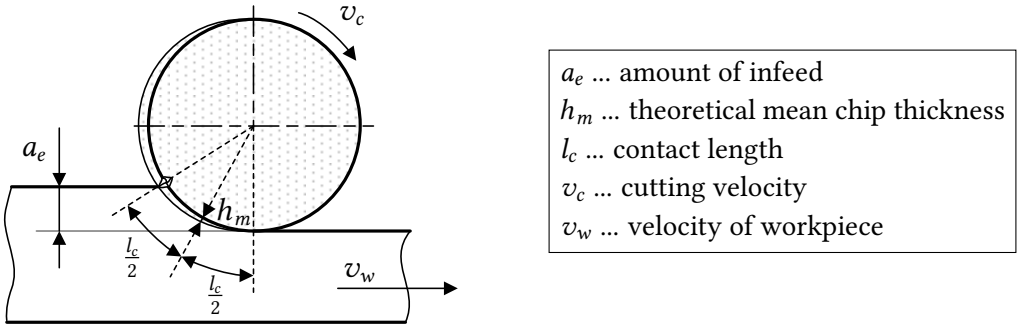

Figure 3.3.3: Theoretical mean chip thickness,
Source: own illustration, based on Meister M, 2011 (p.154).

Nevertheless, the theoretical mean chip thickness gives an idea of the stresses on a single grain. Guide values for the theoretical mean chip thickness h_m for roughing are between $1 \cdot 10^{-4}$ mm

[26] cf. https://www.schleifprofi.com, 2017/07/05, n.p.
[27] cf. Heisel et al., 2014, p.532.

and $5 \cdot 10^{-4}$ mm and for finishing from $5 \cdot 10^{-5}$ mm to $1 \cdot 10^{-4}$ mm. [28] Figure 3.3.3 gives an idea of how the theoretical mean chip thickness h_m is determined.

3.3.4 Specific Material Removal Rate

The specific material removal rate Q'_w is one of the main values for characterising and comparing different grinding processes. It is related to the effective cutting width of the grinding wheel $b_{c_{eff}}$. This is the width in contact with the workpiece and can be smaller or equal to the overall width of the grinding wheel b_g. The volume of removed material per time unit Q_w is correlated to the effective cutting width $b_{c_{eff}}$ in a certain process (unit: $b_{c_{eff}}$ in mm).

$$Q_w = \frac{dV_w}{dt} \tag{3.3.6}$$

$$Q'_w = \frac{Q_w}{b_{c_{eff}}} \tag{3.3.7}$$

Values for the specific material removal rate Q'_w most frequently are represented in the unit $mm^3 \cdot (mm \cdot s)^{-1}$. For cross-circumference external grinding Q'_w is calculated with the following equation. [29]

• plunge-grinding:

$$Q'_w = \frac{\pi \cdot d_w \cdot \cancel{b_{c_{eff}}} \cdot v_{fr}}{\cancel{b_{c_{eff}}}} \tag{3.3.8}$$

$$Q'_w = \pi \cdot d_w \cdot v_{fr} \tag{3.3.9}$$

• longitudinal-grinding:

$$Q'_w = \pi \cdot d_w \cdot n_w \cdot a_e \tag{3.3.10}$$

$$Q'_w = v_w \cdot a_e \tag{3.3.11}$$

[28] cf. Meister M., 2011, p.154.
[29] cf. Heisel et al., 2014, p.532.

3.3.5 Cutting Forces

For **longitudinal-grinding** Figure 3.3.4 shows parameters and resulting grinding forces. The axial force F_a, the tangential force F_t and the force perpendicular to the contact face F_n (normal force) sum up to the resulting cutting force F_{res}. The axial force occurs due to the feed in axial direction. The normal force constitutes to the cutting pressure mainly caused by infeed in normal direction at plunge grinding. The tangential force emerges from friction and the overall cutting process in the contact area. [30]

$$F_{res} = \sqrt{F_a{}^2 + F_n{}^2 + F_t{}^2} \tag{3.3.12}$$

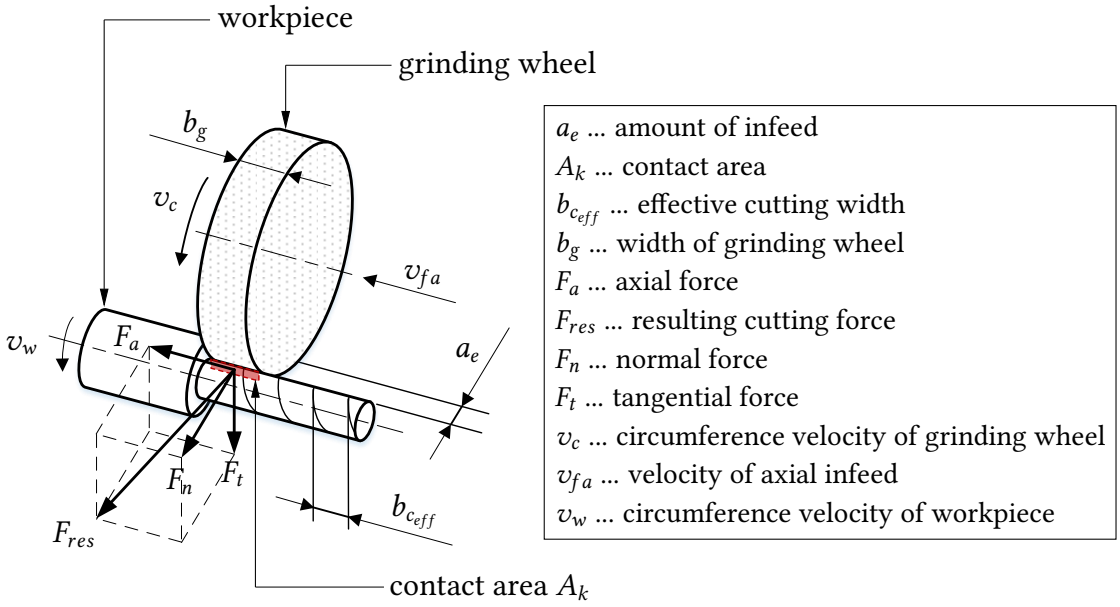

Figure 3.3.4: Parameters for cylindrical longitudinal-grinding,
Source: own illustration.

In contrast to plunge-grinding, the effective cutting width at longitudinal-grinding is not equal to the width of the grinding wheel in general. In order to obtain comparable values for process-forces, the forces are normalized to one millimetre of effective cutting width. [31]

[30] cf. Heisel et al., 2014, p.533.
[31] cf. ibid., p.533.

$$F'_a = \frac{F_a}{b_{c_{eff}}} \tag{3.3.13}$$

$$F'_n = \frac{F_n}{b_{c_{eff}}} \tag{3.3.14}$$

$$F'_t = \frac{F_t}{b_{c_{eff}}} \tag{3.3.15}$$

3.3.6 Process Energy / Power

Grinding is affiliated with a high specific chip removal energy. Therefore, it is important to evaluate the energy in the interaction zone to determine the effect on the tool and the subsurface microstructure of the workpiece. Under consideration of contact conditions, the specific grinding power is an important value to validate a certain process. The power with regard to effective grinding wheel width P'_c is mainly used in the unit: W·mm^{-1}. [32]

$$P'_c = \frac{F_t \cdot v_c}{b_{c_{eff}}} = F'_t \cdot v_c \tag{3.3.16}$$

To get a quantity of energy required for cutting one cubic millimetre of workpiece material, the specific grinding energy is used as a benchmark (unit: J·mm^{-3}). This value gives an insight in the amount of induced heat in the contact zone. [33]

$$U_s = \frac{P'_c}{Q'_w} = \frac{F'_t \cdot v_c}{Q'_w} \tag{3.3.17}$$

3.3.7 Grinding Wheel Wear: G-Ratio

The grinding ratio (G-ratio) is a value which classifies grinding wheel wear. It is the relation of the removed workpiece material volume V_w to the grinding wheel consumption volume V_g.

$$G = \frac{V_w}{V_g} \tag{3.3.18}$$

The grinding ratio is used to compare different grinding wheels for certain grinding processes.

[32] cf. Heisel et al., 2014, p.533.
[33] cf. Meister M., 2011, p.208.

3.4 Classification of Grinding Processes

The specific grinding energy contains information about the chip formation mechanisms in relation to process parameters for specified materials. Same engagement conditions can lead to different chip forms depending on whether the workpiece material is ductile (low-alloy steels) or brittle (ceramics, glass, etc.). Variation of grinding wheel circumference velocity v_c or the amount of infeed a_e has influence on the chip form and thickness.

Figure 3.4.1 shows a classification of grinding processes. Traditionally, grinding is divided in four categories: conventional grinding, deep grinding, high speed grinding (HSG) and high efficiency deep grinding (HEDG) depending on the parameters infeed a_e and cutting velocity v_c.[34] [35] RPM-Synchronous Grinding is mainly characterized by low to medium cutting velocities and small infeed rates. Therefore, it has an overlap with the conventional grinding process in Figure 3.4.1 though higher cutting velocities can be feasible when using super-abrasive tools.

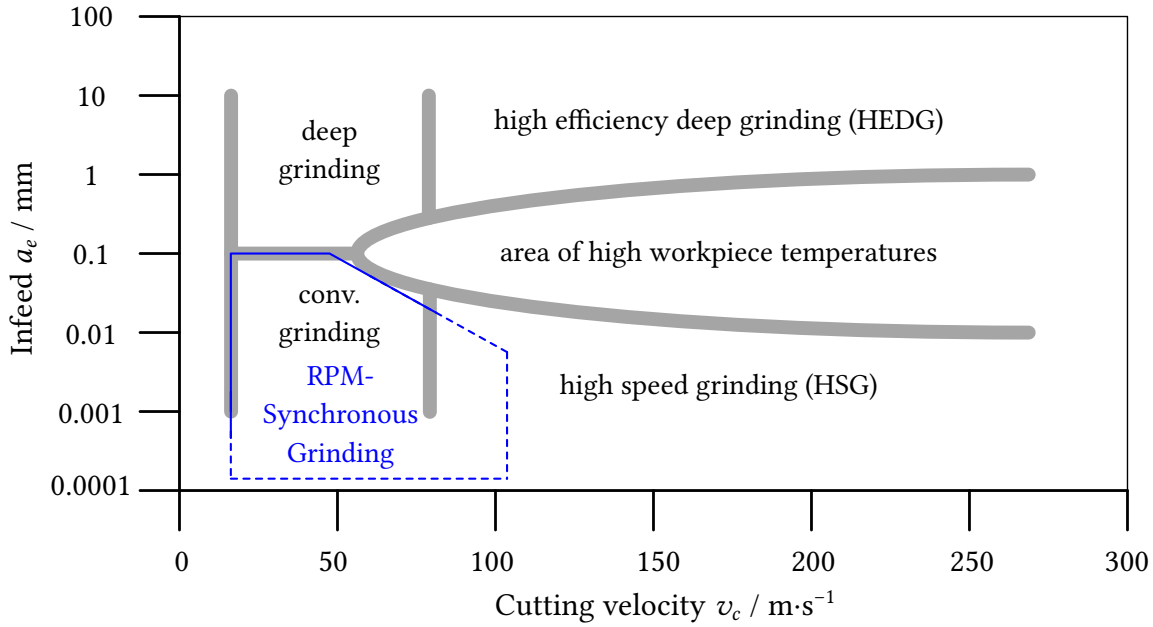

Figure 3.4.1: Classification of grinding processes,
Source: own illustration, based on Heisel et al., 2014 (p.534).

The grinding wheel circumference velocity for high speed grinding (HSG) and high efficiency deep grinding (HEDG) is characterised by $v_c > 80\text{m}\cdot\text{s}^{-1}$. HSG aims for highest surface quality while HEDG is used to achieve a maximum material removal rate Q'_w. These two processes are separated by a zone of high contact area temperatures. Reason for this fact is a complex

[34] cf. Werner, Tawakoli, 1988, n.p.
[35] cf. Heisel et al., 2014, p.534.

correlation between the circumference velocity v_c, the grinding power P_c, the change in chip removal mechanisms, the distribution of heat, the cutting forces and other factors. Moreover, tools and grinding machines must be adjusted to those processes. The power of the drives, damping of the overall system and special cooling nozzles are crucial for these processes. [36] [37]

Operation conditions for HEDG and HSG are: [38]

- well-grindable material
- cooling lubricants in contact zone
- superabrasive Cubic-Boron-Nitrid (CBN) tools

The RPM-Synchronous Grinding method which is mentioned in Figure 3.4.1 represents a special grinding process in which the revolutions per minute (RPM) of the grinding wheel and the workpiece are in a fixed ratio. Chapter 4 - Synchronous Grinding - exclusively deals with this special grinding procedure. In contrast to gear grinding (Reishauer), the coupled machine axes for RPM-Synchronous grinding are parallel.

A distinct classification of the RPM-Synchronous grinding method with kinematic coupling of the interacting process partners according to DIN 8589 Part 11 is not possible. The assignment to both profile grinding and form grinding has integrity. For profile grinding the tool's profile is reproduced on the workpiece. However, in the new synchronous grinding method the resulting workpiece contour is a function of the rotational ratio of the interacting partners during the grinding process. Moreover, the new method can only be assigned to form grinding if the controlled infeed is understood to evoke shape transfer from the grinding wheel onto the workpiece. [39] [40] [41]

[36] cf. Heisel et al., 2014, p.534.
[37] cf. Comley et al., 2006, p.3.
[38] cf. Heisel et al., 2014, p.534.
[39] cf. Spur, Eichhorn, 1993, p.180.
[40] cf. Spur, Eichhorn, 1994, p.36.
[41] cf. Spur, Eichhorn, 1995, p.15.

3.5 Grinding Wheel Composition

Every grinding wheel consists of three major parts. The abrasive **grain** forms the cutting edges. The **bonding** material retains the grains in position and provides cohesion of the grinding wheel structure. Surface **pores** allow space to temporarily take up removed material from the surface of the workpiece. The most important property of abrasive grains is their hardness. Hardness values are often quoted as Knoop hardness expressed in gigapascal. Literature distinguishes between superabrasives and conventional abrasives. [42]

Superabrasives: [43]

- Diamond (64 GPa)
- Cubic-Boron-Nitrid (CBN) (45 GPa)

Conventional abrasives: [44]

- Silicon carbide (24.5 GPa)
- Aluminium oxide
  - Ruby Al_2O_3 (22 GPa)
  - Sintered Al_2O_3 (13.4 GPa)
- Cemented carbides (14 - 18 GPa)
- Quartz (0.78 GPa)
- Glass (0.3 - 0.5 GPa)

Hardness declines with rising temperatures in most abrasives. Cubic-Boron-Nitrid is the second hardest cutting material next to diamond. It is widely used for grinding of steels. Boron-Nitrid does not naturally occur and is obtained via high-pressure - high-temperature synthesis. [45]

Figure 3.5.1 shows CBN grains of a single-layer superabrasive grinding wheel. The image was taken by a KEYENCE VHX-6000 digital microscope. In contrast to conventional tools, such single-layer superabrasives can not be conditioned by dressing, thus is another possibility of differentiation. Such grinding wheels use a metal hub with an electroplated superabrasive

[42] cf. Rowe B., 2014, p.36.
[43] cf. ibid., p.36.
[44] cf. ibid., p.36.
[45] cf. Degner et al., 2015, p.76.

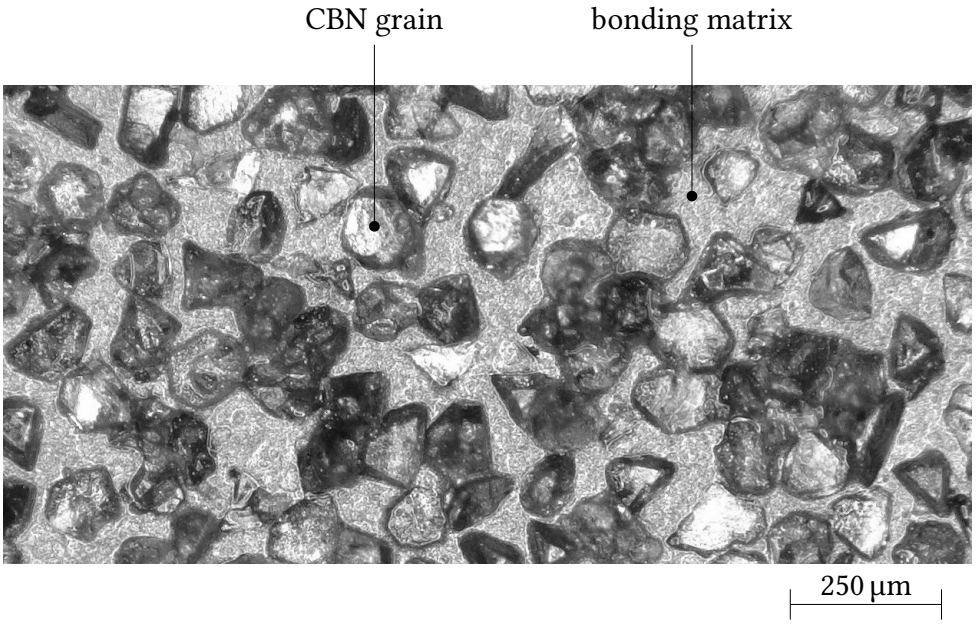

Figure 3.5.1: CBN grains in bonding matrix,
Source: own illustration.

layer. In contrast, CBN grains can be bond (vitrified) to segments which are mounted to a metal or carbon-fiber-reinforced polymer (CFRP) hub via adhesive bonding. Such grinding wheels are mainly dressed inside the grinding machine.

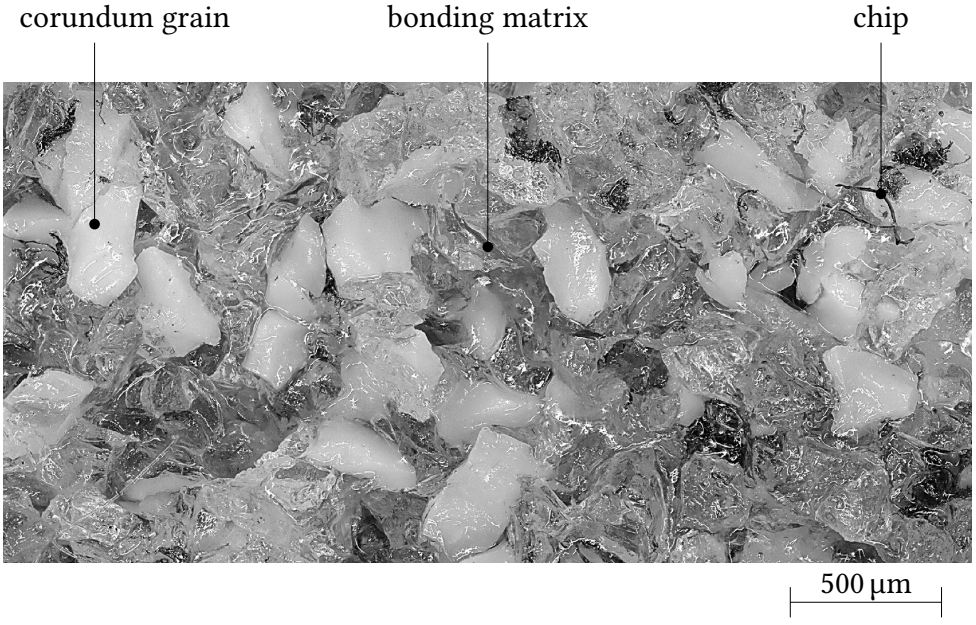

Figure 3.5.2: Corundum grains in ceramic bonding matrix,
Source: own illustration.

Conventional abrasive tools work without hub. Those wheels are mounted with a flange directly on the grinding spindle. Such tools are balanced and dressed inside the machine. Arbitrary shapes can be worked onto such tools with special dressing tools. Figure 3.5.2 shows

aluminium oxide grains in a conventional grinding wheel embedded in vitrified (ceramic) bonding. This image was taken by the KEYENCE VHX-6000 digital microscope as well.

3.6 Grinding Wheel Notation

Within the present work, exclusively conventional abrasives are used. In section 7.4 the grinding wheel specifications and their main fields of application are discussed. Furthermore, the detailed composition of each grinding wheel is outlined.

Subsequently, an example is given to explain the specification of a grinding wheel abbreviation: (This example is based on a TYROLIT product description.)

83A 60 M7 V217 50, 610 x 40 x 304.8 mm, Form 1

- **83**: manufacturer's individual grain designation
- **A**: grain type (A = aluminium oxide, C = Silicon carbide)
- **60**: grit size
- **M**: degree of hardness
- **7**: structure
- **V**: bond type (B = resin, V = ceramic)
- **217**: manufacturer's individual bond designation
- **50**: maximum operation speed in $m \cdot s^{-1}$
- **610**: outside diameter of the tool in mm
- **40**: width of the tool in mm
- **304.8**: diameter of bore in mm
- **Form 1**: shape of the grinding wheel

3.7 Dressing of Grinding Wheels

In preparation for grinding a dressing process is performed on the grinding wheel. With this conditioning method, macroscopic shape as well as microscopic surface structure are worked onto the grinding wheel. Further aspects of dressing (truing) include: [46]

- Elimination of deviations from specified form or straightness
- Sharpening of cutting surfaces
- Accomplishing a uniform and random distribution of cutting edges
- Removing a layer of abrasive which is loaded with workpiece material

3.7.1 Dressing Parameters

The overlap ratio u_d determines the smoothness of the grinding wheels surface after dressing. Depending on the dressing depth a_d, the tool is allocated with an effective cutting width b_d. The overlap ratio allowes the axial dressing feed rate v_{fd} to be determined. [47]

$$u_d = \frac{b_d}{f_d} = \frac{b_d \cdot n_g}{v_{fd}} \tag{3.7.1}$$

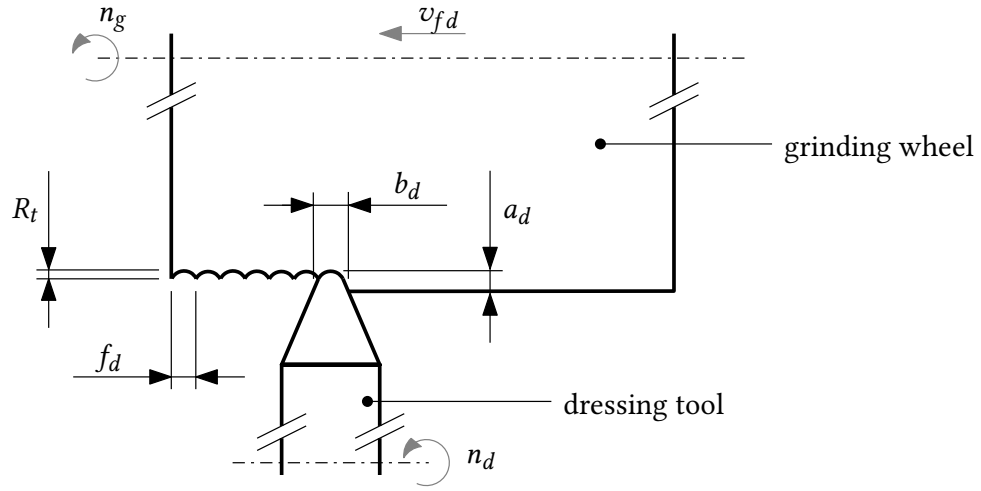

Figure 3.7.1: Overlap at dressing,
Source: own illustration.

Figure 3.7.1 illustrates the main dressing process parameters. This example shows a single-point dressing tool. The dressing tool is traversed across the surface of the grinding wheel.

[46] cf. Rowe B., 2014, pp.63-64.
[47] cf. Marinescu et al., 2016a, p.169.

Thereby, it generates the required form and cutting surface. The dressing depth of cut a_d and the dressing feed per revolution of the grinding wheel f_d create a helical groove on the wheel surface, according to description of Rowe. Moreover, the produced shape depends on the width of the dressing tool b_d in engagement with the grinding wheel. [48]

A low value of overlap ratio u_d creates a higher surface roughness on the grinded workpiece due to sharper cutting surface on the tool. In contrast, a high value of overlap ratio creates a smoother grinding wheel surface. It leads to higher grinding forces and higher specific energy of material removal. For conventional grinding, the overlap ratio should lie within the range $u_d = 2 \dots 20$. [49]

3.7.2 Dressing Tools and Processes

The dressing tools are divided into two major groups:

- Stationary dressing tools
- Rotary dressing tools

Stationary dressing tools are mainly used to dress conventional abrasives. This group includes single-point diamond (SD) and impregnated diamond (ID) dressing tools. They are available in a variety of shapes including round- and knife-shaped for form dressing. [50]

Rotary dressing tools are usually used for truing of vitrified CBN and resin-bonded CBN but in special cases also for dressing of conventional grinding wheels. Diamond wheels are mainly dressed using rotary dressing tools to avoid problems of rapid dressing tool wear. A rotary dressing tool may be a narrow disc with a layer of diamonds set around the periphery. [51]

Experiments within this thesis are exclusively performed using rotary dressing tools. By using this more complex conditioning method, more possibilities of regulation of the resulting surface structure on the grinding wheel are available, even for dressing of conventional abrasives. Especially the dressing-roll speed ratio q_d has major influence on the resulting surface roughness of the grinding wheel, as Figure 3.7.2 shows based on R. Schmitt [52] and E. Saljé. For lower surface roughness and lower dressing forces, the speed ratio should be reduced.

[48] cf. Rowe B., 2014, p.65.
[49] cf. ibid., p.66.
[50] cf. ibid., p.64.
[51] cf. ibid., p.67.
[52] cf. Schmitt, 1968, n.p.

$$q_d = \frac{v_d}{v_c} \tag{3.7.2}$$

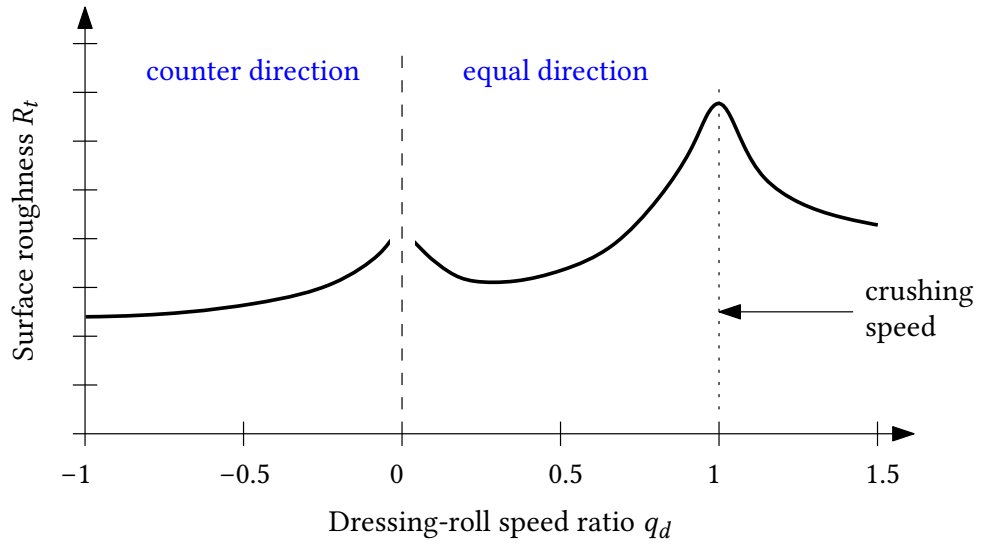

Figure 3.7.2: Influence of dressing-roll speed ratio on the surface roughness, Source: own illustration, based on Schmitt 1968.

Dressing is mostly performed with the grinding wheel running at normal operating speed. It is always important to carefully balance the wheel prior truing in order to reduce unbalance to a minimum.

3.8 Cooling and Lubrication

The majority of grinding processes is performed either with water-based oil-in-water emulsion or with a neat mineral oil or neat synthetic oil. Those cooling and lubricating fluids are transported to the contact area of grinding wheel and workpiece. Depending on the working speed of the grinding tool, the coolant is delivered using a low- or medium-pressure system. For low-speed grinding, fluid is typically supplied through a nozzle from a pump at a pressure in the range of 1 up to 4 bar. For high-speed grinding, much higher pressures (up to 80 bar and more) and higher flow rates are applied. [53]

The main functions of the cooling lubricant besides the obvious cooling and lubricating are:

- flushing and cleaning of the tool

[53] cf. Rowe B., 2014, p.124.

- flushing and cleaning of the workpiece
- transport of heat
- minimization of friction
- transport of removed material in form of chips
- transport of removed grinding wheel debris due to wear
- spark extinguishing

According to Ott, for external circular grinding the cooling nozzles should be arranged in equal direction to the cutting velocity. The lubricant jet should impingement the grinding wheel surface tangentially approximately 10° to 20° ahead of the contact zone of grinding wheel and workpiece. The discharge velocity of this stream should be as high as the grinding wheel circumference velocity. Thus, the lubricant jet penetrates the boundary layer of air at the tool's surface and is picked up. In this way, effective supply of the cooling lubricant can be presumed. [54]

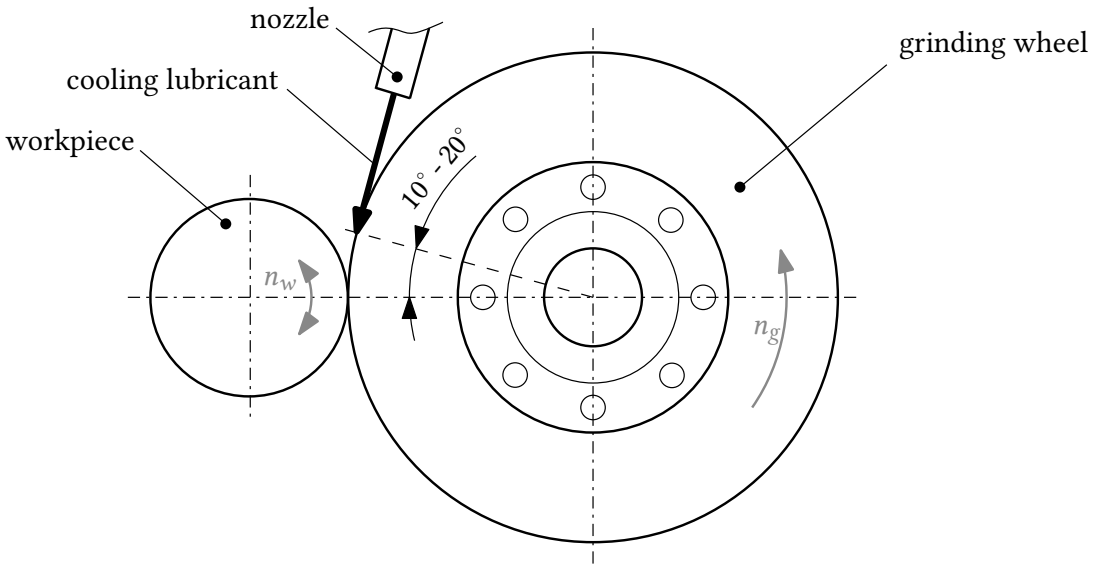

Figure 3.8.1: Equal direction cooling according to Ott,
Source: own illustration, based on Ott 2002.

In relation to the present work, exclusively water-based oil-in-water emulsion is used to cool and lubricate the working area. The grinding machine at IFT is equipped with needle nozzles for coolant supply.

[54] cf. Ott, 2002, pp.7-1.

3.9 Grinding Failures

Grinding is mainly performed as one of the latest processing steps within a value added production chain. Therefore, failures at this stage have a major effect and have to be categorically be excluded.

3.9.1 Categories of Failures

The macroscopic geometrical deviations can be avoided by precise adjustment of grinding machine and tool. The dressing of the grinding wheel is a key-process in order to rule out most of the possible failures. Due to this process step grinding wheel wear is compensated and therefore geometrical deviations on a macro- and microscopic scale can mostly be prevented. A new set of cutting edges is prepared for the upcoming grinding operations. In addition, removed workpiece material in form of chips is removed from the surface of the tool. Thermal damage of the peripheral zone of the workpiece can be counteracted by dressing the grinding wheel. Moreover, the grinding wheel specification concerning grain material and size, hardness, etc. have large impact on the functionality of a single process.

Possible failures are:

- macroscopic geometrical deviations
  - shape: form, cylindricity, parallelism, …
  - dimensions: diameters, length, …
  - chatter marks
- microscopic geometrical deviations
  - surface roughness qualities
  - micro structured surface: twist, …
- metallographical failures
  - grinding burn or burning (thermal damage)
  - micro-crack formation

3.9.2 Thermal Damage (Burning)

As previously mentioned, the thermal damage of the peripheral zone of the workpiece caused by overheating is called grinding burn or burning. During the grinding process high temperatures occur due to friction between the grain and the workpiece material, due to internal

friction in the material and due to friction between grain and chip (according to chapter 3.1). Whenever the emerging heat cannot be removed from the contact area by a cooling lubricant, the temperature rises and thermal damage of the workpiece occurs.

According to Meister and Rowe, thermal damage is mainly preprogrammed when one or more of the following circumstances are met: [55] [56]

- grain specification too hard
- grain blunt - no sharp cutting edges
- bonding too hard
- type of bond does not fit to process
- undersized porosity for the amount of chips
- missing or too little cooling of the contact area
- process parameters exceed process limits

Burning can either be detected by destructive or non-destructive testing. Optical, destruction-free methods are often chosen for the inspection of workpieces. When strong burning has occurred during a grinding process, dark brown and blue discolorations are visible on the grinded surface.

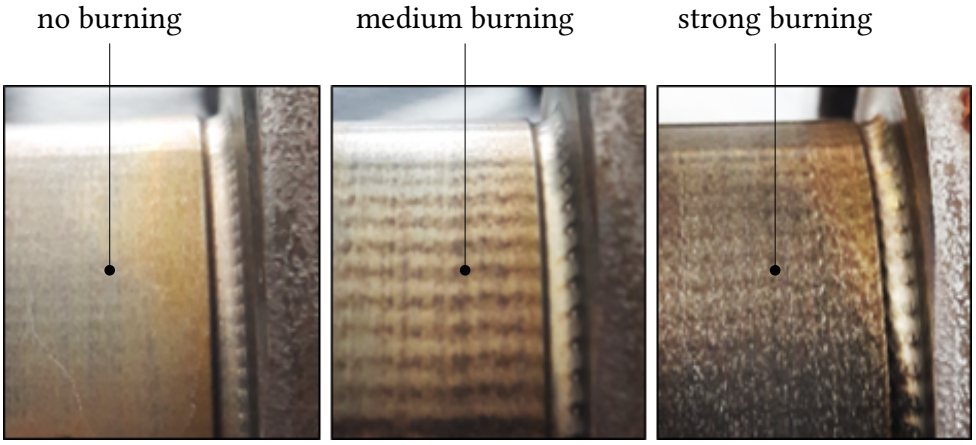

Figure 3.9.1: Visualization of thermal damage - surface etched by 3% Nital, Source: own illustration.

[55] cf. Meister M., 2011, pp.516-519.
[56] cf. Rowe B., 2014, pp.30-31,46.

Such a strong thermal damage can cause micro-crack formation due to strong tensile stresses at the near-surface areas. Workpiece surfaces etched by 3% Nital (according to ISO-14104) show intense coloration even at slightly damaged areas. Measurable characteristics are losses in hardness and alternation of residual stress underneath the workpiece surface.

Figure 3.9.1 shows three different grinding results after Nital etching. On the left photo no typical coloration for burning is visible. The middle picture definitely shows discolorations referring to medium thermal damage. On the right photo a strong response to the 3% Nital etching is visible.

4 Synchronous Grinding

In this section, a processing approach is described in which the revolutions per minute (RPM) of the workpiece and the grinding wheel are synchronized precisely in a fixed ratio. With RPM-Synchronous Grinding (RSG) the same points at the tool and at the workpiece meet repeatedly. This fact opens up various fields of application. It offers new possibilities to generate defined macro- and micro-geometries on workpieces. An effective cutting velocity mainly arises by the diameter difference of tool and workpiece.

Grinding as a finishing machining process is mainly one of the latest steps in a manufacturing chain. Thereby, the final workpiece geometry and the surface quality, profile and surface texture are produced. In hardened condition, workpieces in general are mainly machined by grinding. Process capability has always highest priority to prevent rejection. The more complex workpiece geometries are, the higher production costs have accumulated up to the grinding process and the more energy has already been consumed. Therefore, guaranteeing a stable finishing process has highest priority. Especially novel grinding approaches such as the RPM-Synchronous Grinding process must be well understood before applying to industrial application. Thus, it promises high potential for improvement for the generation of functional macro- and micro-geometries with integral features on workpiece surfaces.

4.1 Micro- and Macrostructure

It was mainly Spur and Eichhorn who used a first test-bench developed by Sawluk and Wiemann [57] to perform first experiments concerning RPM-Synchronous Dressing and Grinding in the nineties of the twentieth century. They dealed with the generation of non-circular grinding wheels in order to produce non-circular workpieces in a single plunge grinding process. Moreover, they experimented on deliberate structuring of the grinding wheels' cutting surface to document the influence on the grinding results. [58] [59]

Approximately two decades later, Ablinger took up the ideas of Eichhorn and Spur and worked

[57] cf. Sawluk, Wiemann, 1985, pp.71-83.
[58] cf. Spur, Eichhorn, 1996a, pp.55-57.
[59] cf. Spur, Eichhorn, 1996b, pp.128-137.

on the development of the process of RPM-Synchronous Non-Circular Grinding. He aimed for the production of arbitrary workpiece shapes on a macroscopic scale. [60]

4.1.1 Macro-geometries

RPM-Synchronous Grinding promises a change of paradigm concerning machining of non-circular workpiece geometries in hardened condition. With conventional technology, various macroscopic non-circular geometries must be grinded subsequently in an oscillating process where the X-axis is coupled with the rotary workpiece-spindle axis. Utilizing the approach of RPM-Synchronous Grinding, workpieces with non-circular and non-cylindrical surface geometries can be machined in a single plunge grinding process for the first time. Therefore, workpieces with any desired shapes - free in three dimensions in space - can theoretically be machined. Some of those geometries could be machined in a conventional non-circular grinding process, but would be extraordinarily work-intensive.

The RPM-Synchronous Grinding concept, where grinding wheel and workpiece rotate in a fixed ratio, opens up various fields of applications. Prominent applications are cam shapes for camshafts or eccentric shafts for valve control of internal combustion engines. Piston and piston rings have non-circular body shapes and could be machined with RPM-Synchronous Non-Circular Grinding. [61] Other examples are injection, delivery and metering pumps as well as diverse components integrated in machine tools. [62] [63] Moreover, positive locking shaft-hub connection such as polygonal profiles DIN 32711 or DIN 32712 which are frequently used for torque transmission in various power trains, could be manufactured utilizing the novel production process.

4.1.2 Micro-geometries

While RPM-Synchronous Non-Circular Grinding is primarily used to manufacture shapes deviating from circular and cylindrical geometries in the radial cross-section, this process promises technological enhancements in other fields too. In addition to the production of macro-geometries, the general RPM-Synchronous Grinding process offers new possibilities to generate defined functional micro-structures on workpieces. As already explained, single points on the grinding wheel meet single points at the workpiece again and again. This

[60] cf. Ablinger, 2014.
[61] cf. ibid., pp. 92-93.
[62] cf. Brill, 1977, p. 623.
[63] cf. Spur, Eichhorn, 1994, p. 35.

property allows structuring of the surface of the workpiece during grinding of circular and non-circular workpiece shapes.

Components with functional surfaces are becoming more and more important in industry. The term functional surfaces describes a deliberate design of a surface to enhance functionality or to add features to the workpiece. Such structures can reduce friction or build cavities for liquids. Defined textures can improve the tribological performance through specifically formed oil reservoirs or reduce flow losses by longitudinally ribbed surfaces (so-called riblets).[64] [65] Therefore, different novel dressing strategies have been created in the past to design a surface texture on the grinding wheel which can be transferred to the workpiece in further consequence during synchronous grinding process.[66] [67] Moreover, Denkena et al. investigated that micro-patterned grinding wheels influence the workpiece surface quality.[68] Such patterned tools even enhance grinding performance.[69]

Figure 4.1.1 illustrates applications of different micro-structures which are machined using various procedures such as fly-cutting, turning and grinding. These structure facilitate the reduction of friction, the storage of information on workpiece surfaces and the reduction of flow losses.[70]

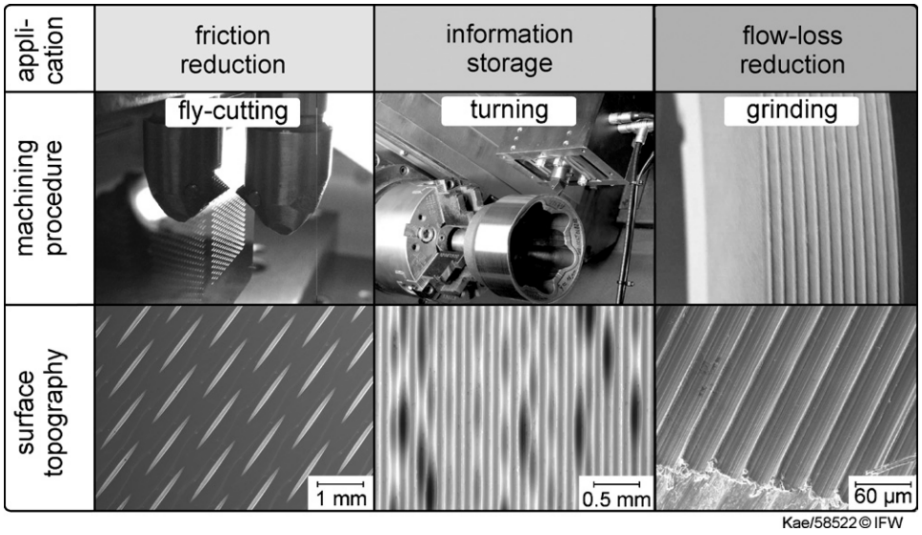

Figure 4.1.1: Micro-structure applications, applied machining processes and resulting surface topographies,
Source: Denkena et al., 2010 (p.68).

[64] cf. Denkena et al., 2009, pp.207–222.
[65] cf. Denkena et al., 2010, pp.67-72.
[66] cf. da Silva et al., 2013, pp.355-358.
[67] cf. Oliveira et al., 2010, pp.361-364.
[68] cf. Denkena et al., 2013, pp.249-252.
[69] cf. Denkena et al., 2015, pp.1935-1941.
[70] cf. Denkena et al., 2010, pp.68.

With the process of RSG the range of functional surface textures produced by grinding can be enlarged. Since same cutting edges on the tool exclusively machine the same points on the workpiece, the generation of 3-dimensional micro-structures is possible.

The process of RPM-Synchronous Grinding allows the separation of specific workpiece surface areas in sections which are processed by different tool qualities and compositions. Figure 4.1.2 gives an idea of this process. For instance, a workpiece with different requirements on surface roughness or different micro-structure can be machined applying RSG in combination with a special tool with advanced sectoral composition.

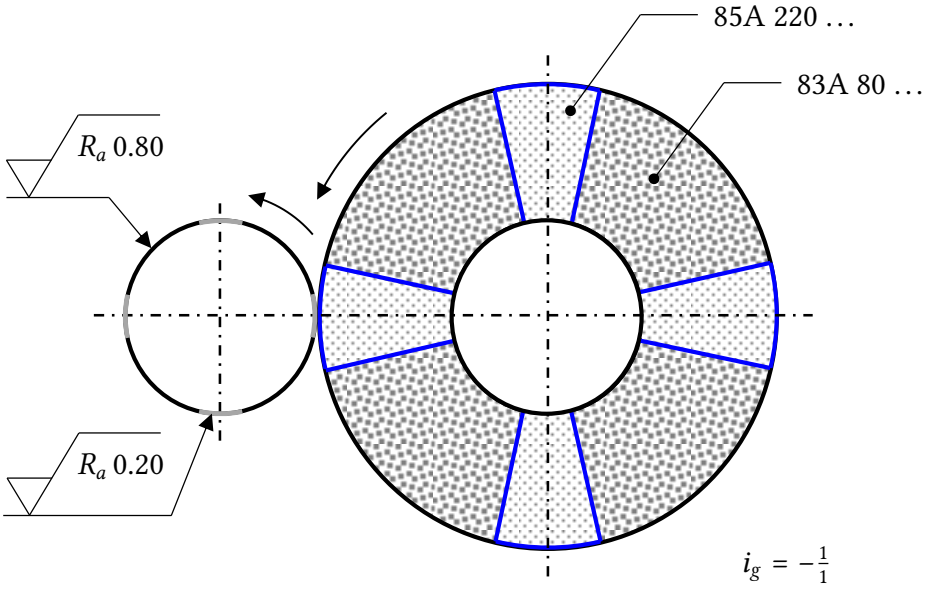

Figure 4.1.2: Advanced sectoral tool composition,
Source: own illustration.

Micro-structuring in general promises improvement in special properties of various workpieces. More precisely, such functional surfaces are applied to:

- Reduction of friction or flow losses
- Improvement of efficiency
- Life-time extension
- Reduction of emissions
- Preservation of resources

4.2 Coupling of Rotational Axes

Spur and Eichhorn described the advantages of rigid kinematic coupling of the interacting partners in grinding machining processes in 1993. [71] In the following years, they published several paper concerning similar topics emphasize their original work. With the concept for non-circular grinding, no contour-generating relative movement between workpiece axis and grinding wheel rotation axis is necessary. [72] [73] They used a test bench developed by Sawluk and Wiemann, especially designed for kinematic coupled dressing and grinding. Thereby, a mechanical gear fixed the rotational ratio between grinding wheel and workpiece. [74]

In all conventional non-circular grinding processes the grinding wheel is characterized by a circular cross-section. With present technology various non-circular geometries on a workpiece must be grinded subsequently in an oscillating process where X- and Q-axis of the machine are coupled. In addition, a movement of the grinding spindle in Z-directions is necessary for three-dimensional non-circular workpieces grinded with conventional technology. Figure 4.2.1 shows the process kinematic on the left side.

With the approach of RPM-Synchronous Non-Circular Grinding such workpieces can be machined in an ordinary plunge grinding process. Therefore, the workpiece and the grinding wheel revolutionary rate are in a fixed ratio. A non-circular grinding wheel is used to transfer its geometry onto the workpiece. At the right side in Figure 4.2.1, the RPM-Synchronous Non-Circular Grinding process is illustrated. Both processes show the example of machining of a workpiece with a quadratic cross-section. To prevent unbalance, the grinding wheel geometries should be rotationally symmetrical for all grinding processes (circular and non-circular). [75]

In this context, Spur and Eichhorn described three basic principles for rigid coupling of the interacting partners in grinding and dressing: [76]

- The **symmetry-principle** of contour generation: The circumference contour is determined in radial direction and consists of multiple repetitive elements. All operating partners (dressing tool and grinding wheel) are rotationally symmetric. Their rotational axis passes the areal centroid of all radial sections.

[71] cf. Spur, Eichhorn, 1993, p.180.
[72] cf. Spur, Eichhorn, 1994, p.36.
[73] cf. Spur, Eichhorn, 1995, p.15.
[74] cf. Sawluk, Wiemann, 1985, pp.71-83.
[75] cf. Spur, Eichhorn, 1997b, p.269.
[76] cf. Spur, Eichhorn, 1997a, pp.243-244.

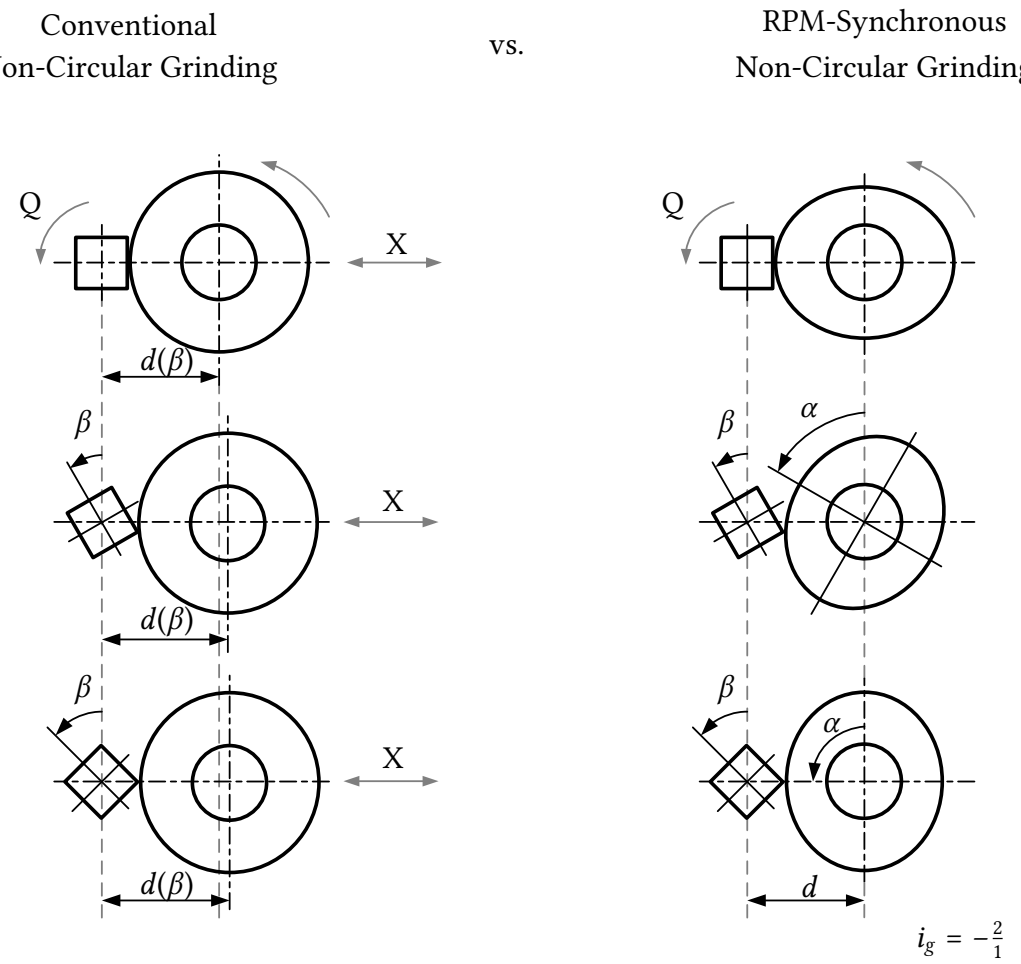

Figure 4.2.1: Kinematics of non-circular grinding,
Source: own illustration.

- The **equality-principle** for dressing tool and workpiece: In general, dressing tool and workpiece can have different geometric shapes. It is reasonable that the profile-roll used for dressing has the exact same geometry as the workpiece. In the case, the equality-principle is postulated.
- The **reversibility-principle** states the transferability of a grinding wheel contour onto the workpiece and vice versa. Therefore, every point at the outline on the circumference of the tool must necessarily meet the same point on the operating partner over and over. The grinding wheel acts as form transmitter between dressing tool and workpiece.

In 1996, Spur and Eichhorn described properties of a RPM-synchronous dressing process. Thereby, a gear coupling between grinding wheel and dressing tool was used to ensure constant and repeatable conditions in the contact zone during dressing. With this approach, the actual surface roughness on the grinding wheel could be enhanced essentially in comparison to conventional dressing with velocity ratio $q_d = 1$. At the same time, the actual surface

roughness on the grinding wheel is independent of the dressing infeed a_p. [77]

Later the same year, Spur and Eichhorn investigated the effects of RPM-synchronous dressing on the grinding process. Since contact ratio is decreased by increasing of the actual surface roughness on the grinding wheel, significantly higher wear on the grinding wheel was noticed. Due to the lower number of kinematic cutting edges, the tangential force and the power demand of the dressing process were lower in contrast to grinding after conventional dressing. Moreover, the grinded workpiece surface showed more distinct roughness properties. The rigid coupling of grinding- and dressing wheel promises potential for processes with continuous dressing strategies. It enlarges grinding wheel wear what decreases the process' economy and brings no advantages at finishing due to the higher expected surface roughness on the workpiece. [78]

In addition, Spur and Eichhorn evaluated kinematically rigid coupled external plunge grinding and its working results. This RPM-Synchronous Grinding process revealed that the tangential force at grinding is higher in comparison to conventional grinding no matter what type of coupling and speed ratio was used. This is caused by the more pronounced surface roughness of the grinding wheel and larger contact area in the RPM-Synchronous Grinding process. [79]

In 2012, Ablinger et al. used an electronical gear for coupling of the workpiece- and the grinding wheel spindle for the first time. He performed first general tests on an adapted FORTUNA grinding machine. These experiments proved the concept for further research on RPM-Synchronous Non-Circular Grinding (RSNG). Since the machine was not fully capable to meet the requirements of this special process, the resulting surface qualities were not yet satisfying industrial demands. In fact, the experiments revealed possible applications for the RSNG process, such as the simultaneous machining of a whole camshaft or polygon-profiles for shaft-hub connections. In addition, Ablinger et al. conducted a rough assessment of cost reduction capabilities of the RPM-Synchronous Grinding process. The main argument here was the shortening of process time due to simultaneous machining of several non-circular zones with different orientations on a single workpiece. [80] [81]

At last, in 2014, Ablinger aggregated his efforts concerning the topic of RPM-Synchronous Non-Circular Grinding from a theoretical point of view in his doctoral thesis. Ablinger applied

[77] cf. Spur, Eichhorn, 1996a, pp.55-57.
[78] cf. Spur, Eichhorn, 1996b, pp.128-137.
[79] cf. ibid., pp.134-137.
[80] cf. Ablinger et al., 2012a, pp.55-58.
[81] cf. Ablinger et al., 2012b, pp.193-199.

for two patents together with Dr. Schmid and DAIMLER AG.

Patent applications:

> "Method for non-circular grinding of workpiece, involves rotating workpiece and grinding wheel around respective parallel axes, where grinding surface of wheel is non-circular and non-cylindrical, and workpiece is displaced by cardanic driving." [82] (German Patent DE 102012015754 A1)

> "Method for non-circular grinding of cam of assembled camshaft in combustion engine of lorry, involves displacing workpiece and grinding roller relative to each other such that grinding path at surface of roller follows non-circular helix." [83] (German Patent DE 102012015752 A1)

[82] Ablinger, Schmid, 2014b.
[83] Ablinger, Schmid, 2014a.

4.3 Non-Circular Geometries

With the process of RPM-Synchronous Non-Circular Grinding, non-circular workpieces are manufactured in one simple plunge grinding process. Thereby, the grinding wheel shape represents the corresponding negative geometry of the workpiece.

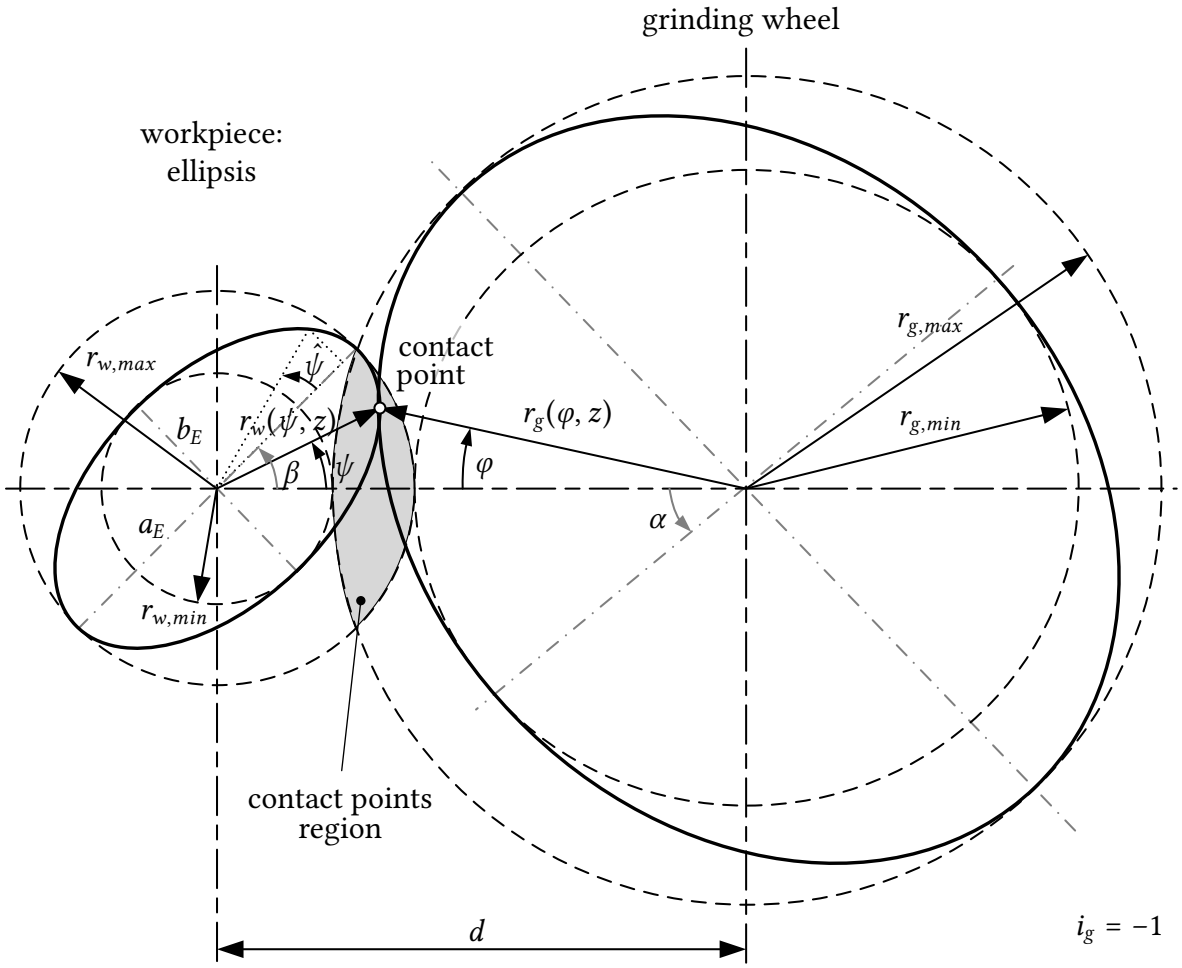

Figure 4.3.1: Geometry for RPM-Synchronous Non-Circular Grinding,
Source: own illustration.

The workpiece geometry together with the chosen rotational ratio i_g during grinding and the rotation direction (equal direction or counter direction) determine the geometry of the grinding wheel. The rotational ratio i_g is negative ($i_g < 0$) for counter direction grinding and positive ($i_g > 0$) for equal direction grinding.

$$i_g = \frac{n_g}{n_w} \tag{4.3.1}$$

The center distance d between workpiece and grinding wheel is given by the radius of the inner circle of workpiece $r_{w,min}$ and the maximum grinding wheel radius $r_{g,max}$. Moreover, the minimum and maximum radii of both workpiece and grinding wheel set the region of possible contact points where actual grinding is performed.

$$d = r_{w,min} + r_{g,max} \tag{4.3.2}$$

$$d = r_{w,max} + r_{g,min} \tag{4.3.3}$$

Figure 4.3.1 exemplarily shows a contact point in a certain angular position and the intersection area of possible contact points for the whole geometry marked in grey.

When dressing a non-circular grinding wheel geometry with a common, circular form-roll in an oscillating process, the X-Q-axis relation has to be calculated precisely. According to Ablinger, a direct calculation of the demanded grinding wheel geometry is not possible in general [84]. He calculated the non-circular geometries for his experiments iteratively.

As per Eichhorn, it is theoretically conceivable to describe an envelope of a fixed form element of the grinding wheel geometry analytically. Eichhorn discussed theoretical aspects of geometries calculation in his doctoral thesis. Within his work, he analysed contact points for convex and concave workpieces, contact angles, curvatures, relative velocities, etc. Moreover, he mentioned the emergence of envelopes at contouring:

It is theoretically conceivable to describe the enveloping curve analytically for a specific form element. However, since the array of contour curve is depending on both the time parameter t and the contour of the dressing tool $r_R(\phi_R)$, the calculations are very complex and are not dealt with in Eichhorn's work. [85]

4.4 Direct Calculation of Geometries

Whenever the perimeter of a two dimensional cross-section of the workpiece is representable as a mathematical function, it is possible to calculate certain parts of the corresponding grinding wheel shape directly. By rotating this function (e.g. in parameter notation) around a pivot

[84] cf. Ablinger, 2014, p.52.
[85] cf. Eichhorn, 1997, p.142.

point in distance of the center distance between workpiece and grinding wheel and around its own center of rotation, an array of curves appears. If a curve exists which is tangent to all curves of the array this particular curve is called envelope of the array [86]. An envelope can be the result of the wanted grinding wheel perimeter in a two dimensional cross-section. Depending on the complexity of the mathematical function, the envelope can consist of irrelevant parts as well. Due to this fact, this direct calculation is impractical for application upon the tangible issue.

4.4.1 Analytical Solution

Equation 4.4.1 and 4.4.3 show mathematical calculation of the array of curves for the example of an elliptic workpiece perimeter. $\vec{R}_g$ is the rotation matrix for the rotation around a pivot point in distance of the center distance $\vec{D}$ between workpiece and grinding wheel. $\vec{R}_w$ is the rotation matrix of the ellipsis $\vec{W}$. The envelope is calculated for each cross section (constant variable z) by converting one of the equations for x or y into one of the unknown variables and inserting them into the respective other equation [87].

$$\vec{P}(\alpha, i_g, \hat{\psi}) = \vec{R}_g \cdot [\vec{D} + \vec{R}_w \cdot \vec{W}] \tag{4.4.1}$$

$$\vec{P}(\alpha, i_g, \hat{\psi}) = \begin{pmatrix} x \\ y \\ z \end{pmatrix} \tag{4.4.2}$$

$$\vec{P}(\alpha, i_g, \hat{\psi}) = \begin{pmatrix} cos(\alpha) & sin(\alpha) & 0 \\ -sin(\alpha) & cos(\alpha) & 0 \\ 0 & 0 & 1 \end{pmatrix} \cdot \left[\begin{pmatrix} d \\ 0 \\ z \end{pmatrix} + \begin{pmatrix} cos(i_g \cdot \alpha) & sin(i_g \cdot \alpha) & 0 \\ -sin(i_g \cdot \alpha) & cos(i_g \cdot \alpha) & 0 \\ 0 & 0 & 1 \end{pmatrix} \cdot \begin{pmatrix} a_e \cdot cos(\hat{\psi}) \\ b_e \cdot sin(\hat{\psi}) \\ z \end{pmatrix} \right] \tag{4.4.3}$$

[86] cf. Erven, Schwägerl, 2011, pp.354-356.
[87] cf. ibid., pp.354-356.

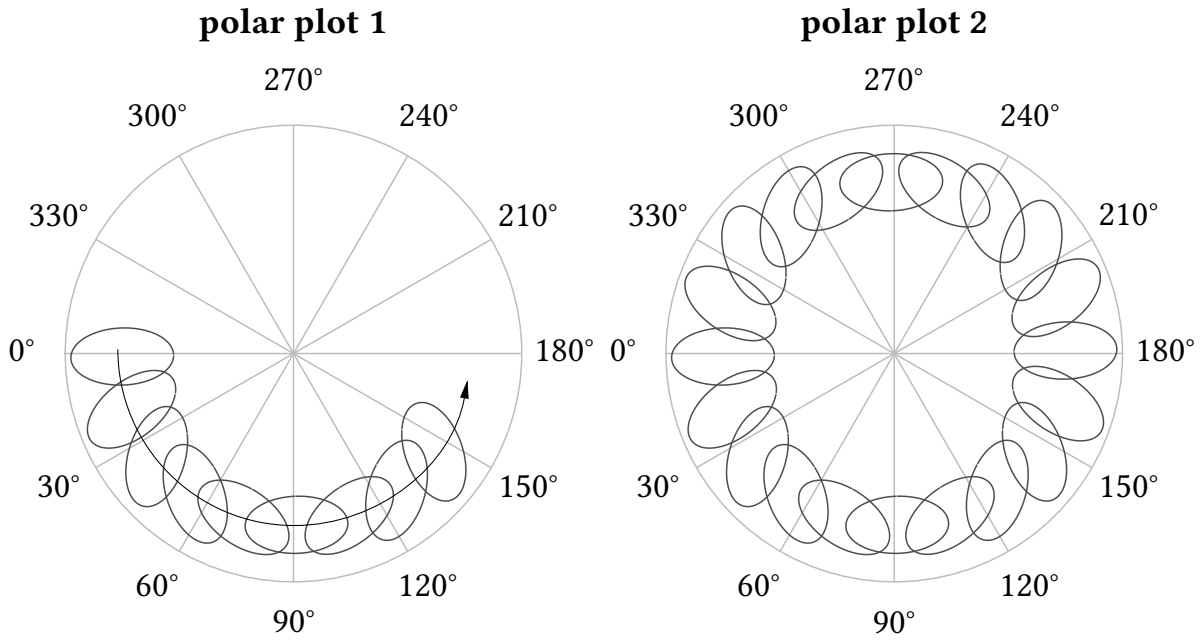

Figure 4.4.1: Rotation of an ellipsis around itself and a pivot point: low resolution, Source: own illustration.

Figure 4.4.1 shows Equations 4.4.1 to 4.4.3 applied on the elliptical workpiece in a certain center distance as pivot point of the polar plots. Polar plot 1 represents nine stages of the ellipsis. For better illustration of the relevant part of the envelope, Figure 4.4.2 displays a higher rotational resolution for the same elliptical workpiece as demonstrated in the previous graphics.

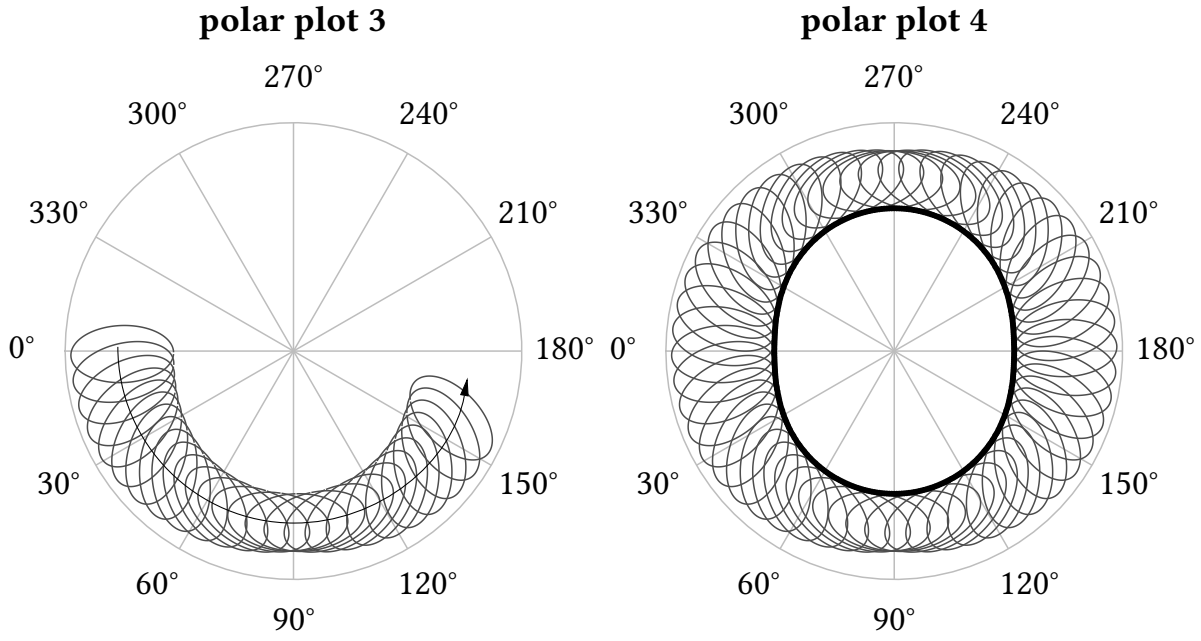

Figure 4.4.2: Rotation of an ellipsis around itself and a pivot point: high resolution, Source: own illustration.

4.4.2 Point-wise Solution

Another more practical solution is to calculate the workpiece geometry with a distinct step-wise approach. Therefore, the workpiece geometry must be representable as a mathematical function as well. A discrete mesh-grid is defined which is filled with point-wise solutions of the rotation of the workpiece geometry around the grinding wheel pivot point and around itself. The software package MATLAB (MATrix LABoratory) is designed to solve such matrix operation instantly. The polar plot 5 in Figure 4.4.3 displays a mesh-grid with 10°-steps for the rotation of the ellipsis around the pivot point and 10°-steps around the rotational axis of the grinding wheel ($i_g = 1$). At the right-hand side, the grey dots in polar plot 6 show results in a mesh-grid with a significantly higher resolution of 2°-steps concerning both grinding wheel and workpiece. Additionally, a minimum-function is applied on the whole solution matrix which generates the final solution for the grinding wheel geometry. This result is yet plotted as black dots accumulated to a line in polar plot 6.

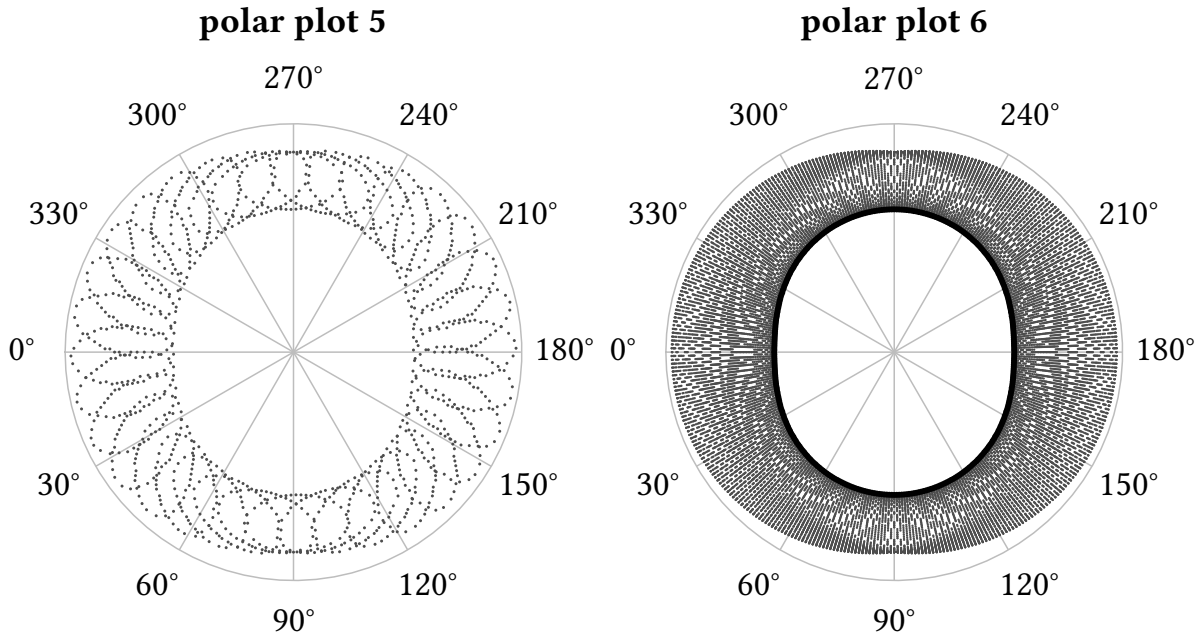

Figure 4.4.3: Calculation in a mesh-grid,
Source: own illustration.

Utilizing this point-wise calculation approach allows rapid calculation of the wanted grinding wheel geometry using for instance the software package MATLAB. A prerequisite is the full representability of the workpiece geometry as a mathematical function. For three-dimensional workpieces the change of the workpiece geometry in Z-direction must be representable as a mathematical function as well.

4.5 Iterative Calculation of Geometries

In his doctoral thesis, Ablinger explicitly described procedures for stepwise calculation of grinding wheel geometries. Whenever a workpiece geometry is not or just partly representable as a mathematical function, an iterative calculation of the associated grinding wheel geometry is inevitable. Therefore, different approaches for this geometry calculation are feasible. [88]

The most expedient calculation strategy, the **beam-length-calculation-technique (BLCT)**, is described here. The workpiece geometry is point-wise given in tabular form with values for radius r_w and angle $\hat{\psi}$. The center distance d has also be defined prior calculation. Starting at the rotational axis of the grinding wheel, virtual beams with discrete angular spacing point in every direction among 0° and 360°. Figure 4.5.1 demonstrates the general idea of the beam-technique and shows some of the beams which point in the workpieces direction.

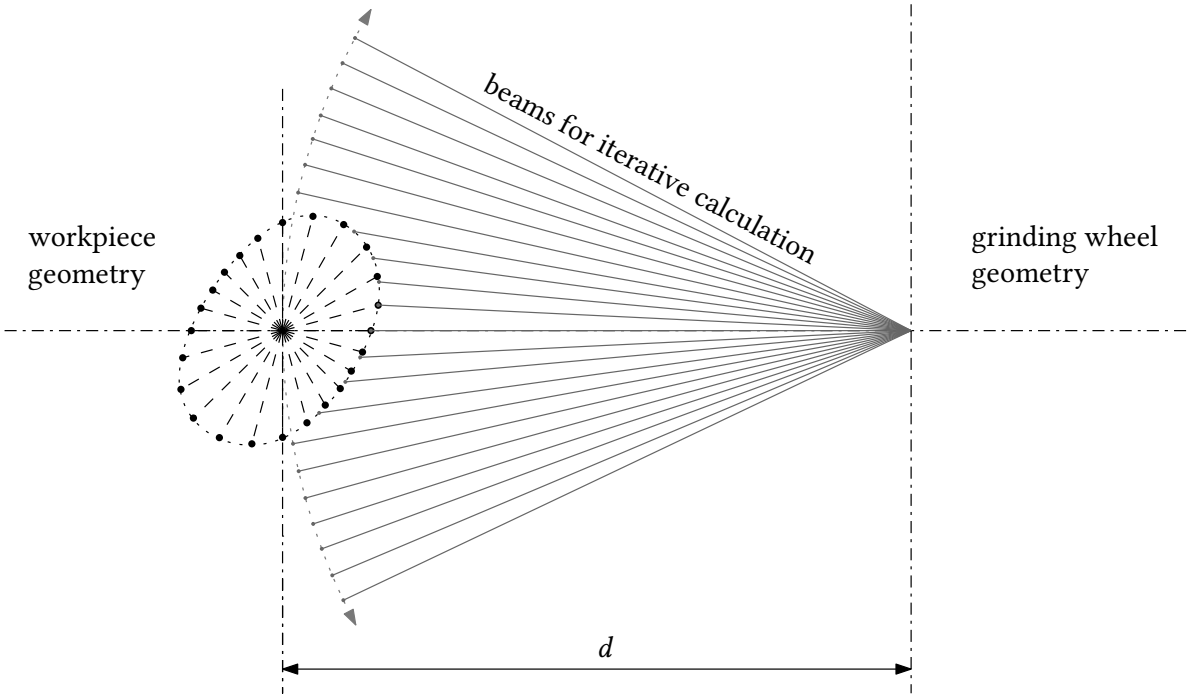

Figure 4.5.1: Virtual beams for iterative calculation of the grinding wheel geometry, Source: own illustration.

The idea behind BLCT is the following: In every angular position of the workpiece and the grinding wheel, the beams are cut at the workpieces lateral surface and the radius $r_g(\hat{\varphi})$ is stored in a matrix. Depending on the rotational ratio i_g, both workpiece and grinding wheel are rotated stepwise around their rotational axis. r_g is again trimmed at the lateral surface

[88] cf. Ablinger, 2014, pp.51-61.

of the workpiece. In case the current radial distance $r_g(\hat{\varphi})$ is smaller than the stored value, it is overwritten by the new figure. After incrementally rotating the grinding wheel and the workpiece 360°, all minimum values representing the shortest radial distances r_g depending on their corresponding angle $\hat{\varphi}$ are the result for the wanted grinding wheel geometry.

Given workpiece geometry points and grinding wheel beams just meet by chance. In general, beams point anywhere between two known points of the workpiece, as Figure 4.5.2 presents. For explicit calculation of the beam number $IV.$ at a certain rotational angle, the grey marked triangle in Figure 4.5.2 and 4.5.3 is consulted. The strategy uses a linear interpolation between two given points of the workpieces geometry. Therefore, the workpiece must be defined with high resolution or a pre-interpolation must be performed.

The dimensions of $\Delta x_{(n)}$ and $\Delta y_{(n)}$ are needed to calculate the angle $\delta_{(n)}$ as Equations 4.5.1 to 4.5.7 state. The index n stands for Arabic characters and therefore refers to the workpiece side. In contrast, all abbreviations with index m correlate to Roman characters and hence to workpiece beams and angles.

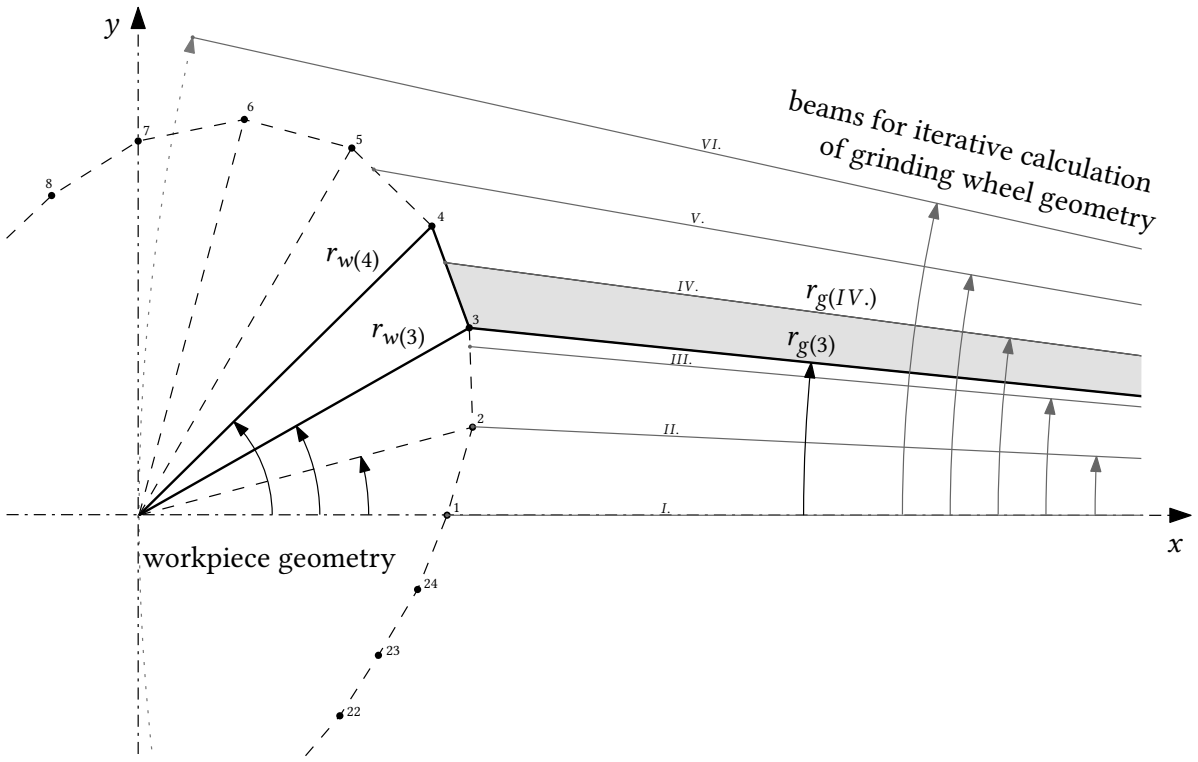

Figure 4.5.2: Geometry calculation method BLCT: overview,
Source: own illustration.

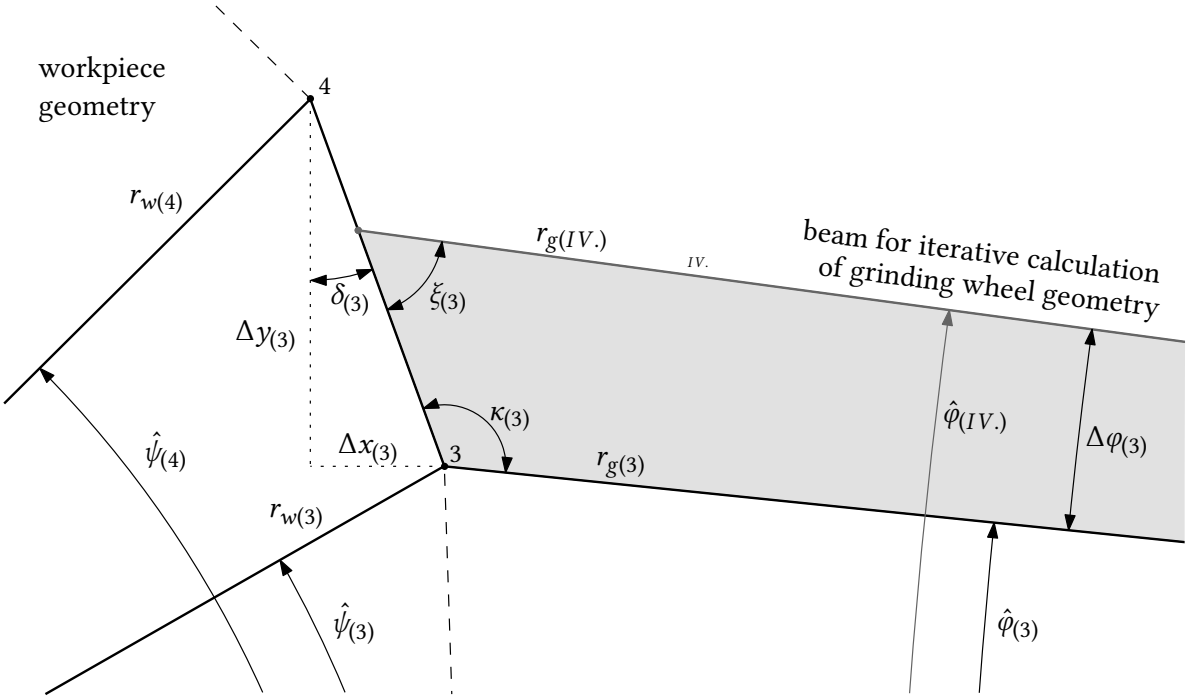

Figure 4.5.3: Geometry calculation method BLCT: detailed depiction,
Source: own illustration.

$$x_{(n)} = r_{w(n)} \cdot \cos(\hat{\psi}_{(n)}) \tag{4.5.1}$$

$$x_{(n+1)} = r_{w(n+1)} \cdot \cos(\hat{\psi}_{(n+1)}) \tag{4.5.2}$$

$$y_{(n)} = r_{w(n)} \cdot \sin(\hat{\psi}_{(n)}) \tag{4.5.3}$$

$$y_{(n+1)} = r_{w(n+1)} \cdot \sin(\hat{\psi}_{(n+1)}) \tag{4.5.4}$$

The angles $\Delta\varphi_{(n)}$, $\xi_{(n)}$ and $\kappa_{(n)}$ define the grey highlighted triangle. Together with the dimension for $r_{g(n)}$ the sine theorem can be applied in order to calculate the wanted beam length $r_{g(m)}$ (Equation 4.5.13).

$$\Delta x_{(n)} = x_{(n+1)} - x_{(n)} \tag{4.5.5}$$

$$\Delta y_{(n)} = y_{(n+1)} - y_{(n)} \tag{4.5.6}$$

$$\delta_{(n)} = \tan^{-1}\left(\frac{|\Delta x_{(n)}|}{\Delta y_{(n)}}\right) \tag{4.5.7}$$

Utilizing this strategy on all beams which are crossing the workpiece geometry stepwise in

every single rotational position, brings up the resulting grinding wheel geometry. This iterative process works for all imaginable workpiece geometries unaffected by concave or convex parts of the geometry.

$$r_{g(n)} = d - x_{(n)} \tag{4.5.8}$$

$$\hat{\varphi}_{(n)} = \tan^{-1}\left(\frac{y_{(n)}}{r_{g(n)}}\right) \tag{4.5.9}$$

$$\Delta\varphi_{(n)} = \hat{\varphi}_{(m)} - \hat{\varphi}_{(n)} \tag{4.5.10}$$

$$\xi_{(n)} = 90^{\circ} - \hat{\varphi}_{(m)} - \delta_{(n)} \tag{4.5.11}$$

$$\kappa_{(n)} = 180^{\circ} - \xi_{(n)} - \Delta\varphi_{(n)} \tag{4.5.12}$$

$$r_{g(m)} = \frac{\sin(\kappa_{(n)}) \cdot r_{g(n)}}{\sin(\xi_{(n)})} \tag{4.5.13}$$

Though, it must be noted, that not every random concave geometry part is producible with every rotational ratio i_g and rotational direction (equal or counter direction) and the axial distance d. In order to get information about boundary conditions for RPM-Synchronous Non-Circular Grinding processes concerning producibility of complex geometries, a software was written in MATLAB. Figure 4.5.4 illustrates the graphical user interface of the software (GUI).

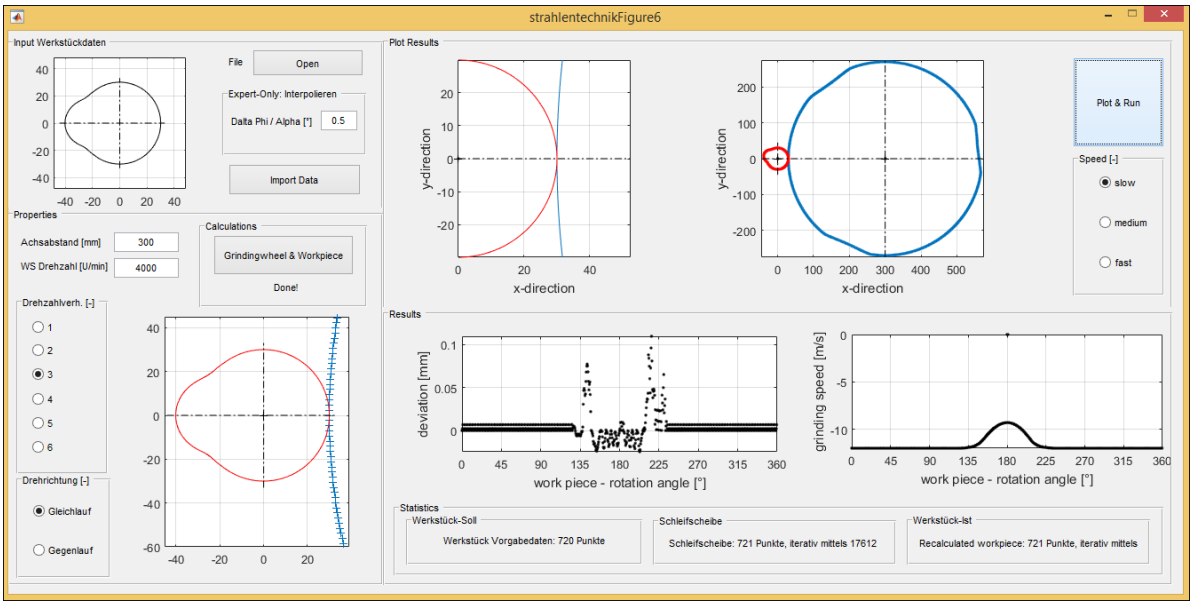

Figure 4.5.4: Graphical user interface,
Source: own illustration.

4.6 Dressing of Non-Circular Grinding Wheels

In general, there are two possibilities for dressing of non-circular grinding wheels. Those tool types mainly differ in their geometry and the rotational speed in use.

- Non-circular dressing profile-roll
- Circular, narrow disc

Both dressing approaches have their advantages and disadvantages and have already been used in the past for dressing of non-circular grinding wheel for the process of RSNG.

The first option is to take a **non-circular dressing profile-roll** which copies its geometry onto the grinding wheel. Rotational rates of dressing tool and grinding wheel during truing depend on the rotational ratio as they must be coupled during operation.

Spur and Eichhorn used this approach in 1993 to generate a non-circular grinding wheel. They employed a dressing profile-roll set with diamond for three dimensional contour generation. This particular dressing tool was mechanically coupled in rigid kinematics with the grinding wheel and the workpiece spindle. The dressing profile-roll was used to copy its geometry onto the grinding wheel by applying the same rotational ratio during dressing i_d (Equation 4.3.1) as later used during grinding i_g (Equation 4.6.1). [89] [90]

$$i_d = \frac{n_d}{n_g} \tag{4.6.1}$$

Grinding of non-circular workpieces with non-circular grinding wheels involves non-uniform grinding conditions over the circumference of the abrasive tool. The same applies for conditioning of grinding wheels with profile-rolls. Spur and Eichhorn recognized increased wear of the dressing tool at areas of heavy curvature. [91] [92]

The second option is to use a standard **cylindrical dressing form-roll** to generate a non-circular grinding wheel by coupling Q-axis of the grinding wheel with the X-axis position of the grinding support. A non-circular geometry is generated at the grinding wheel by a oscillating movement of the X-axis slide. In particular, dressing works like a conventional non-circular grinding process with the only difference that the machined part now is the grinding

[89] cf. Spur, Eichhorn, 1993, p.180.
[90] cf. Spur, Eichhorn, 1994, p.36.
[91] cf. Spur, Eichhorn, 1993, p.184.
[92] cf. Spur, Eichhorn, 1994, p.40.

wheel itself[93]. Ablinger described this particular process in his doctoral thesis. For dressing with a non-circular profile-roll, no change in process-parameters can be conducted to alter the grinding wheels structure. In contrast, parameters like velocity ratio for dressing q_d, overlap in Z-direction u_d or dressing infeed a_p can be changed any time to optimize the result of the dressing process utilizing the oscillation method for dressing. In this context, the terminology of rough-dressing and fine-dressing is introduced. For raw shaping of the non-circular grinding wheel contour from a standard circular blank, a rough-dressing process is used. Here, the dressing overlap is chosen comparably low and dressing infeed rather high. Once the demanded shape is reached, fine-dressing parameters are used for gaining a fine structure on the surface of the abrasive. This ensures high roughness quality properties on the target workpiece.

Figure 4.6.1 explicitly shows the corresponding axes of the grinding machine. The X-axis of the compound slide is perpendicular to the Q-axis which is the rotational axis of the workpiece.

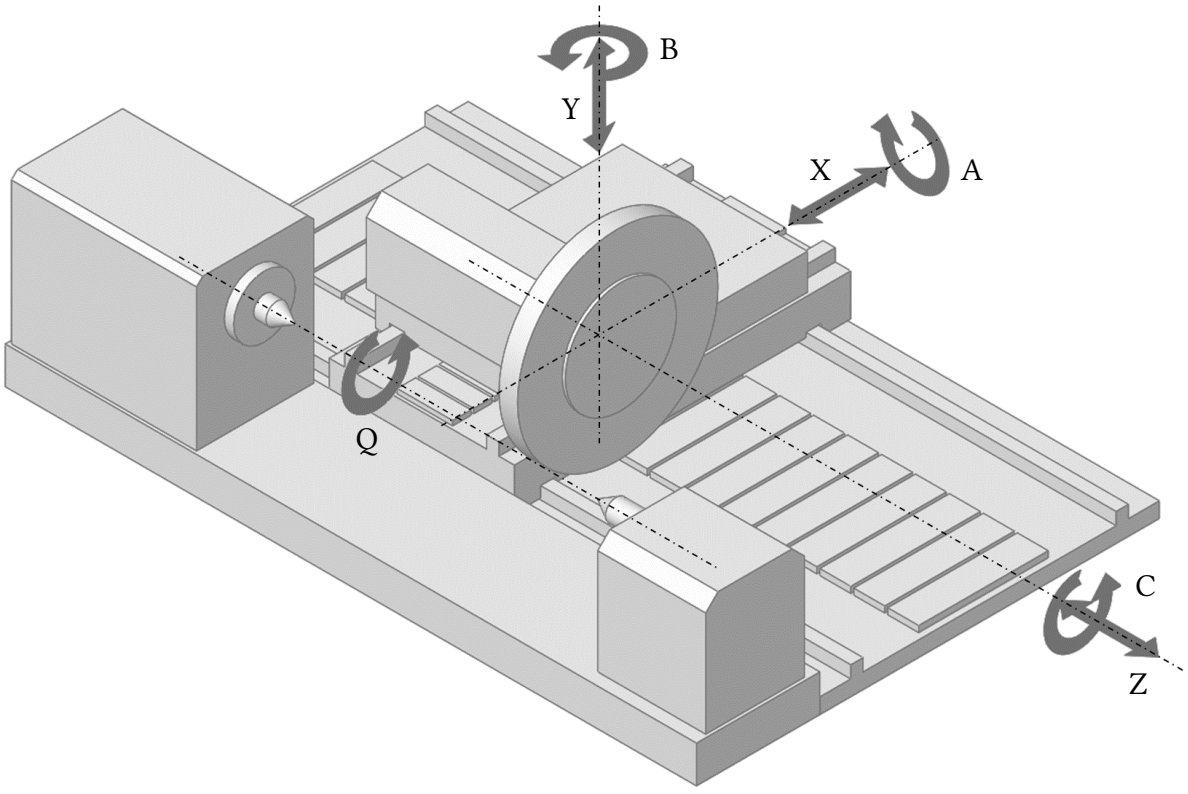

Figure 4.6.1: Grinding machine axes,
Source: own illustration.

However, not all geometries can be created via the oscillation dressing method. The radius of the dressing tool determines the minimum concave radius on the grinding wheel in case the

[93] cf. Ablinger, 2014, pp.9-13.

grinding wheel shapes consists of concave contour parts. No limitations occur for grinding wheel geometries without required concave contour parts.

For RPM-Synchronous Grinding, the values for the dressing overlap u_d must be chosen deliberately. For RPM-Synchronous finishing, values for u_d must be chosen even higher compared to conventional dressing processes. Values up to 80 might be necessary in some cases. In contrast, for RPM-Synchronous roughing, standard values for u_d can be chosen. In case, the RPM-Synchronous grinding process is employed for surface micro-structuring, values of $u_d < 1$ are reasonable.

5 Adaptive Control for Grinding

In the past several authors described control strategies for grinding process adaption in their works. The reasons for such process interference concepts are diverse, but all of them aim for the optimization of the grinding process in any way. Some improved geometrical accuracy of the finished workpiece due to measurement of grinding energy or deformation on tool-holders for internal grinding. Others achieved a minimal thermal damage on the workpiece surfaces by using process adaption concepts on top of the standard machine control logic.

5.1 Machine-to-Machine Communication via OPC UA

OLE for Process Control (OPC) in its latest generation is called Unified Architecture (UA) and is today better known by its abbreviation OPC UA. OPC Unified Architecture (OPC UA) is a standardized communication protocol for the industrial environment. As an industrial standard, it is mainly used in automation systems. It offers a uniform interface between industrial applications and field devices of various types and manufacturers. In addition, OPC UA is applicable for the exchange of information and for the control and regulation of various processes. [94] Today's industrial software systems have to work independently of operating systems and platforms. OPC UA offers open platform-independent communications and is future-oriented and therefore a good choice for web-based industrial automation. [95]

Wang et al. realized data recording of CNC machine tools over OPC access to the machine controller. Through this research, unmanned control, fault warning and condition monitoring of CNC machine tool parts were achieved. [96]

M.S. Mahmoud et al. used the OPC technology for a study on distributed control systems as a cost-effective and flexible research tool for the development and testing of modern process control systems. MATLAB and LabVIEW were integrated and their functionality was determined in combination with OPC server and client technology. [97]

[94] cf. OPC Foundation, 2015, pp.7-10.
[95] cf. Tan et al., 2009, p.262.
[96] cf. Wang et al., 2016, ; pp.387-388.
[97] cf. Mahmoud et al., 2015, p.155, p.165.

CNC machines with Siemens numerical controller such as the SINUMERIK 840Dsl have access to OPC UA when using the license "Access MyMachine / OPC UA". The SINUMERIK 840Dsl machine controller supports the binary protocol, which is optimized for low overhead, low resource consumption and interoperability. OPC UA Data Access is currently offered as the only service. Because there is no deterministic timing guaranteed for this communication, real-time tasks are not solvable with the standard OPC UA Data Access interface. The number of simultaneously monitored variables for SINUMERIK 840Dsl is limited to a maximum of 200 variables. [98]

OEMs and system integrators have high demands for real-time data access. Time-critical applications often require cycle times as low as two milliseconds.

> "From a technical standpoint, it would certainly be feasible to add real-time capability to OPC UA itself, but doing so would involve considerable effort and would still have disadvantages." [99]

Together with its partner, the company B & R has proven the ability of OPC UA Time Sensitive Networking (TSN) to meet communication requirements from the line level up to the ERP level under real-world conditions. [100]

Using standard OPC UA, several factors influence the reaction time. Most importantly, the lower the number of monitored items, the faster and more reliable are the writing, reading and searching of data. [101] MATLAB offers the possibility to access OPC UA Data Access Servers using the OPC Toolbox™. Data can be written, read and logged. The OPC Toolbox™ allows access to current and historical OPC data directly from MATLAB and SIMULINK. [102]

In addition, MATLAB's Data Acquisition Toolbox™ provides functions to connect the software to data-acquisition hardware. This toolbox supports a variety of hardware, including National Instruments (NI) and other vendors. [103] The Ethernet NI CompactDAQ Chassis can be used to retrieve analogue/digital-converted data on a standard personal computer (PC) via Ethernet. [104]

[98] cf. Siemens AG, 2017/06/05, pp.7-21.
[99] Albisser et al., 2014, p.7.
[100] cf. ibid., pp.5-7.
[101] cf. Tan et al., 2009, p.262.
[102] cf. MathWorks, 2017/07/07b, p.1-2.
[103] cf. MathWorks, 2017/07/07a, p.1-2.
[104] cf. National Instruments, 2014, p.1.

5.2 Control Concepts

Most control concepts for grinding either deal with the problem of avoiding grinding burn or handle geometric deviations due to deflection. Often thin shafts of internal grinding tools require a distinct process control strategy to be able to generate the demanded geometry with internal grinding. Hecker et al., for instance, described a control concept for cylindrical grinding with an inner repetitive position control loop based on the grinding energy. A PI-controller was used to obtain a constant power consumption of a process. The radial speed (feed rate) of the grinding tool was used as a regulating variable. [105]

Other optimization concepts were designed to get grip on the avoidance of grinding burn on the finished workpiece. In 2002, Li et al. even went one step further. In order to minimize process times, they published a multi-parameter optimization for the cylindrical grinding process. During roughing, the grinding process was carried out with such high feed rates that the known limits for the generation of grinding burns were deliberately exceeded. During finishing and spark-out overheated material was removed to obtain proper components. Li et al. proved enormous saving potential considering process time. Moreover, the industrial implementation of an optimal controlling system was demonstrated. [106]

In 2004, Dong et al. used a similar strategy for internal grinding. The grinding process is divided into the three sectors for roughing, finishing and spark out processing. In the case of roughing, the radial feed rate was chosen higher than the critical speed for thermal damage of the workpiece. For gaining the desired sizing and surface roughness, the radial feed rate was limited during finishing. For the control, the active power at the drive motor of the grinding spindle is used as the main control variable. Since this is an internal grinding process with small grinding wheel diameters and thus low torques, this measurement of the active power sufficiently and accurately reflects the instantaneous performance in the grinding zone. [107] [108]

In the years 2015 and 2016, the bilateral CORNET II project was performed in order to build up an *adaptive grinding processes*. The research within the project AGriPro was conducted by the following partners: the Fraunhofer Institute for Machine Tools in Chemnitz and Forming Technology, the Friedrich-Wilhelm-Bessel-Institute in Bremen and the Institute of Production Engineering in Graz. Thereby, control concepts were developed to avoid burn at the surface area of workpieces with the focus on non-circular grinding.

[105] cf. Hecker et al., 2002, pp.642-646.
[106] cf. Li et al., 2002, pp.232-236.
[107] cf. Dong et al., 2004a, pp.327-332.
[108] cf. Dong et al., 2004b, pp.338-339.

At the IFT, the industrial standard OPC Unified Architecture (OPC UA) was used for the communication between a PID-controller and the SINUMERIK grinding machine tool control system. Thermal damage could be prevented by subsequently adjusting the feed rate v_{fr} of a cylindrical grinding process. As a conclusion, the established control loop worked properly, even though real-time tasks cannot be processed with SINUMERIK in combination with the OPC UA Data Access interface. [109] Since the grinding process itself reacts very slowly to changes in the radial feed rate, a cycle time of 50 milliseconds is sufficient to control the process. [110]

[109] cf. Siemens AG, 2017/06/05, pp.7-21.
[110] cf. Steffan et al., 2017, pp.137-140.

6 Machine Tool Development

Since mid 2016, a new Research Grinding Machine (RGM) is at disposal at the Institute of Production Engineering at Graz University of Technology. It was developed in close cooperation by the Austrian company Gesellschaft für Schleiftechnik GmbH (GST) and the Institute. The machine design is focused on the processes of conventional circular and non-circular grinding as well as on the research topic of RPM-Synchronous Grinding. Therefore, it is custom-made for the demands of the IFT in terms of size, layout, power and quality. This Research Grinding Machine constitutes a role model of design and sensor integrity for the production of the future from the perspective of precision machine tools.

In 2015 & 2016, the machine was produced by GST in Sierndorf, Austria and is now situated at IFT in Graz. Figure 6.0.1 shows a photograph of the front side of the machine.

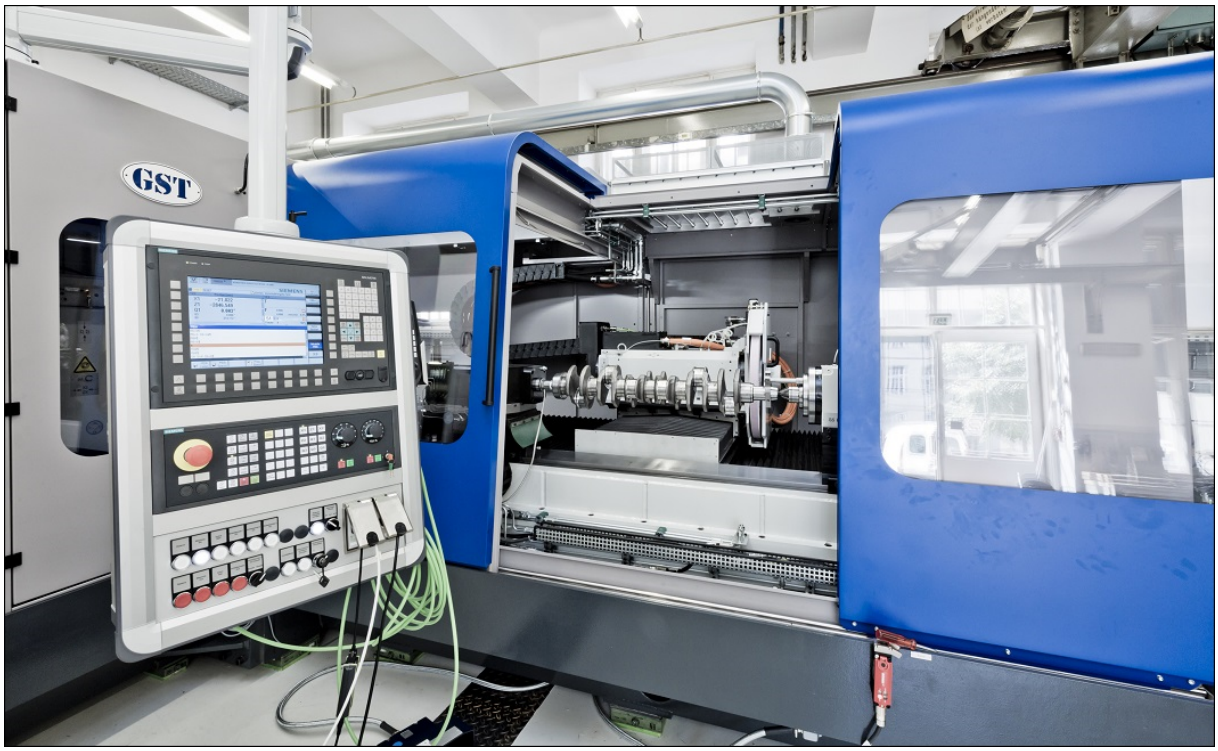

Figure 6.0.1: Research Grinding Machine at IFT,
Source: ©Lunghammer - TU Graz.

The machine is equipped with direct drive motor spindles and with high-precision rotary encoders on every rotation axis. Hydrostatic bearings guide the linear motions of the two separate X-axis slides which are ideal for damping of vibrations and for high precision.

The overall system of the machine tool as the experimental facility builds the center of this

thesis' common (red) thread. The development of new grinding processes such as RPM-Synchronous Grinding or the design of novel adaptive control concepts or individual tool dressing strategies require an open and prepared machine tool. Key parts of the machine system are evolved during this thesis and the major technical features are described in the actual chapter.

6.1 Machine Layout and Drives

The machine configuration consists of two compound slides. Graphic 6.1.1 illustrates the top view on the inner machine components, where two slides X1-Z1 and X2-Z2 are visible. The main compound slide X1-Z1 with spindle S1 is able to move between both grinding units: the RPM-Synchronous Grinding unit (RSG-unit) at the left-hand side and the conventional circular & non-circular grinding unit (CG-unit) at the right-hand side of the machine.

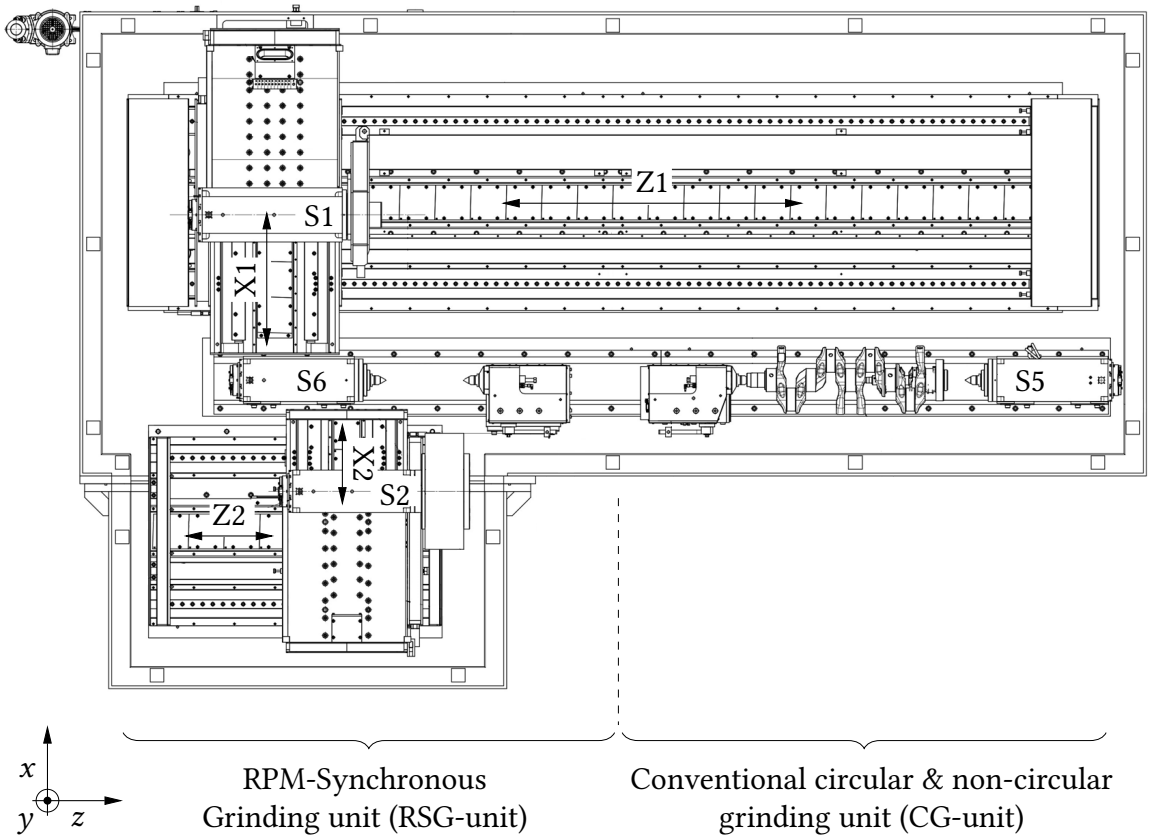

Figure 6.1.1: Layout of the Research Grinding Machine at IFT,
Source: own illustration.

The design of the X1-axis slide was analysed via finite-element-method and structurally optimized in terms of weight. In chapter 6.5 this weight reduction of the X-axis slide is described in order to gain highest dynamics of movements in X-direction. This is particularly claimed

for grinding of non-circular shapes with conventional non-circular grinding processes, where X- and Q-axis are coupled. Examples are the classic pin chasing process for machining of crankshafts and the standard non-circular grinding operation for the production of camshafts or shaft-hub connections. Even more important regarding this work, these higher dynamics have great influence on the efficiency of the dressing process of non-circular grinding wheel geometries for the RPM-Synchronous Non-Circular Grinding process.

RPM-Synchronous Grinding (RSG) Unit

As mentioned in chapter 4 discussing RPM-Synchronous Grinding, grinding wheel and workpiece rotate in a fixed rotational ratio during machining. Macroscopic non-cricular workpiece geometries can be produced by a non-circular grinding wheel in a simple plunge grinding process. On a microscopic scale, functional surfaces with integral features such as cavities for oil or other friction reducing surface designs are grindable with the RPM-Synchronous Grinding procedure.

Since workpiece and grinding wheel are rotationally coupled, the effective cutting velocity is determined by diameter difference of grinding wheel and workpiece, by the grinding direction (equal or counter) and by the rotation rates at both sides. The workpiece drive S6 has to reach a unusual and extraordinarily high number of revolutions per minute for a grinding workpiece spindle. Table 6.1.1 shows the key data of all drive systems within the machine. The spindle S2 on the compound slide X2-Z2 serves either as a support disc spindle or is used in a two step process. Thereby, roughing and finishing is performed consecutively with different grinding wheels on the opposing spindles.

Conventional Grinding (CG) Unit

The conventional grinding unit is optimized for high performance deep grinding and high speed grinding on circular and non-circular workpieces. Therefore, the main grinding spindle S1 is equipped with a power $P_{drive} = 72.6\,\mathrm{kW}$ direct drive which offers a torque of $M_{nenn} = 204\,\mathrm{Nm}$ at a nominal speed of $3400\,\mathrm{min}^{-1}$ and a maximum speed of $6000\,\mathrm{min}^{-1}$ as Table 6.1.1 denotes. Workpieces for the automotive industry such as camshafts or crankshafts are usually manufactured on machines with equal kinematics.

At the mentioned conventional grinding unit the spindle S5 is located on the right-hand side of the workpiece and the tailstock is situated on the left-hand side. The tailstock clamps the workpiece due to an axial movement driven by a pneumatic cylinder supported by a spring.

Table 6.1.1: Data and dimensions of drives of the RGM.

linear axes

describtion	**speed** v_{max}	**length** l_{ld}	**force** F_N
X1: X-axis slide	50 m·min^{-1}	600 mm	5185 N
X2: X-axis slide	50 m·min^{-1}	360 mm	3460 N
Z1: Z-axis slide	40 m·min^{-1}	3500 mm	5185 N
Z2: Z-axis slide	40 m·min^{-1}	600 mm	3890 N

rotatory axes

describtion	**RPM** n_{max}	**torque** M_{nenn}	**power** P_{drive}
S1: grinding spindle	6000 min^{-1}	204 Nm	72.6 kW
S2: grinding spindle	4000 min^{-1}	130 Nm	31.0 kW
S5: workpiece spindle	800 min^{-1}	332 Nm	16.3 kW
S6: workpiece spindle	4500 min^{-1}	130 Nm	15.0 kW

Machine Control Unit

The research grinding machine is equipped with the latest SIEMENS SINUMERIK 840D solution line (sl) machine control system. It offers possibilities for programming following standardized G-code but also programming in high level language (Siemens) for further functionalities.

- Systemsoftware NCU: V 04.05 + SP 05
- Systemsoftware PCU / PC HMI: V 04.05 + SP 05

On top of the SINUMERIK a special human machine interface (HMI) is provided by the manufacturer GST. A *CRIP-Cyle* is used for non-circular grinding of crankshafts or other non-circular workpieces in conventional processes. The license *Access MyMachine / OPC UA* is necessary for changing values of certain parameters via OPC UA standards.

6.2 Grinding Force Measurement

Force measurement is a basic need for scientifically characterizing single machining processes. Brinksmeier and Meyer developed a sensor-fitted grinding tool for process monitoring. They used piezoelectric 3-component forces sensors and thin film thermocouples to gather information about the general grinding process. [111]

6.2.1 Three Component Force Sensor

A quartz sensor is used for measuring three orthogonal components of the resulting grinding force. Mounting the force sensor at the tailstock provides direct force measurement in the force flux. The benefits are a high sensitivity, measuring accuracy and repeatability. Moreover, a good linearity and low hysteresis may be presumed. [112] This sensor allows simple, direct and very precise measurements with the following properties: [113]

- Measurement of cutting forces during machining
- Interdependency of the force application point
- Measurement of vibration forces
- Wide frequency range
- Compact dimensions
- Stainless steel, sealed sensor case
- Rugged multipole plug connection

Figure 6.2.1 shows the sensor made by KISTLER. The sensor of type 9047C offers a force range of $F_x, F_y = -15 \dots 15\,\text{kN}$ and $F_z = -30 \dots 30\,\text{kN}$ at standard mounting with preload of 70 kN in Z-direction. The sensor's threshold is lower than 0.01 N. Its sensitivity for X- and Y-direction is approximately $\approx -8.1\,\text{pC}\cdot\text{N}^{-1}$ and in Z-direction approximately $\approx -3.7\,\text{pC}\cdot\text{N}^{-1}$.

The stiffness of every force measuring system is an important factor. It mainly influences resulting geometries of grinded workpieces and vibrational behaviour of the overall system

[111] cf. Brinksmeier, Meyer, 2004, pp.81-89.
[112] cf. http://www.kistler.com/, 2017/06/07b, p.44.
[113] cf. http://www.kistler.com/, 2017/06/07a, pp.1-2.

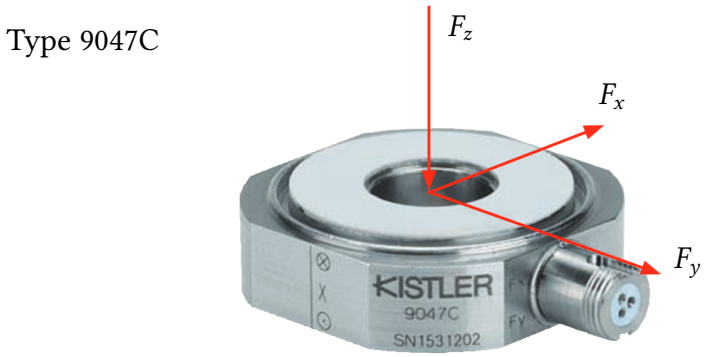

Figure 6.2.1: 3-Component force sensor,
Source: www.kistler.com (2017/06/07).

during the process. This particular sensor is stated with a rigidity of $c_x, c_y \approx 600\,\mathrm{N{\cdot}\mu m^{-1}}$ in X- and Y-direction and $c_z \approx 1400\,\mathrm{N{\cdot}\mu m^{-1}}$ in Z-direction. [114]

The sensor is equipped with a cable type 1698ACsp which ensures the level of protection IP67 according to EN60519. Since the cable is welded to the sensor, it is not detachable. Additional data from the KISTLER 3-component force sensor is listed in the Table 6.2.1. [115]

Table 6.2.1: Technical Data KISTLER Type 9047C.

	force component	value
dimensions		40 x 40 x14 mm
force range	F_x, F_y F_z	−15 ... 15 kN −30 ... 30 kN
momentum load	M_x, M_y M_z	−150 ... 150 Nm −150 ... 150 Nm
threshold	F_x, F_y, F_z	< 0.01 N
sensitivity	F_x, F_y F_z	$\approx -8.1\,\mathrm{pC{\cdot}N^{-1}}$ $\approx -3.7\,\mathrm{pC{\cdot}N^{-1}}$
rigidity	c_x, c_y c_z	$\approx 600\,\mathrm{N{\cdot}\mu m^{-1}}$ $\approx 1400\,\mathrm{N{\cdot}\mu m^{-1}}$
temperature range		−40 ... 120 °C
degree of protection according to EN60519 with cable type 1698ACsp		IP67

This specific force sensor is mounted at the tailstock side of the grinding machine. It is either installed at the dead center on the conventional circular & non-circular grinding unit as described in subsection 6.2.2 or it is used in combination with the RPM-Synchronous Grinding unit with a rotating center according to subsection 6.2.3.

[114] cf. http://www.kistler.com/, 2017/06/07a, pp.1-2.
[115] cf. ibid., pp.1-2.

The sensor indirectly measures the occurring forces due to the grinding process but also forces appearing from clamping, workpiece weight and imbalance of the rotation workpiece. More precisely, when the sensor is subjected to a mechanical load, it generates a charge signal that is directly proportional to the acting force. [116] This charge is transferred via a highly isolated cable to a distribution box outside the machine. A KISTLER charge amplifier converts the charge produced by the piezoelectric sensor into a proportional voltage. [117] This voltage is analog-to-digital converted by a NATIONAL INSTRUMENTS (NI) C-series module in a CompactDAQ chassis. The digitalized data is sent to a measurement PC with a MATLAB data-acquisition software via Ethernet connection. The whole force measuring chain among the grinding machine with all required hardware is illustrated in Figure 6.2.2.

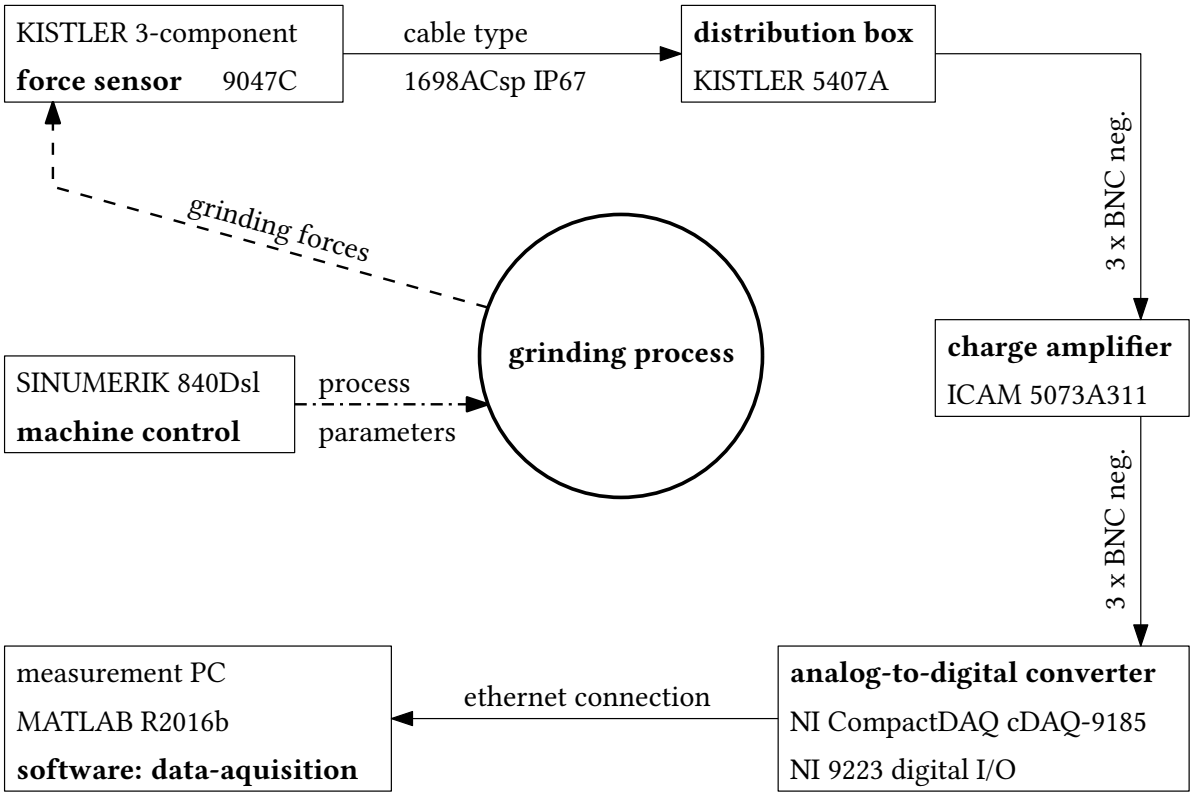

Figure 6.2.2: Force measuring chain among the grinding machine,
Source: own illustration.

6.2.2 Force Measuring at Dead Tailstock Center

For conventional circular and non-circular grinding a dead center at the grinding machine's tailstock is commonly used. It supports the weight of the workpiece and the occurring forces due to the cutting process. Usual rotational rates at the workpiece spindle are between 30 and

[116] cf. http://www.kistler.com/, 2017/06/07b, p.43.
[117] cf. ibid., p.43.

200 revolutions per minute. Lubricating grease is used to lower friction between the rotating inside of the centering bore in the workpiece and the stationary center. Additionally, the dead center is equipped with a carbide insert to minimize abrasion and wear of the center. Usually, cooling lubricant is guided to the friction zone for heat removal.

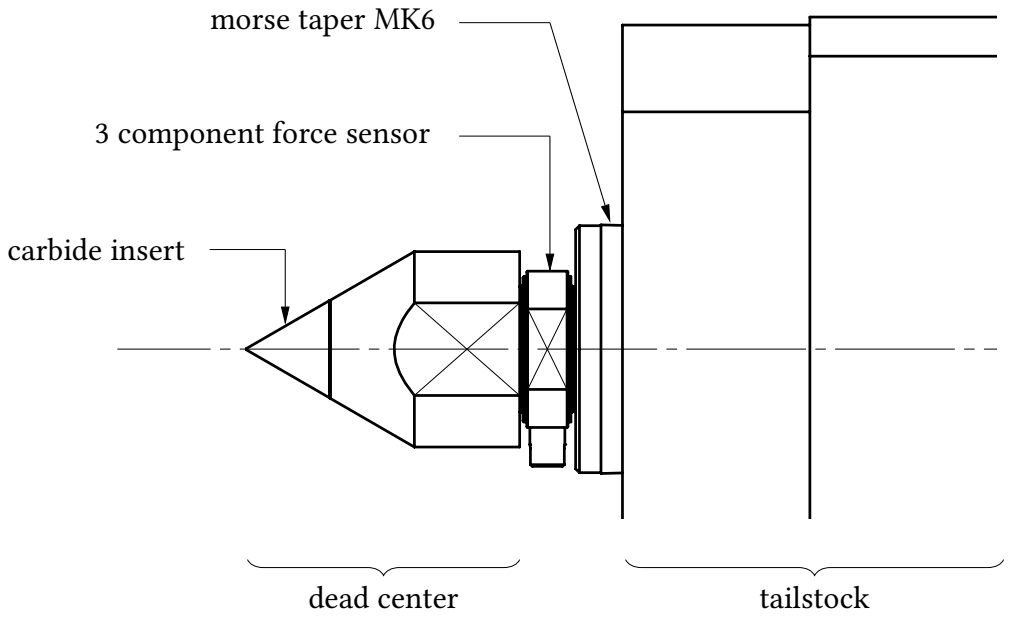

Figure 6.2.3: Dead center at the grinding machine's tailstock with force sensor, Source: own illustration.

Figure 6.2.3 illustrates the design of the dead center at the tailstock. The presented arrangement allows a measurement of the occurring forces during the grinding process. The KISTLER 3-component force sensor is directly placed in the force flux. It is mounted between the center and a MK6 morse taper which serves as a connecting component to the machine's tailstock. Center, sensor and morse tamper are connected by a threaded bolt of the dimension M14x1.5 and are assembled with preload of 70 kN.

The dynamic or quasistatic force acting in an arbitrary direction during the process can either be absorbed by a chuck's clamping jaws or a center at the workpiece spindle in combination with a tailstock center. In case the 3-component force sensor is used, the workpiece is put in between the tip of the center at the spindle side and the support of the center in the tailstock. Figure 6.2.4 schematically presents this grinding force measurement configuration. To get the information about the occurring radial and tangent forces due to the grinding process, the values measured by the sensor must be transformed to the tools coordinate system. Formulas 6.2.1 to 6.2.4 give the correlation between the sensors' force value and the actual radial force F_r and tangent force F_t at the contact zone of workpiece and tool.

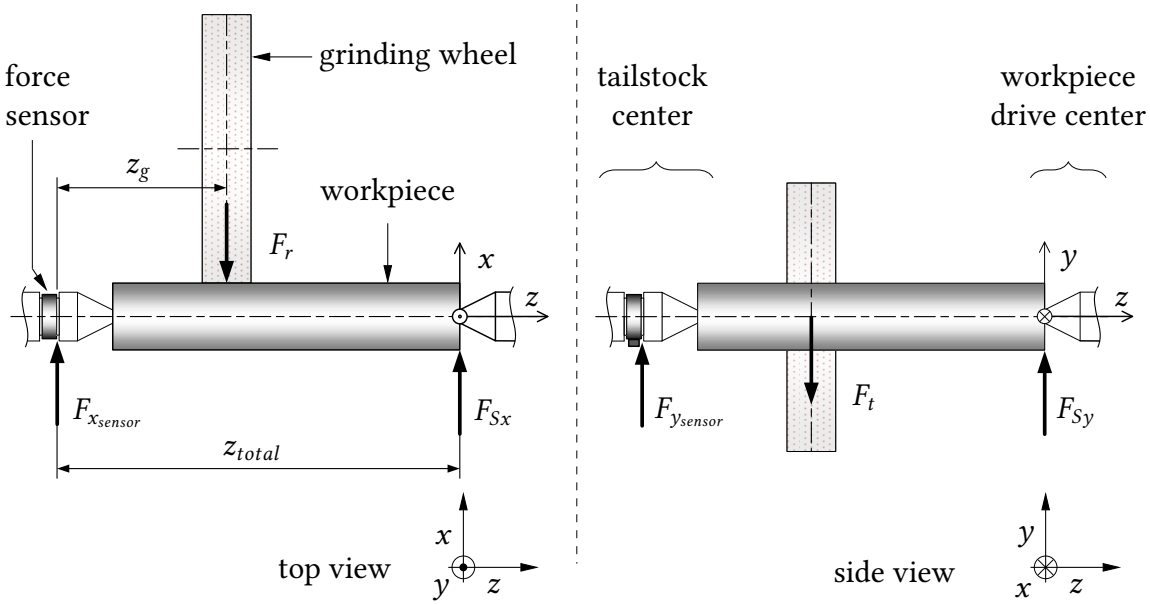

Figure 6.2.4: Grinding force measurement configuration,
Source: own illustration.

$$\sum T_c = 0 = F_r \cdot \left(z_{total} - z_g\right) - F_{x_{sensor}} \cdot z_{total} \tag{6.2.1}$$

$$\sum T_c = 0 = F_t \cdot \left(z_{total} - z_g\right) - F_{y_{sensor}} \cdot z_{total} \tag{6.2.2}$$

$$F_r = F_{x_{sensor}} \cdot \frac{z_{total}}{z_{total} - z_g} \tag{6.2.3}$$

$$F_t = F_{y_{sensor}} \cdot \frac{z_{total}}{z_{total} - z_g} \tag{6.2.4}$$

6.2.3 Force Measuring at Rotating Tailstock Center

For higher rotational rates ($n_w > 300\,\mathrm{min}^{-1}$), a dead tailstock center cannot be used. Due to the axial clamping force and the friction between center and workpiece, overheating and deformation occurs. In this case, rotating centers are commonly used.

Especially for the process of RPM-Synchronous Grinding, a rotating center is required. This process is characterized by rotational rates at the workpiece spindle up to $4500\,\mathrm{min}^{-1}$. With the special construction shown in Figure 6.2.5, highest rotational rates are permissible by con-

currently having the 3-component force sensor in the direct force flux. The major idea for this design is adopted from the dead center at the grinding machine's tailstock. Again, rotating center, sensor and morse tamper are connected by a threaded bolt and are assembled with preload of 70 kN.

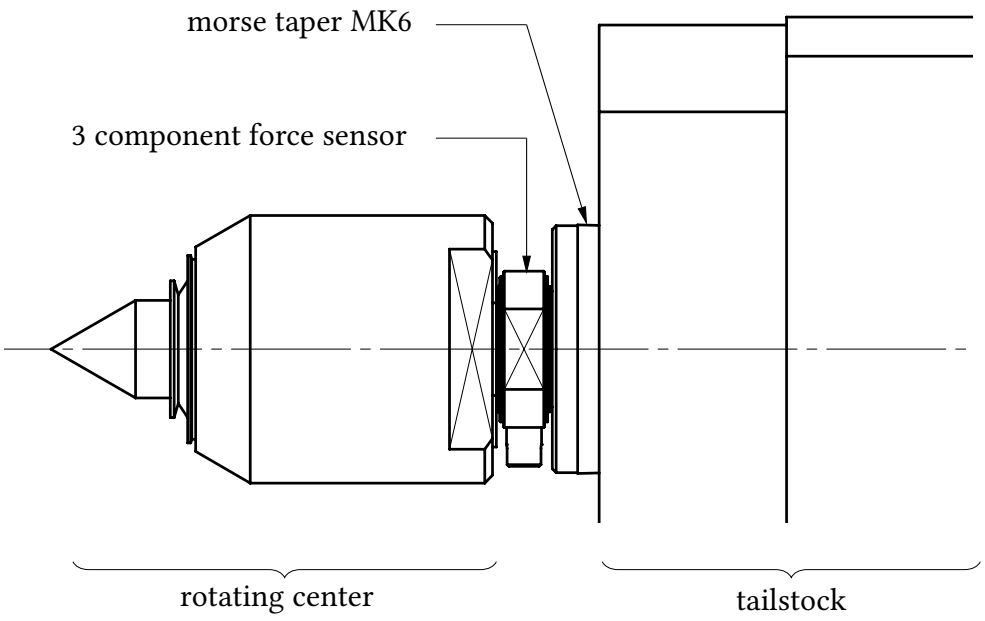

Figure 6.2.5: Rotating center at the grinding machine's tailstock with force sensor, Source: own illustration.

6.3 Temperature Sensors

The machine bed of the research grinding machine consists of a reinforcement steel encasement filled with special Hydropol® concrete. It was designed and produced by the Austrian company FRAMAG.

The machine bed contains two separate cooling circuits in two different layers within the Hydropol®. One loop is situated close to the upper side of the bed where the main linear drive components and linear guidances are fixed. The other cooling circuit is located at a height of approximately 200 mm according to Figure 6.3.1.

Additionally, twenty-two temperature sensors type PT100 are infused in the machine bed. The sensors are spread among the whole machine bed in different layers and positions as illustrated in the following figures. Figure 6.3.1 shows the side-view of the machine bed.

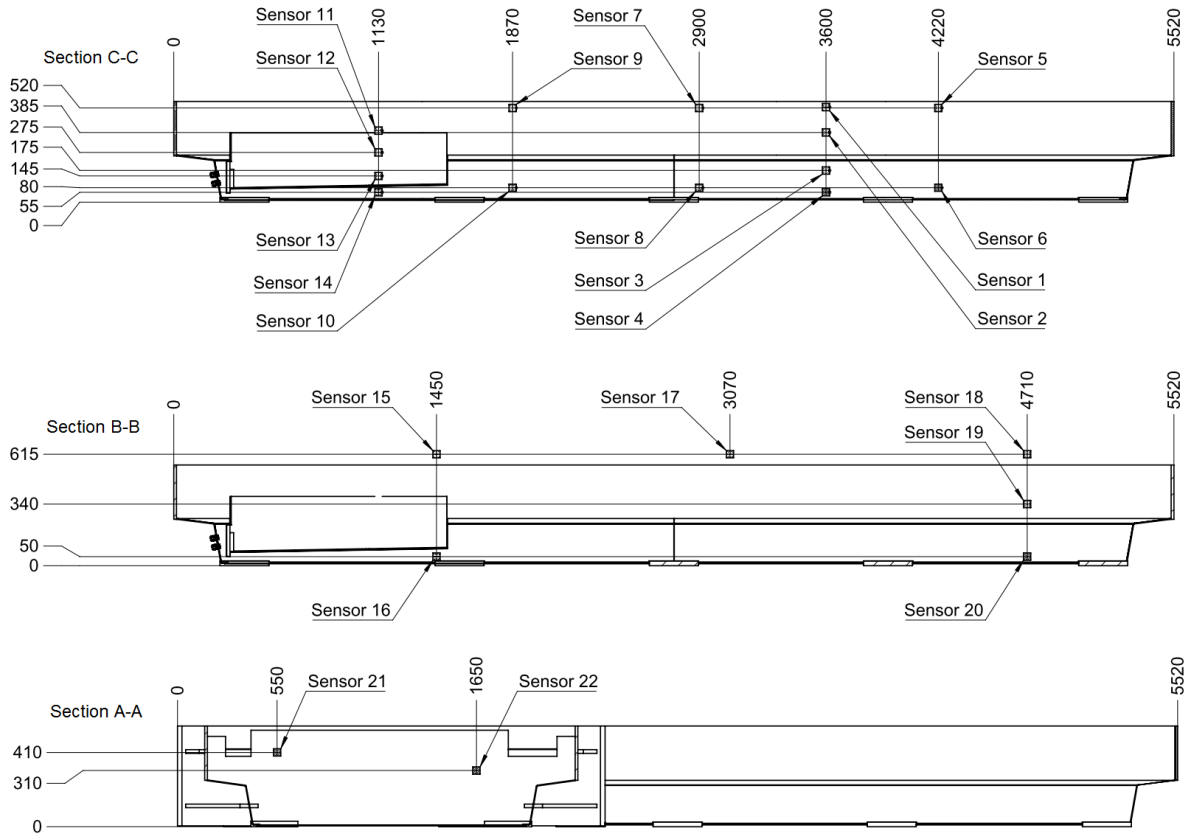

Figure 6.3.1: Temperature sensors infused in the machine bed - side-view, Source: own illustration.

The PT100 sensors enable temperature monitoring during grinding. In order to rule out distortion or warping of the machine bed, temperature control strategies can be implemented. The two cooling circuits can be supplied separately with cooling water from the in-house providing to take appropriate countermeasures.

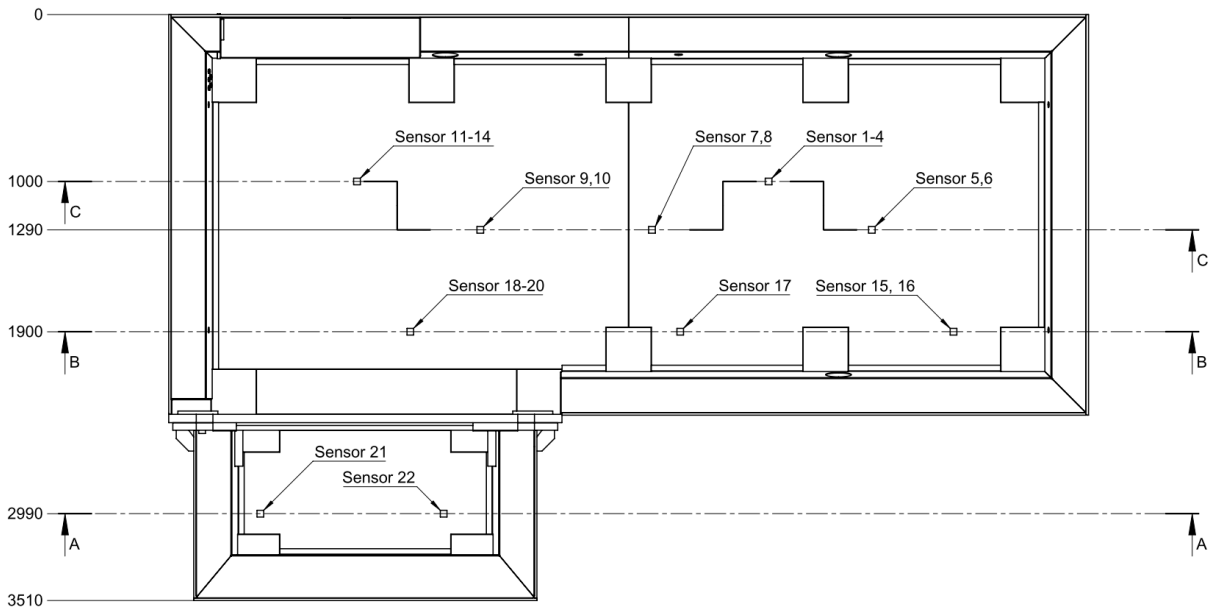

Figure 6.3.2: Temperature sensors infused in the machine bed - top-view, Source: own illustration.

Figure 6.3.2 shows the top-view of the machine bed. The locations of the 22 sensors are marked within the layout.

6.4 Axial Measurement and Volumetric Compensation

Accurate positioning of every axis is of highest priority for a high precision grinding machine. The accuracy of machine tools is mainly affected by the axial deviation from the ideal geometry. Errors are often caused by mounting and part assemblies, by the measuring systems and by the transmission of force and torque. Moreover, variation in temperature during machining of large workpieces result in high precision losses. These deviations can partly be measured during commissioning of the machine. Some can be compensated during operation. Reference measurements based on the machine internal position-value sensors and rotary encoders in comparison with external measurement equipment are used to fill compensation tables with necessary data. For this purpose, modern CNC controls - such as SIEMENS SINUMERIK 840Dsl - have axis-specific effective compensation functions. [118]

In this section, the measurement of the grinding machines linear axis is described. Every machine axis may have six errors. In general, in a Cartesian grid three additional squareness errors may occur. The possible errors for the main compound slide (X1 & Z1) at the research grinding machine are: [119]

- pitch (X- & Z-axis)
- yaw (X- & Z-axis)
- roll (X- & Z-axis)
- vertical straightness (X- & Z-axis)
- horizontal straightness (X- & Z-axis)
- linear positioning (X- & Z-axis)
- squatness between X- and Z-axis

Figure 6.4.1 illustrates the direction of each of the possible errors.
The external measurement equipment is a RENISHAW laser interferometer type ML10 Gold Standard. Measurement procedures are performed on the X1-axis and the Z1-axis of the main compound slide. The following measurements are conducted:

- X- & Z-axis: measurement of pitch
- X- & Z-axis: measurement of yaw
- X- & Z-axis: measurement of linear positioning

[118] cf. https://www.siemens.com/, 2017/06/12, p.225.
[119] cf. http://www.volumetric.com./, 2017/06/12, p.16.

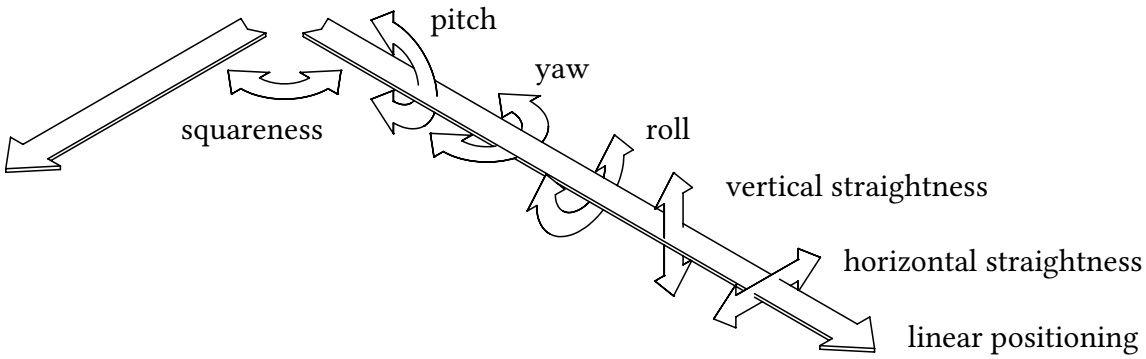

Figure 6.4.1: Errors of machine axis,
Source: own illustration.

- X-axis: measurement of vertical straightness: sag in Y-direction
- X-axis: measurement of horizontal straightness: sag in Z-direction
- Z-axis: measurement of vertical straightness: sag in Y-direction
- Z-axis: measurement of horizontal straightness: sag in X-direction

The SIEMENS SINUMERIK 840D sl/828D Function Manual Extended Functions [120] describes the compensation course of action in detail. Gathered data from the laser interferometer is transferred in tabular form and used as input for the machine axis compensation. As a next step, the same measurement procedure is repeated and the improvement documented. In case the result is not yet satisfying, the procedure is reiterated. It must be noted that geometric errors may vary with temperature. All measurements were conducted at an ambience temperature between 22 °C and 25 °C.

The following volumetric errors in the grinding machine tool are compensated:

- Z-axis: compensation of linear positioning
- X-axis: compensation of horizontal straightness: sag in Z-direction
- Z-axis: compensation of horizontal straightness: sag in X-direction

[120] cf. https://www.siemens.com/, 2017/06/12, pp.225-279.

6.4.1 Compensation of Linear Positioning

Compensation of linear positioning - Z1-axis

Figure 6.4.2 shows the measurement results for axis Z1 concerning linear positioning. The dash-dotted line shows the position accuracy before compensation. The maximum deviation according to the measured values of the laser interferometer occurs at Z1 = 1450 mm and accounts for 50.5 µm. After compensation, the maximum deviation is reduced to 2.0 µm. The solid line in Figure 6.4.2 represents the measurement result after compensation of linear positioning of the Z1-axis.

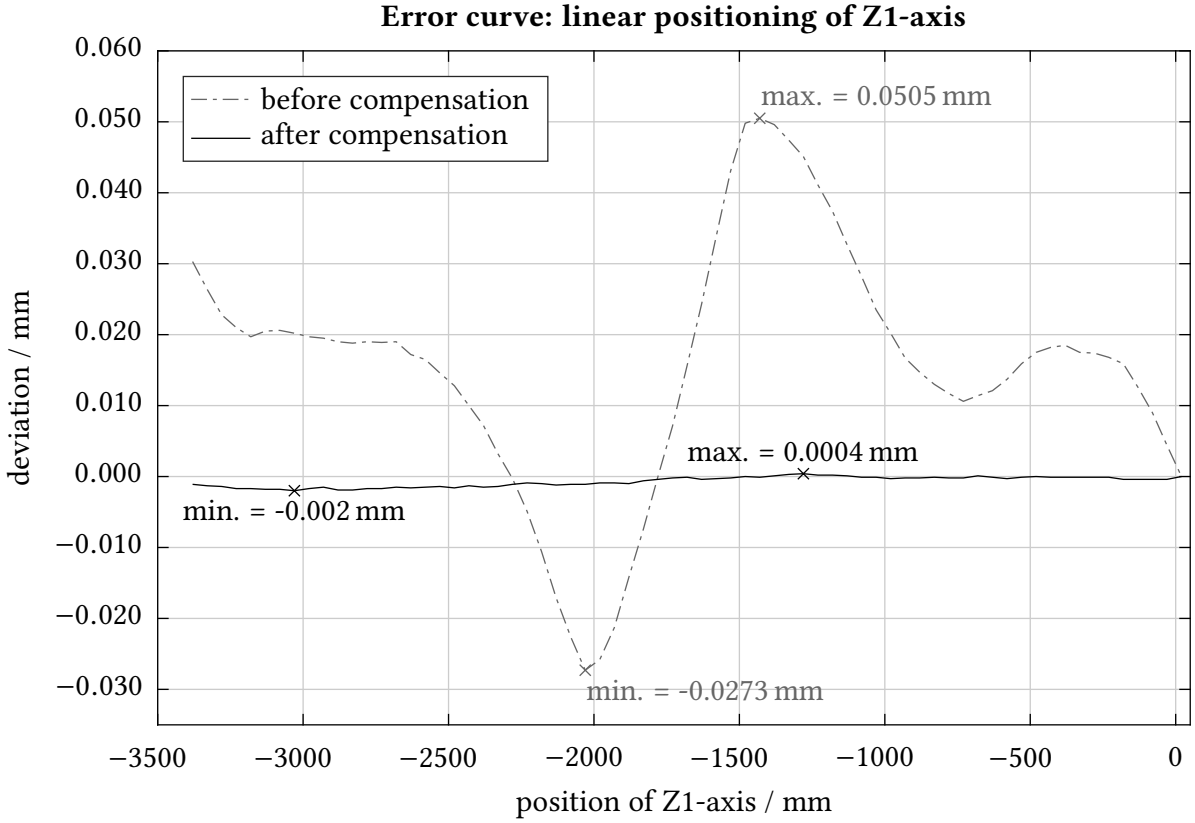

Figure 6.4.2: Compensation of linear positioning of Z1-axis,
Source: own illustration.

Linear positioning and temperature - X1-axis

The measurement of linear positioning of axis X1 brought up different phenomena. Since geometric errors may vary with temperature, all components with enforced temperature application lack in accuracy. Especially the linear positioning precision of the X-axis slides strongly depends on the hydraulic oil temperature. The pressurized oil that flows through the hydrostatic bearings heats up the whole slides structure. Figure 6.4.3 shows the deviation of linear

positioning of the X1-axis slide during its warm-up phase shortly after starting the machine.

At the very first cycle, with a overall temperature of about 24 °C, the deviation is approximately 18 µm. During the warm-up phase and with higher temperature the machine axis slide expands according to the temperature distribution in the slides structure and the thermal coefficient of linear expansion for steel ($\alpha_{steel} = 12 \cdot 10^{-6}\,\mathrm{K}^{-1}$) [121].

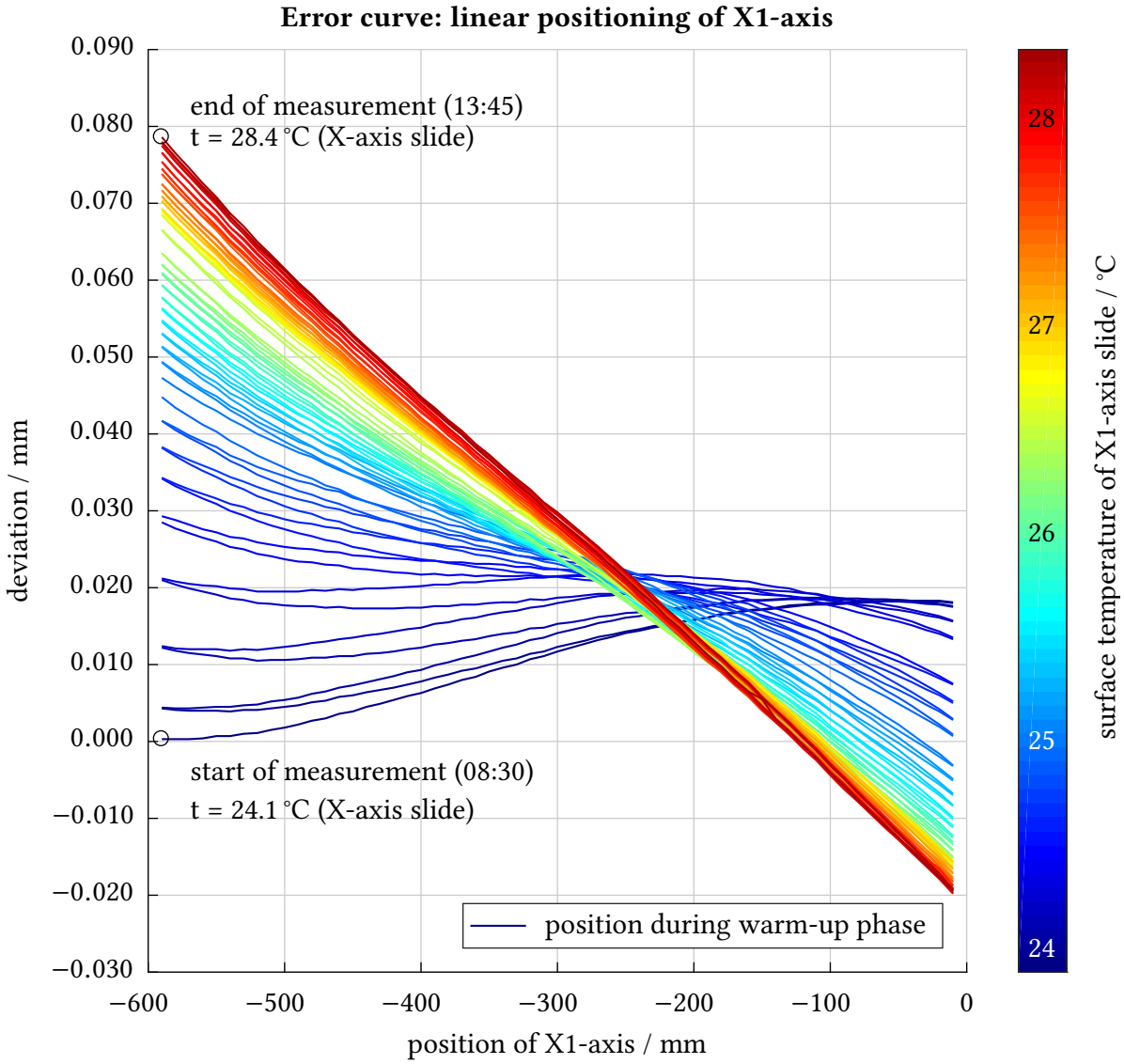

Figure 6.4.3: Variance in linear positioning over time and temperature before adjustment of hydraulic-oil cooling strategy (X1-axis),
Source: own illustration.

After several measurement cycles and about five hours later the hydraulic oil had 40 °C and therefore the outside temperature of the X-axis slide increased by about 4 °C to a value of 28 °C. The absolute deviation was measured 98 µm but distributed linearly over the whole length of

[121] cf. Böge, Eichler, 2008, p.97.

the slide of 600 mm. In order to minimize this deviation caused by rising temperatures of the slides structure, different approaches can be chosen. The plainest attempt to solve the highly temperature dependent linear positioning accuracy of the X1-axis is to improve the hydraulic-oil cooling strategy. Therefore, the leakage at the hydraulic unit is piped through the mounted heat exchanger. As an result, the hydraulic oil inside the tank can be cooled as desired. The accuracy in linear positioning of the axis X1 is enhanced strongly, but still depending on the ambient- and oil temperature.

A further possibility would be to provide an active temperature compensation table to the SIEMENS SINUMERIK control unit. Therefore, additional temperature sensors would have to be placed inside the slides structure. The already installed temperature sensors inside the machine bed could serve as a basis for machine temperature information. The procedure is described in the SIEMENS SINUMERIK 840D sl/828D Function Manual Extended Functions. [122] Even with this highly complex compensation method a deviation in X1-direction can not be definitively excluded. Reasons are inhomogeneous temperature distribution during the heat-up phase and the dependence of the warming-up on the single process.

[122] cf. https://www.siemens.com/, 2017/06/12, pp.226-233.

6.4.2 Compensation of Horizontal Straightness

To compensate horizontal straightness of an axis (base axis), the absolute position of another axis has to be modified. Errors are evoked by the own weight of the axis or by the manufacturing precision of single parts or by inaccurate assembly of those parts of the axis. Thus, this "sag compensation" is a cross-axis compensation. [123]

Compensation of horizontal straightness - Z1-axis (sag in X-direction)

Figure 6.4.4 illustrates the measurement results for axis Z1 concerning horizontal straightness (sag). The dash-dotted line shows the deviation before compensation. The maximum error occurs at Z1 = 1740 mm and accounts for 32.8 µm, according to the measured values of the laser interferometer. The solid line in Figure 6.4.4 represents the measurement result after compensation of horizontal straightness of the axis. At this stage, maximum deviation is reduced to 3.1 µm, what is acceptable for a Z-axis.

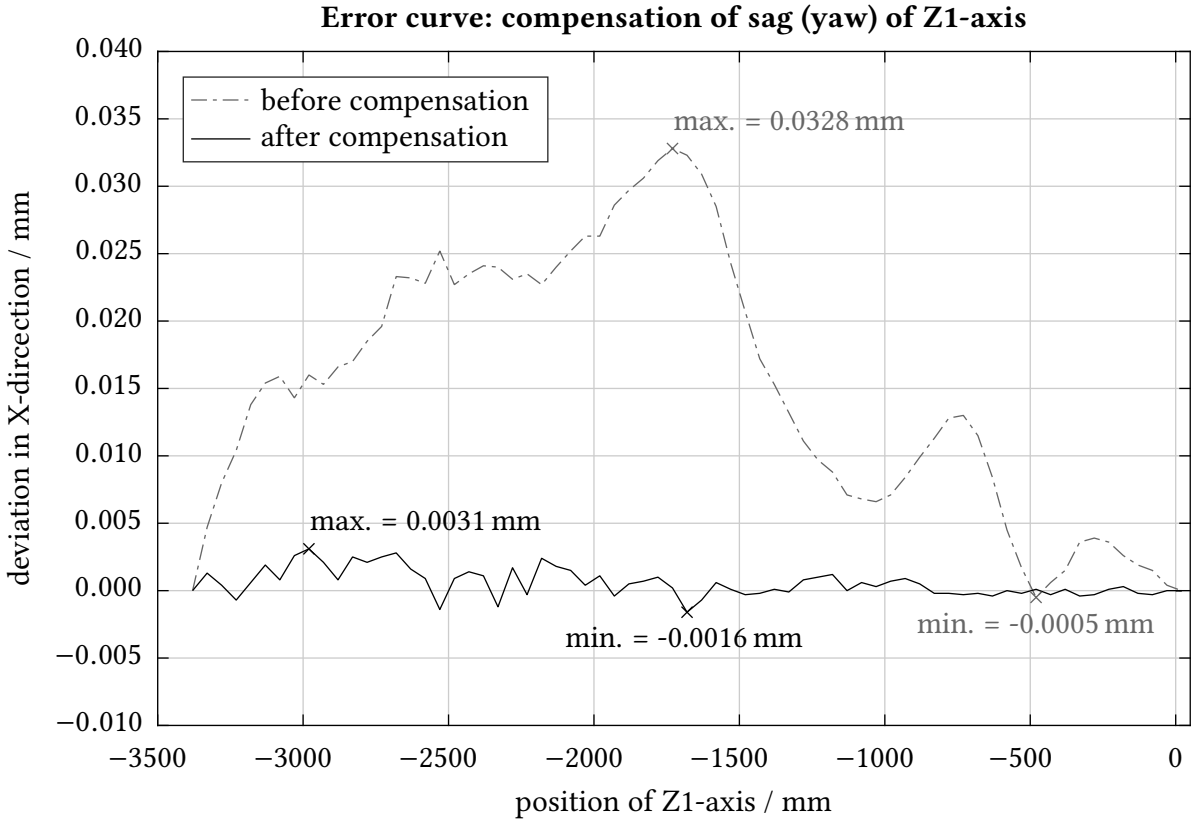

Figure 6.4.4: Compensation of horizontal straightness of Z1-axis,
Source: own illustration.

[123] cf. https://www.siemens.com/, 2017/06/12, p.245.

Compensation of horizontal straightness - X1-axis (sag in Z-direction)

Even without compensation, the measurement of horizontal straightness of the X1-axis already reveals high accuracy. The values are plotted in Figure 6.4.4. The dash-dotted line shows the deviation before compensation with a maximal error of 3.6 µm. The solid line in figure represents the measurement result after compensation of horizontal straightness of the X1-axis, according to the measured values with the laser interferometer. The maximum deviation is reduced to 0.7 µm.

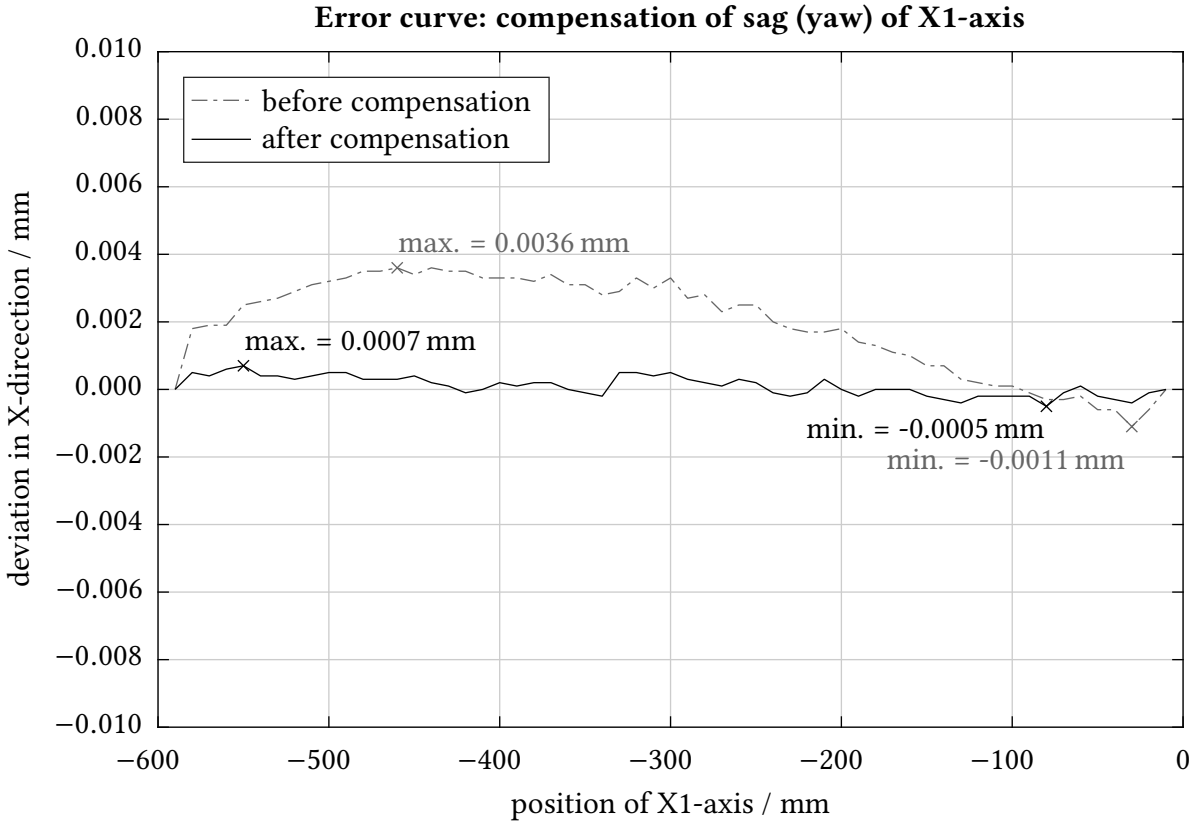

Figure 6.4.5: Compensation of horizontal straightness of X1-axis,
Source: own illustration.

6.5 Weight-Optimized X-Axis Slide

Weight reduction of moving parts plays an important role in mechanical engineering. Whenever a linear axis is synchronized to a rotational axis, the linear slide must instantly follow the rotation. In case of the research grinding machine, the workpiece spindle Q5 can electronically be coupled with the axes X1 and X2 for conventional non-circular grinding and for dressing of non-circular grinding wheels. A structural optimization concerning weight reduction is necessary to gain advantages in dynamics for those two main research topics:

- conventional high-end non-circular **grinding** processes
  - crankshafts: grinding of the bearing pins
  - camshafts: grinding of point-wise given non-circular geometries
  - shaft-hub connections: polygonal profiles
  - ...
- **dressing** of non-circular grinding wheels for RPM-Synchronous Non-Circular Grinding
  - point-wise given geometries
  - 3D non-circular geometries
  - ...

6.5.1 Dynamics of Motion

A linear motor generates a specific force maximum. The maximum acceleration of a slide mainly depends on its mass and the force the linear drive generates. The inertia force resulting from the sequence of motion that the motor must compensate is proportional to the acceleration a and the dynamic mass m with opposite direction of acceleration. [124]

$$F = m \cdot a \tag{6.5.1}$$

The higher the maximum acceleration of the X-axis slide is, the more revolutions per time unit of the workpiece spindle Q according to Figure 4.6.1 are possible in a synchronized moment. A higher rotational speed leads to a shorter cycle time. Ultimately, the reduction of the cycle period is a major productivity factor and therefore a valuable selling point for grinding machine manufacturers.

[124] cf. https://www.siemens.com/, 2017/10/16, p.83.

The demanded acceleration multiplied by the mass of the overall moving system results in the necessary force for the driving system. A linear motor provides a constant force. In case of the research grinding machine, the drive for the X1-axis is a SIEMENS product composed of a primary part and seven segments of secondary parts.

The linear drive is a SIEMENS linear motor with a maximum froce of $F_{MAX} = 8810\,\text{N}$ and a rated force of $F_N = 5185\,\text{N}$. [125] The SIEMENS Simodrive Configuration Manual describes the determination of the continuous thrust for motor dimensioning in the following way:

> "In addition to the peak thrust, the required continuous thrust of the motor is decisive for its dimensioning. The maximum continuous thrust of the motor F_{eff} is calculated from the square mean of the motor thrust over the entire time of a sequence of motion and may not exceed the rated thrust F_N." [126]

$$F_{eff} = \sqrt{\frac{1}{t_{ges}} \cdot \int_0^{t_{ges}} F(t)^2 \, dt} \leq F_N \tag{6.5.2}$$

$$F(t) = \sum F_i(t) = m \cdot a(t) + F_r(t) + F_{infeed}(t) \tag{6.5.3}$$

Within the Equations 6.5.2 and 6.5.3 $F(t)$ is the sum of all appearing forces in the direction of the linear drive at the time t. Those are: inertia forces $m \cdot a(t)$, friction forces $F_r(t)$ and forces coming from the grinding process itself $F_{infeed}(t)$.

> "[...] the frictional force $F_r(t)$ consists of a constant component F_{rc} and a component $F_{rv}(t)$ that is proportional to the speed $v(t)$." [127]

$$F_r(t) = F_{rv}(t) + F_{rc} \tag{6.5.4}$$

$$F_r(t) = \mu_{rv} \cdot v(t) \cdot F_n + \mu_{rc} \cdot F_n \tag{6.5.5}$$

State of the art non-circular grinding machines interlink the velocities of X- and Q-axis. They reduce rotational rates at the Q-axis in order to limit the needed linear acceleration at the

[125] cf. https://www.siemens.com/, 2016/08/04.
[126] https://www.siemens.com/, 2017/10/16, p.85.
[127] Ibid., p.81.

X-axis slide. For camshaft grinding, the Q-axis is programmed to reduce angular velocity at the beginning of the cam geometry and accelerate the rotational speed when the operation is alike circular grinding.

6.5.2 Design Optimization

The design of the X1-axis slide is optimized to pursue the target of highest dynamics in motion during non-circular grinding and dressing. Usually, a heavy full-steel sheet is used to merge spindle-stock with hydrostatic bearing in X-direction. In case of the weight reduced slide, a complex, honeycomb-like geometry is fabricated by milling. This geometry is developed by means of a finite element optimization process. Compared to the conventional design, the overall height of the carriage is enlarged to gain stiffness. At the same time the honeycomb-shaped pockets with different wall thicknesses are implemented to reduce volume. The main focus is laid on weight reduction by simultaneously keeping the stiffness properties of the overall part. Picture 6.5.1 shows the differences in design between the original version of the slide and the weight optimized version.

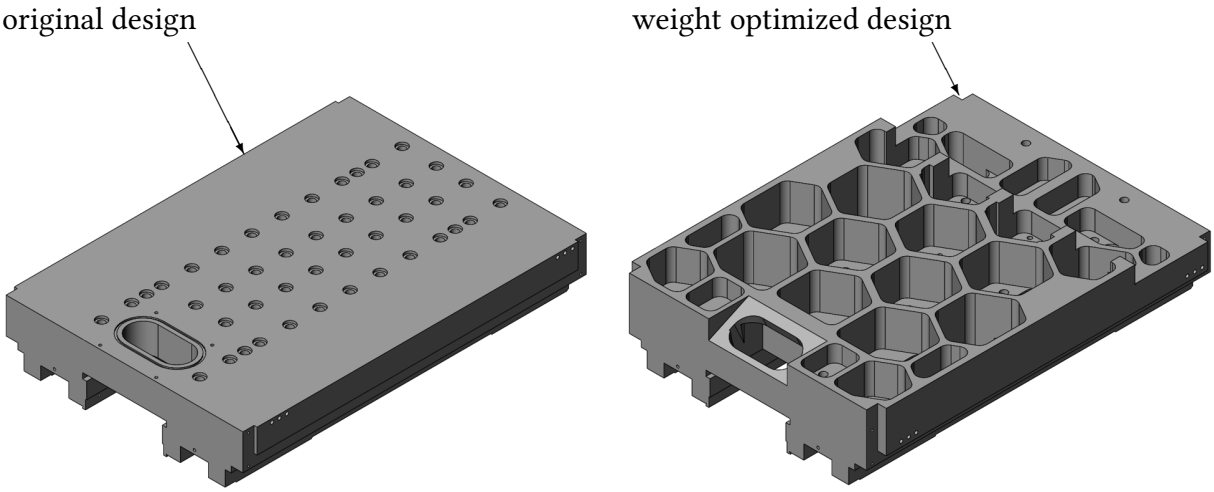

Figure 6.5.1: Comparison of design of the X-axis slide,
Source: own illustration.

The natural frequencies of the part must stay in the same region, although design and mass are changed. The harmonic excitation is caused by the oscillation of the slide itself and by the rotational rates of each workpiece and grinding wheel. Table 6.5.1 shows the difference between the traditional and the optimized design concerning weight, critical natural frequencies and production costs. Regarding natural frequencies, the critical regions are in lower bands: The target for slide oscillation is set to a workpiece rotation of 120 min^{-1}. Therefore, the slides

oscillation accordingly corresponds at $2\,s^{-1}$. Corundom grinding wheels are usually limited to a circumferential speed of maximum $50\,m{\cdot}s^{-1}$ what yields in $24.5\,s^{-1}$ for a wheel diameter of 650 mm. The rotational speed of spindle S1 is limited to $6000\,min^{-1}$ what implies an excitation frequency of $100\,s^{-1}$. Bottom line, both designs are considered non-critical, hence the excitation frequencies are lower than the critical eigenfrequencies of the slide.

Table 6.5.1: Properties of designs of the X-axis slide.

properties:	original design	weight optimized design
mass:	498 kg	385 kg
first eigenfrequency:	$258.4\,s^{-1}$	$329.3\,s^{-1}$
second eigenfrequency:	$424.3\,s^{-1}$	$455.1\,s^{-1}$
production costs:	€ 3, 980.00	€ 4, 420.00

6.5.3 Effects on Non-Circular Grinding and Dressing

For the analysis of the effects of the weight-optimization, a standard process is chosen. The considered object is machined eccentrically to its rotational axis but is circular. Therefore, the kinematics of this process can mathematically be described straightforward. Moreover, this process corresponds to the machining process of crankshaft bearing pins. For this analyses, it is irrelevant if a grinding wheel machines a workpiece or a dressing tool treats a grinding wheel. Therefore, the results are equally valid for conventional non-circular grinding and for non-circular dressing of non-circular grinding wheels for the RSNG-process.

On the next pages, results are given on the example of the grinding process of pin-bearings of crankshafts. This machining cycle is called pin-chasing process. Here, the workpiece crankshaft is clamped between centres concentrically with its rotation axis of its subsequent installation position in the combustion engine.

For the pin-chasing grinding process the maximum demanded acceleration depends on the following factors:

- diameter of crank bearing pin
- eccentricity crank bearing pin
- diameter of grinding wheel
- number of revolutions at workpiece (constant rate)

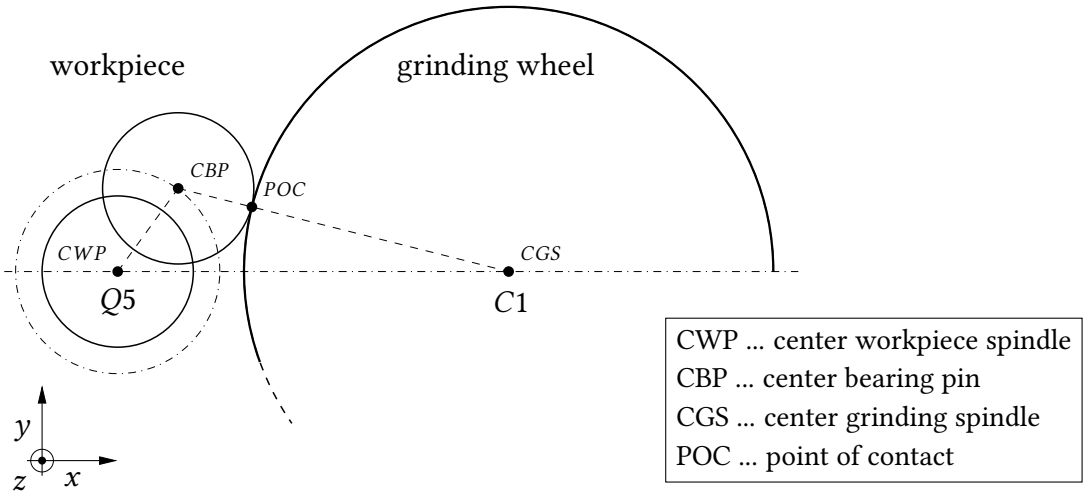

Figure 6.5.2: Geometric properties for the pin-chasing process,
Source: own illustration.

Figure 6.5.2 shows a view perpendicular to the axis of the workpiece which is marked by the centre point of the workpiece (CWP). A carrier transfers the driving torque backlash-free in order to rotate the workpiece during this process.

The bearing pin rotates with constant angular velocity around the workpiece spindle axis (Q5) which is marked as CWP in the figure. A full stroke of this pin corresponds to two times the eccentricity of the bearing pin e_{pb}, as marked in Figure 6.5.3. The location of the point of contact between workpiece and grinding wheel (POC) depends on several factors: The diameter of the bearing pin $2 \cdot r_{pb}$, the diameter of the grinding wheel $2 \cdot r_g$, the eccentricity of the bearing pin e_{pb} and the angular coordinate of the bearing pin γ. The pin-chasing grinding process is carried out by a linear movement of the grinding wheel on the straight line between center point of the workpiece spindle CWP and the rotation center of the grinding wheel spindle CGS. This movement direction corresponds to the X-axis direction of the grinding machine according to Figure 4.6.1. The slide is embedded in hydrostatic bearings which are characterised by very low movement losses and high damping rates.

Table 6.5.2: Geometric properties of crankshafts.

properties:	passenger car engine	large engine
alias name in figures:	crankshaft 1	crankshaft 2
bearing pin diameter:	35 mm	80 mm
stroke:	40 mm	130 mm
bearing pin radius: r_{pb}	17.5 mm	40 mm
bearing pin eccentricity: e_{pb}	20 mm	65 mm

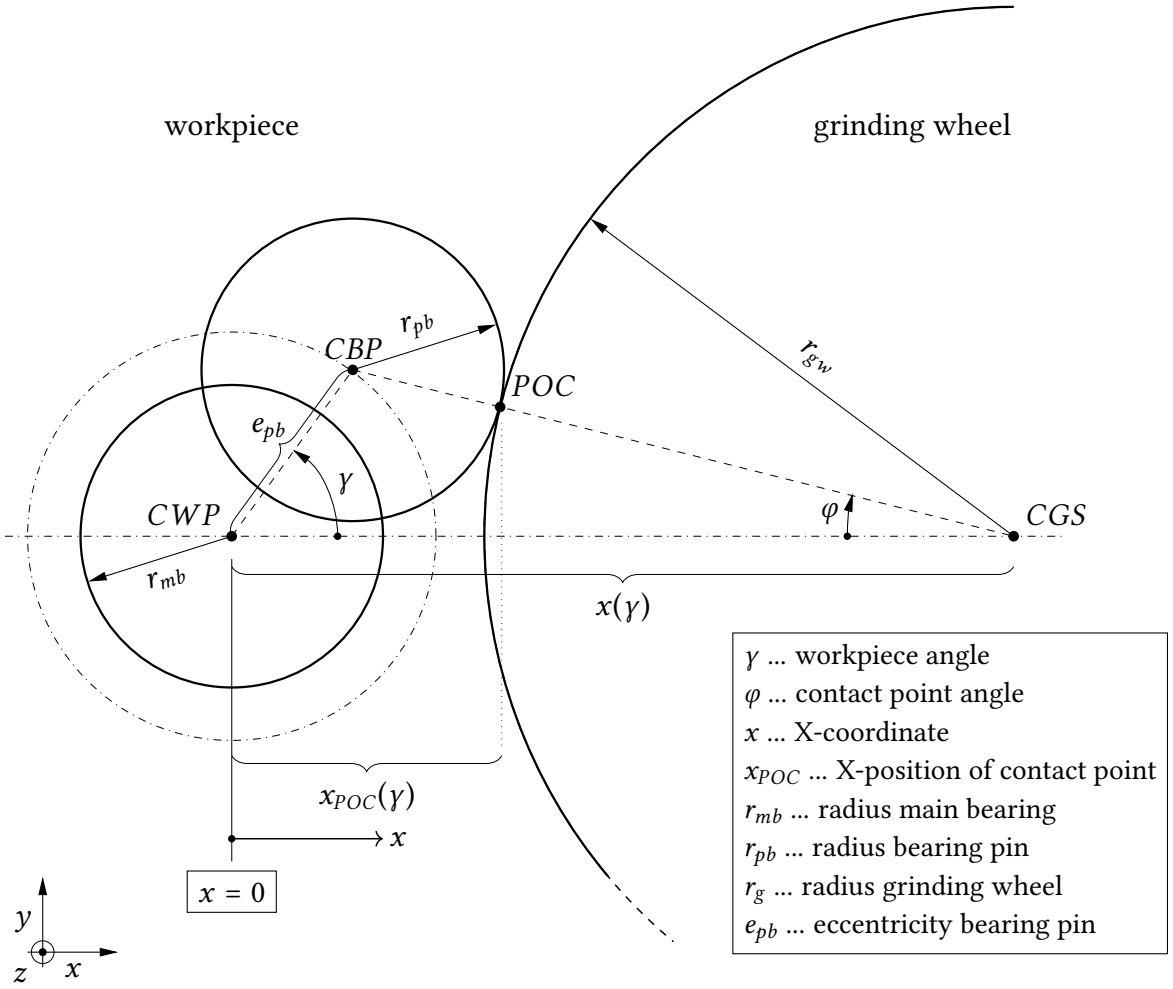

Figure 6.5.3: Kinematics of the pin-chasing process,
Source: own illustration.

$$r_{gwpb} = r_{gw} + r_{pb} \tag{6.5.6}$$

$$x(t) = e_{pb} \cdot cos(\gamma(t)) + \sqrt{r_{gwpb}^2 - e_{pb}^2 \cdot \sin^2(\gamma(t))} \tag{6.5.7}$$

$$\cos(\varphi(t)) = \frac{x(\gamma(t)) - x_{POC}(\gamma(t))}{r_{gw}} \tag{6.5.8}$$

$$\sin(\varphi(t)) = \frac{r_{pb} \cdot \sin(\gamma(t))}{r_{gwpb}} \tag{6.5.9}$$

$$x_{POC}(t) = x(t) - r_{gw} \cdot \cos\left[\arcsin\left(\frac{e_{pb} \cdot \sin(\gamma(t))}{r_{gwpb}}\right)\right] \tag{6.5.10}$$

Determining the theoretical maximum of revolution rate requires the understanding of the geometrical parameters for pin chasing processing. In the following examples, two different crankshafts are compared to demonstrate the differences in kinematics. The first crankshaft is a standard passenger car engine part, while the second crankshaft is a large engine component. Table 6.5.2 states the geometric properties of those two workpieces.

For calculating the position of the point of contact between grinding wheel and workpiece (POC) relative to the rotation axis of the workpiece spindle, the following formulas (6.5.6 to 6.5.10) are necessary. The general triangle CWP - CPB - CGS is separated in two rectangular triangles to get the distance x as a function of the rotation angle γ. The X-position x_{POC} is subsequently derived of $x(\gamma)$ by subtracting the right side of POC on the straight between CWP and CGS. Figure 6.5.4 shows the results for the x-position x_{POC} over a single rotation of the crankshaft. It demonstrates the differences in kinematics and movements between similar workpieces with different dimensions.

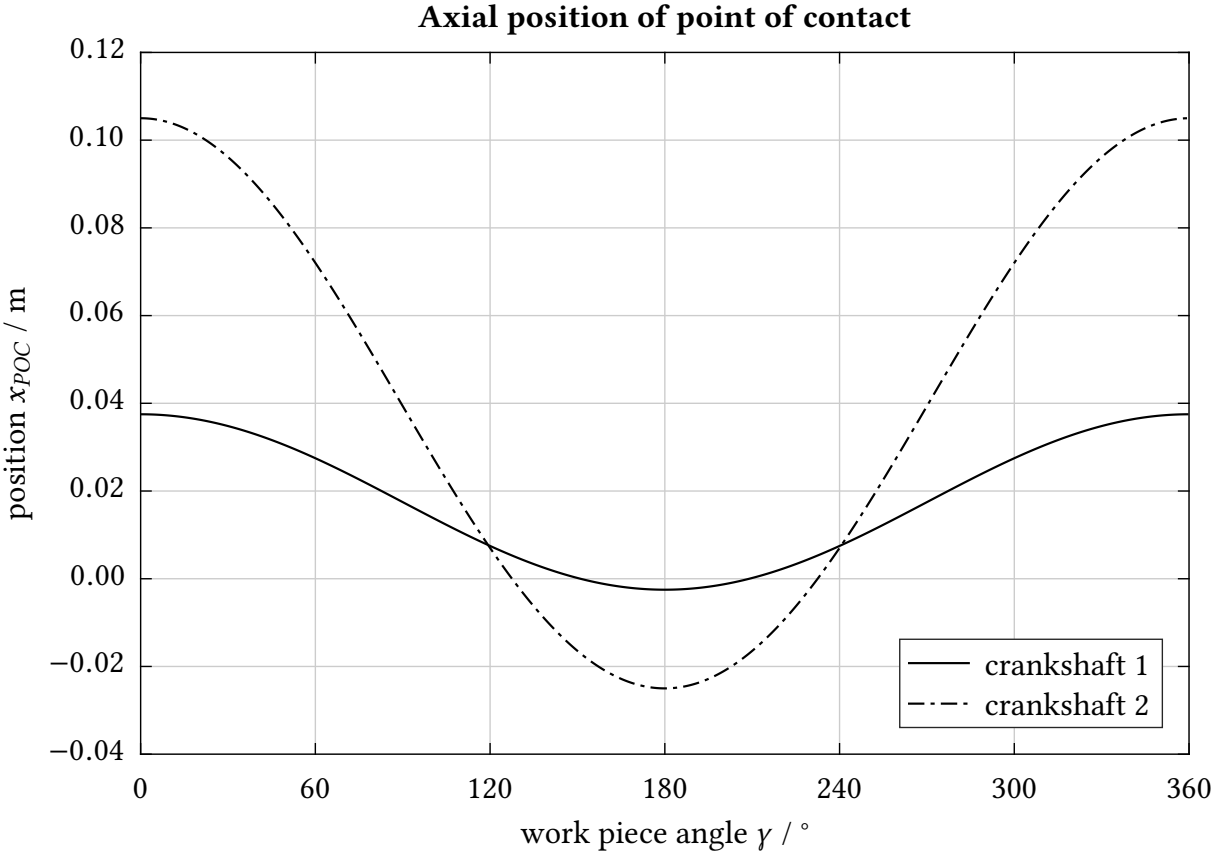

Figure 6.5.4: X-position of point of contact (POC) between workpiece and grinding wheel, Source: own illustration.

According to the following relationship Equation 6.5.11 demonstrates the general coherence among acceleration, velocity and distance which are necessary to evaluate the dynamic be-

haviour of the moving system. [128] Since the workpiece is constantly rotating during the pin-chasing process ω_w, the time derivative of the angle γ is constant. (Equation 6.5.12)

$$a(t) = \frac{dv}{dt} = \frac{d^2x(t)}{dt^2} \tag{6.5.11}$$

$$\omega_w = \frac{d\gamma}{dt} = \text{const.} \tag{6.5.12}$$

Equation 6.5.13 states the velocity of the X-slide in X-direction for the pin chasing processing. The velocity $v(t)$ is the time derivative of the position $x(t)$.

$$v(t) = \frac{dx(t)}{dt} \tag{6.5.13}$$

$$v(t) = -e_{pb} \cdot \sin(\gamma(t)) \cdot \omega_w - \frac{e_{pb}^2 \cdot \sin(\gamma(t)) \cdot \cos(\gamma(t)) \cdot \omega_w}{\sqrt{r_{gwpb}^2 - e_{pb}^2 \cdot \sin^2(\gamma(t))}} \tag{6.5.14}$$

The evaluation of this equation on behalf of the two different chrankshaft over one rotation is shown in Figure 6.5.5. This graph also demonstrates the advantage of the weight reduced X-axis slide in comparison to the slide before weight reduction. The black lines in the graph represent the weight reduced slide as it is installed in the research grinding machine at IFT. The grey lines stand for the same workpieces but more heavy X-axis slide. Since the mounted linear drive is the same for both slide designs, the maximum force and the rated force are equal. By neglecting friction forces, process forces $F_r(t)$ and forces arising from radial infeed $F_{infeed}(t)$ in Equation 6.5.3, the inertia forces evoke a difference in form of varied achievable acceleration rates. These acceleration rates influence the maximum velocity what explains the differences among the black and grey lines in Figure 6.5.5.

Equation 6.5.15 states the acceleration of the X-axis slide in X-direction for the pin chasing processing. Acceleration $a(t)$ is the time derivative of the velocity $v(t)$ and the second derivative of the position $x(t)$.

$$a(t) = \frac{d^2x}{dt^2} \tag{6.5.15}$$

[128] https://www.siemens.com/, 2017/10/16, p.82.

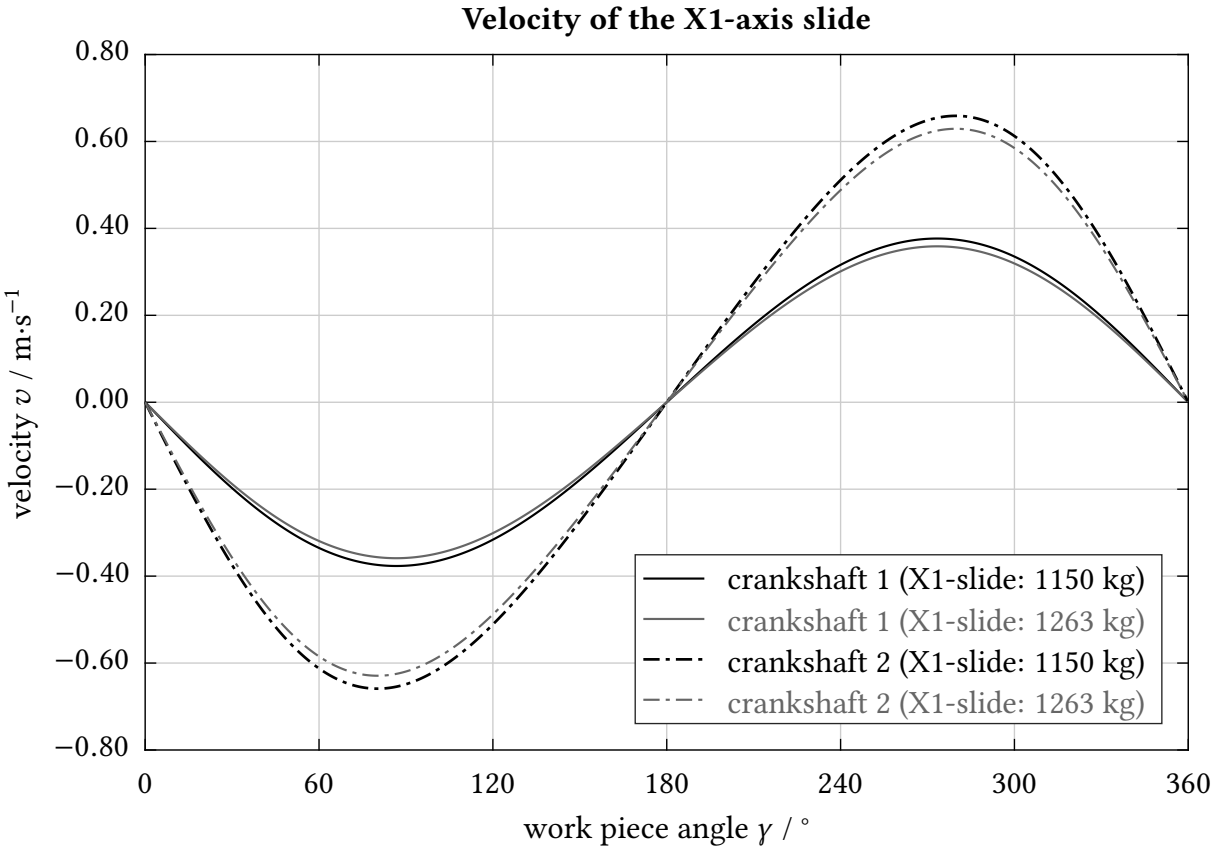

Figure 6.5.5: Velocity of X-axis slide in X-direction,
Source: own illustration.

$$a(t) = \frac{e_{pb}^2 \cdot \omega_w^2 \cdot \left(\sin^2(\gamma(t)) - \cos^2(\gamma(t))\right)}{\sqrt{r_{gwpb}^2 - e_{pb}^2 \cdot \sin^2(\gamma(t))}} - \ldots$$
$$\ldots - \frac{e_{pb}^4 \cdot \sin^2(\gamma(t)) \cdot \cos^2(\gamma(t)) \cdot \omega_w^2}{\left(r_{gwpb}^2 - e_{pb}^2 \cdot \sin^2(\gamma(t))\right)^{3/2}} - e_{pb} \cdot \cos(\gamma(t)) \cdot \omega_w^2 \tag{6.5.16}$$

The acceleration of the X-axis slide does not only depend on geometric properties of the workpiece but also on the number of rotations of the workpiece. Accordingly, this is valid for the calculation of a specific velocity. The angular velocity ω_w is proportional to the number of rotations of the workpiece per minute.

$$\omega_w = \frac{2 \cdot \pi \cdot n}{60} \tag{6.5.17}$$

Figure 6.5.6 shows the acceleration rate for both crankshafts 1 & 2. Again, the black line stands for the weight reduced version of the X-axis slide while the grey line represents the standard

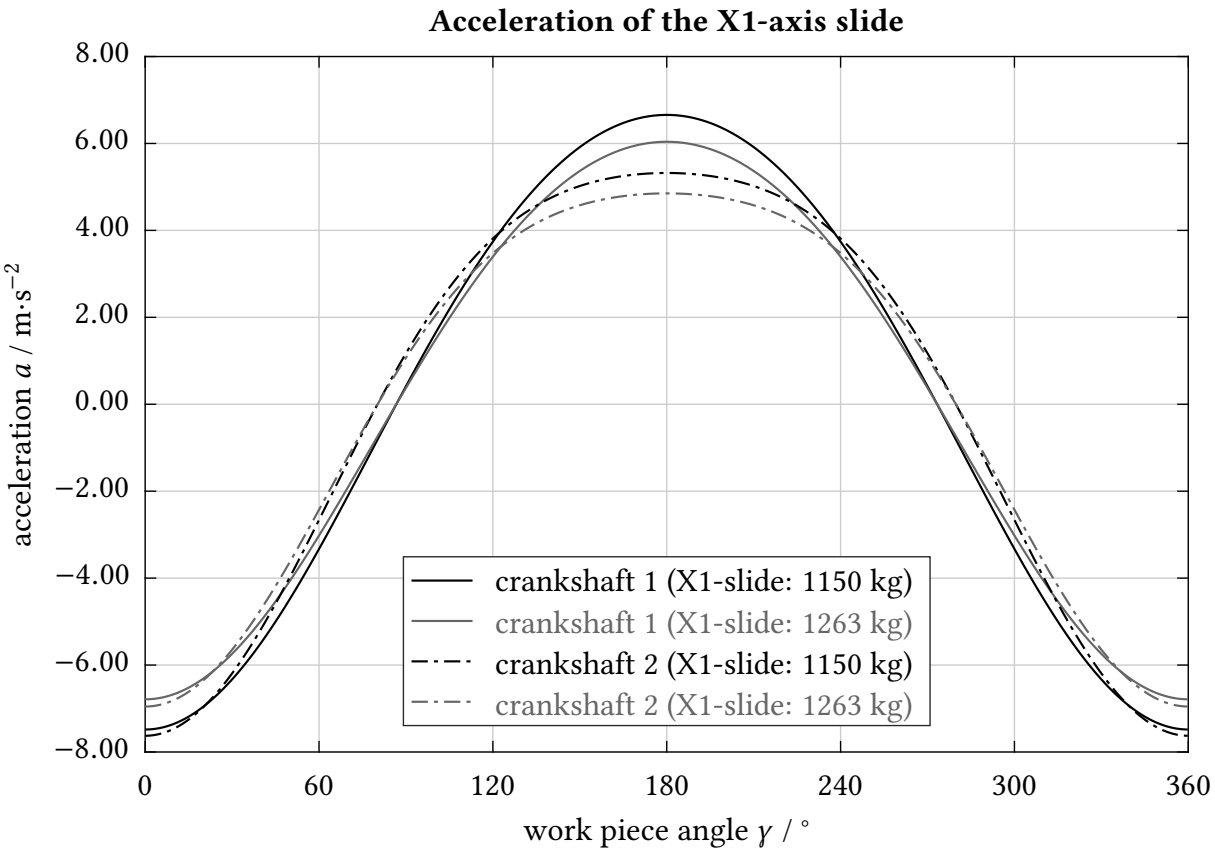

Figure 6.5.6: Acceleration of X-axis slide in X-direction,
Source: own illustration.

and heavier version. These accelerations over 360° rotation of the workpiece are resulting from the dimensioning of the linear drive. In case of the research grinding machine this linear motor is a SIEMENS Simodrive 1FN3450-4NB80-0BA1 with a maximum force of F_{MAX} = 8810 N and a rated force of F_N = 5185 N.[129]

Table 6.5.3: Demanded forces for X-axis slide acceleration.

	F_{MAX}	F_N	F_{eff}
SIEMENS Simodrive 1FN3450-4NB80-0BA1[130]	linear drive properties: 8810 N	5185 N	! $F_{eff} \leq F_N$
crankshaft 1 at (X-slide 1150 kg)	8605 N	$F_{eff} = F_N$	5185 N
crankshaft 2 at (X-slide 1150 kg)	8810 N	$F_{eff} < F_N$	4814 N

Either the maximum thrust F_{MAX} or the maximum continuous thrust F_{eff} (effective froce) limits the acceleration. The peak force can never be higher than the maximum thrust. Likewise, the effective force must be smaller or equal to the rated force of the linear drive. For the two chosen crankshafts both restrictions come into account, as Figure 6.5.7 demonstrates. For grinding the large engine crankshaft 2, the maximum force of F_{MAX} = 8810 N can be reached at an angular

[129] cf. https://www.siemens.com/, 2016/08/04.

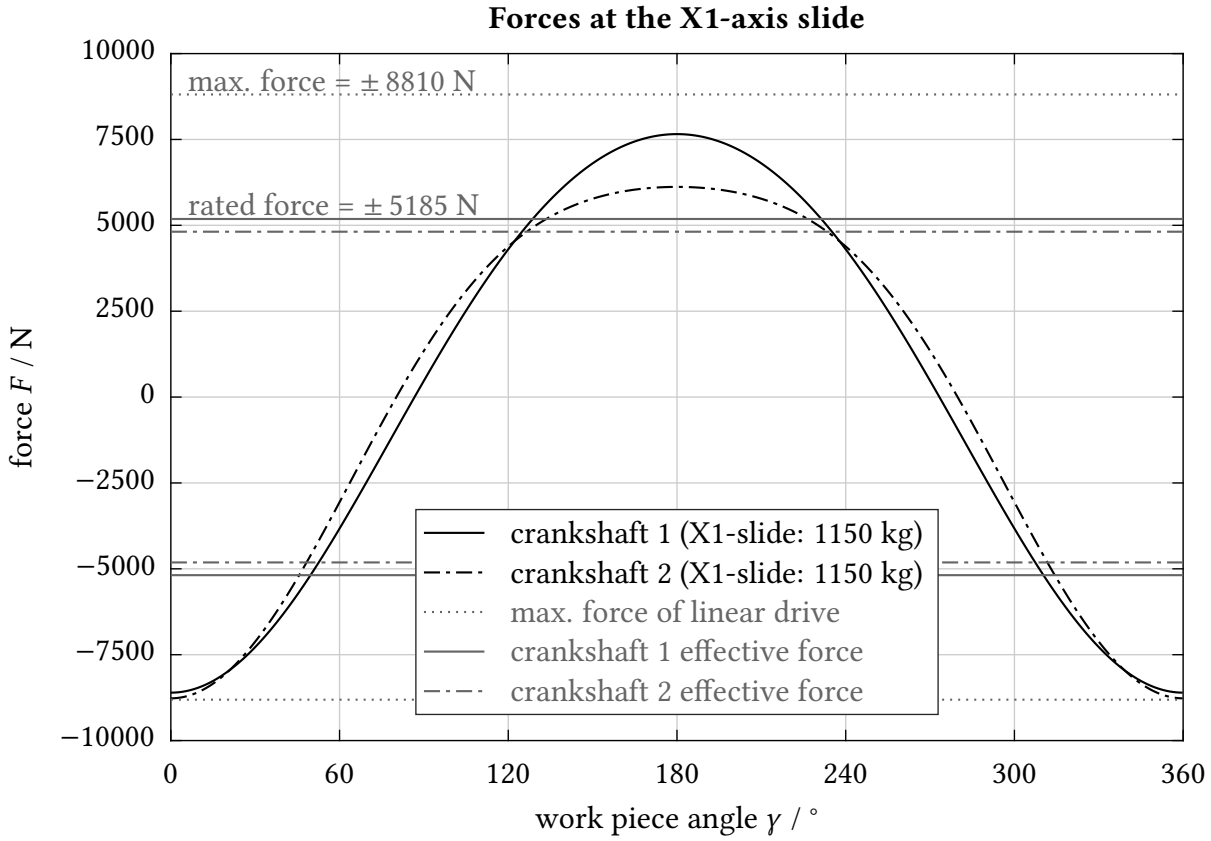

Figure 6.5.7: Force of the linear drive in X-direction,
Source: own illustration.

position of 0°, since the effective force over the cycle period (F_{eff} = 4814 N) is smaller than the rated force of F_N = 5185 N. Machining the passenger engine crankshaft 1 does not allow pushing the force to the drives maximum, since the effective force over the cycle period would be higher than the maximum rated force. In this case, the process is confined by this maximum rated force and reaches a maximum force peak at F_{MAX} = 8605 N.

These forces and accelerations are reached at specific rates of revolutions per minute at the workpiece spindle. Tabular 6.5.4 summarizes these rpm values as boundary conditions for grinding crankshaft 1 and crankshaft 2 with the weight reduced X-axis slide (1150 kg) and the standard X-axis slide (1263 kg). The maximum theoretical revolutions per minute at the workpiece spindle for the passenger car engine crankshaft 1 is 179.5 min^{-1}, while for the large engine crankshaft 2 the value is 98.9 min^{-1}. Even though the weight reduction adds up to roughly 10%, the gain in pendulum frequency is approximately 5% depending on the geometry of the workpiece.

As a conclusion, the weight reduction of approximately 115 kg accounts for roughly 5% gain in productivity. Conventional non-circular grinding processes are as well advanced as dressing processes of non-circular grinding wheels. For further weight reduction of the overall X1-

Table 6.5.4: Rotations per minute of crankshafts.

	workpiece rpm	$\triangleq$ pendulum frequency
crankshaft 1 at (X-slide 1150 kg)	179.5 min^{-1}	2.99 s^{-1}
crankshaft 1 at (X-slide 1263 kg)	171.0 min^{-1}	2.85 s^{-1}
crankshaft 2 at (X-slide 1150 kg)	98.9 min^{-1}	1.64 s^{-1}
crankshaft 2 at (X-slide 1263 kg)	94.6 min^{-1}	1.57 s^{-1}

axis slide the protective cover which is mandatory for grinding operations could be weight optimized.

6.6 Smart Machining

Handling the information coming from diverse sensors during machining processes enables reaction in process guidance. This interference in standard procedures due to live data acquired by diverse meteorology is often called **smart machining**. [131] In relation to this work, the Research Grinding Machine at IFT is prepared for smart machining and process adaptation within the scope of the CORNET II project Adaptive Grinding Process (AGriPro).

6.6.1 Grinding Burn Limits

The production process grinding is one of the latest steps in a value-added manufacturing chain. Considerable costs and energy have already been spent on components up to this process stage. In order to avoid production rejects, significant safety reserves are calculated for material removal and feed rates as well as for dressing intervals according to the present state of the art. This safety reserves are applied for the purpose of ruling out thermal damage (according to chapter 3.9) of the peripheral zones of the workpiece due to frictional overheating through sub-optimal cutting conditions. The thermal influence of grinding burn is one of the main limitations of the grinding processes. [132]

In 1978, Malkin S. and Lenz E. [133] recognized that the introduced specific grinding energy can be used as an indicator in order to distinguish operating points with risk of thermal damage of the edge zone and operating points without expected thermal damage. The relationship between critical grinding energy U_s in the case of burning and the technological process parameters can thus be used as a limitation in the optimization of grinding processes. This optimization determines a maximum possible specific material removal rate Q'_w of a particular grinding process. [134] Adaptive control concepts must consider both, the operating parameters of the grinding process itself and the dressing parameters of conventional grinding wheels. [135]

Moreover, R. Vits pointed out the causality between specific grinding energy U_s and the direct effect on the workpiece edge zone. If the specific grinding energy U_s required for the machining of a specific material volume is plotted over the specific material removal rate Q'_w, hyperbolic curves are obtained. The reason for this trend of the curves lies in the energetically unfavourable chipping with small specific material removal rates. A high number of grains in

[131] cf. Jerard et al., 2009, pp. 119-120.
[132] cf. Malkin, Guo, 2007, p. 760.
[133] cf. Malkin, Lenz, 1978, p. 234.
[134] cf. Malkin et al., 1976, pp. 457-463.
[135] cf. Malkin, Mayne, 1976, pp. 468-473.

the grinding wheel contribute to the grinding force but do not contribute to material removal. Furthermore, the particular material, the grinding wheel and the type and composition of the cooling lubricant have a major influence on the retained curves. [136]

Within the project AGriPro, the interrelation of Vits is used to build up a control concept. This particular concept is characterized by the fact that there is no risk of thermal surface damage at any time during the grinding process below the specific grinding energy $U_s(Q'_w)$. A mathematical model $U_s(Q'_w)$ 6.6.1 is introduced which approximates the boundary curve. Figure 6.6.1 schematically shows this relationship and the approximation of empirical test points by a power function.

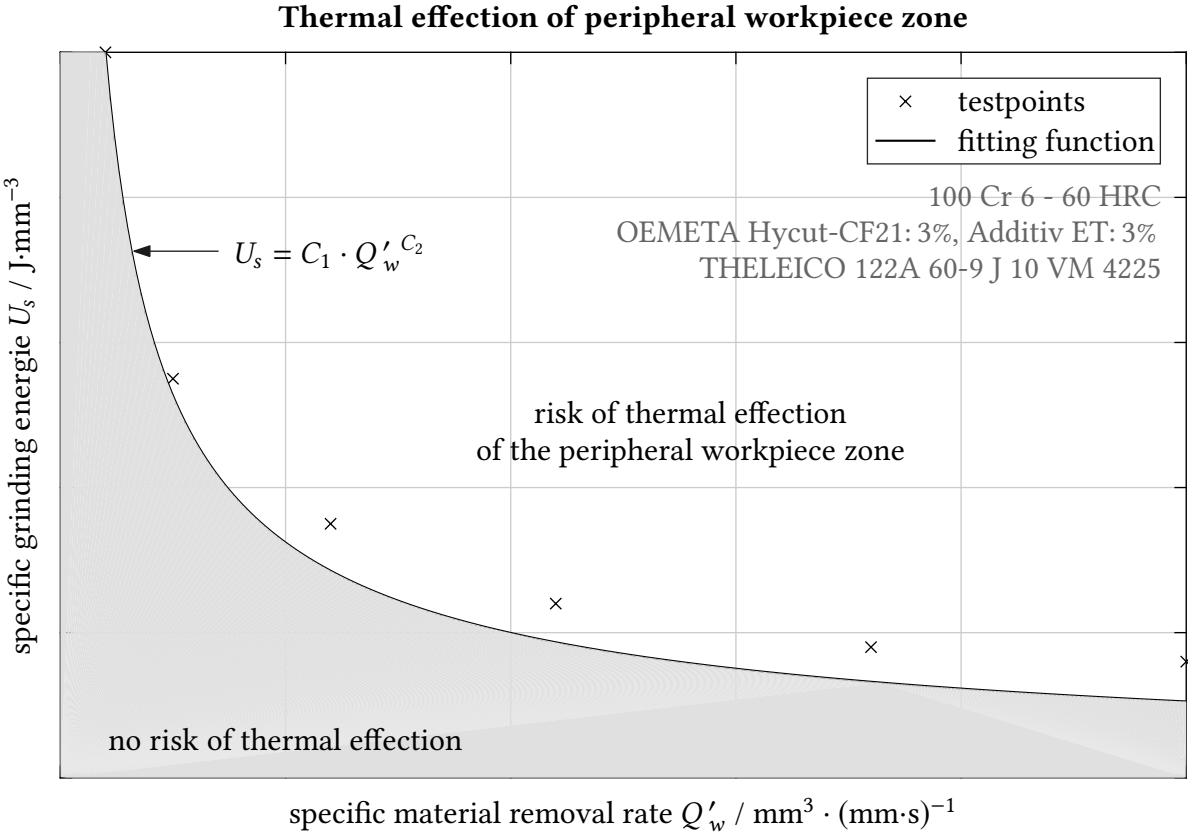

Figure 6.6.1: Relation between specific grinding energy and specific material removal rate, Source: own illustration, based on R. Vits 1985 (pp.71-73).

[136] cf. Vits, 1985, pp. 71-73.

$$U_s(Q'_w) = C_1 \cdot Q'^{C_2}_w \tag{6.6.1}$$

$$F_{t,max}(v_{fr}) = C_1 \cdot [v_{fr}]^{(1+C_2)} \cdot C_3 \tag{6.6.2}$$

$$C_3 = \frac{b_{eff}}{v_c} \cdot [\pi \cdot d_w]^{(1+C_2)} \tag{6.6.3}$$

Within the presented formulas 6.6.1 to 6.6.3, the constants C_1 and C_2 are empirically calculated to approximate the burning limit test points by a fitting function. C_3 represents a geometry-constant. The feed rate v_{fr} must be employed in the unit mm·min^{-1}, the cutting velocity in the unit m·s^{-1} and the workpiece diameter as well as the effective grinding width b_{eff} in the unit mm. The units for all other variables are described in Chapter 3.3.

By transforming the Equations 3.3.9, 3.3.17 and 6.6.1, a function for the tangential force is found which provides a permissible boundary tangential force $F_{t,max}(v_{fr})$ (Equation 6.6.2) in the grinding process. This function serves as a set-point force for the controller, regulating the radial feed rate v_{fr}. The constants C_1 and C_2 determine the shape of the power function to adequately describe the empirical results of Vits.

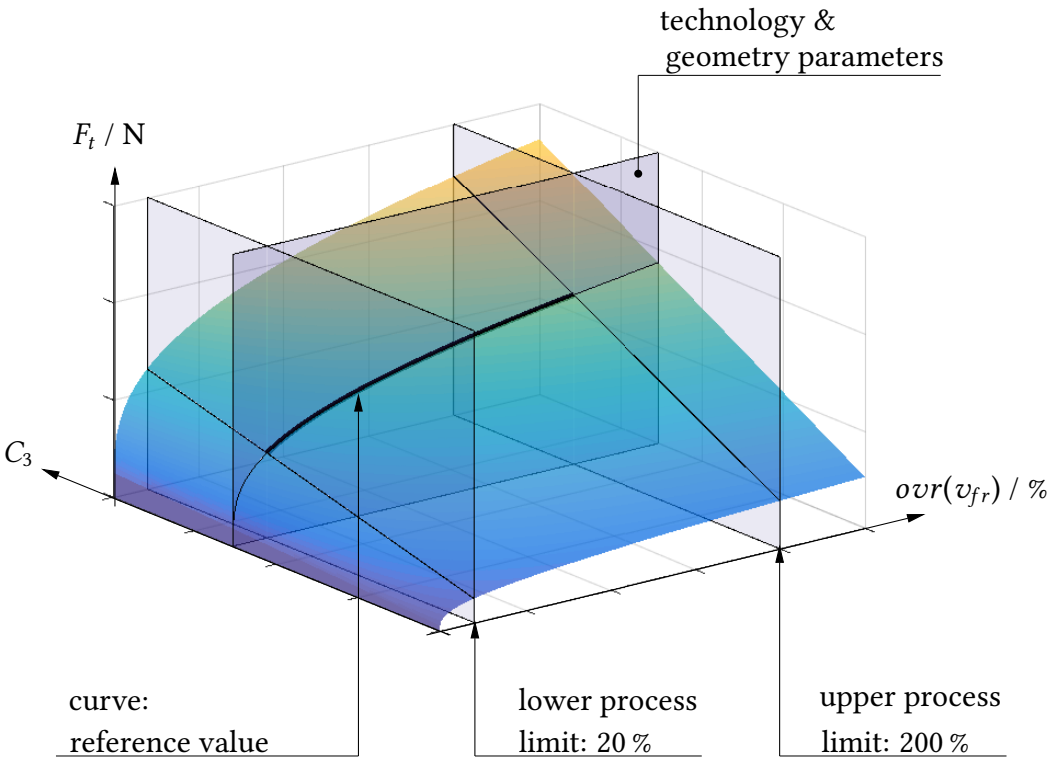

Figure 6.6.2: Three-dimensional relationship provides the reference variable for the PID-controller,
Source: own illustration.

All the necessary geometric and technological parameters of the grinding process are taken into account and are calculated in the constant C_3 (Equation 6.6.3). A three-dimensional field emerges from the connections, as displayed in Figure 6.6.2. The 3D graph shows the tangential force F_t plotted against the radial feed rate v_{fr} and the technology and geometry constant C_3.

The field is limited on two sides by a maximum override u of the radial feed rate v_{fr} of 200 % on the potentiometer and a minimum override of 20 %. The effective grinding wheel width b_{eff}, the workpiece diameter d_w as well as the cutting speed v_c in a specific process determine a plane cut through the field. This creates a two-dimensional correlation at a certain point on the technology and geometry constant C_3 axis. This resulting curve of boundary tangential force $F_{t,max}(v_{fr})$ against the feed rate v_{fr} separates two types of processes, without endangering the peripheral zone by thermal effects and others with the risk of thermal damage. The controller uses this relation to gain a set-point variable during the grinding process.

6.6.2 Implementation of the Control Concept

Thermal damage of the workpiece can be avoided at any time during the process by adjusting the feed rate v_{fr} of a cylindrical grinding process. Therefore, the grinding force F_t during the process is measured and filtered. Figure 6.6.3 shows the implementation of the controller based on the measurement of the tangential grinding force.

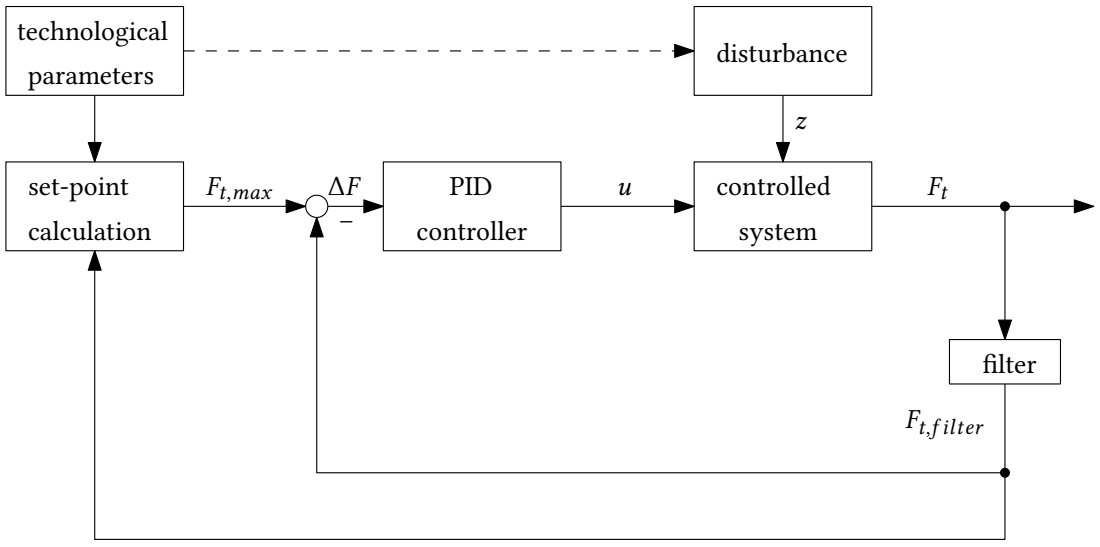

Figure 6.6.3: Implementation of the controller based on tangential grinding force, Source: own illustration.

The set-point force $F_{t,max}$ is obtained by relating the current feed rate v_{fr} to the permitted tangential force $F_{t,max}$ according to Equation 6.6.2. The PID controller minimizes the control

deviation ΔF between the set-point $F_{t,max}$ and the filtered actual tangential force $F_{t,filter}$ by updating the feed rate override as regulating variable u. Moreover, a disturbance variable z is added to the system to check the robustness of the control algorithm. Figure 6.6.3 illustrates the control concept.

To implement the control concept, a piezoelectric three-component force sensor is installed in the free end of the tailstock of the research-grinding machine (according to chapter 6.2). A National Instruments CompactDAQ chassis measures the forces and transfers the measuring data to an external PC where a MATLAB-programme realizes a PID controller based on the transferred data. The radial feed rate v_{fr} during the grinding process is the main influence on the resulting tangential force F_t. The PID controller adapts the feed rate override u at the software potentiometer of the numerical machine controller between 20 % and 200 %. The override corresponds to the parameter $R1$, which is transmitted to the grinding machine as a regulating variable. The communication is realized via OPC UA, whereby the Siemens SINUMERIK 840D sl control acts as a server and the software on the measuring computer as a client. Figure 6.6.4 shows a graphical representation of the control loop.

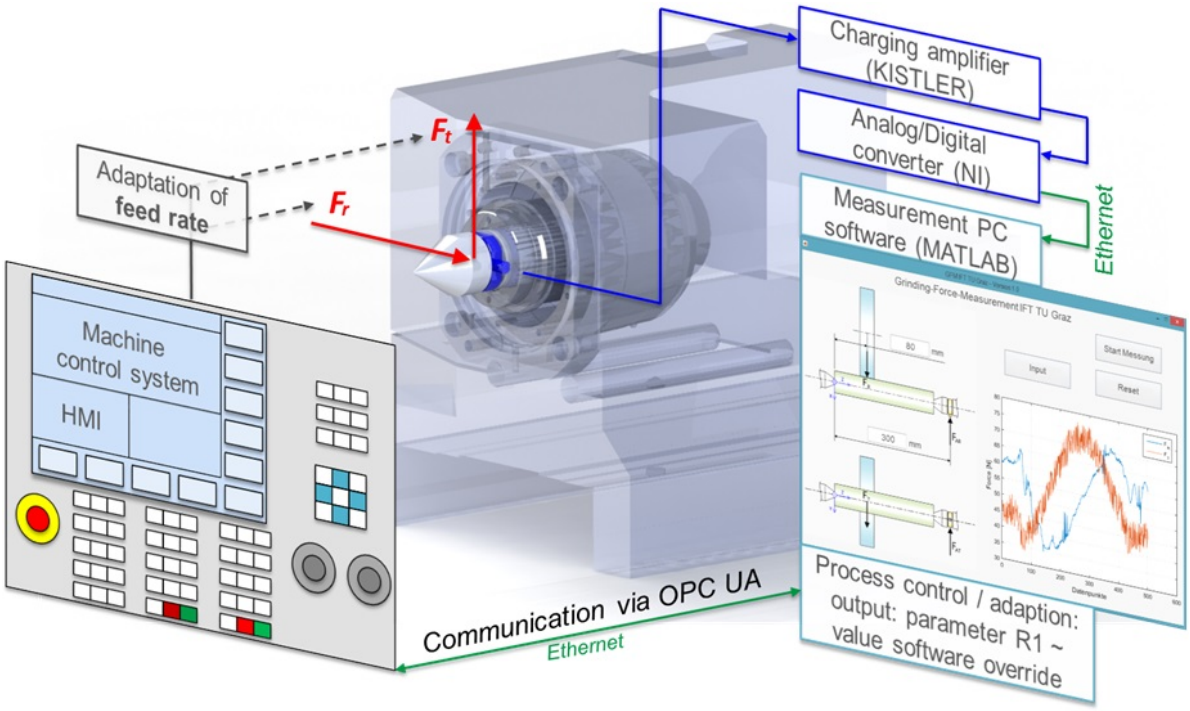

Figure 6.6.4: Schematic representation of the control loop,
Source: own illustration.

6.6.3 Results and Potential of the Adaptive Process Guidance

The selected mathematical model creates a target curve for the set-point force $F_{t,max}$, which is reached by varying the radial feed rate v_{fr} via the override u during the process. In the presented model, the specific grinding energy U_s limits the radial feed rate v_{fr} in the process as a function of the specific material removal rate Q'_w.

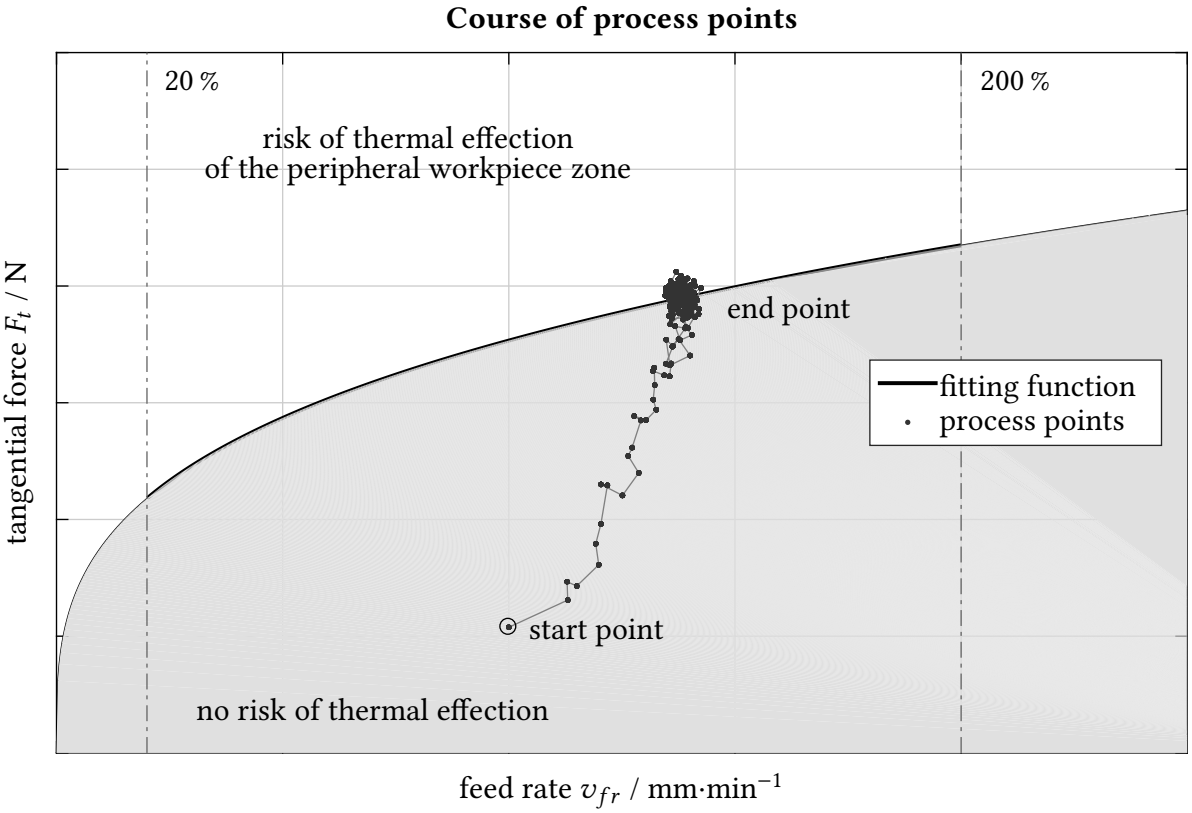

Figure 6.6.5: Progression of the adaptive grinding process,
Source: own illustration.

Figure 6.6.5 shows the temporal progression of the tangential force F_t in the process as a function of the radial feed rate v_{fr}. Two seconds after touching the grinding surface and therefore starting the control process for rough machining, the controller has reached its final feed rate. For a certain test case, processing time could be reduced in comparison to uncontrolled grinding processes with constant feed rates by approaching the grinding burn limit. Thus, a significant reduction in the overall machining time can be realized in grinding which leads to a higher productivity.

As described, real-time tasks cannot be processed with SINUMERIK in combination with the OPC UA Data Access interface. [137] Since the grinding process reacts very slowly to changes

[137] cf. Siemens AG, 2017/06/05, pp.7-21.

in the radial feed rate, a cycle time of 50 milliseconds is sufficient to control the process. The presented control uses only one value, the feed rate override u, as control variable, which is updated using OPC UA. Extensive practice tests confirm the suitability of the OPC communication concept regarding reliability and response time. For research applications, the concept of data transfer via this standardized interface is very flexible and cost-efficient. Tests on the cylindrical plunge grinding process approve this control concept. The control strategy can easily be adapted to other grinding processes with different focusing, such as the novel RPM-Synchronous Grinding process.

7 Experimental Setup

7.1 Research Grinding Machine

In the course of this work, the RPM-Synchronous Grinding unit is used exclusively. It is designed for this novel grinding approach where workpiece and grinding spindle rotation are coupled electronically. Therefore, the rotational rates at the workpiece spindle have to be extraordinarily high compared to conventional grinding processes. Highest revolution rates on the workpiece spindle are mandatory for the functionality of the RPM-Synchronous Grinding process, since the workpiece revolution rate must be as high as those of the grinding wheel when using the rotational ratio $i_g = 1$ for grinding.

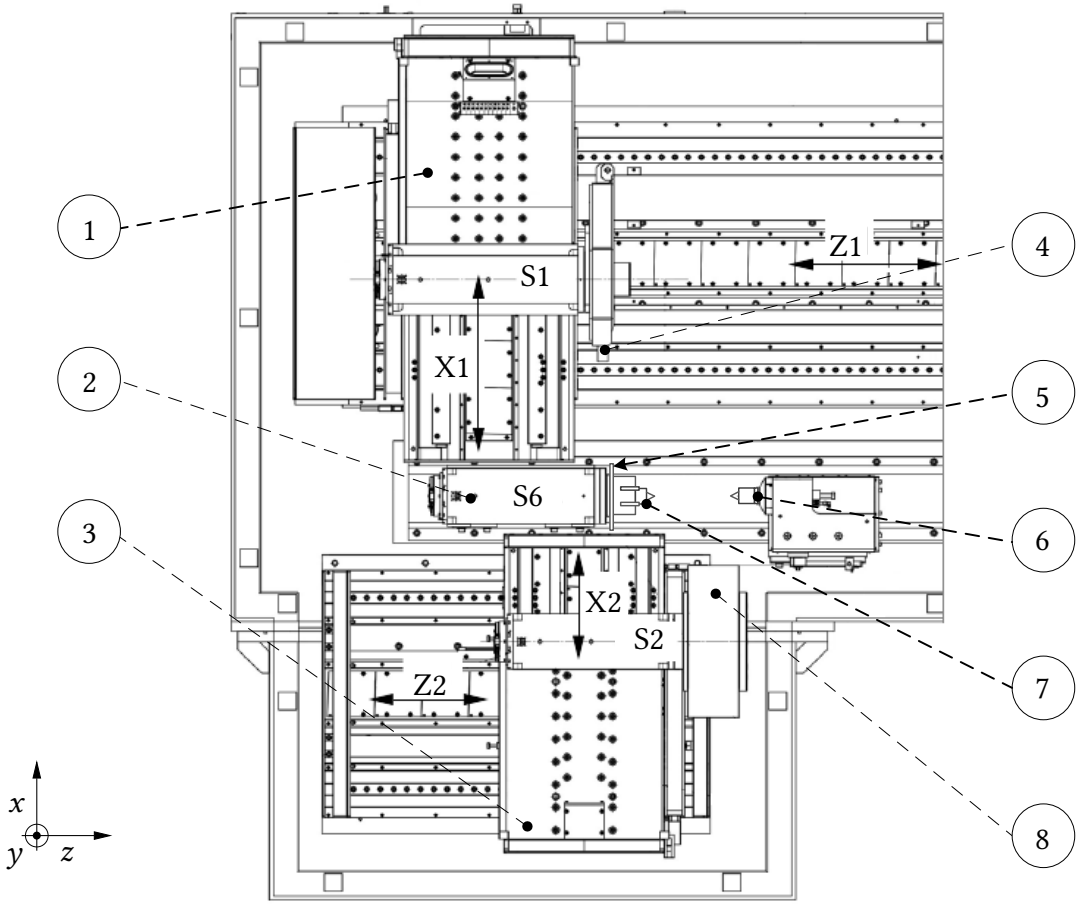

Figure 7.1.1: Experimental setup at the RSG-unit,
Source: own illustration.

The machine layout allows a successive two-step process. Roughing and finishing are performed consecutively among the same clamping of the workpiece (spindle S6) with two locally separated grinding spindles S1 and S2, as Figure 7.1.1 shows. Spindles S1 and S2 are located on compound slides for in X- and Z-direction. At first, roughing is performed using a specially selected grinding wheel on grinding spindle S1. This tool for roughing is classified by large to medium sized grains for gaining high material removal rates. Subsequent to rough machining, finishing is conducted within the same clamping of the workpiece. This procedure is employed by grinding spindle S2. Therefore, a tool with a rather fine grain size is used. At the same time, high dressing overlaps are employed in order to gain best surface roughness qualities.

Table 7.1.1 represents the technical key-data of the RPM-Synchronous Grinding station at the Research Grinding Machine concerning the following experiments.

Table 7.1.1: Experimental setup key-data according to Figure 7.1.1.

Position	Description	Technical key-data
①	X1-Z1 compound slide	grinding spindle S1: 72.6 kW
②	workpiece spindle	workpiece spindle S6: 15.0 kW
③	X2-Z2 compound slide	grinding spindle S2: 31.0 kW
④	grinding wheel: roughing	$v_{c,max}$ = 50 (80) m·s^{-1} (conv.)
⑤	dressing tool	narrow form-roll width: 5 mm, ∅ 260 mm
⑥	rotating center with force measurement	KISTLER piezoelectric 3-component force sensor F_x, F_y, F_z;
⑦	face driver in a clamping chuck	RÖHM concentricity adjustable
⑧	grinding wheel: finishing	$v_{c,max}$ = 50 (80) m·s^{-1} (conv.)

Roughing of the non-circular workpiece geometry is performed with grinding spindle S1 by a mainly highly porous grinding wheel consisting of large grain size (Figure 7.1.1, position 4). It ensures high specific material removal rates for efficiently producing a non-circular geometry close to the demanded geometry after finishing.

For finishing, a grinding wheel with a fine grain size is set up on grinding spindle S2 (position 8). This process step is performed right after the roughing procedure in order to shorten overall process time.

Dressing is done with a circular form-roll which is installed on the workpiece spindle S6 as well (Pos. 5). The dressing process is realized with a pendulum movement to generate a non-circular geometry on the grinding wheel. In order to shorten auxiliary process time, dressing of both grinding wheels is done during grinding of the respectively other grinding unit.

7.2 Sample Workpiece Geometry and Material

7.2.1 Geometry of Blanks

All experiments within this work are performed on special blanks. The geometry of these sample workpieces is shown in Figure 7.2.1. There are blanks in two different lengths available: 79.5 mm and 149.5 mm. All grinding experiments are conducted on the cylindrical area with diameter ∅ 39.8 mm. All blanks are pre-machined by turning between centering pins to guarantee high accuracy in cylindricity.

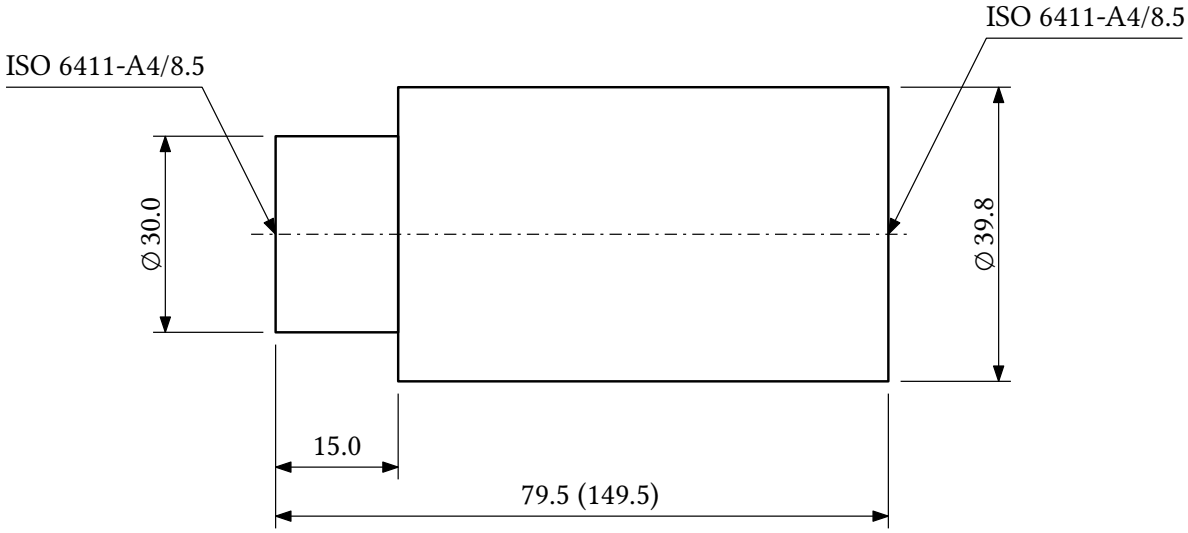

Figure 7.2.1: Sample workpiece dimensions,
Source: own illustration.

7.2.2 Sample Workpiece Material

The properties of materials and their workability vary with the exact composition. Even slight changes in mixture or production process draw distinctions. Therefore, all sample workpieces originate from the same batch of material.

The sample workpiece material is a Q & T steel: **42 Cr Mo 4** (1.7225)

The specific material is commonly used in automotive industry and engineering in general. Its field of application ranges from crankshafts, toothed wheel (gears), stub axles to connecting rods and many different parts.

7.3 Clamping Situation

For clamping of test workpieces (probes), two different clamping situations are deployed. The first clamping situation - such as presented in Figure 7.3.1 by a top-view photography - a face driver is used on the spindle side of the machine. This arrangement is used especially for roughing.

The piezoelectric force sensor registers grinding forces during machining in tangential and normal direction. Utilizing the presented clamping allows highly accurate determination of the machining forces. The probes for roughing have a diameter of ∅ 39.8 mm and a length of 79.5 mm. Needle nozzles support the grinding zone with cooling lubricant. The rotating center supports the workpiece on the tailstock-side of the machine.

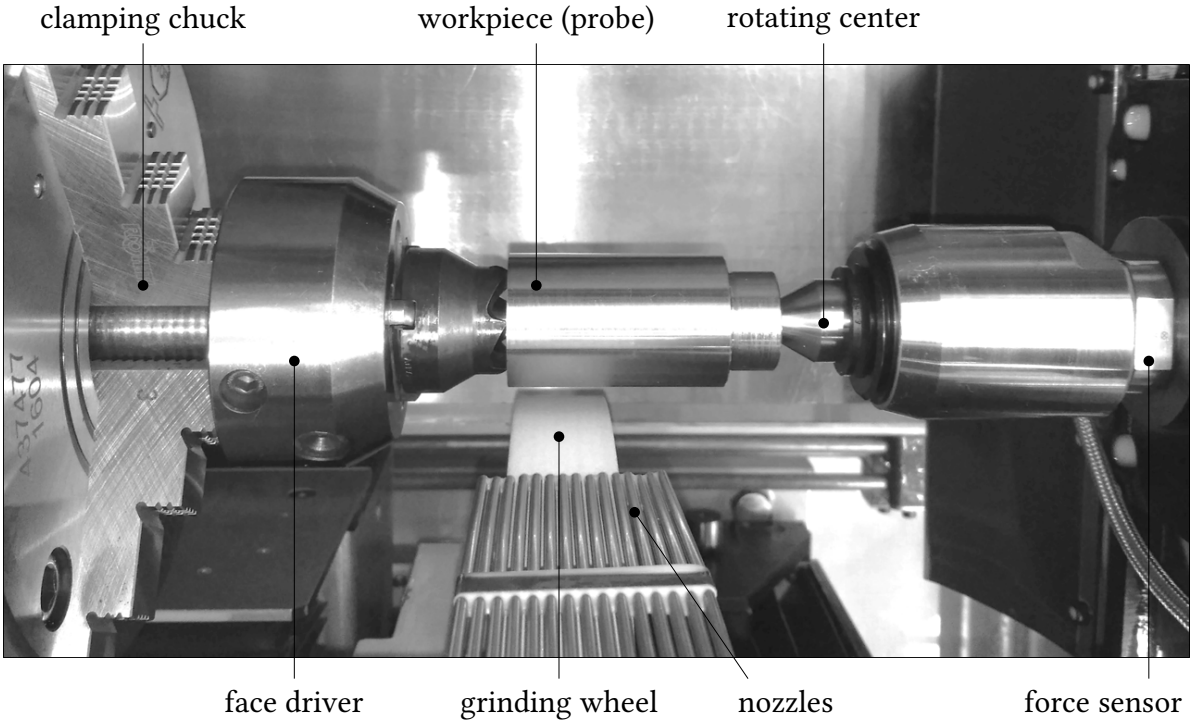

Figure 7.3.1: Clamping situation at the RSG-unit: face driver - rotating center, Source: own illustration.

A disadvantage of this type of clamping is its stability. Due to the high workpiece speed rates for RPM-Synchronous Grinding, this relatively unstable structure tend to vibrate. This fact has no major impact on roughing results. For finishing, where surface roughness is essential, a more rigid fastening must be chosen in order to avoid chatter marks on the workpiece.

The second clamping situation is shown in Figure 7.3.2. The probe of diameter ∅ 39.8 mm is directly clamped in the chuck. The concentricity of this RÖHM product is adjustable. The photograph shows this 3-component force sensor on the opposition side. It is mounted between

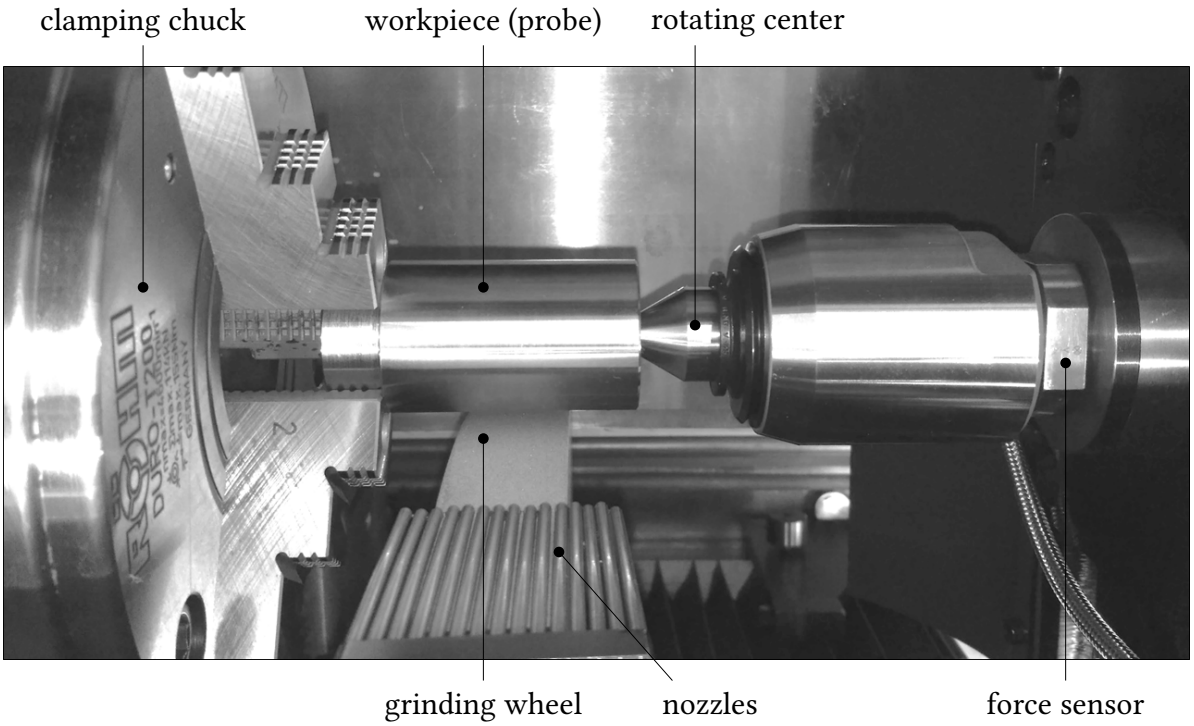

Figure 7.3.2: Clamping situation at the RSG-unit: clamping chuck - rotating center, Source: own illustration.

the rotating center and a morse taper 6 (MK 6) fixture fitted at the tailstock-side. Needle nozzles are used to guide the cooling lubricant into the grinding gap. The rotating center supports the workpiece for more rigid clamping while machining.

7.4 Grinding Wheel Specifications

Since the process of RPM-Synchronous Grinding strongly differs from conventional grinding processes, until now little is known when it comes to the selection of tools. Within this thesis, several different grinding wheels are used. Those tools come from different producers, differentiate in grain material, type and size, disagree in bonding matix, etc. In summary, they vary in their whole composition.

A benchmark will define which product can be used for the process of RPM-Synchronous Grinding. Moreover, it will demonstrate the fields of application and process limits for each different tool.

In the following list, all used grinding wheels are itemized. Some key data is given here. In the subsequent chapters and sections exclusively abbreviations are used. A detailed information about the grinding wheel notation is given in subsection 3.6.

THELEICO Grinding Wheel

85C220-0O4B9240 50, 610 x 60 x 304.8 mm, Form 1

- THELEICO
- Silicon carbide (SiC)
- Resin bond
- Field of application: finishing

TYROLIT Grinding Wheels

CS83A60JJ4VK1 80, 610 x 30 x 304.8 mm, Form 1

- TYROLIT
- Mixture of sintered and fused corundum grains: Al_2O_3
- Vitrified bond
- Field of application: roughing

CS85A60JJ4VK1 80, 610 x 30 x 304.8 mm, Form 1

- TYROLIT
- Mixture of sintered and fused corundum grains: Al_2O_3
- Vitrified bond
- Field of application: roughing

CS83A60II5VK1 80, 610 x 30 x 304.8 mm, Form 1

- TYROLIT
- Mixture of sintered and fused corundum grains: Al_2O_3
- Vitrified bond
- Field of application: roughing

CS55A220II5VK1 80, 610 x 30 x 304.8 mm, Form 1

- TYROLIT
- Fused corundum grains: Al_2O_3
- Vitrified bond
- Field of application: finishing

CS85A220II4VK1 80, 610 x 30 x 304.8 mm, Form 1

- TYROLIT
- Mixture of sintered and fused corundum grains: Al_2O_3
- Vitrified bond
- Field of application: finishing

The grinding wheel with grain type 55A exclusively consists of fused corundum abrasive grains. In comparison, the type 85A and 83A are mixtures of sintered and fused Al_2O_3 grains. Thereby, the proportion of sintered grains is higher at the specification 85A compared to the type 83A.

Concerning the degree of hardness of the listed TYROLIT grinding wheels, different structures are available. The specification JJ4 consists of a higher proportion of core-material and bond-material compared to II5. Therefore, it acts harder in grinding processes.

8 Experimental Execution and Evaluation of Results

8.1 Design of Experiments

A statistic parameter study is performed on a set of parameters whose influence in the resulting surface quality is not yet fully clear. Especially the novel process of RPM-Synchronous Grinding may bring up different effects compared to conventional grinding processes. Moreover, the Design of Experiments (DoE) method allows analysis of different influences of several factors on the observed results of experiments as well as the interaction between different input factors and their dependence. [138] In Table 8.1.1 the major process parameters applied for this DoE are summarized.

Table 8.1.1: Grinding process parameters for DoE.

Parameter	**Value**
grinding machine	GST Research Grinding Machine @ IFT
grinding wheel specification	THELEICO 85C220-0O4B9240
grinding wheel dimensions	600 x 60 x 304.8 mm
workpiece diameter	∅ 39.8 mm
workpiece material	42CrMo4
dressing direction	counter direction
dressing overlap Z-direction	$u_d = 8$
velocity ratio dressing	$q_d = -0.3 \cdots -1.0$
dressing infeed	$a_p = 0.001 \ldots 0.010$ mm
grinding feed rate	$v_{fr} = 0.050 \ldots 0.500$ mm·min^{-1}
grinding direction	counter direction
cutting velocity	$v_c = 50$ m·s^{-1}
rotational ratio	$i_g = -1$

For all presented results of RPM-Synchronous Grinding within this DoE study, a silicon carbide grinding wheel bound with synthetic resin is used. It is a THELEICO product type 600 mm x 60 mm x 304.8 mm 85C220-0O4B9240, which consists of a grains size of about 60 µm. Due to the maximum circumference velocity of $v_{c,max} = 50\,\mathrm{m{\cdot}s^{-1}}$, the rotational speed is chosen 1590 min^{-1}. The workpieces are cylindrical probes with a length of 79.5 mm and a diameter of 39.8 mm consisting of Q & T steel (42CrMo4). The workpiece spindle is electronically coupled

[138] cf. Siebertz, van Bebber, 2010, p.12-19.

by the rotational ratio i_g = 1 and therefore revolves with 1590 min^{-1} as well.

For dressing, a narrow, cylindrical form-roll is used. With this diamond set tool the grinding wheel can be conditioned in different ways. Especially the dressing overlap in Z-direction has significant influence in later surface roughness qualities of the workpiece but is held constant over all experiments concerning this parameter study.

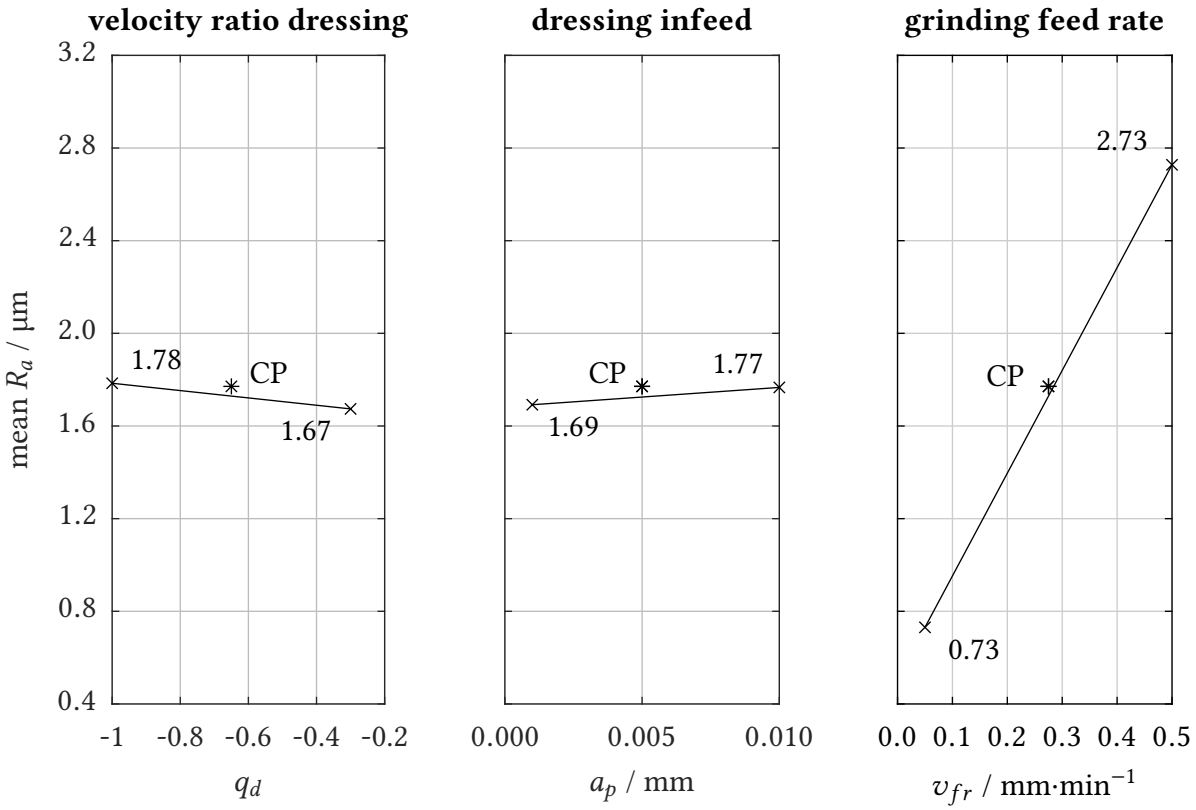

Figure 8.1.1: Main effects of full-factorial design with center point (DoE), Source: own illustration.

The three parameters velocity ratio at dressing (q_d), infeed at dressing (a_p) and feed rate at grinding ($v_f r$) are examined in a full-factorial DoE with center point. The measured target value is the resulting surface roughness R_a on the workpiece.

In contrast to Spur and Eichhorn, dressing is done without synchronization of the interacting partners, since this is not necessary for dressing with form-rolls in general. The velocity ratio at dressing here is varied between q_d = −0.3 and q_d = −1.0. Dressing infeed is modified between a_p = 0.001 mm and a_p = 0.010 mm and the grinding feed rate between v_{fr} = 0.050 mm·min^{-1} and v_{fr} = 0.500 mm·min^{-1}. The overlap in Z-direction is held constant at a value of u_d = 8.

The main effects are shown in Figure 8.1.1. The parameters velocity ratio at dressing (Figure

8.1.1 left) and the dressing infeed (Figure 8.1.1 middle) show no significant influence on the grinding results concerning surface roughness on the workpiece probe confirming the grinding results of Spur and Eichhorn. [139] [140]

In contrast, the feed rate at grinding (Figure 8.1.1 right) demonstrated considerable influence on the grinding result. Higher feed rate means higher surface roughness due to higher process forces and oscillations and the thereto-related grinding wheel wear.

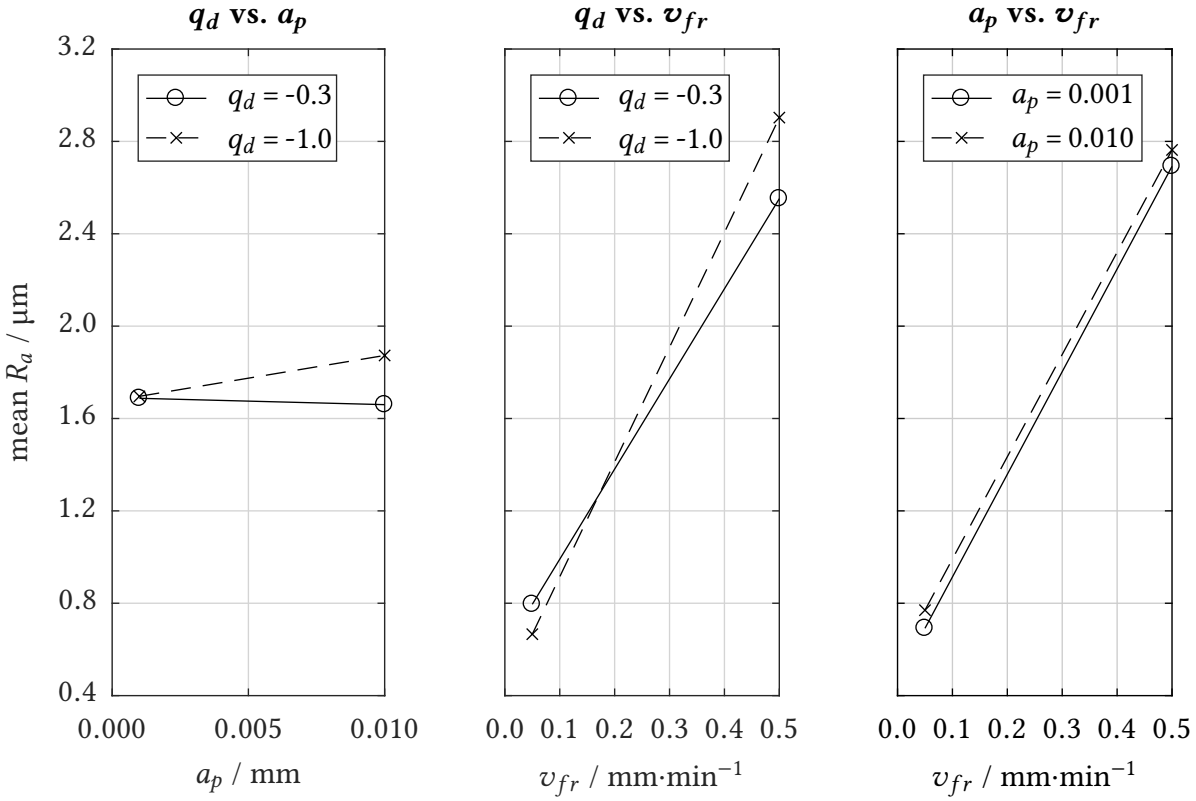

Figure 8.1.2: Interactions of the varied parameters (DoE),
Source: own illustration.

The center point examination confirmed the results. A linear dependency of the three varied process parameters can be assumed. [141] The interactions between all varied parameters are shown in Figure 8.1.2. The parameters dressing infeed and grinding feed rate show no interactions at all (Figure 8.1.2 right). A light reciprocity is stated for the velocity ratio at dressing and dressing infeed (Figure 8.1.2 left). However, strong interaction results from the combination of the variation of the velocity ratio at dressing and the grinding feed rate (Figure 8.1.2 middle).

Other parameters such as overlap in Z-direction at dressing u_d were not investigated in the

[139] cf. Spur, Eichhorn, 1996a, pp. 48–58.
[140] cf. Spur, Eichhorn, 1996b, pp. 126–137.
[141] cf. Siebertz, van Bebber, 2010, p.38-40.

presented DoE because the coherence concerning resulting surface roughness is generally known: The higher the overlap is chosen, the smoother the resulting workpiece surface after machining. The surface roughness results of all experiments within the DoE study reveal that the dressing overlap $u_d = 8$ is much too less to gain technical suitable RPM-Synchronous Grinding results. This fact distinguishes conventional grinding and the process of RPM-Synchronous Grinding.

All resulting data of the performed Design of Experiments analysis can be reviewed in Table 8.1.2.

Table 8.1.2: Full-factorial DoE main effects and interactions with center point.

$q_d \cdots$	velocity ratio dressing	$0 \cdots -0.3$	$1 \cdots -1.0$
$a_p \cdots$	dressing infeed	$0 \cdots$ 0.001 mm	$1 \cdots$ 0.010 mm
$v_{fr} \cdots$	grinding feed rate	$0 \cdots$ 0.05 mm·min^{-1}	$1 \cdots$ 0.50 mm·min^{-1}

	q_d	a_p	v_{fr}	$q_d \cdot a_p$	$q_d \cdot v_{fr}$	$a_p \cdot v_{fr}$	$q_d \cdot a_p \cdot v_{fr}$	$\overline{R_a}$
V01	0	0	0	1	1	1	0	0.930
V02	0	0	1	1	0	0	1	2.445
V03	0	1	0	0	1	0	1	0.661
V04	0	1	1	0	0	1	0	2.659
V05	1	0	0	0	0	1	1	0.453
V06	1	0	1	0	1	0	0	2.939
V07	1	1	0	1	0	0	0	0.879
V08	1	1	1	1	1	1	1	2.867
$x_d(-)$	1.674	1.691	0.731	1.678	1.609	1.731	1.852	
$x_d(+)$	1.785	1.767	2.728	1.780	1.849	1.727	1.607	
effect	−0.111	−0.075	−1.997	−0.102	−0.240	0.004	0.245	

all numeric value in µm

Center Point:

q_d =	−0.65
a_p =	0.005 mm
v_{fr} =	0.275 mm·min^{-1}
$\overline{R_a}$ =	1.771 µm

8.2 Performance of RPM-Synchronous Grinding

On the basis of first grinding experiments within the Design of Experiment study, different grinding wheel specifications are chosen in close cooperation with the Austrian manufacturer TYROLIT. These specific grinding tools are listed in section 7.4. Three different abrasive tools for roughing and two for finishing are at disposal. In this section all five specifications are tested and the results aggregated and presented.

8.2.1 Tools for Rough Machining - Roughing

The chosen tool specifications for the rough machining process together with the major process parameters are listed in Table 8.2.1. Subsequently, all results for each grinding wheel are discussed.

Table 8.2.1: Grinding wheel test - process parameters.

Parameter	**Value**
grinding machine	GST Research Grinding Machine @ IFT
grinding wheel specification	TYROLIT - CS85A60JJ4VK1 80 TYROLIT - CS83A60JJ4VK1 80 TYROLIT - CS83A60II5VK1 80
grinding wheel dimensions	610 x 30 x 304.8 mm, Form 1
workpiece diameter	∅ 39.8 - ∅ 30 mm
workpiece material	42 Cr Mo 4
dressing direction	counter direction
dressing overlap Z-direction	$u_d = 4$
velocity ratio dressing	$q_d = -0.25$
dressing infeed	$a_p = 0.005$ mm
specific material removal rate	$Q'_w = 0.5 \ldots 30\ \mathrm{mm^3 \cdot (mm \cdot s)^{-1}}$
grinding direction	counter & equal direction
cutting velocity	$v_c = 50\ \mathrm{m \cdot s^{-1}}$
rotational ratio	$i_g = 1, -1, -2$, non-synchronized
cooling pressure	$p_c = 8$ bar

The main focus of all rouging experiments is laid on the evaluation of grinding forces and the grinding wheel wear in relation to the specific material removal rate. The resulting surface roughness quality is just a minor parameter for this roughing operation, since a finishing step is inevitable.

All grinding experiments are performed with a circumference velocity of $50\ \mathrm{m \cdot s^{-1}}$ to get results which are comparable to other specifications. Moreover, $50\ \mathrm{m \cdot s^{-1}}$ is a very common maximum admitted velocity for conventional grinding tools of other manufacturers as well.

TYROLIT - CS85A60JJ4VK1 80

The first grinding wheel specification in the presented series of tests is the CS85A60JJ4VK1 with the maximum admitted circumference velocity of 80 $m \cdot s^{-1}$. A total amount of 33 experiments is performed in order to get detailed information about the behaviour of this grinding wheel in the special RPM-Synchronous Grinding process. The specific material removal rate is increased from one experiment to the next. All other parameters - concerning dressing and grinding - are held constantly to obtain comparable results.

Figure 8.2.1 presents the evaluation of the grinding forces of three experiments with comparatively small specific material removal rates and RPM-Synchronous counter direction grinding.

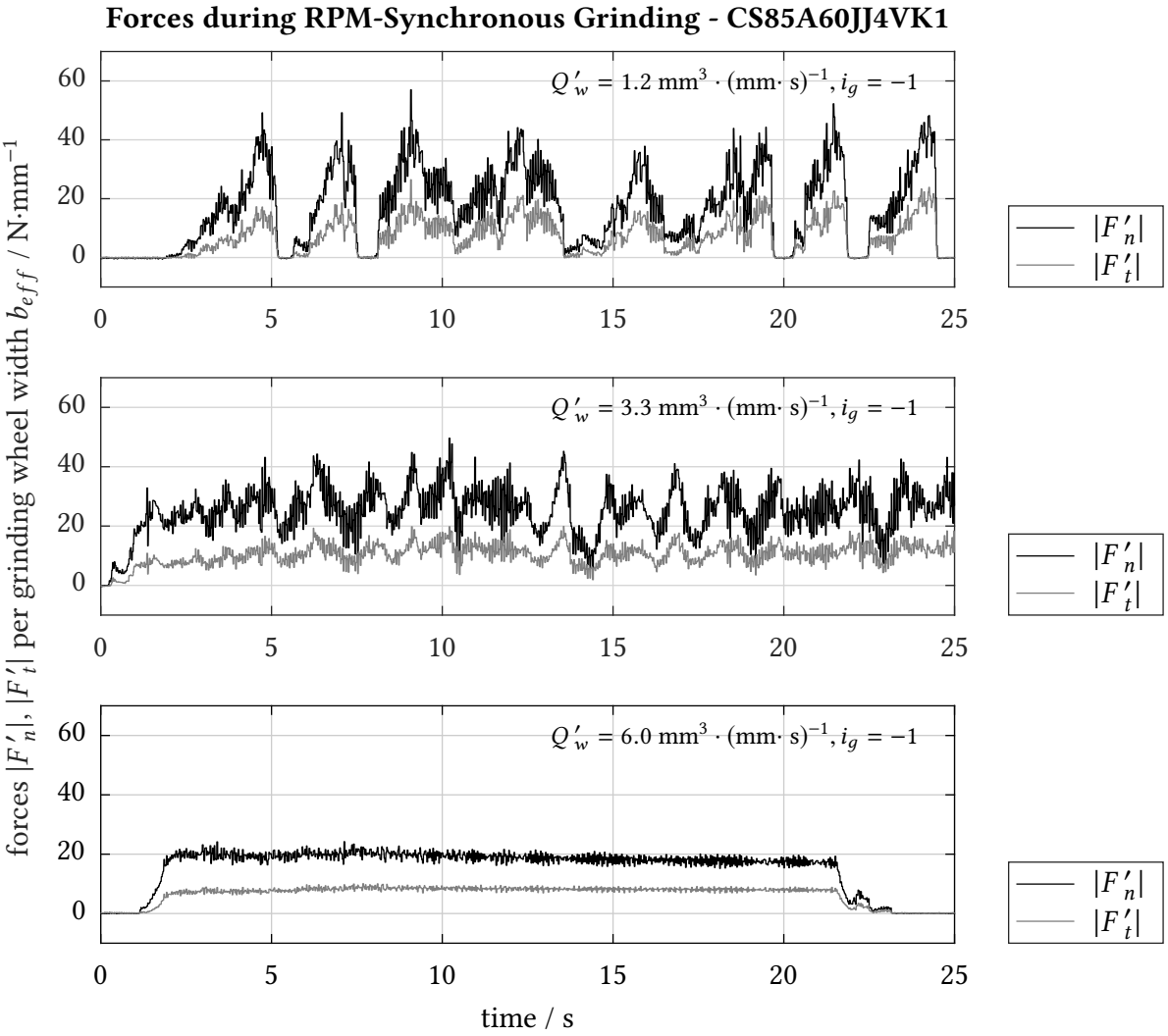

Figure 8.2.1: Forces during RSG at different values for Q'_w - ($i_g = -1$), Source: own illustration.

The top graph in Figure 8.2.1 represents specific grinding forces in normal and tangential direction utilizing a specific material removal rate Q'_w of 1.2 $mm^3 \cdot (mm \cdot s)^{-1}$. During grinding

loud noise is noticeable and strong oscillations seem to appear. These noise and the oscillations immediately stop at one point. Approximately one second later, the same behaviour restarts.

When the specific material removal rate is increased, a more constant noise level appears. Oscillations in force are not that high any more, as is documented in Figure 8.2.1 in the middle. Here, a value for Q'_w of 3.3 $\text{mm}^3\cdot(\text{mm}\cdot\text{s})^{-1}$ is realized.

The bottom graph in Figure 8.2.1 demonstrates force measurement results of yet another, higher specific material removal rate. The oscillation is much smaller compared to the previous experiments. Moreover, the noise level is very constant and much lower. The tangential and normal grinding forces show no unexpected peaks and there is a clear separation of mean force level and superimposed oscillation.

It is obvious that higher specific material removal rates have a positive impact in the overall process behaviour. Less oscillations during the process benefit the resulting surface roughness on the workpiece. Since this process step is meant for roughing, this factor is minor, but is valuable information for the later finishing operation with different grinding wheel specifications.

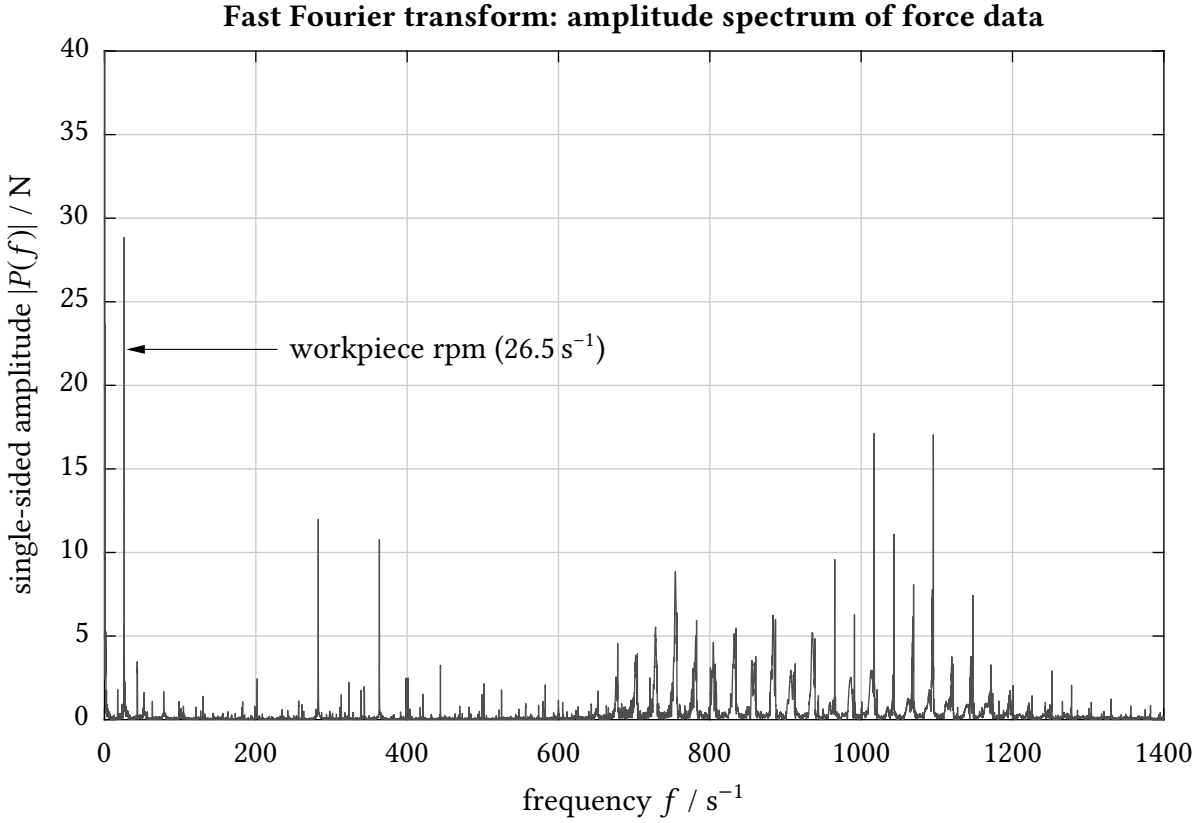

Figure 8.2.2: Fast Fourier transform of tangential force data,
Source: own illustration.

Figure 8.2.2 exemplarily shows the Fast Fourier transform (FFt) analysis of the following grinding process. A counter direction roughing procedure is performed at a specific material removal rate of $Q'_w = 20.7\ \mathrm{mm^3{\cdot}(mm{\cdot}s)^{-1}}$ and a rotational ratio of $i_g = -1$, utilizing the tool CS85A60JJ4VK1. The first and highest peak, besides the very low frequent force amplitude of less than $2\ \mathrm{s^{-1}}$, is caused by the rotational speed caused by the rotational speed of the workpiece and the grinding wheel at $f = 26.5\ \mathrm{s^{-1}}$. At higher frequencies, peaks arise which are multiples of this well-known frequency. The peaks of force amplitude at frequencies between $800\ \mathrm{s^{-1}}$ and $1200\ \mathrm{s^{-1}}$ result from the surface topography the the grinding wheel. This topography is mainly determined by the tool composition (grain size) and the dressing operation.

Figure 8.2.3 shows the results of force measurement for higher specific material removal rates. For this illustration and for Figure 8.2.4, 8.2.5 and 8.2.6 the same low-pass filter is applied on all data to get a clearer overview of the forces' behaviour during grinding. The filter eliminates influences evoked by the rotational speed of the workpiece and the grinding wheel at $f = 26.5\ \mathrm{s^{-1}}$ and all high-frequent oscillations mainly arouse by the topology of the tool, as previously described.

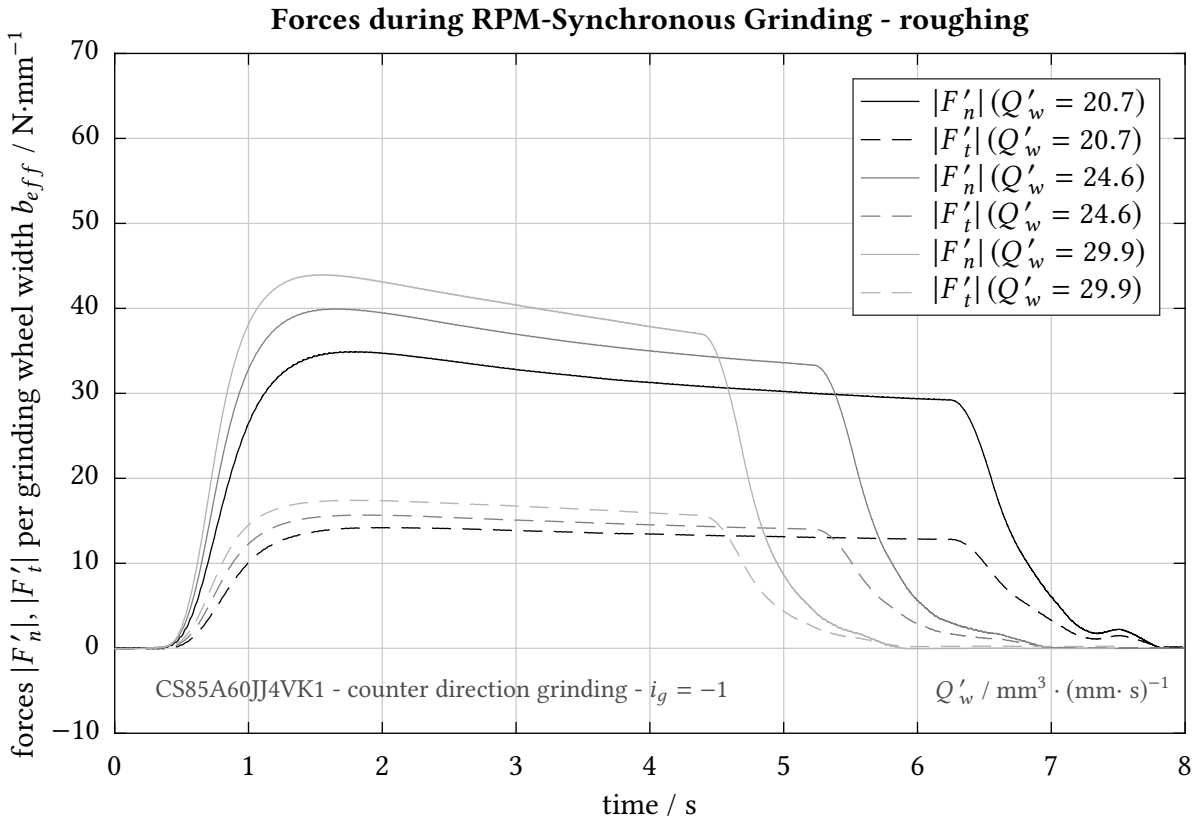

Figure 8.2.3: Forces during RSG at different values for Q'_w - roughing - ($i_g = -1$), Source: own illustration.

The RPM-Synchronous Grinding process presented in Figure 8.2.3 is still performed in counter direction. Values for Q'_w are chosen between 20 and 30 $mm^3 \cdot (mm \cdot s)^{-1}$. These values are relatively high for conventional vitrified bonded tools in an external circular grinding process. For the performed counter direction grinding, circumference velocities of grinding wheel (v_c = 50 $m \cdot s^{-1}$) and workpiece (v_w = 3.27 $m \cdot s^{-1}$) add up to an effective cutting velocity (v_{eff} = 53.27 $m \cdot s^{-1}$) which is slightly higher than the cutting velocity of the grinding wheel. Grinding forces are increasing with higher material removal rates, what could be expected. The noise during processing has almost disappeared and no major oscillations are recognized during force measuring.

While the rotational ratio of the RPM-Synchronous Grinding processes i_g was chosen −1 for all experiments done on this grinding wheel specification, now the ratio is changed to i_g = −2. The grinding wheel still rotates with a rpm-value of about 1565 min^{-1} what corresponds to the aimed cutting velocity of 50 $m \cdot s^{-1}$. The workpiece, on the other hand, rotates with exactly one-half of the tools rpm-rate in order to obtain the rotational ratio of −2. Figure 8.2.4 presents the occuring grinding forces during the described process.

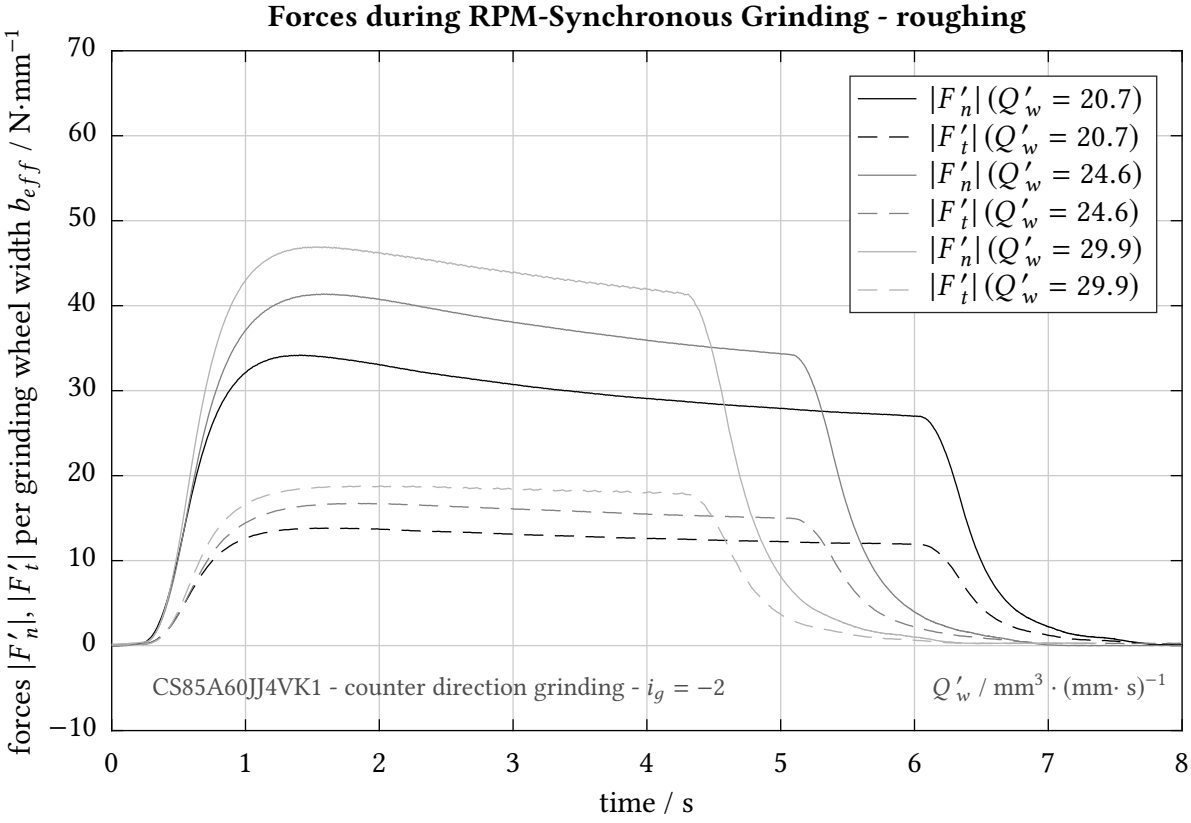

Figure 8.2.4: Forces during RSG at different values for Q'_w - roughing - (i_g = −2), Source: own illustration.

The normal and tangential grinding forces appear to be slightly higher compared to the pre-

vious process with rotational ratio of $i_g = -1$. No unexpected oscillation or disturbance is documented.

As a next step, the grinding direction is changed. Instead of counter direction grinding, equal direction grinding is performed in a RPM-Synchronous process. For all previous experiments the circumference velocity values added up to the effective cutting velocity. Now, since the velocity vectors of grinding wheel and workpiece point in the same direction, the resulting effective velocity is reduced to a value of $v_{eff} = 46.73\,\mathrm{m{\cdot}s^{-1}}$.

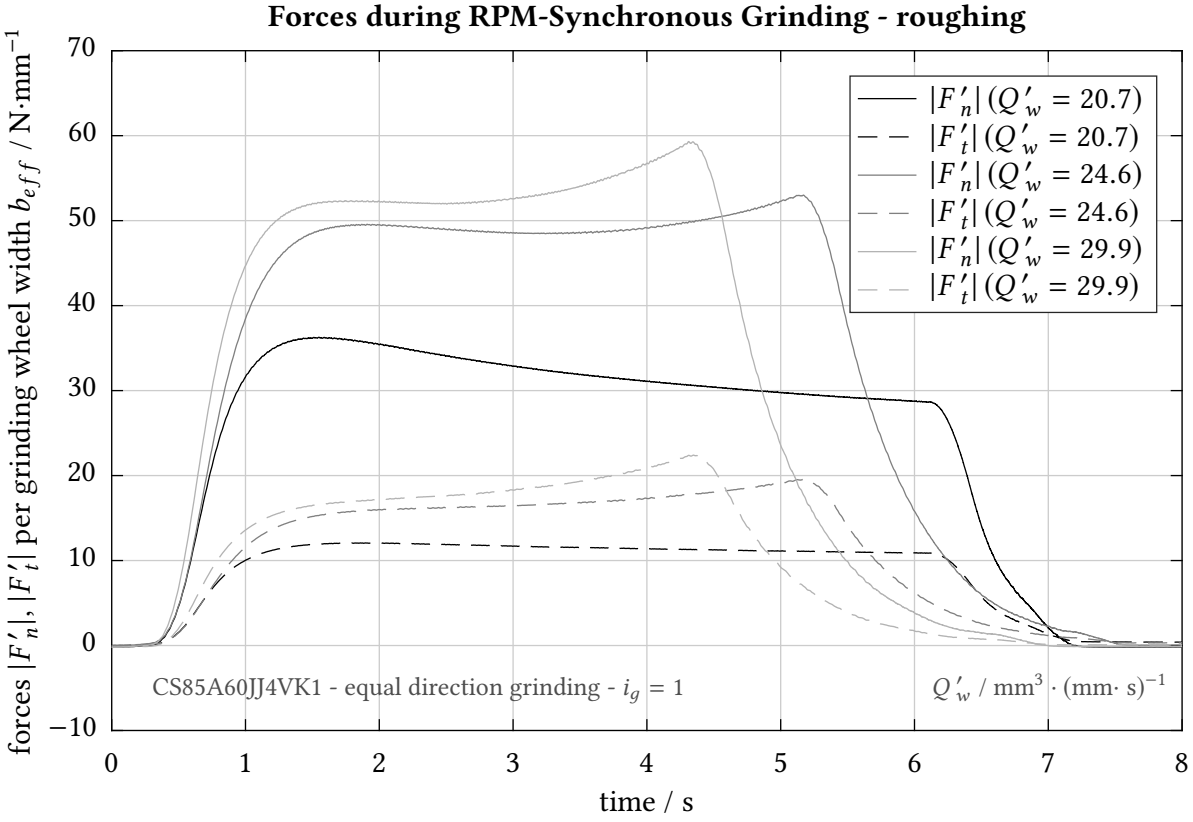

Figure 8.2.5: Forces during RSG at different values for Q'_w - roughing - ($i_g = 1$), Source: own illustration.

Again, Figure 8.2.5 illustrates force measurement results of the mentioned process. Especially the normal forces appear to be even higher than measured for counter direction grinding. The peak at the end of every experiment comes from a short time period with oscillation right at the beginning of the spark-out phase of the grinding process. Altogether, the noise and oscillation level is very similar to the performed counter direction grinding experiments.

The comparison of those RPM-Synchronous Grinding experiments with conventional grinding experiments under same conditions is one of the most interesting points in the development of this novel grinding approach. Therefore, same specific material removal rates on the same workpiece are applied in order to benchmark the processes.

Figure 8.2.6 shows the results of the conventional grinding experiments. Here, the workpiece rotates with 120 min^{-1} which is a standard value for external circular grinding. Grinding is performed in counter direction with the grinding wheel still rotating at 1565 rpm. The circumference velocity of the workpiece (v_w = 0.25 $\mathrm{m{\cdot}s^{-1}}$) now has no major impact on the effective cutting velocity.

The normal and tangential specific grinding forces are definitely higher compared to all the RPM-Synchronous Grinding processes. That fact is quite remarkable. Many critics of this novel process in the past claimed that the RPM-Synchronous process is more a rolling than a grinding process. Therefore, the grains would be pressed into the workpiece rather than cutting the material. In big contrast, these hypothesis can be refuted. RPM-Synchronous Grinding forces are smaller or in some cases equal to conventional grinding forces what can be explained by a different chip form.

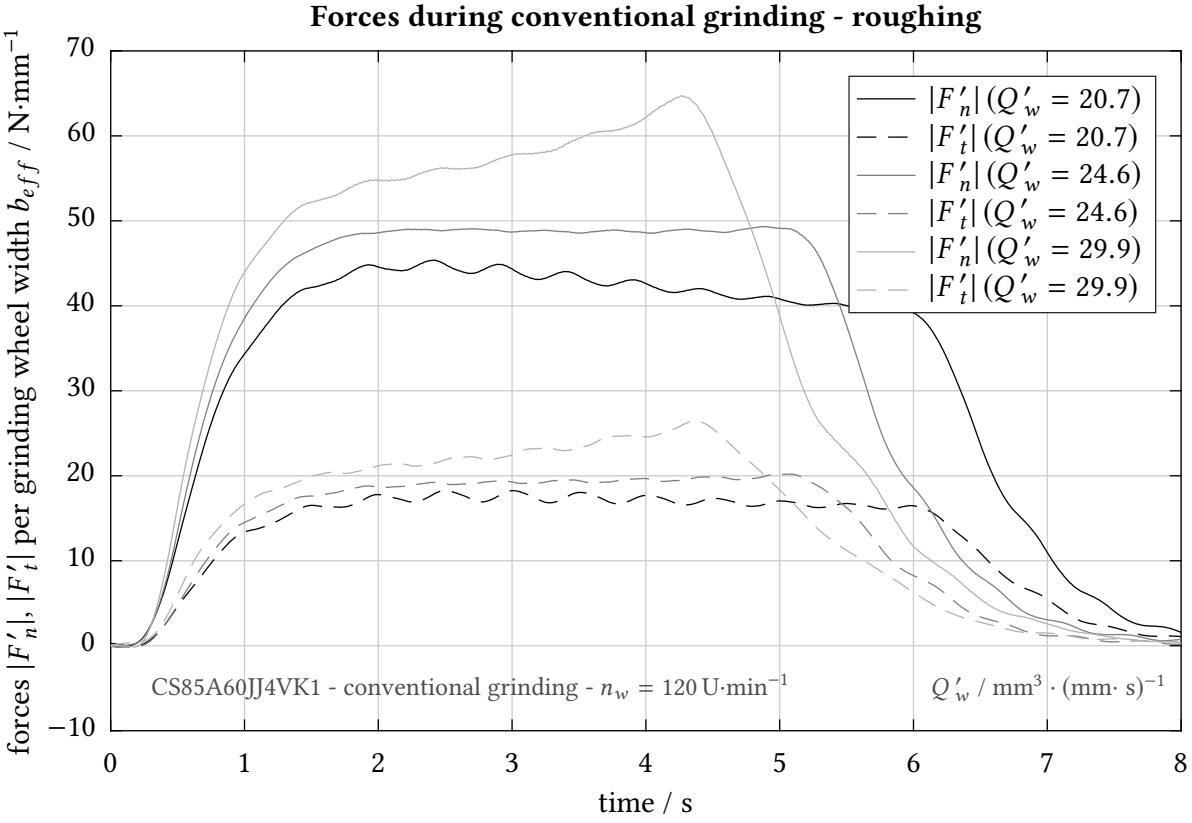

Figure 8.2.6: Forces during CG at different values for Q'_w - roughing, Source: own illustration.

Equally, or even more important than the specific grinding forces during RPM-Synchronous and conventional grinding processes is the related grinding wheel wear. This decline in grinding wheel radius is measured in µm as a difference in radius before and after each grinding process. Therefore, within every single experiment the exact same volume of workpiece ma-

terial is removed and the wheel wear is measured. The results are graphically prepared in a G-ratio / specific material removal rate diagram. The higher the G-ratio G is, the smaller is the grinding wheel wear.

Figure 8.2.7 sums up all results of grinding wheel wear of the TYROLIT grinding wheel specification CS85A60JJ4VK1. Extensive experiments have been performed on RPM-Synchronous counter direction grinding with a rotational ratio of $i_g = -1$. For all following experiments the number of trails have been reduced, but all interesting points are examined.

Grinding wheel wear is documented with analogous behaviour to what was recorded for the grinding forces. The process with smallest grinding forces shows smallest amount of grinding wheel wear. This fact could be anticipated, since the force defined the stress on each grain in the bond matrix.

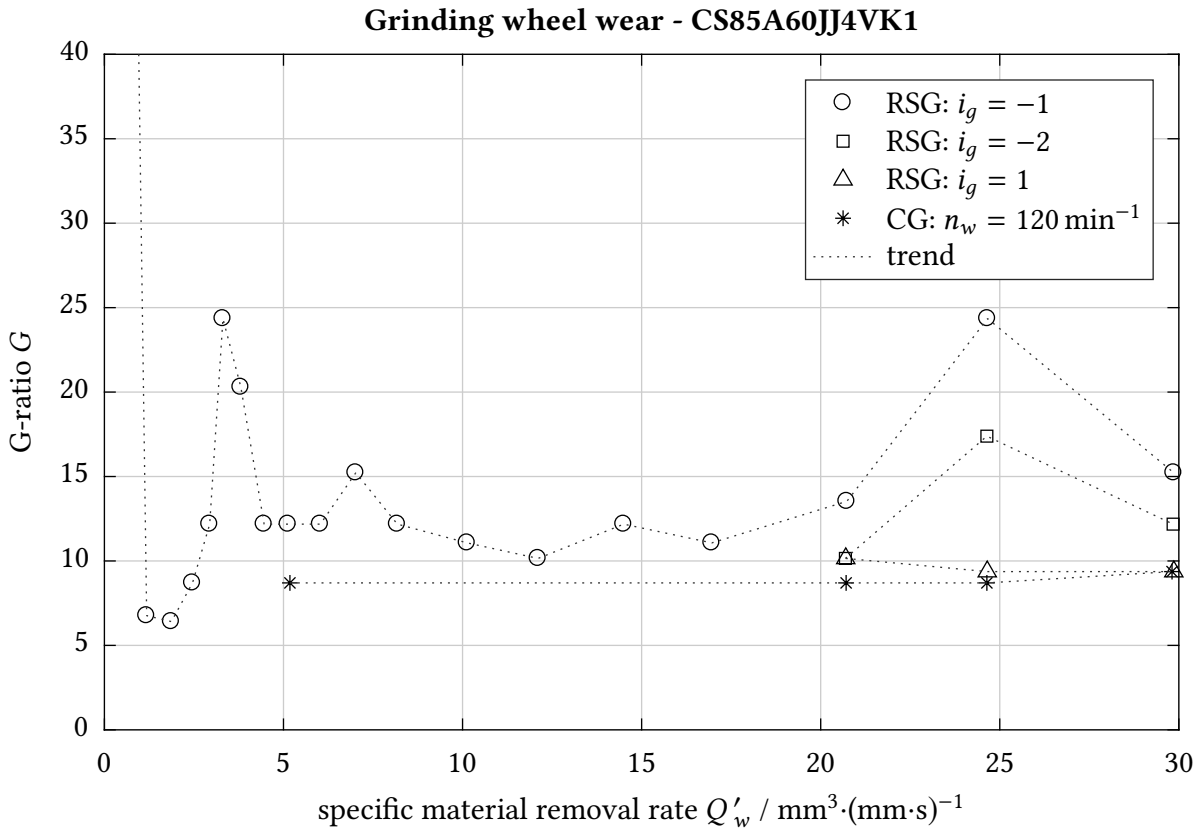

Figure 8.2.7: Grinding wheel wear - CS85A60JJ4VK1,
Source: own illustration.

According to a vague statement of the grinding wheel manufacturer, a specific material removal rate Q'_w of 5 to 10 $\mathrm{mm}^3\cdot(\mathrm{mm}\cdot\mathrm{s})^{-1}$ is expectable for this novel RPM-Synchronous Grinding process. The results of grinding force measurement and grinding wheel wear approve even higher rates, what underlines the functionality and efficiency of the approach.

To summarise the results of the grinding experiments utilizing the CS85A60JJ4VK1 grinding wheel, Figure 8.2.8 illustrates the specific normal forces in a bar diagram. The bandwidth of the oscillation amplitude is as well presented on terms of an errorbar. This specific figure allows a comparison of the three different grinding wheel specifications.

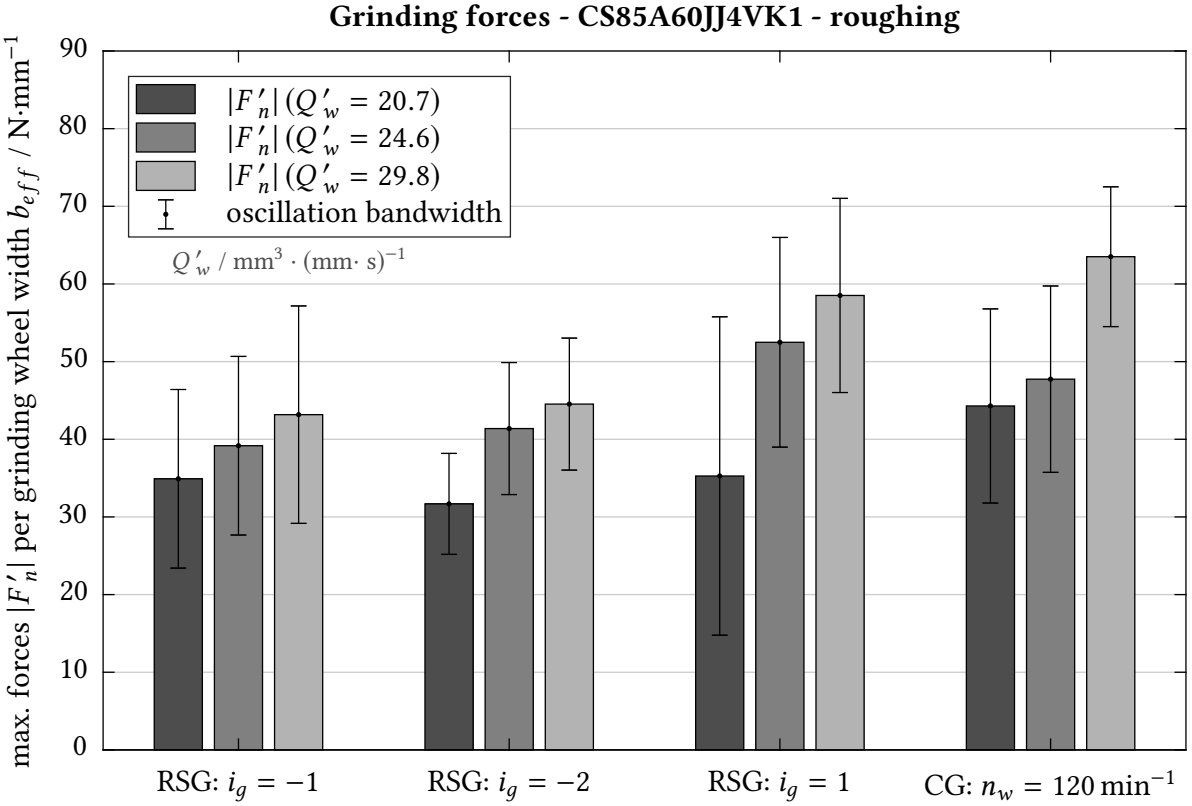

Figure 8.2.8: Grinding forces during RSG and CG - CS85A60JJ4VK1 - roughing, Source: own illustration.

Figure 8.2.8 gives a good overview of the results concerning specific grinding forces. It demonstrates once again the highest measured specific normal force for the conventional grinding process at a specific material removal rate of around $Q'_w = 30\,\text{mm}^3\cdot(\text{mm}\cdot\text{s})^{-1}$.

TYROLIT - CS83A60JJ4VK1 80

The second grinding wheel specification within the present series of tests is CS83A60JJ4VK1 with the maximum admitted circumference velocity of 80 $m \cdot s^{-1}$. The total amount of experiments is reduced, since basic data for the behaviour of the novel RPM-Synchronous Grinding process is already available. Nevertheless, the specific material removal rate is increased from one experiment to the next. All other parameters - concerning dressing and grinding - are held constantly to obtain comparable results.

The major process parameters, which are listed in Table 8.2.1, are still valid for all experiments utilizing the second type of TYROLIT grinding wheels for roughing processes.

In comparison to CS85A60JJ4VK1, the specification CS83A60JJ4VK1 varies just in the amount of sintered Al_2O_3 grains. According to the manufacturer, the amount of fused corundum grains is higher in the 83A type, while at the same time the percentage of sintered corundum grains is reduced. Concerning the degree of hardness, both grinding wheel specifications are at the same level (JJ4).

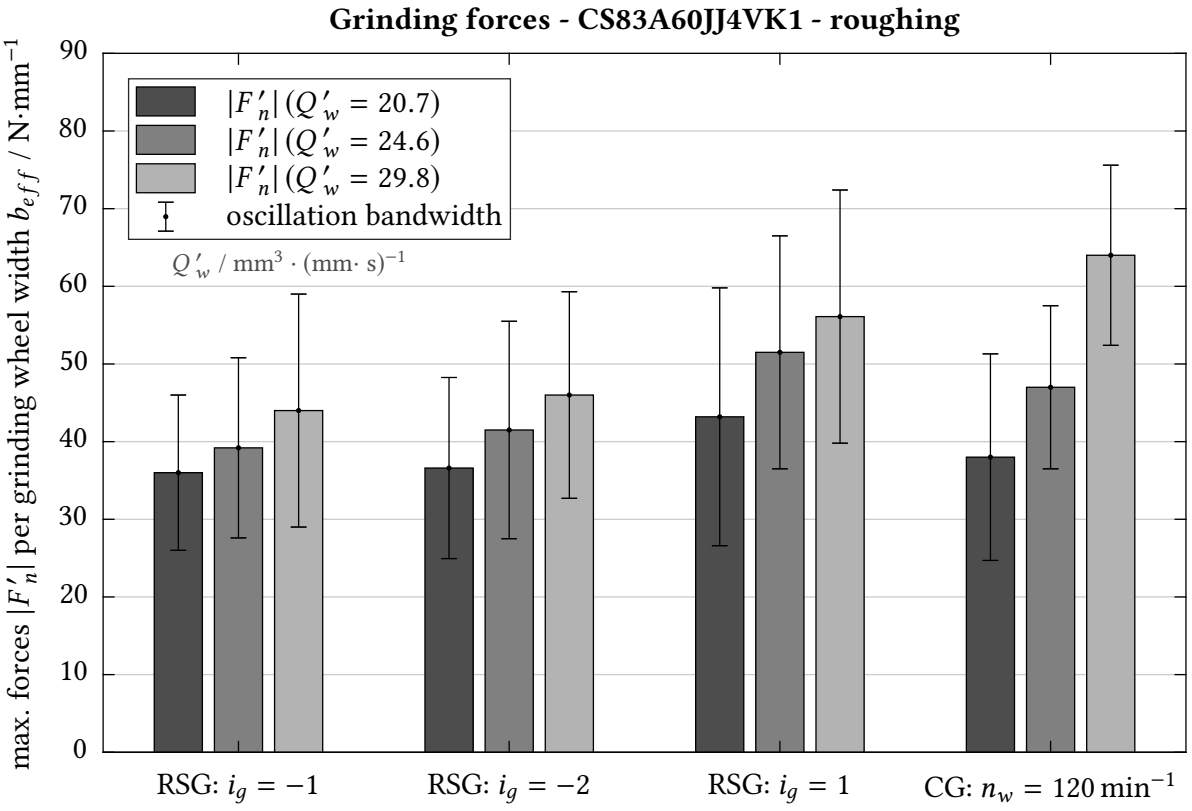

Figure 8.2.9: Grinding forces during RSG and CG - CS83A60JJ4VK1 - roughing, Source: own illustration.

Figure 8.2.9 represents the specific normal forces during grinding in a bar plot again. No

significant difference in force values or oscillation amplitude can be determined. Yet again, the conventional grinding (CG) process shows the highest measured normal force.

In addition, grinding wheel wear is evaluated. Figure 8.2.10 shows the results graphically prepared in a G-ratio / specific material removal rate diagram. Yet again, no significant difference in wheel wear could be registered. Conventional grinding brings up very constant wear. For RPM-Synchonous Grinding in equal and counter direction with a rotational ratio of 1 and −1 the wheel wear increases with rising values for the specific material removal rate Q'_w. A comparison of all grinding wheel wear values of all three roughing specifications is presented in the following subsection.

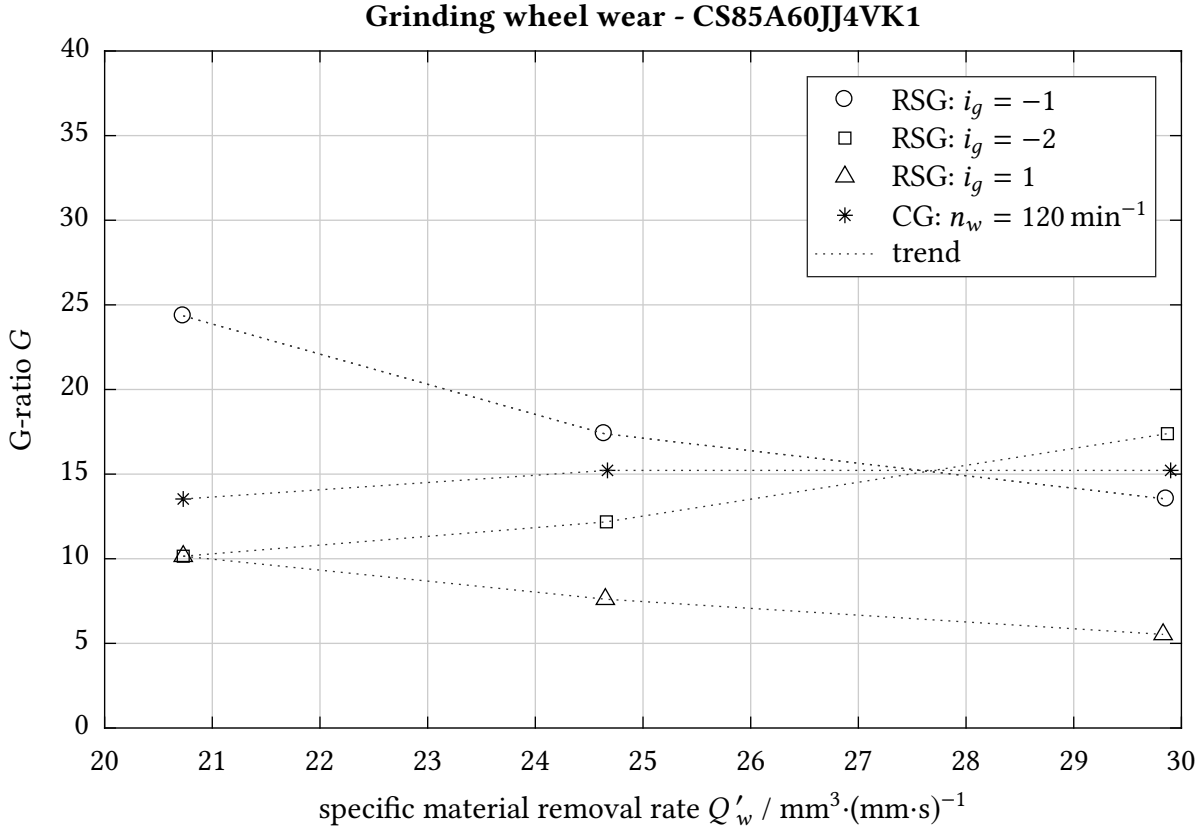

Figure 8.2.10: Grinding wheel wear - CS83A60JJ4VK1,
Source: own illustration.

TYROLIT - CS83A60II5VK1 80

The third grinding wheel specification within the present series of tests is CS83A60II5VK1 with the maximum admitted circumference velocity of 80 $m \cdot s^{-1}$. The total amount of experiments and the focus of test points is equal to the previously performed test-case.

The abrasives specification CS83A60II5VK1 consists of the same grain mixture as the previous type (CS83A60JJ4VK1). The difference is made in hardness of the tools composition. The specification II5 consists of a lower proportion of core-material and less bond-material compared to JJ4. Therefore, it acts softer in the grinding process what means that the effective hardness of the tool's composition is reduced.

The results of grinding with this specification shows completely different behaviour compared to the already performed tests. A huge oscillation can be recognized during some of the experiments. Even though different specific material removal rates were tested, no process window could be found with constant grinding conditions. In some cases, the oscillations enforces enormous grinding wheel wear. G-ratios with values below 1 appeared what states that more material on the grinding wheel was removed than workpiece material. Whole grains got ripped out of the bond matrix.

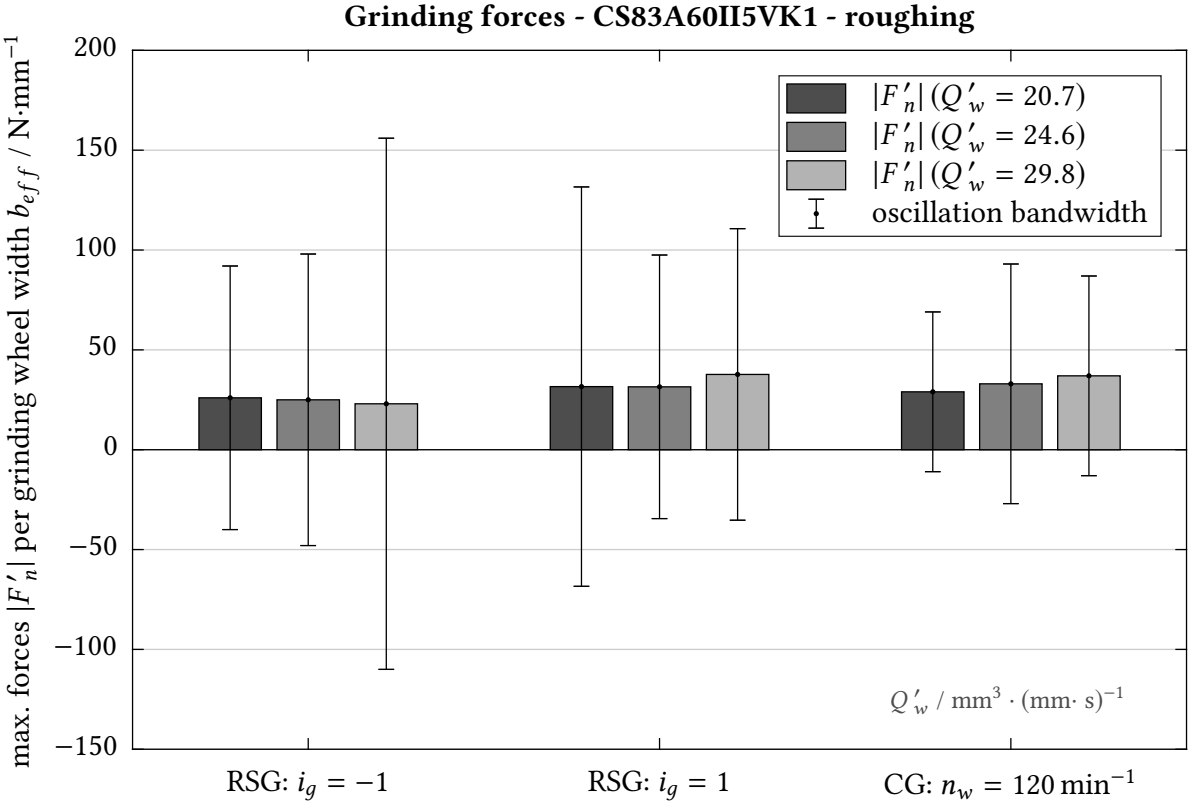

Figure 8.2.11: Grinding forces during RSG and CG - CS83A60II5VK1 - roughing, Source: own illustration.

Some other experiments worked better. The results of those experiments are shown in Figure 8.2.11. The mean normal forces appear to be smaller, but the oscillation amplitudes are significantly higher - in some cases ten times as high.

Even for those picked "well-working" processes, grinding wheel wear is drastically higher compared to the other two grinding wheel specifications. Figure 8.2.12 shows a comparison of all TYROLIT grinding wheels for roughing.

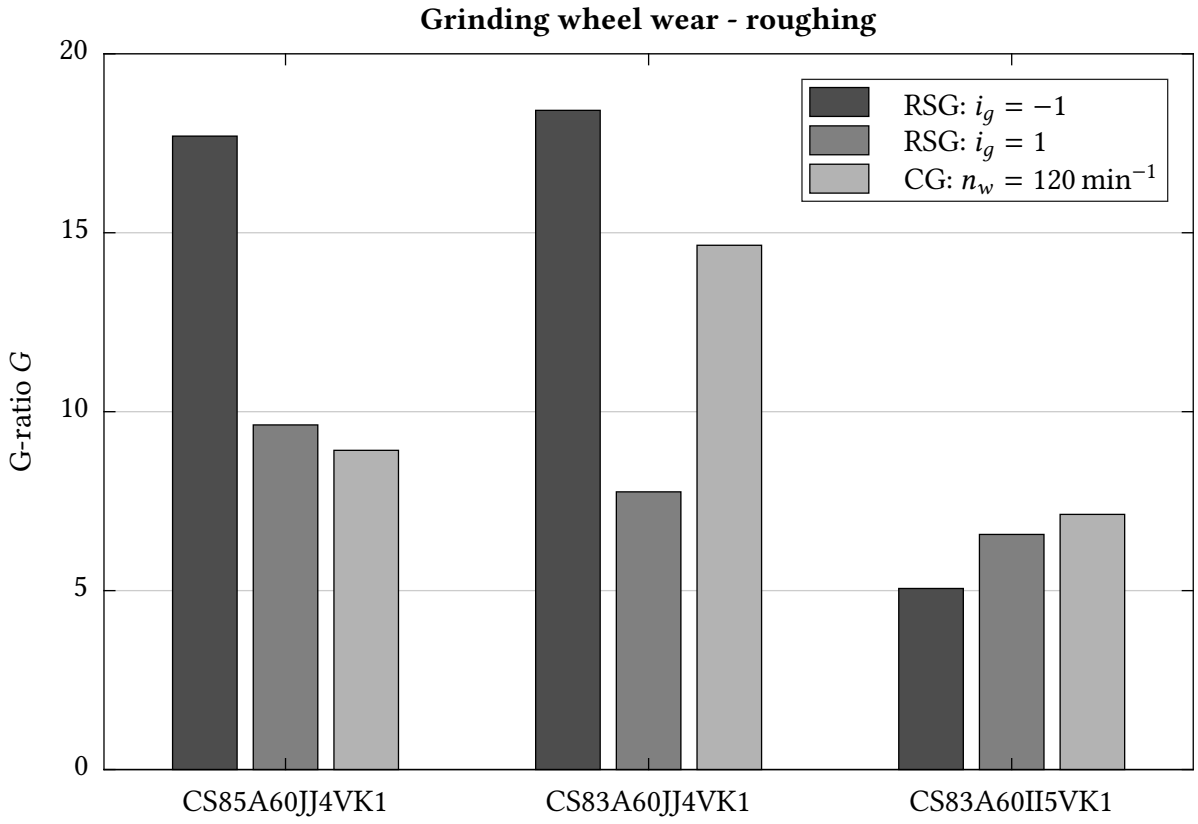

Figure 8.2.12: Comparison of TYROLIT grinding wheels for roughing,
Source: own illustration.

Conclusion for roughing

The three specifications of the TYROLIT grinding wheels show various results. Type CS85A60-JJ4VK1 and CS83A60JJ4VK1 are both recommendable for roughing in a RPM-Synchronous Grinding process. The results were equally good or even better in comparison to conventional grinding processes. Therefore, this novel grinding approach has proven its entitlement in case of roughing. Moreover, there is no significant influence in the grain mixture ascertainable. The TYROLIT grain mixture types 85A and 83A work equally well.

The type CS83A60II5VK1 does not seem to be the right choice for RPM-Synchronous rough

grinding operations. An enormous noise level due to oscillations appear during the process what could be documented by force measurements. No reliable and constant process-parameter window could be found. The core- and bond-material density is too low and the resulting grinding wheel composition too soft for RPM-Synchronous Grinding.

Especially for machining of non-circular workpieces, roughing plays an important role in the overall process efficiency. In most cases, cylindrical blanks are used, from which non-circular shapes are crafted. Therefore, the amount of material which has to be removed is significantly higher compared to standard circular grinding processes. Within the presented experiments, tools could be found which offer appealing specific material removal rates. That fact confirms their operational capability at RPM-Synchronous Grinding and certify the entitlement of this process concerning rough machining in general.

8.2.2 Tools for Fine Machining - Finishing

Following the previous subsection, the chosen tool specifications for the fine machining precess together with the major process parameters are listed in Table 8.2.2. Subsequently, all results for each grinding wheel are discussed.

Table 8.2.2: Grinding wheel test - process parameters.

Parameter	Value
grinding machine	GST Research Grinding Machine @ IFT
grinding wheel specification	TYROLIT - CS85A220II4VK1 80 TYROLIT - CS55A220II5VK1 80
grinding wheel dimensions	610 x 30 x 304.8 mm, Form 1
workpiece diameter	∅ 39.8 - ∅ 37 mm
workpiece material	42 Cr Mo 4
dressing direction	counter direction
dressing overlap Z-direction	$u_d = 8 \dots 78$
velocity ratio dressing	$q_d = -0.70$
dressing infeed	$a_p = 0.005$ mm
specific material removal rate	$Q'_w = 0.1 \dots 0.9$ mm$^3 \cdot$ (mm$\cdot$ s)$^{-1}$
grinding direction	counter & equal direction
cutting velocity	$v_c = 50$ m$\cdot$s^{-1}
rotational ratio	$i_g = 1, -1$, non-synchronized
cooling pressure	$p_c = 8$ bar

The main focus of all finishing experiments is laid on the evaluation of accessible workpiece surface qualities. Previous experiments reveal that the dressing overlap has major influence in the resulting surface after grinding. Being able to achieve high quality levels with the process of RPM-Synchronous Grinding is of prime importance in order to offer an alternative for conventional grinding.

Surface qualities are measured tactile and optical. For the majority of grinding probes as output from extensive grinding experiments, a JENOPTIK HOMMEL-ETAMIC W20 skidless probe is used. The traverse length lt is chosen 4.8 mm and $lc = 0.8$ mm. For cut-off, a ratio of $lc/ls = 30$ is chosen according to ISO 16610-21.

TYROLIT - CS85A220II4VK1 80

The first grinding wheel specification for finishing in the presented series of tests is the TYROLIT product CS85A220II4VK1 with a maximum admitted circumference velocity of 80 m$\cdot$s^{-1}. Analogously to the roughing experiments, the specific material removal rate is increased from one experiment to the next, but on a lower scale. The smallest Q'_w is chosen 0.1 mm$^3\cdot$(mm$\cdot$s)$^{-1}$ and the maximum 0.9 mm$^3\cdot$(mm$\cdot$s)$^{-1}$. Such values are standard for finishing using grinding

tools. All other parameters - concerning dressing and grinding - are yet again held constant to obtain comparable results.

Figure 8.2.13 presents the evaluation of the grinding forces of three experiments during RPM-Synchronous counter direction grinding. For this experiments, a dressing overlap of $u_d = 26$ is employed.

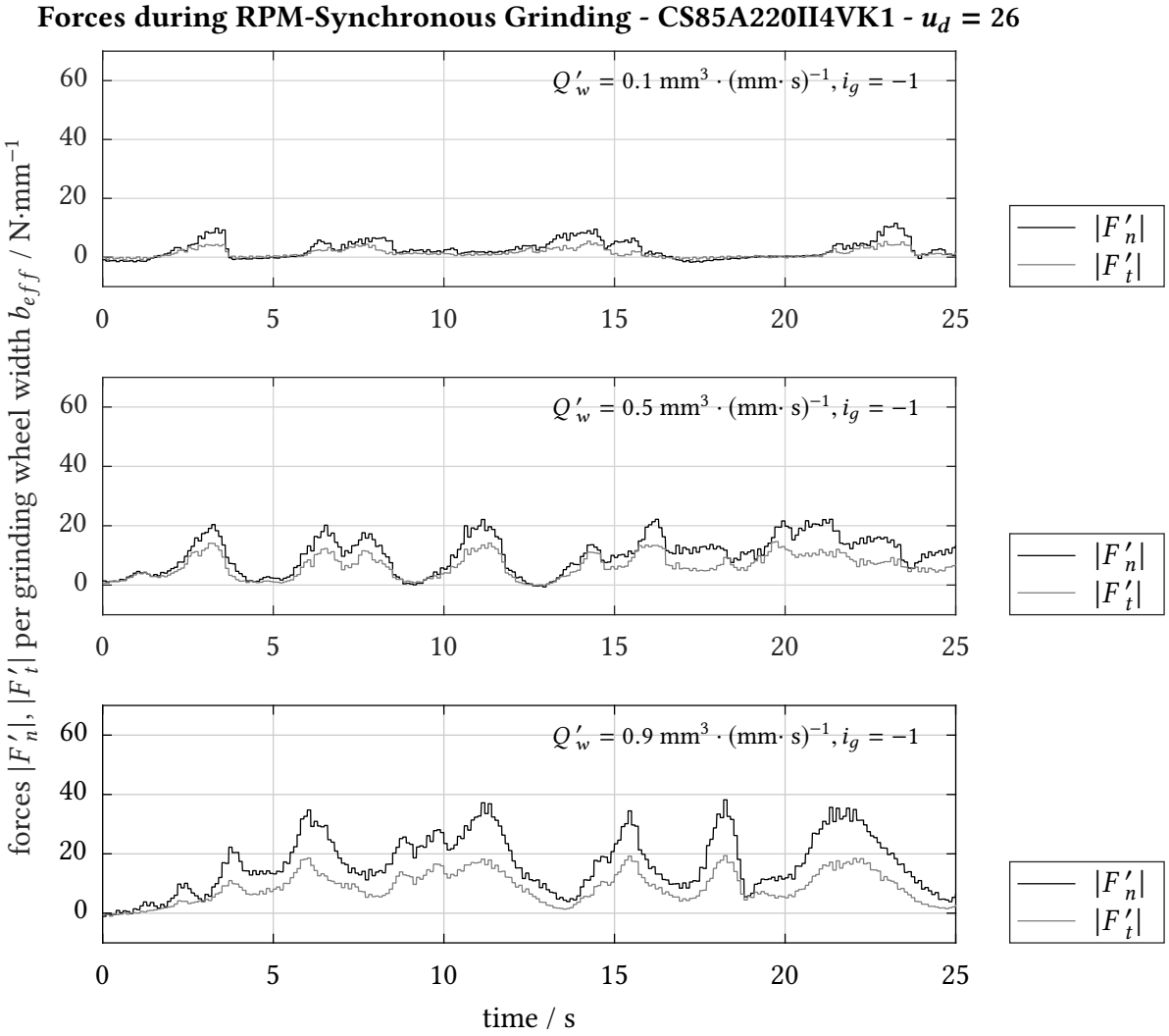

Figure 8.2.13: Forces during RSG - finishing ($u_d = 26$) - $i_g = -1$,
Source: own illustration.

This figure exemplarily demonstrated that constant grinding forces during RPM-Synchronous finishing are not existing. The process is characterized by oscillations which vary depending on the radial grinding infeed and therefore the specific material removal rate.

The top graph in Figure 8.2.13 shows almost no forces in tangential or normal direction during long time periods throughout the process, even after filtering all other process-related disturbances. The graph represents the process with smallest specific material removal rates

of $Q'_w = 0.1\,\mathrm{mm^3 \cdot (mm \cdot s)^{-1}}$. The major disorders are: forces due to rotational rates at the unbalanced workpiece, forces evoked by the cooling lubricant pressure in the contact zone of grinding wheel and workpiece, etc.

The bottom graph in Figure 8.2.13 shows forces in tangential or normal direction during the process even after filtering all mentioned process-related disturbances. It can be seen that the progression of the process is very inconsistent. A low frequent oscillation appears during finishing at a $Q'_w$of $0.9\,\mathrm{mm^3 \cdot (mm \cdot s)^{-1}}$.

The graph in the center of Figure 8.2.13 represents force measurement results of grinding with a specific material removal rates of $Q'_w = 0.5\,\mathrm{mm^3 \cdot (mm \cdot s)^{-1}}$. The whole figure sums up three different sets of process parameters Q'_w which are investigated further on concerning surface roughness qualities.

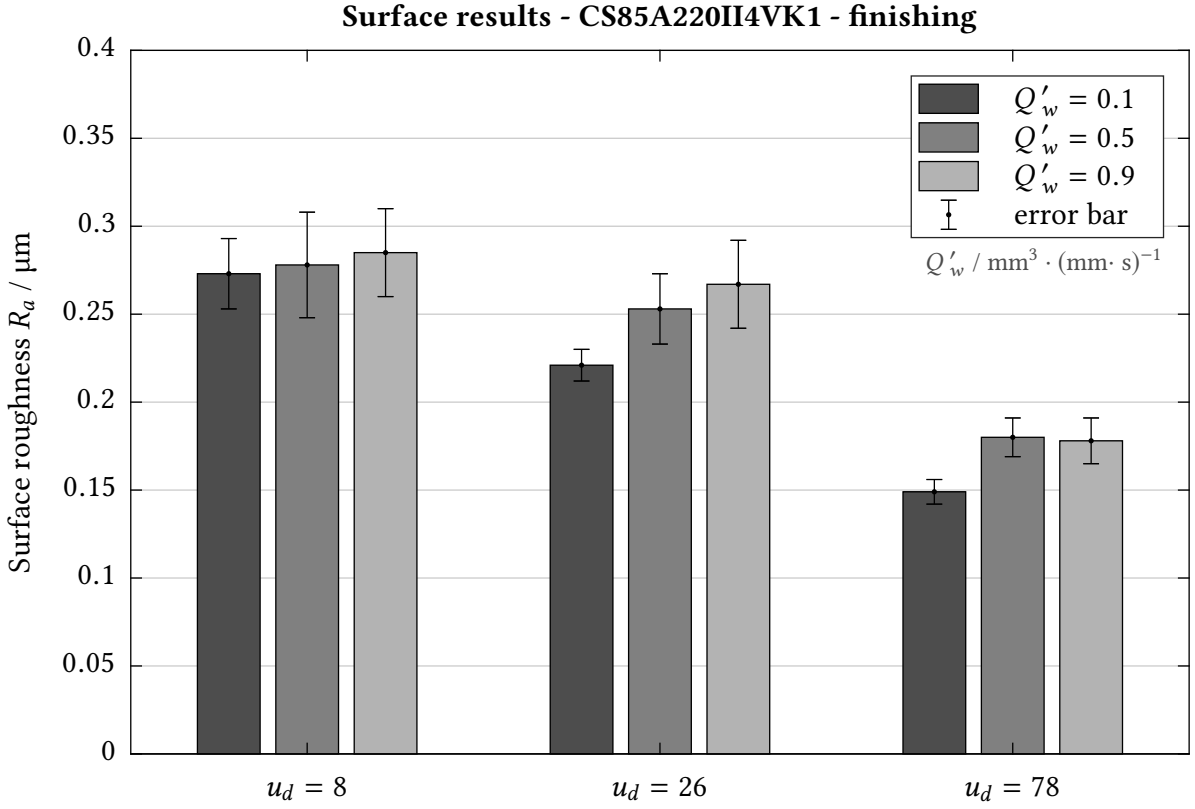

Figure 8.2.14: Surface roughness qualities at RSG with differing dressing overlaps, Source: own illustration.

Figure 8.2.14 represents a bar-plot of grinding results regarding the roughness of workpieces probes after finishing. Three different dressing overlaps were chosen since this parameter is known to have major influence in resulting surface properties. A dressing overlap of $u_d = 8$ is described in literature as a standard value for finishing. To get an comparison, the dressing overlap is in further consequence increased to $u_d = 26$ and $u_d = 78$.

The set of experiments imposingly confirm the assumption that the dressing overlap actually has major influence in the resulting surface roughness qualities of synchronously grinded workpieces. This effect has even more impact than the specific material removal rated during grinding. This information is well illustrated in Figure 8.2.14. The values for the arithmetical mean deviation R_a (according to EN ISO 4287) in case of a dressing overlap of $u_d = 8$ are quite constant for all tested material removal rates but vary by repeated measurement on a single probe - what is illustrated by the error bar in the plot. For a dressing overlap of $u_d = 26$ surface roughness qualities appear to be smoother by evaluating the R_a, especially for the lowest material removal rate. Once u_d is raised to a value of 78, surface roughness is significantly lower. Values around $R_a = 0.2\,\mu m$ are reached constantly.

TYROLIT - CS55A220II5VK1 80

The second grinding wheel specification within the present series of tests is CS55A220II5VK1 with the maximum admitted circumference velocity of $80\,m{\cdot}s^{-1}$. The total amount of experiments is reduced since basic data for the behaviour of the novel RPM-Synchronous finishing is available. Again, all other parameters - concerning dressing and grinding - are held constant.

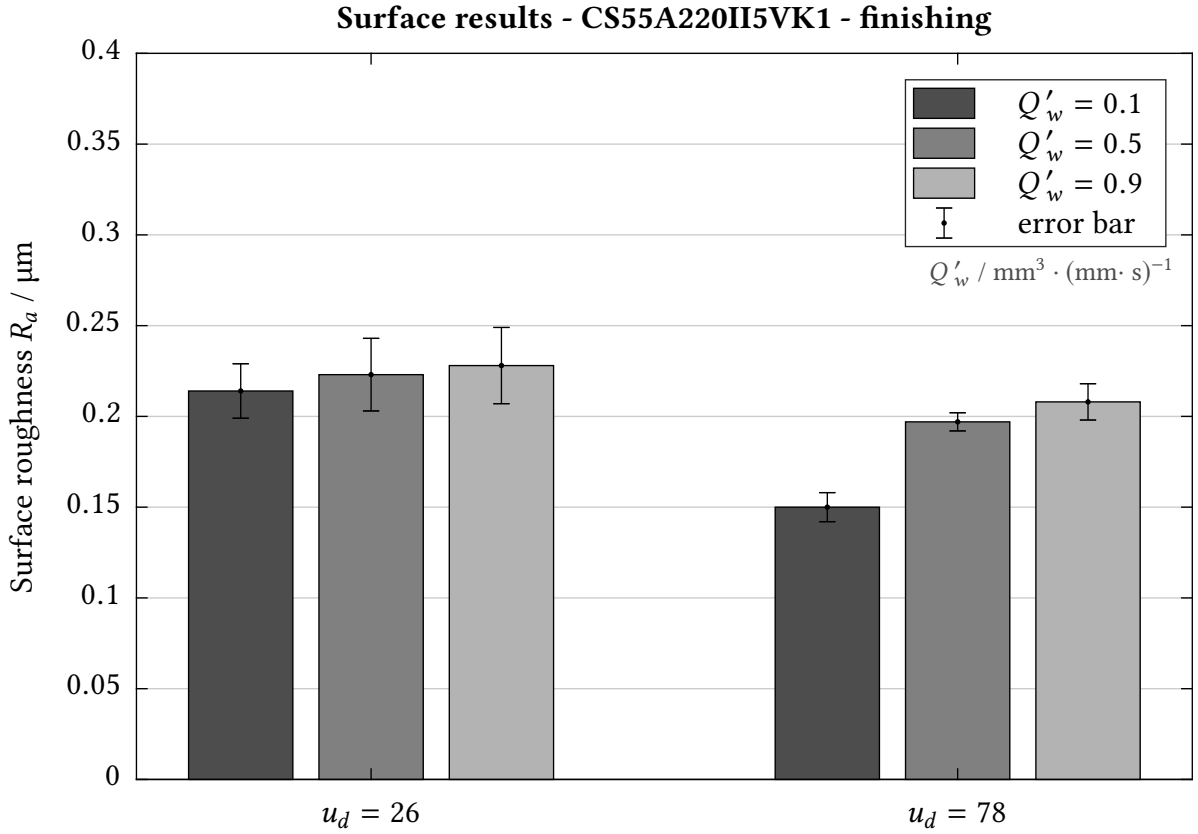

Figure 8.2.15: Surface roughness qualities after grinding with differing dressing overlaps, Source: own illustration.

The major process parameters which are listed in Table 8.2.2 are still valid for all experiments utilizing the second type of TYROLIT grinding wheels for roughing processes.

Figure 8.2.15 represents the results of the performed test for RPM-Synchronous finishing. The specific material removal rate is varied between $Q'_w = 0.1$ and $0.9\,\mathrm{mm^3 \cdot (mm \cdot s)^{-1}}$. The dressing overlap is chosen $u_d = 26$ and $u_d = 78$.

Analogously to the previous results, grinding wheel CS55A220II5VK1 produces the better surface rougness results, the higher the dressing overlap is employed. Again, the variance in measurement results using the JENOPTIK HOMMEL-ETAMIC W20 skidless probe on a single workpiece is smaller for higher dressing overlaps. Therefore, the surface seems to be not only smoother but also more consistent in its properties at higher values of the dressing parameter u_d.

Conclusion for finishing

Figure 8.2.16 illustrates a conclusion of RPM-Synchronous finishing processes with these two different TYROLIT grinding wheel specifications.

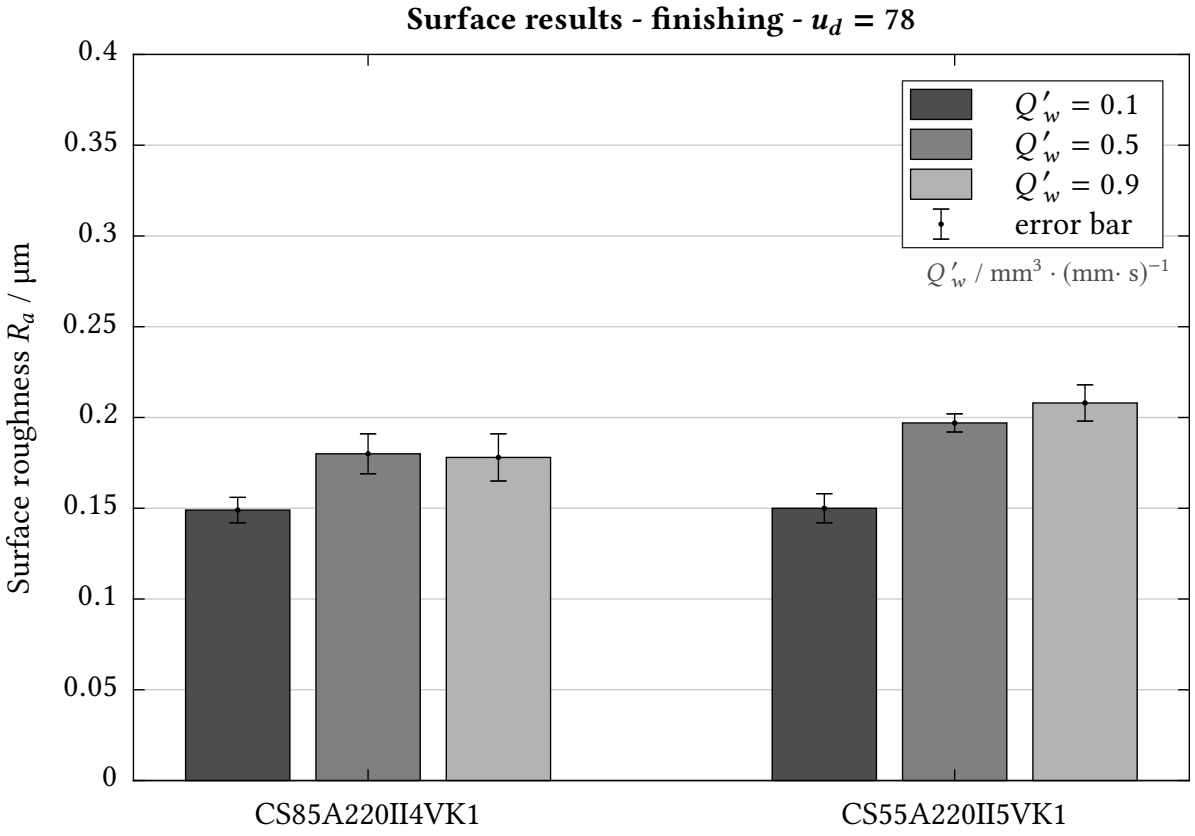

Figure 8.2.16: Surface roughness qualities - conclusion,
Source: own illustration.

Both grinding wheels show a good performance. Surface roughness qualities of the grinded workpieces are almost equal by employing same parameters for dressing and grinding.

It is obvious that the dressing overlap has major influence in the resulting surface roughness. Highest values are necessary for obtaining appealing results, what stays in big contrast to conventional grinding processes. Moreover, high dressing overlaps are needed for gaining consistent surface qualities around the circumference of the workpiece. At lower values - like values for conventional grinding finishing at $u_d = 8$ - regions of lower and higher surface roughness alternatingly occur.

A very interesting condition is documented in Figure 8.2.17. For the presented series of tests, after the plunge grinding process an oscillation in Z-direction is applied. Before the spark-out phase, the grinding wheel is moved 0.3 mm in Z+ direction, back, and in Z- direction with a feed rate of $v_{fa} = 1\,\mathrm{mm{\cdot}min^{-1}}$. At same dressing and grinding parameters, the surface roughness qualities can be reduced from $R_a = 0.150\,\mu\mathrm{m}$ at standard plunge grinding to $R_a = 0.066\,\mu\mathrm{m}$ at plunge grinding with oscillation.

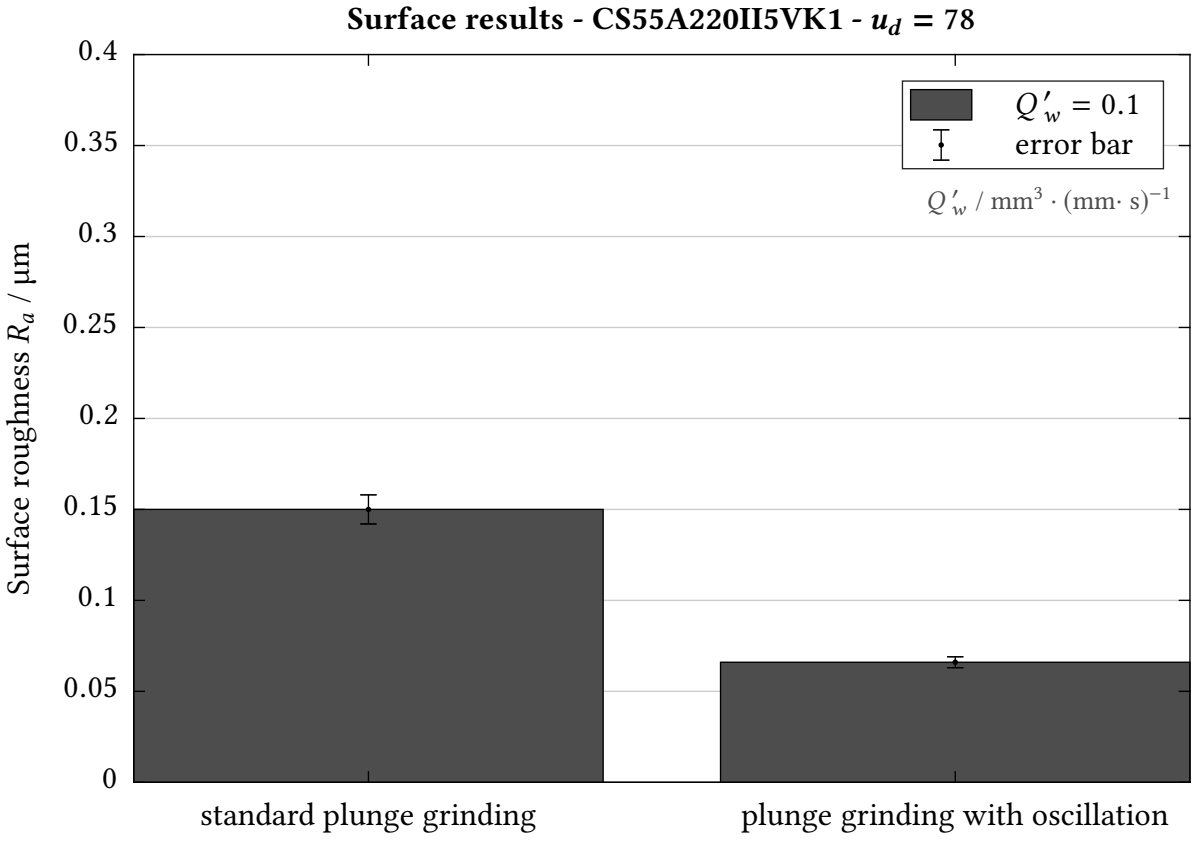

Figure 8.2.17: Surface roughness qualities - conclusion,
Source: own illustration.

Altogether, the RPM-Synchronous Grinding process in case of finishing is able to cope with

the demands on grinded surface qualities. Both tested grinding wheels - the CS55A220II5VK1 and the CS85A220II4VK1 - work well for finishing. The difference in structure (number 4 and number 5) is too minor to bring up major differences at finishing. The 85A mixture of sintered and fused corundum grains appears to have slight advantages at higher specific material removal rates in terms of resulting surface roughness qualities compared to pure fused corundum grains in the 55A specification.

8.3 Optical Surface Measurement

In this section, results of optical 3D surface measurements are presented. The figures emphasize the difference in surface texture resulting from conventional plunge grinding and from RPM-Synchronous Grinding. The following tables (8.3.1 & 8.3.2) represent the process parameters of the CG-process and the RSG-process. The two presented probes (VIII.: CG & XII.: RSG) exhibit very similar arithmetical mean deviations R_a (VIII.: $R_a = 0.142\,\mu m$ & XII.: $R_a = 0.148\,\mu m$) measured by the JENOPTIK HOMMEL-ETAMIC W20 skidless probe.

Table 8.3.1: Process parameters - CG.

Parameter	Value
grinding machine	GST Research Grinding Machine @ IFT
grinding wheel specification	TYROLIT - CS85A220II4VK1 80
grinding wheel dimensions	610 x 30 x 304.8 mm, Form 1
workpiece diameter / material	∅ 39.8 mm / 42 Cr Mo 4 / (probe: VIII.)
dressing direction	counter direction
dressing overlap Z-direction	$u_d = 8$
velocity ratio dressing	$q_d = -0.70$
dressing infeed	$a_p = 0.005$ mm
specific material removal rate	$Q'_w = 0.5\,\mathrm{mm}^3 \cdot (\mathrm{mm} \cdot \mathrm{s})^{-1}$
grinding direction	counter direction
cutting velocity	$v_c = 50\ \mathrm{m \cdot s}^{-1}$
rotational ratio	i_g: non-synchronized ($n_w = 120$ rpm)
cooling pressure	$p_c = 8$ bar

Table 8.3.2: Process parameters - RSG.

Parameter	Value
grinding machine	GST Research Grinding Machine @ IFT
grinding wheel specification	TYROLIT - CS55A220II5VK1 80
grinding wheel dimensions	610 x 30 x 304.8 mm, Form 1
workpiece diameter / material	∅ 39.8 mm / 42 Cr Mo 4 / (probe: XII.)
dressing direction	counter direction
dressing overlap Z-direction	$u_d = 78$
velocity ratio dressing	$q_d = -0.70$
dressing infeed	$a_p = 0.005$ mm
specific material removal rate	$Q'_w = 0.1\,\mathrm{mm}^3 \cdot (\mathrm{mm} \cdot \mathrm{s})^{-1}$
grinding direction	counter direction
cutting velocity	$v_c = 50\ \mathrm{m \cdot s}^{-1}$
rotational ratio	i_g: -1
cooling pressure	$p_c = 8$ bar

Confocal Method

The following measurements were performed with the 3-dimensional optical surface metrology system LEICA DCM8. This device offers high lateral resolution applying confocal microscopy. [142]

Figure 8.3.1 shows a representative result of a conventional grinding process. The texture of the surface is typical for plunge grinding: In X-direction, which corresponds to the peripheral direction of the grinded cylinder, straight scratches of similar depth are identifiable. In Z-direction, which refers to the axial-direction of the grinded cylinder, a much more rippled structure occurs.

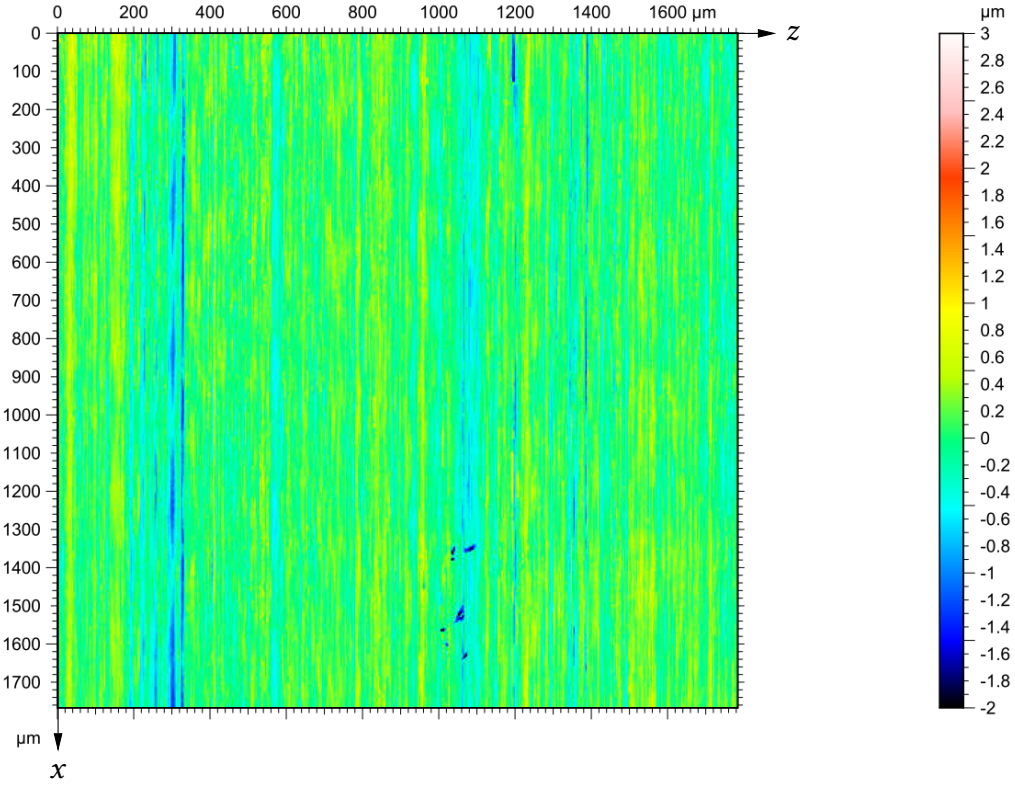

Figure 8.3.1: Surface texture after CG, LEICA DCM8,
Source: own illustration.

This surface structure can be interpreted as follows: Single grains on the grinding move on a slightly larger flight circle (radius) than others. Since the grinding wheel RPM are much higher than the workpiece RPM at CG, such protruding grains evoke material removal all around the circumference of the workpiece. During spark-out those grains are the last ones which have contact to the workpiece. Therefore, they are responsible for the finished surface roughness. A

[142] cf. LEICA Microsystems AG, 2017/10/8, p.2.

typical structure with straight scratches in X-direction occurs. The higher the dressing overlap u_d is chosen, the more equal the flight circles of every single grain are and the smoother the resulting surface on the workpiece gets.

Figure 8.3.2 shows a representative result of a single plunge grinding step utilizing a RPM-Synchronous Grinding process. In X-direction, which again corresponds to the peripheral direction of the grinded cylinder, scratches are identifiable. They are much shorter compared to CG and not primarily evident for the occurring structure. There appear plateaus of varying heights.

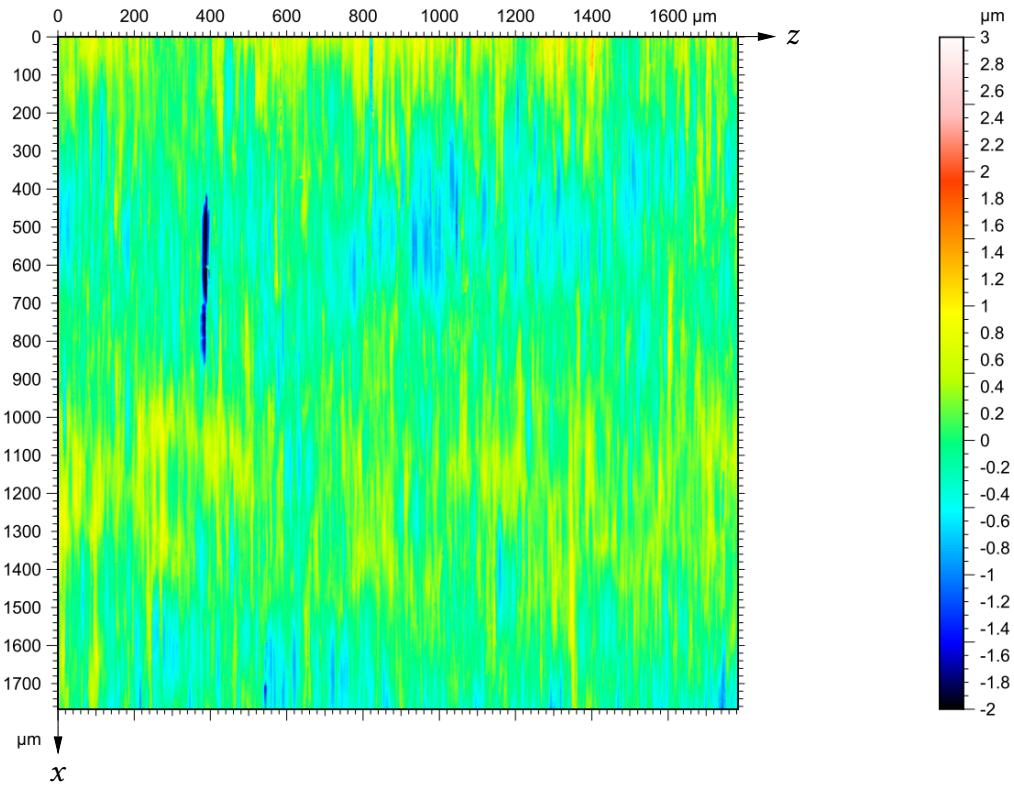

Figure 8.3.2: Surface texture after RSG, LEICA DCM8,
Source: own illustration.

Again, single grains on the grinding move on a slightly larger flight circle (radius) than others. In contrast to CG, grinding wheel RPM and workpiece RPM are synchronized at RSG. In the specific example both rotational rates are the same ($i_g = -1$). Therefore, single grains exclusively machine the same point on the workpiece. This mechanism results in a structure which is even more depending on the dressing overlap. Confirming the observations made in section 8.2.2, extraordinary high values for u_d are necessary in order to machine surfaces of low roughness values. The higher the overlap is chosen, the more equal the flight circles of all grains are. Furthermore, less difference in height of the plateaus on the workpiece surface

emerge from the RPM-Synchronous Grinding process.

The standard ISO 25178 describes the properties surface roughness on workpieces. The value S_a (arithmetical mean height) is the extension of the arithmetical mean deviation R_a (evaluation of a line) to a surface.

Values for the arithmetical mean height S_a are:

- probe VIII., CG: S_a = 0.201 µm (R_a = 0.142 µm in X-direction)
- probe XII., RSG: S_a = 0.241 µm (R_a = 0.148 µm in X-direction)

This differences occur mainly due to the different kinematics of those processes. The rotational rates of the workpiece are much higher utilising RSG compared to CG. Therefore, the contact length of a single grain is much shorter at RPM-Synchronous Grinding what leads to different resulting surface topologies.

Nevertheless, Figure 8.3.2 proves that surfaces can be micro-structured using the process of RPM-Synchronous Grinding. The key for deliberate surface design lies in the appropriate dressing strategy. The properties of such surface structures and the deliberate generation of functional surfaces by means of RSG constitute a future field of research.

8.4 Adaptive Control for RPM-Synchronous Grinding

The low-frequent oscillation, especially during the finishing step of the RPM-Synchronous Grinding process, has negative influence on the grinding results and on the amount of grinding wheel wear. As documented in subsection 8.2.2, higher oscillation amplitudes during finishing generate higher values of arithmetical mean deviation R_a. The cutting surface of the grinding wheel is conditioned by the dressing process and mainly determined by the parameter u_d, the dressing overlap. In case of strong oscillation during the grinding stage this well prepared surface gets damaged at random. In order to avoid this fact, control concepts are developed which aim to minimize these oscillations. As a result, the cutting surface of the grinding wheel should not be harmed any more. In further consequence, the resulting surface on the workpiece is improved.

In this section two individual control algorithms are presented. Both use data which is acquired from the same piezoelectric three-component force sensor located at the tailstock-side of the grinding machine which was described earlier. Figure 8.4.1 illustrates the process chain for the adaptive RPM-Synchronous Grinding process.

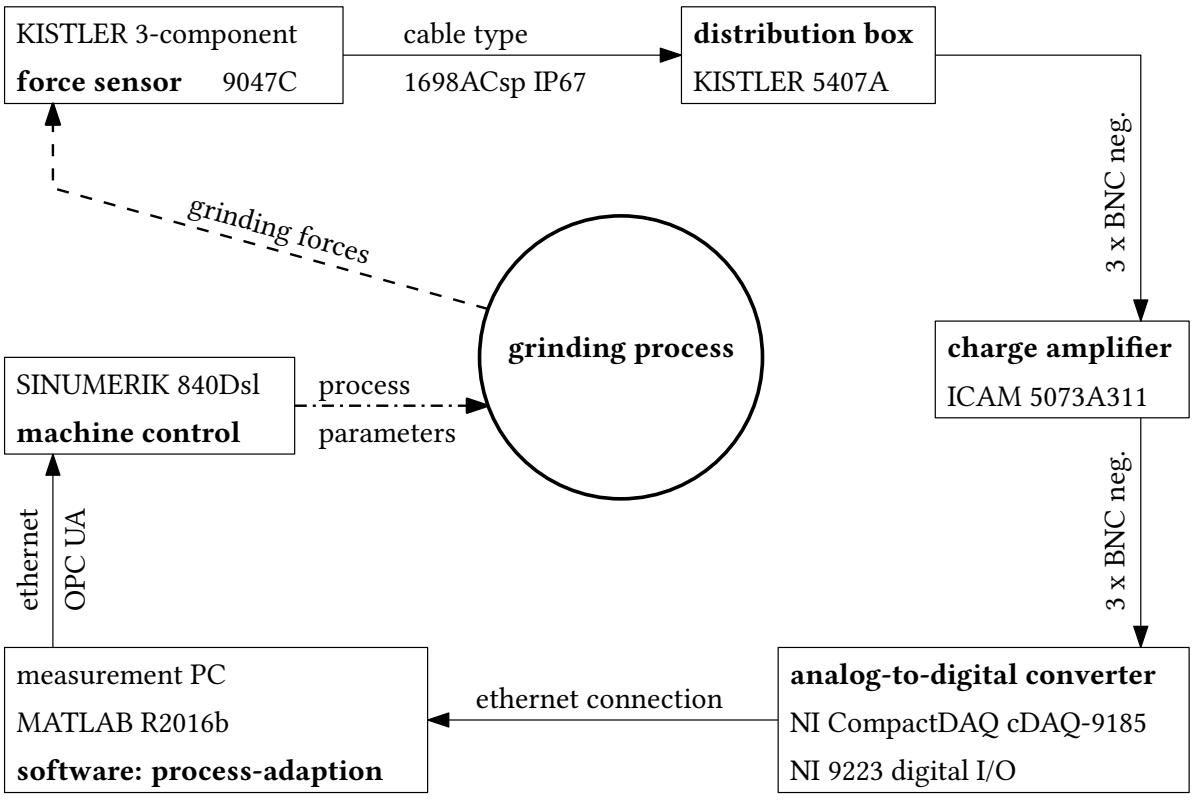

Figure 8.4.1: Process chain for adaptive control,
Source: own illustration.

The major process parameters applied for the development of control concepts concerning the adaptive RPM-Synchronous Grinding process are listed in Table 8.4.1.

Table 8.4.1: Grinding process parameters for control concept development.

Parameter	**Value**
grinding machine	GST Research Grinding Machine @ IFT
grinding wheel specification	THELEICO - 85C220-0O4B9240 50
grinding wheel dimensions	600 x 60 x 304.8 mm, Form 1
workpiece diameter	∅ 39.8 mm - ∅ 39 mm
workpiece material	42 Cr Mo 4
dressing direction	counter direction
dressing overlap Z-direction	$u_d = 90$
velocity ratio dressing	$q_d = -0.5$
dressing infeed	$a_p = 0.001 \ldots 0.010$ mm
grinding feed rate roughing	$v_{fr} = 0.100$ mm·min^{-1} (100%)
grinding feed rate finishing	$v_{fr} = 0.050$ mm·min^{-1} (100 %)
grinding direction	counter & equal direction
cutting velocity	$v_c = 50$ m·s^{-1}
rotational ratio	$i_g = 1, -1$
cooling pressure	$p_c = 8$ bar

For each grinding experiment, same conditions are created. While dressing, the overlap in Z-direction is held constant at a value of $u_d = 90$. This value is much higher than standard overlaps for roughing and finishing in conventional grinding processes. The results in subsection 8.2.2 demonstrate that technical relevant surface roughness is attainable only by high dressing overlap values. The dressing infeed is chosen $a_p = 0.050$ mm and a velocity ratio at dressing is selected $q_d = -0.5$. The radial feed rate while grinding is chosen $v_{fr} = 0.100$ mm·min^{-1} what is equivalent to a specific material removal rate of $Q'_w = 0.2$ mm^3·(mm·s)$^{-1}$ for medium finishing speeds. The radial feed rate for low finishing speed is chosen $v_{fr} = 0.050$ mm·min^{-1} what is equivalent to a specific material removal rate of $Q'_w = 0.1$ mm^3·(mm·s)$^{-1}$. The presented experiments are performed in counter and equal grinding direction.

Control concepts for low and medium finishing feed rates

To improve the special RPM-Synchronous Grinding process, two different control strategies are developed. Both use the same measured data as input for the algorithm. The piezoelectric three-component force sensor, which is installed at the tailstock-side inside of the grinding machine, acquires information about the process at any time. A National Instruments CompactDAQ chassis handles the data of the occurring oscillations during the RPM-Synchronous Grinding process and transfers them to an external PC. There, a customized MATLAB-software

realizes a controller which manipulates the radial feed rate corresponding to a mathematical model. The controller adapts the feed rate override at the software potentiometer of the numerical machine controller between 5% and 200%. The override corresponds to the parameter R1, which is transmitted to the grinding machine as a regulating variable.

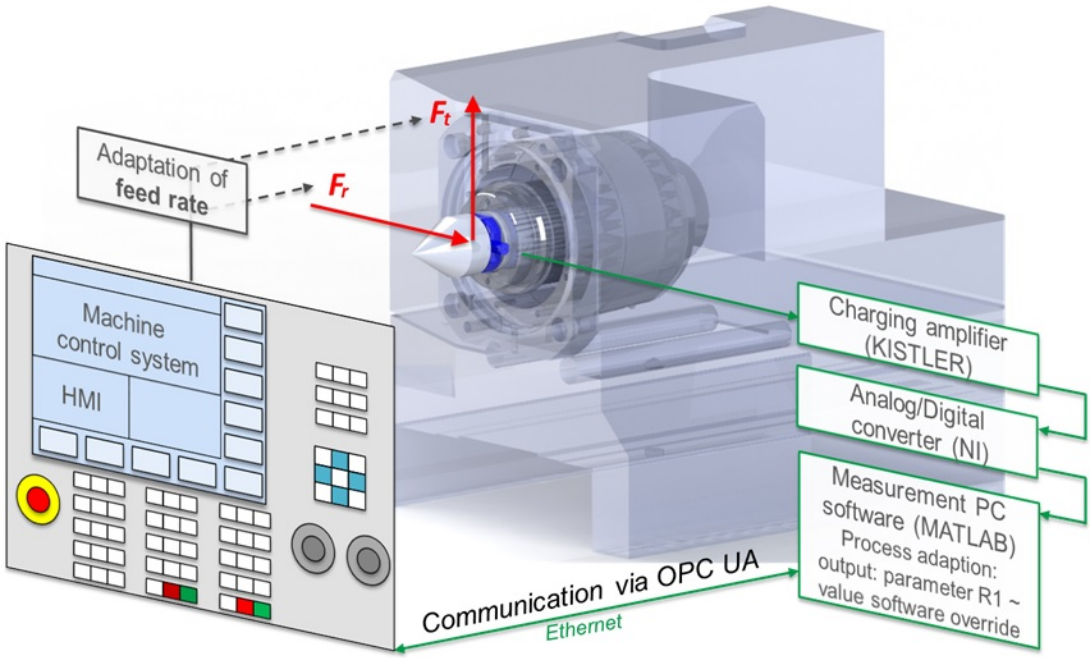

Figure 8.4.2: Schematic representation of the control loop,
Source: own illustration.

The communication is realized via OPC UA (according to chapter 6.6.2). The Siemens SINUMERIK control system at the grinding machine acts as a server, while the software on the measuring computer works as a client. Figure 8.4.2 shows a graphical representation of the control loop.

Due to the synchronous movement and high rotational rates for RPM-Synchronous Grinding processes, the clamping and therefore the process stability are critical conditions. Mechanical oscillation occurs caused by the periodical excitation of the grinding wheel and the workpiece. The piezoelectric sensor measures the oscillation. The control algorithm works to minimize the amplitude of the occurring peaks. These peaks are significantly higher than the basic oscillation and appear periodically.

Figure 8.4.3 displays the behaviour of these oscillations and peaks. They appear at any point and decrease again after just some seconds. Several seconds later a new peak appears with approximately the same amplitude as all other appearing peak. This behaviour can not only

be seen in such plots but is also audible for the machine operator during the grinding process.

The major effect of the oscillating behaviour during the process is a wrecking and shattering of the grinding wheel structure in case the grinding wheel composition in combination with the processed material appear rather soft. This property is valid for the THELEICO - 85C220-0O4B9240 50 tool. That leads to both, a higher surface roughness on the workpiece and a geometrical deviation.

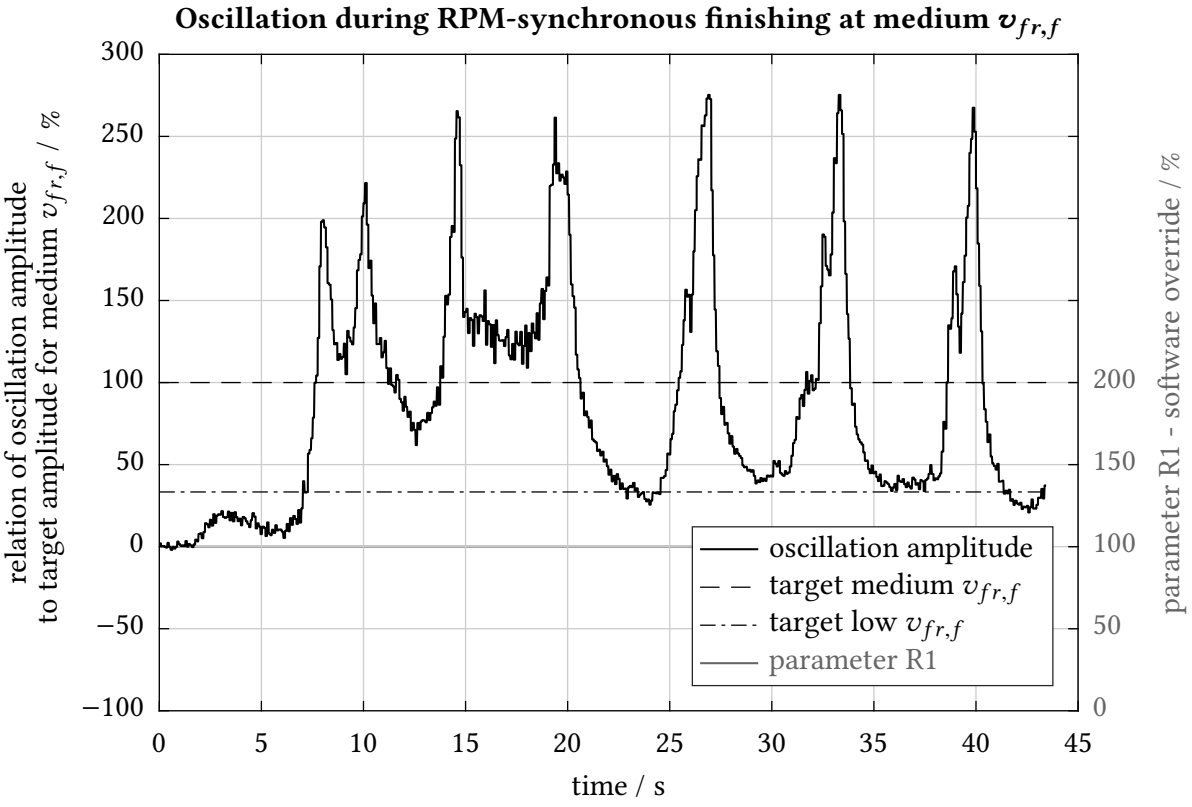

Figure 8.4.3: Oscillation amplitude at roughing (constant radial feed rate), Source: own illustration.

With the control concept for medium finishing feed rates (medium $v_{fr,f}$), the software override of the machine is manipulated between 5 % and 200 % by adjusting the parameter R1 on the machine.

With a controlled RPM-Synchronous Grinding process, the peaks of oscillation can be reduced by altering the feed rate velocity. A target amplitude for medium finishing feed rate is set as a control target (100 % at the left ordinate). As Figure 8.4.4 shows, the peaks are reduced slightly compared to the uncontrolled process with same parameters. In fact, the controller alters the software override just slightly above and underneath 100 % depending on the actual oscillation amplitude. This tuning of the controller brings up quite passive parameters and

therefore sluggish behaviour which works best over all test-cases utilizing medium basic feed rate.

Even the minor reduction of the oscillation amplitude has major effects. A wrecking of the grinding wheel composition is prevented and therefore wear is reduced. The roughness quality of the workpiece surface is improved simultaneously.

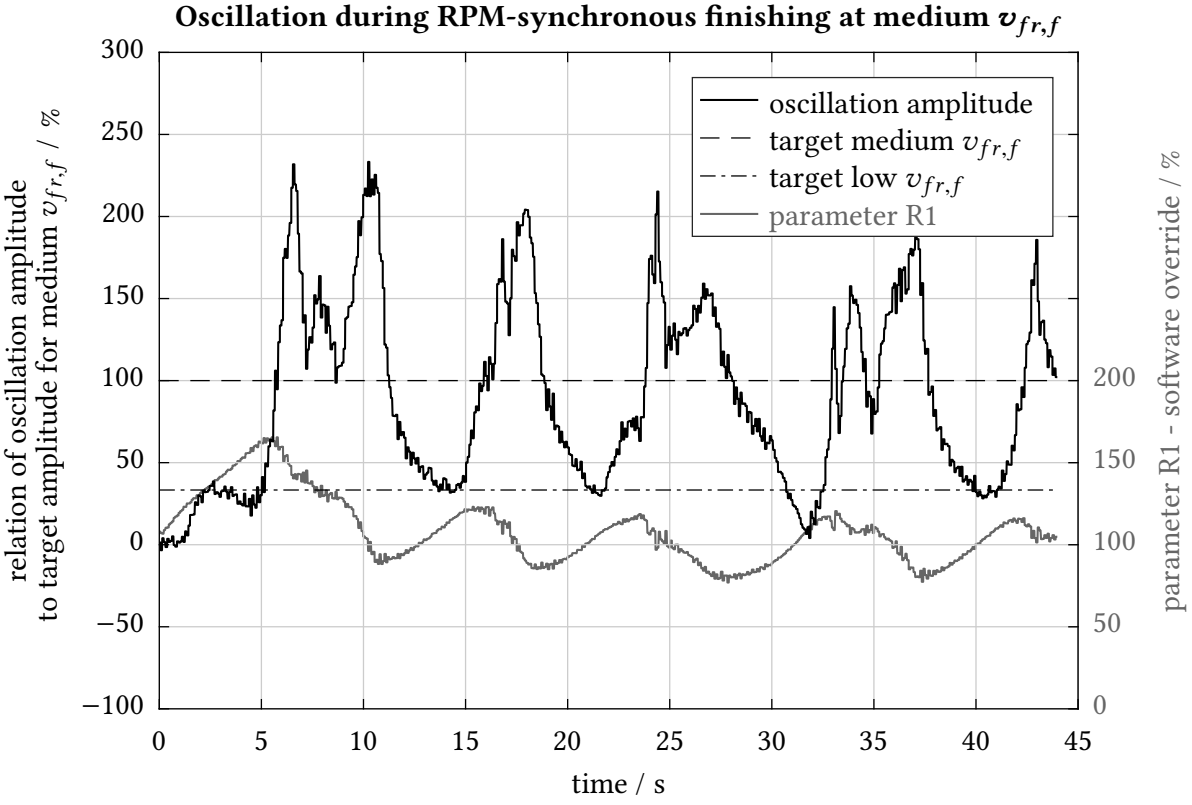

Figure 8.4.4: Oscillation amplitude at medium finishing feed rate with control strategy, Source: own illustration.

The resulting surface roughness qualities for RPM-Synchronous finishing with medium feed rates can be improved by approximately 10% concerning the arithmetical mean deviation R_a. In best cases, surface qualities of $R_a = 0.28\,\mu m$ can be documented on the workpiece surface.

This value is not sufficient enough to meet the high demands on general grinding processes. On basis of the results of the Design of Experiments study, the radial feed rate during the grinding process has major influence on the resulting surface roughness. On this basis, the feed rate for finishing is reduced to $v_{fr} = 0.050\,mm{\cdot}min^{-1}$ what is equivalent to a specific material removal rate of $Q'_w = 0.1\,mm^3{\cdot}(mm{\cdot}s)^{-1}$. The dressing overlap has major influence on the resulting surface roughness, but is held constant in order to get comparable results.

This specific control strategy works satisfactorily for medium finishing feed rates but just

with restrictions for finishing utilizing low plunge grinding feed rates. Numerous tests reveal that the RPM-Synchronous Grinding process with medium feed rates acts more passively than the one applying low feed rates. This can be confirmed, even when the controller is tuned proactively. Figure 8.4.5 displays the finishing process with a constant feed rate of $v_{fr} = 0.050\,\mathrm{mm{\cdot}min^{-1}}$. The peaks occur more rarely, their amplitude is not as high any more, but their rising edge is still very steep.

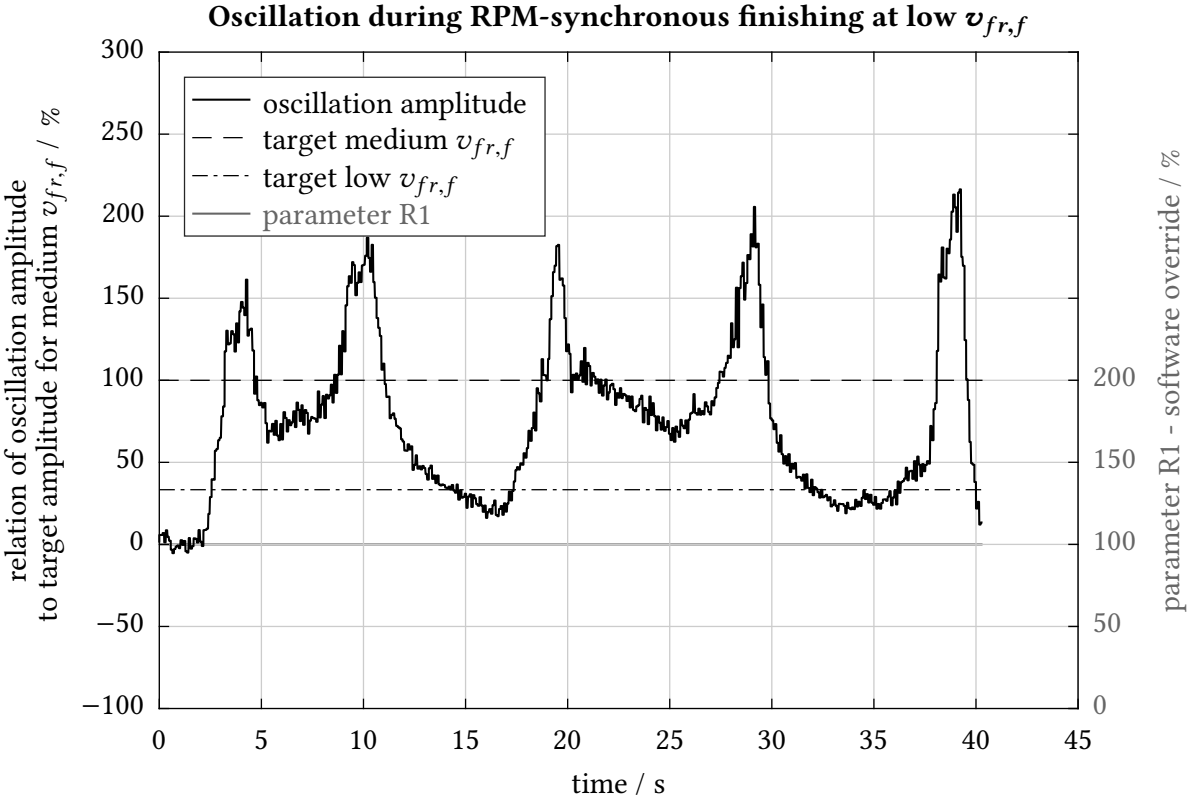

Figure 8.4.5: Oscillation amplitude at finishing (constant radial feed rate), Source: own illustration.

For this RPM-Synchronous Grinding process with low finishing feed rates different concepts of process adaption strategies are tested in a series of experiments. The thereby developed algorithm is implemented with a two-point controller. This digital process adaption strategy is characterized by just two feasible states of the software override: 1 equals 100% feed rate, 0 equals 20 % feed rate.

In comparison to the uncontrolled process, Figure 8.4.6 shows the behaviour of the grinding process with digital process adaption. This mentioned strategy works like a step function which is sent to the parameter R1 on the grinding machine. This parameter acts as software override for the feed rate during the process.

The target amplitude for finishing constitutes one third of the target amplitude for medium

finishing feed rate. Whenever this 33.3% are exceeded, the algorithm sets the software override of the radial feed rate from 100% to 20%. In the presented experiments, the default feed rate of v_{fr} = 0.050 mm·min^{-1} is reduced to v_{fr} = 0.010 mm·min^{-1}. This has two major effects: First, the amplitudes of the oscillation during the process get smaller and the oscillation abates more quickly. Second, during occurring oscillations less workpiece material is removed due to the significantly reduced feed rate. Therefore, the damage at the workpiece and the grinding wheel caused by the oscillation are minimized.

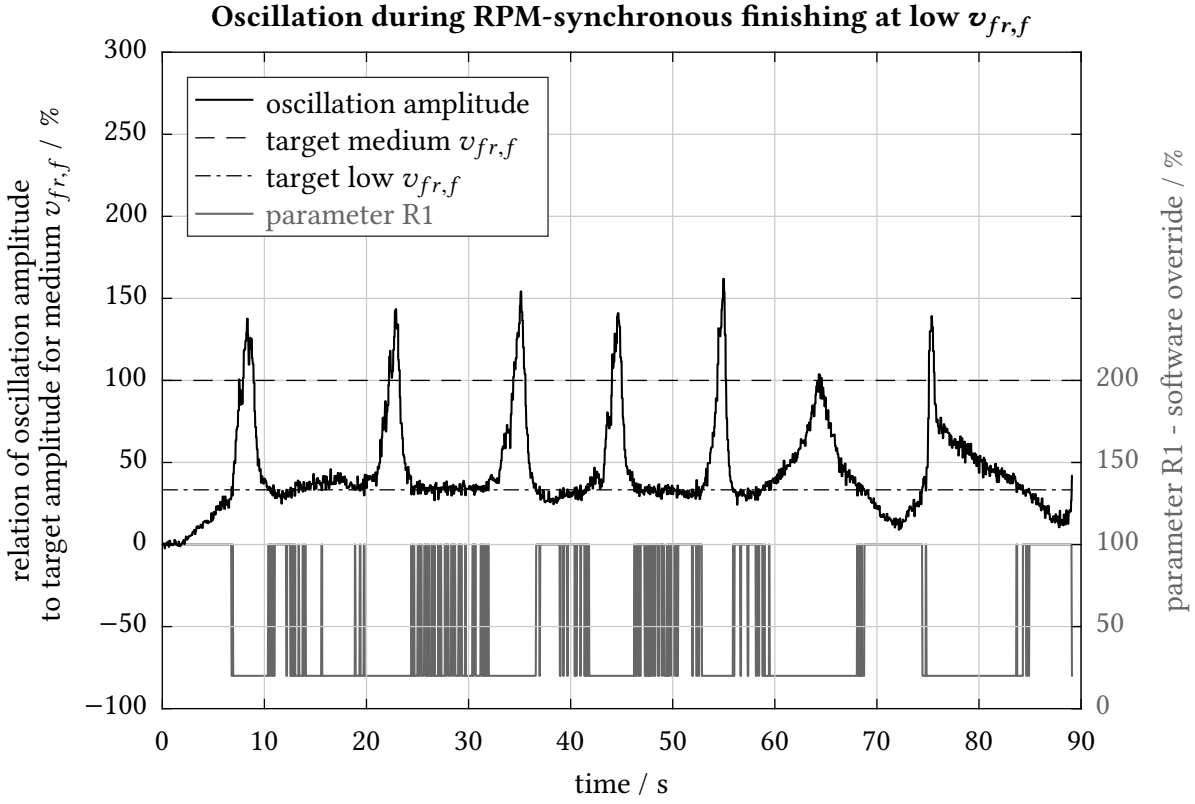

Figure 8.4.6: Oscillation amplitude at finishing with digital process adaption, Source: own illustration.

At the same time, a wrecking of the grinding wheel composition can be excluded. The tool wear is reduced and the surface of the grinding wheel remains undamaged. As a major result, the roughness quality of the workpiece surface is improved simultaneously.

Conclusion for the application of control concepts

With the presented control and adaption strategy for low finishing feed rate, an arithmetical mean deviation of R_a = 0.20 µm could be reached for counter direction grinding. For equal direction grinding almost the same results can be approved. In the latter case, a surface roughness of R_a = 0.22 µm could be gained. Both results state an improvement of approximately 15%

in surface roughness quality. Figure 8.4.7 shows these improvements for equal and for counter direction grinding in the RPM-Synchronous Grinding process with low finishing feed rates and the application of a two-point controller.

The presented control strategy for medium finishing feed rates shows significant improvement concerning values for R_a as well. Though, it still could not reach the high demands on general grinding processes. This fact is also explainable by the inappropriate choice of grinding wheel composition. The THELEICO - 85C220-0O4B9240 is rather soft and therefore very difficult to handle within the RPM-Synchronous Grinding process.

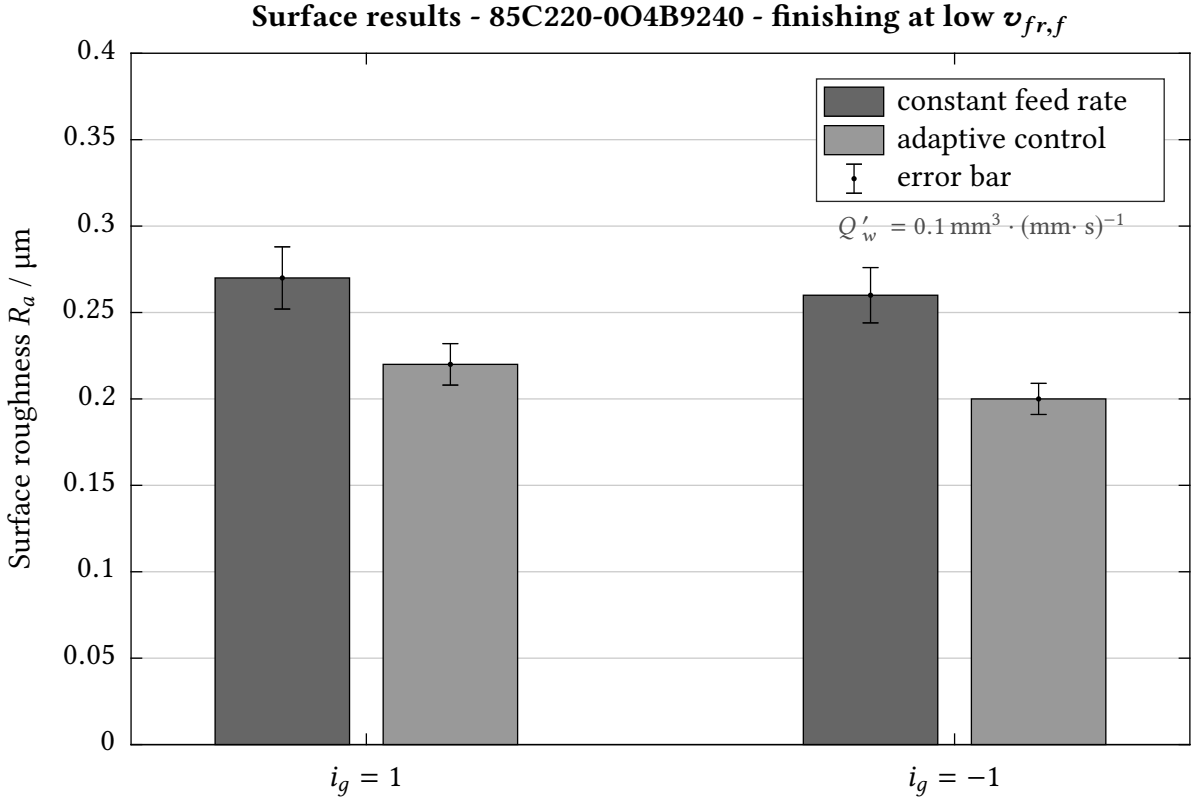

Figure 8.4.7: Surface roughness qualities with and without digital process adaption, Source: own illustration.

Bottom line, the presented control strategies have their justifications. They show the ability to improve surface roughness qualities on the workpiece as well as reducing the tool wear during the process. The correct selection of the grinding wheel in a previous step (according to the results of section 8.2.2) is inevitable in order to achieve optimal results.

9 Summary and Outlook

The new approach of RPM-Synchronous Grinding offers high potential especially for final processing of macro- and micro-structured workpieces. The rotatory synchronization of the workpiece and the grinding wheel allows the machining of non-circular and non-cylindrical parts in a single plunge grinding process for the first time. Simultaneously, it is possible to produce functional surfaces which lower friction, improve efficiency, reduce emissions and therefore contribute to sustainability.

The aim of the last chapter is to summarize the major results and to give key messages for further research on the topic of Synchronous Grinding.

9.1 Recapitulation of Topics

The **research grinding machine** at the Institute of Production Engineering at Graz University of Technology is prepared for today's and upcoming demands in scientific grinding studies:

- The machine design is realized incorporating two grinding units within a single machine concept: One RPM-Synchronous Grinding (RSG) unit and one Conventional Grinding (CG) unit which can both be applied for circular and non-circular grinding.
- Weight optimization of the X-axis slide enables highly dynamic dressing of non-circular grinding wheels for the RPM-Synchronous Non-Circular Grinding process and for highly efficient conventional grinding of non-circular workpieces.
- 3-component force measurement is incorporated into the machine design for measuring and instant analysis of machining forces during processing.
- External control is attached to enable process interference during machining cycles.
- Adaptive grinding process guidance and control strategies are developed. They allow reaction on changes of major conditions during single grinding processes based on the force sensor's signal.

The general functionality of the **RPM-Synchronous Grinding** is confirmed using carefully selected tool specifications and processing strategies:

- For the first time, industry-relevant surface roughness qualities on workpieces could be reached applying the technology of RPM-Synchronous Grinding.
- The RPM-Synchronous Grinding process shows similar results for equal- and counter-direction grinding. Therefore, a minimum ratio in diameter of the grinding wheel and the workpiece of at least 15:1 is a fundamental requirement.
- Using common grinding wheel specifications, the RPM-Synchronous Grinding process has to be divided in a roughing and a finishing sub-process to achieve both, considerable material removal rates and high surface qualities.
- During roughing, grinding forces tend to be smaller or equal implementing RSG compared to CG. Therefore, grinding wheel wear of equal dimension is documented using an appropriate tool.
- The resulting surface roughness on the workpiece after finishing depends on the following factors:
  - tool's grain size (180 - 220 mesh)
  - dressing overlap (must be chosen significantly higher for RSG)
  - grinding feed rate
  - process adaption strategy (optional)
- In general, sintered corundum grains or a mixture of sintered and fused corundum grains work well for rouging and finishing.
- The degree of hardness of the bonding and its structure have major influence on the functionality of the process concerning the amount of tool wear.
- The following results can be achieved using RSG:
  - specific material removal rate: up to $Q'_w = 30\,\mathrm{mm^3 \cdot (mm \cdot s)^{-1}}$ at roughing
  - surface roughness: arithmetical mean deviation $R_a < 0.150\,\mu\mathrm{m}$ at plunge grinding
  - surface roughness: arithmetical mean deviation $R_a < 0.070\,\mu\mathrm{m}$ at plunge grinding plus Z-oscillation during spark-out
  - reduction of surface roughness of 15% applying an adaptive control strategy

RPM-Synchronous Grinding provides various **fields of application**:

- Generation of non-circular and non-cylindrical workpieces in a plunge grinding process (RPM-Synchronous Non-Circular Grinding).
  - steel piston, piston ring
  - shaft-hub connection
  - cam, camshaft
  - …
- Generation of micro-structured workpiece surfaces, so called functional surfaces. Such patterned interfaces contain cavities (riblets) which serve as oil reservoirs or reduce flow losses. Major benefits for diverse product families are:
  - reduction of friction
  - reduction of flow losses
  - improvement of efficiency
  - life-time extension
  - reduction of emissions
  - preservation of resources
  - …
- The process of RPM-Synchronous Grinding allows the separation of specific workpiece surface areas in sectors which are processed by different tool qualities and compositions.

9.2 Prospect for Future Tasks

The perspective promises upcoming demands for the process of RPM-Synchronous Grinding in the near and intermediate future. Especially the demand for further optimization of workpieces concerning their ecological footprint leads to a rethinking of their production concepts. Thereby, RPM-Synchronous Grinding provides a possible answer.

The general functionality of the process could be proved. But there are still several open questions concerning tool and process:

- The **grinding wheel development** constitutes a major point.
  - Is it feasible to apply the same tool for RSG-roughing and -finishing?
  - Different grain types and sizes could possibly be used in one grinding wheel composition to allow roughing and finishing by adopting the dressing strategy.
  - The tool could be developed in such a way that different areas are used for roughing rather than for finishing.
- The **software development** for the calculation of the dressing procedures for the generation of non-circular grinding wheels should be one of the major tasks for future considerations.
  - It is necessary to provide a software (CAM) which generates a G-code of dressing of non-circular tool derived from a 3-dimensional CAD part. Especially for industrial application of the RPM-Synchronous Grinding process a convenient data handling is necessary.
- A **dressing concept** for micro-structuring of grinding wheel surfaces has to be developed, tested and evaluated in order to generate riblets on circular and non-circular workpieces.

The vision of the future is the implementation of RPM-Synchronous Grinding in industry as a highly efficient machining process. If the advantages of this process are deployed purposefully, workpieces with optimized shape and surface properties will be generated. The use of these parts will lead to the overall reduction of losses and therefore to a preservation of resources. The presented thesis constitutes a solid basis for further research on the topic of RPM-Synchronous Grinding and introduces a tailor-maid machine tool system. With RSG manufactured workpieces provide the opportunity to improve the ecological legacy of their particular field of application.

List of Figures

List of Tables

Bibliography

3M Deutschland GmbH online (2017/07/05). *Kontinuierliches Wälzschleifen von Verzahnungen.* URL: https://www.schleifprofi.com/schleifverfahren/zahnflankenschleifen/kontinuierliches-waelzschleifen-von-verzahnungen/.

Ablinger R. (2014). *Drehzahlsynchrones Unrundschleifen.* Doctoral Thesis, Graz University of Technology.

Ablinger R., Edler J., Mortsch M. (2012a). *Basic Research in RPM-Synchronous Non-Circular Grinding*. Bulletin of Engineering, V/4, pp.55–58.

– (2012b). *Reduction in costs using rpm-synchronous noncircular grinding.* Management of Technology Step to Sustainable Production, Zadar, pp.193–199.

Ablinger R., Schmid A. (2014a). *Method for non-circular grinding of cam of assembled camshaft in combustion engine of lorry, involves displacing workpiece and grinding roller relative to each other such that grinding path at surface of roller follows non-circular helix.* DE Patent App. DE201,210,015,752. Google Patents (2017/08/10), URL: https://www.google.com/patents/ DE 102012015752A1?cl=en.

– (2014b). *Method for noncircular grinding of workpiece, involves rotating workpiece and grinding wheel around respective parallel axes, where grinding surface of wheel is noncircular and non-cylindrical, and workpiece is displaced by cardanic driving.* DE Patent App. DE201,210,015, 754. Google Patents (2017/08/10), URL: https://encrypted.google.com/patents/DE102012015 754A1?cl=en.

Albisser E., Albasini F., Rossmann F. J., Henzmann H., Hensel S., Zimmerling E., Kaufleitner F., Klingler-Deiseroth C., Stern M., Potter C., Ruf R., Sachse S. (2014). *OPC UA: Ready for real time.* Bernecker + Rainer Industrie-Elektronik Ges.m.b.H., The B&R Technology Magazine, automotion 11.16, pp. 1-68. (2017/07/10) URL: https://www.br-automation.com/smc/de28df b1a87363af2dd9163915d8057ba5ef7557.pdf.

Böge A., Eichler J. (2008). *Physik für technische Berufe.* 11., aktualisierte und erweiterte Auflage, Vieweg+Teubner.

Brill J. (1977). *Contour grinding in series and mass production.* Werkstatt und Betrieb; No. 9, p. 623.

Brinksmeier E., Meyer L. (2004). *Schleifprozessüberwachung mit sensorbestückten Werkzeugen.* (Hrsg.) Klocke F., Pritschow. G; Automome Produktion; Springer-Verlag Berlin Heidelberg.

Comley P.,Walton I., Jin T., Stephenson D.J. (2006). *A High Material Removal Rate Grinding Process for the Production of Automotive Crankshafts.* Annals of the CIRP Vol. 55/1/2006.

da Silva E.J., de Oliveira J. F. G., Salles B. B., Cardoso R.S., Reis V. R. A., (2013). *Strategies for production of parts textured by grinding using patterned wheels.* CIRP Annals – Manufacturing Technology 62; pp. 355-358.

Degner W.,Lutze H., Smejkal E. (2015). *Spanende Formung.* Carl Hanser Verlag GmbH & Co. KG, 17. aktualisierte Auflage.

Denkena B., Boehnke D., Wang B. (2009). *Manufacturing of functional microstructured surfaces by grinding with vitrified SiC- and cBN-wheels.* Int. J. Abracive Technology, Vol. 2, No. 2; pp. 207–222.

Denkena B., Grove T., Göttschnigg T., da Silva E. J., Coelho R. T., Filleti R. (2015). *Enhanced grinding performance by means of patterned grinding wheels.* Int. J. Adv. Manuf. Technol., 77; pp. 1935-1941.

Denkena B., Kästner J., Wang B. (2010). *Advanced microstructures and ist production through cutting and grinding.* CIRP Annals - Manufacturing Technology 59; pp. 67-72.

Denkena B., Köhler J., Göttschnig T. (2013). *Influence of micro patterned grinding wheels on the workpiece quality.* Proceedings of the 13th euspen International Conference - Berlin; pp. 249-252.

DIN 8580 (2003-09). *Manufacturing processes. Terms and definitions, division.* Ed. by DIN. Beuth Verlag Berlin.

Dong S., Danai K., Malkin S., Deshmukh A. (2004a). *Continuous Optimal Infeed Control for Cylindrical Plunge Grinding. Part 1: Methodology.* Journal of Manufacturing Science and Engineering; ASME; Vol. 126, pp. 327-333.

– (2004b). *Continuous Optimal Infeed Control for Cylindrical Plunge Grinding. Part 2: Controller Design and Implementation.* Journal of Manufacturing Science and Engineering; ASME; Vol. 126, pp. 334-340.

Eichhorn H. (1997). *Drehzahlsynchronisation der Wirkparameter beim Abrichten und Schleifen.* Doctoral Thesis, Fraunhofer Institute for Production Systems and Design Technology (IPK), Berlin.

Erven J., Schwägerl D. (2011). *Mathematik für Ingenieure. 4., korrigierte Auflage.* Oldenbourg Verlag München.

Hecker R.L., Liang S.Y., Woodruff G.W. (2002). *Power Feedback Control in Cylindrical Plunge Grinding with an Inner Repetitive Position Control Loop.* Proceedings of the 2002 IEEE, International Symposium on Intelligent Control, Vancouver, Canada, pp. 642–647.

Heisel U., Klocke F., Uhlmann E., Spur G. (2014). *Handbuch Spanen*. Carl Hanser Verlag GmbH & Co. KG.

Jerard R. B., Fussell B. K., Suprock C. A.; Cui Y., Nichols J., Hassan R. Z., Esterling D. (2009). *Integration of wireless sensors and models for a smart machining system*. Proceedings of the ASME International Manufacturing Science and Engineering Conference, MSEC2009, pp. 119-128.

Kassen G. (1969). *Beschreibung der elementaren Kinematik des Schleifvorgangs*. Doctoral Thesis, RWTH Aachen.

KBA. n.d. In Statista - Das Statistik-Portal. (2017/07/04a). *Anzahl der Neuzulassungen von Elektroautos in Deutschland von 2003 bis 2017**. URL: https://de.statista.com/statistik/daten/studie/244000/umfrage/neuzulassungen-von-elektroautos-in-deutschland/.

KBA, VDA, IHS, EurotaxSchwacke. n.d. In Statista - Das Statistik-Portal. (2017/07/04b). *Anzahl der Neuzulassungen von Pkw in Deutschland von 1955 bis 2019 (in Millionen)*. URL: https://de.statista.com/statistik/daten/studie/74433/umfrage/neuzulassungen-von-pkw-in-deutschland/.

KISTLER GmbH online (2017/06/07a). *3-Component Force Sensor, Type 9047C*. URL: https://www.kistler.com/ ?type=669&fid=59552. pp.1-4.

– (2017/06/07b). *Force Sensors, Basics of Measurement Technology*. URL: https://www.kistler.com/ ?type=669& fid=278& model=download& callee=frontend.

Klocke F., König W. (2005). *Fertigungsverfahren. Band 2: Schleifen, Honen, Läppen*. Springer-Verlag, Berlin Heidelberg New York, ISBN 13: 978-3-540-23496-8.

LEICA Microsystems AG online (2017/10/8). *Leica DCM8*. pp. 1-16. URL: http://www.leica-microsystems.com/fileadmin/downloads/Leica%20DCM8/Brochures/Leica_DCM8_Brochure_EN.pdf.

Li G.F., Wang L.S., Yang L.B. (2002). *Multi-parameter optimization and control of the cylindrical grinding process*. Journal of Materials Processing technology 129, pp. 232-236.

Lortz W. (1975). *Schleifscheibentopographie und Spanbildungsmechanismus beim Schleifen*. Dissertation, RWTH Aachen.

Mahmoud M.S., Sabih M., Elshafei M. (2015). *Using OPC technology to support the study of advanced process control*. ISA Transactions 55; pp. 155-167.

Malkin S., Guo C. (2007). *Thermal Analysis of Grinding*. Annals of the CIRP Vol. 56/2, pp. 760-782.

Malkin S., Lenz E. (1978). *Burning Limit for Surface and Cylindrical Grinding of Steels*. Annals of the CIRP Vol. 27/1, pp. 233-236.

Malkin S., Mayne R.W. (1976). *Optimization of Operating Parameters for Grinding of Steels*. J. Engineering for Industry, Trans. ASME; Vol. 98, pp. 468-473.

Malkin S., Mayne R.W., Varadarajan G. (1976). *Optimization of Precision Grinding Processes for Maximum Removal Rate*. Proc. Fourth North American Metalworking Research Conference; Columbus, Ohio, pp. 457-463.

Marinescu I. D., Hitchiner M. P., Uhlmann E., Rowe W. B., Inasaki I. (2016a). *Handbook of Machining with Grinding Wheels*. Second Edition, CRC Press, Taylor and Francis Group.

Marinescu I. Hitchiner M., Uhlmann E., Rowe B., Inasaki I. (2016b). *Handbook of Machining with Grinding Wheels*. CRC Press, Boca Raton, ISBN: 978-1-4822-0670-8.

Masslow E. N. (1952). *Grundlagen der Theorie des Metallschleifens*. Vertag Technik, Berlin.

Mautz A. (2003). *Untersuchungen zum CNC-Unrundschleifen mit Schwerpunkt Formabweichung*. Doctoral Thesis, Graz University of Technology.

Mayr R. (1993). *Formschlüssige Welle-Nabe-Verbindung mit Innenschleifbarer Kontur*. Doctoral Thesis, Graz University of Technology.

Meister M. (2011). *Vademecum des Schleifens*. Carl Hanser Verlag, München, ISBN: 978-3-446-42618-4.

Messer J. (1983). *Abrichten konventioneller Schleifscheiben mit stehenden Werkzeugen*. Doctoral Thesis, RWTH Aachen.

National Instruments Corporation (2014). *NI cDAQ-9184 4-Slot Ethernet NI CompactDAQ Chassis Ordering Information*. National Instruments Corporation; pp.1-5; (2017/10/5) URL: http://www.ni.com/datasheet/pdf/en/ds-427.

Oliveira J. F. G., Bottene A. C., Franca T. V. (2010). *A novel dressing technique for texturing of ground surfaces*. CIRP Annals – Manufacturing Technology 59; pp. 361-364.

OPC Foundation (2015). *OPC Unified Architecture Specification. Part 1: Overview and Concepts Release 1.03*. OPC Foundation, October 10, pp. 7–21. URL: https://opcfoundation.org/developer-tools/specifications-unified-architecture/part-1-overview-and-concepts PDF file.

Ott H. W. (2002). *Richtig gekühlt ist halb geschliffen - eine eher physikalische Betrachtung*. Moderne SChleiftechnologie, 4. Seminar 25.04.2002, Villingen-Schwenningen, HRSG. Prof. Dr.-Ing. T. Tawakoli pp. 7-1.

Patzig C. (2002). *Maschinenintegrierte Post-Process Form-Messung beim CNC-Unrundschleifen*. Doctoral Thesis, Graz University of Technology.

Riemenschneider C. (2009). *Untersuchung und Adaption von Fertigungsverfahren für die Bearbeitung unrunder Konturen am Beispiel der Polygonprofile nach DIN 32711 und DIN 32712*. Doctoral Thesis, Graz University of Technology.

Rowe B. (2014). *Principles of Modern Grinding Technology. Second Edition.* Elsevier Inc., ISBN: 978-0-323-24271-4.

Sawluk W., Wiemann H.-J. (1985). *Advanced Technique in Application of Diamond Dressing Rollers.* The Winter Annual Meeting of the Society of Mechanical Engineers, Miami Beach, Florid, USA, Nov. 17-22.

Schmid A. (1986). *Unrundschleifen auf prozessrechner-gesteuerten Rundschleifmaschinen.* Doctoral Thesis, Graz University of Technology.

Schmitt R. (1968). *Truing of Grinding Wheels with Diamond Studded Roller.* Doctoral Thesis, TU Braunschweig.

Siebertz K., van Bebber D. (2010). *Statistische Versuchsplanung, Design of Experiments (DoE).* Springer-Verlag Berlin Heidelberg.

SIEMENS AG online (2016/08/04). *1FN3450-4NB80-0BA1.* https://mall.industry.siemens.com/mall/de/pl/Catalog/Product/ 1FN3450-4NB80-0BA1.

– (2017/06/05). *SINUMERIK Integrate for Engineering Access MyMachine / OPC UA, 2014.* Inbetriebnahmehandbuch 6FC5397-1DP40-3AA2, pp. 7–21. URL: https://cache.industry.siemens.com/dl/files/062/89536062/att_908540/v1/840D_OPCUA_10-14_de-DE.pdf.

– (2017/06/12). *SINUMERIK 840D sl / 828D Erweiterungsfunktionen Funktionshandbuch, 03/2013, 6FC5397-1BP40-3AA1. K3: Kompensationen.* https://cache.industry.siemens.com/dl/files/016/-74523016/att_35520/ v1/FB2sl_0313_de_de-DE.pdf.

– (2017/10/16). *Continuous Load Motors of the 1FN3 Product Family. SIMODRIVE 611. 6SN1197-0AB74-0BP3 2008. Configuration Manual 03/2008 Edition.* https://cache.industry.siemens.com/dl/files/239/32800239/att 74577/v1/PHB_1FN3-SLM_SIMODRIVE_0408_en_en-US.pdf.

Spur G., Eichhorn H. (1993). *Unrundschleifen durch starre kinematische Kopplung der Wirkpartner.* Industrie-Diamanten-Rundschau, 27/3, pp. 179–187.

– (1994). *Contour grinding by rigid kinematic coupling of the interacting partners.* Industrial diamond review, 54/560, pp. 35–42.

– (1995). *Contour grinding by rigid kinematic coupling of the interacting partners.* Production Engineering, 2/2, pp. 15–20.

– (1996a). *Drehzahlsynchrones Abrichten – Einfluss der Einstellparameter auf das Abrichtergebnis.* Industrie-Diamanten-Rundschau, 30/1, pp. 48–58.

– (1996b). *Drehzahlsynchrones Abrichten – Einfluss der Schneidenraumstruktur auf das Schleifergebnis.* Industrie-Diamanten-Rundschau, 30/2, pp. 126–137.

– (1997a). *Drehzahlsynchrones Unrundschleifen.* Industrie-Diamanten-Rundschau, 31/3, pp. 242–246, 248–254.

Spur G., Eichhorn H. (1997b). *Drehzahlsynchronisiertes Unrundschleifen auf einer Zahnradhonmaschine.* Zeitschrift für wirtschaftlichen Fabrikbetrieb, 92/6, pp. 268-272.

Steffan M., Edler J., Zopf P., Haas F. (2017). *Optimierung der Schleifbearbeitung mittels OPC UA.* Zeitschrift für wirtschaftlichen Fabrikbetrieb, 03/2017/112; pp.137-140.

Steffens K., Lauer-Schmaltz H. (1978). *Spanbildungstheorie für das Schleifen.* Industrie-Anzeiger 100, pp.49-50.

Tan V.V., Yoo D.S., Yi M.J. (2009). *An Approach to Remote Monitoring and Control based on OPC Connectivity.* IFAC Proceedings Volumes; Volume 42, Issue 3; pp.259-262.

The MathWorks, Inc. (2017/07/07a). *Data Acquisition Toolbox User's Guide, R2017a.* The MathWorks, Inc.; pp.1-254, URL: http://www.mathworks.com/help/pdf_doc/daq/daqug.pdf.

– (2017/07/07b). *OPC Toolbox User's Guide, R2017a.* The MathWorks, Inc.; pp.1-614, URL: http://cn.mathworks.com/help/pdf_doc/opc/opc.pdf.

Vits R. (1985). *Technologische Aspekte der Kühlschmierung beim Schleifen.* Doctoral Thesis, City Print Verlag, Aachen, pp. 71-73.

VOLUMETRIC online (2017/06/12). *Volumetric Compensation System for SINUMERIK 840D sl, January 2009.* http://www.volumetric.com.br/cases/volumetric-compensation-system.pdf.

Wagner G. (1993). *Process Monitoring beim CNC – Unrundschleifen.* Doctoral Thesis, Graz University of Technology.

Wang W., Zhang X., Li Y., LI Y. (2016). *Open CNC machine tool's state data acquisition and application based on OPC specification. 9th International Conference on Digital Enterprise Technology - DET 2016 – Intelligent Manufacturing in the Knowledge Economy Era; pp.384-388.* Procedia CIRP 56.

Werner G., Tawakoli T. (1988). *Fortschritte beim HEDG-Verfahren mit CBN-Schleifscheiben.* Industrie Diamanten Rundschau 221.

Zuderstorfer G. (2006). *KelPoly – Software für das Unrundschleifen. Entwicklung und wissenschaftliche Grundlagen.* Doctoral Thesis, Graz University of Technology.